



Swansea University  
Prifysgol Abertawe



## Swansea University E-Theses

---

# Low Reynolds number heat transfer prediction employing large eddy simulation for electronics geometrics.

Tyacke, James C

### How to cite:

---

Tyacke, James C (2009) *Low Reynolds number heat transfer prediction employing large eddy simulation for electronics geometrics..* thesis, Swansea University.

<http://cronfa.swan.ac.uk/Record/cronfa42811>

### Use policy:

---

This item is brought to you by Swansea University. Any person downloading material is agreeing to abide by the terms of the repository licence: copies of full text items may be used or reproduced in any format or medium, without prior permission for personal research or study, educational or non-commercial purposes only. The copyright for any work remains with the original author unless otherwise specified. The full-text must not be sold in any format or medium without the formal permission of the copyright holder. Permission for multiple reproductions should be obtained from the original author.

Authors are personally responsible for adhering to copyright and publisher restrictions when uploading content to the repository.

Please link to the metadata record in the Swansea University repository, Cronfa (link given in the citation reference above.)

<http://www.swansea.ac.uk/library/researchsupport/ris-support/>

# Low Reynolds number heat transfer prediction employing Large Eddy Simulation for electronics geometries

by

**James C. Tyacke**

Submitted to Swansea University as partial fulfillment of the requirements for  
the Degree of Doctor of Philosophy of Engineering

*Civil and Computational Engineering Centre, School of Engineering, Swansea  
University, Singleton Park, Swansea, SA2 8PP.*

2009

ProQuest Number: 10807587

All rights reserved

INFORMATION TO ALL USERS

The quality of this reproduction is dependent upon the quality of the copy submitted.

In the unlikely event that the author did not send a complete manuscript and there are missing pages, these will be noted. Also, if material had to be removed, a note will indicate the deletion.



ProQuest 10807587

Published by ProQuest LLC (2018). Copyright of the Dissertation is held by the Author.

All rights reserved.

This work is protected against unauthorized copying under Title 17, United States Code  
Microform Edition © ProQuest LLC.

ProQuest LLC.  
789 East Eisenhower Parkway  
P.O. Box 1346  
Ann Arbor, MI 48106 – 1346



# Contents

<b>Contents</b>	<b>viii</b>
<b>Summary</b>	<b>ix</b>
<b>Declaration</b>	<b>xi</b>
<b>Acknowledgments</b>	<b>xii</b>
<b>List of Tables</b>	<b>xiv</b>
<b>List of Figures</b>	<b>xxi</b>
<b>Nomenclature</b>	<b>xxix</b>
<b>1 Introduction</b>	<b>1</b>
1.1 Background . . . . .	1
1.1.1 Historical challenges of electronics cooling . . . . .	1
1.1.2 Use of numerical modelling . . . . .	3

---

1.2	Objectives of the study . . . . .	5
1.3	Thesis outline . . . . .	6
<b>2</b>	<b>Literature review</b>	<b>7</b>
2.1	Introduction . . . . .	7
2.2	Ribbed channel and similar flows . . . . .	8
2.3	Flow around cubes and square cylinders . . . . .	9
2.4	Full systems and other relevant geometries . . . . .	12
2.5	LES modelling . . . . .	13
2.6	Summary . . . . .	14
<b>3</b>	<b>Turbulence Modelling</b>	<b>15</b>
3.1	Introduction . . . . .	15
3.2	Turbulence . . . . .	15
3.3	Kolmogorov hypotheses and turbulent scales . . . . .	16
3.4	Approaches to turbulence modelling . . . . .	18
3.4.1	Direct numerical simulation (DNS) . . . . .	18
3.4.2	Reynolds-averaged Navier-Stokes (RANS) . . . . .	19
3.4.3	Large eddy simulation (LES) . . . . .	20
3.4.4	Hybrid RANS-(I)LES . . . . .	21

---

3.5	Governing equations . . . . .	22
3.6	Turbulence modelling - RANS . . . . .	23
3.6.1	Reynolds stresses . . . . .	23
3.6.2	Eddy-viscosity models . . . . .	24
3.7	Turbulence modelling - (I)LES . . . . .	27
3.7.1	Residual/Subgrid stresses . . . . .	27
3.7.2	Filtering . . . . .	30
3.7.3	Grid independence of LES . . . . .	32
3.7.4	Linear eddy-viscosity models (LEVMS) . . . . .	33
3.7.5	Mixed nonlinear models . . . . .	37
3.7.6	ILES . . . . .	41
3.8	Turbulence modelling - hybrid RANS-(I)LES . . . . .	42
3.8.1	$k-l$ based RANS-LES . . . . .	42
3.8.2	$k-l$ based RANS-ILES . . . . .	43
3.9	Summary . . . . .	44
<b>4</b>	<b>NEAT code details and numerical methods</b>	<b>45</b>
4.1	Introduction . . . . .	45
4.2	NEAT code details . . . . .	47
4.3	Finite volume method overview . . . . .	47

---

4.4	Spatial discretisation . . . . .	48
4.4.1	False diffusion . . . . .	51
4.4.2	Second order central difference . . . . .	53
4.4.3	Second order upwind . . . . .	53
4.4.4	QUICK . . . . .	54
4.4.5	Fourth order central difference . . . . .	54
4.5	Basic solution procedure . . . . .	55
4.6	Changes made to the NEAT code . . . . .	56
4.7	Summary . . . . .	57
<b>5</b>	<b>Performance optimisation</b>	<b>58</b>
5.1	Introduction . . . . .	58
5.2	Starting conditions . . . . .	58
5.3	Successive grid refinement . . . . .	60
5.4	Parallel computation . . . . .	62
5.5	Convergence criteria . . . . .	65
5.5.1	Typical residual and RMS monitoring . . . . .	65
5.5.2	Fourier analysis . . . . .	67
5.6	Recommendations . . . . .	72



---

<b>6</b>	<b>High order validation and verification</b>	<b>74</b>
6.1	Introduction . . . . .	74
6.2	1D cell face interpolation test . . . . .	74
6.3	Tollmien-Schlichting wave propagation . . . . .	76
6.4	Convection of a vortex . . . . .	80
6.5	Sources of second order errors . . . . .	85
6.5.1	Cell topology . . . . .	85
6.5.2	Staggered grid . . . . .	86
6.5.3	Surface quadrature . . . . .	86
6.5.4	Time integration . . . . .	87
6.6	Summary . . . . .	87
<b>7</b>	<b>Electronics heat transfer test cases</b>	<b>88</b>
7.1	Introduction . . . . .	88
7.2	Heated ribbed channel . . . . .	89
7.2.1	Case description . . . . .	89
7.2.2	Flow structure . . . . .	92
7.2.3	Average errors . . . . .	93
7.2.4	Mean velocity distributions . . . . .	98
7.2.5	Higher order statistics . . . . .	98

---

7.2.6	Reattachment length . . . . .	102
7.2.7	Heat transfer . . . . .	102
7.2.8	Pressure differentials . . . . .	105
7.2.9	Conclusions . . . . .	106
7.3	Array of wall mounted cubes . . . . .	107
7.3.1	Case description . . . . .	107
7.3.2	Flow structure . . . . .	111
7.3.3	Average errors . . . . .	112
7.3.4	Mean velocity distributions . . . . .	112
7.3.5	Higher order statistics . . . . .	119
7.3.6	Heat transfer . . . . .	122
7.3.7	Pressure differentials . . . . .	126
7.3.8	Conclusions . . . . .	126
7.4	Complex CPU case . . . . .	128
7.4.1	Case description . . . . .	128
7.4.2	Flow structure . . . . .	131
7.4.3	Average errors . . . . .	133
7.4.4	Mean velocity profiles . . . . .	133
7.4.5	Turbulence intensity profiles . . . . .	137

---

7.4.6	Heat transfer . . . . .	137
7.4.7	Conclusions . . . . .	139
<b>8</b>	<b>LES model applicability</b>	<b>141</b>
8.1	Introduction . . . . .	141
8.2	Assumption of a long inertial subrange . . . . .	141
8.3	Filter choice . . . . .	147
8.4	Summary . . . . .	148
<b>9</b>	<b>Conclusions and future work</b>	<b>149</b>
9.1	Conclusions . . . . .	149
9.2	Recommendations for future work . . . . .	151
	<b>References</b>	<b>161</b>
<b>A</b>	<b>Full results</b>	<b>162</b>
A.1	Ribbed channel plots . . . . .	162
A.2	Array of cubes plots . . . . .	181
A.3	CPU case plots . . . . .	222
<b>B</b>	<b>Derivation and implementation of discretisation schemes</b>	<b>226</b>
B.1	Second order upwind scheme with positive coefficients . . . . .	226

---

B.2 QUICK scheme with positive coefficients . . . . .	231
B.3 Implementation of generalised cell face approximations . . . . .	240

---

## Summary

The accurate prediction of convective heat transfer within electronics systems has always been of great importance for the reliability of such systems. Current computational methods based on the Reynolds-Averaged Navier-Stokes equations do not provide reliable predictions due to the inability of current methods to capture complex time dependent flow features. This study investigates the use of time dependent Large Eddy Simulation and hybrid methods to make more reliable thermal predictions. These methods are tested on a heated ribbed channel, a heated cube in an array of cubes and a complex CPU case. A variety of models and methodologies are applied and analysed. It is apparent that the most important scales are the large vortices generated by geometrical features. Due to the low Reynolds number flows found in electronics systems, there is a relatively small range of scales to capture. This gives rise to some unpredictability in model choice and grid resolution, though consistency is much improved over traditional methods. Important sources of error are considered to be problem definition and boundary conditions for which unsteady data is not available. Use of nonlinear models and higher order discretisation did not provide adequate improvements in accuracy for the increase in computational expense. Combining Reynolds-Averaged Navier-Stokes and Implicit Large Eddy Simulation into a hybrid model seems to provide fair reliability when compared to other modelling methods on a range of grid resolutions.

---

## Declaration

This work has not previously been accepted in substance for any degree and is not being concurrently submitted in candidature for any degree.

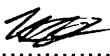
Signed .....(candidate)

Date *31/3/10*.....

### STATEMENT 1

This thesis is the result of my own investigation, except where otherwise stated. Where correction services have been used, the extent and nature of the correction is clearly marked in a footnote(s).

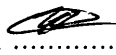
Other sources are acknowledged by footnotes giving explicit references. A bibliography is appended.

Signed .....(candidate)

Date *31/3/10*.....

### STATEMENT 2

I hereby give consent for my thesis, if accepted, to be available for photocopying and for inter-library loan, and for the title and summary to be made available to outside organisations.

Signed .....(candidate)

Date *31/3/10*.....

---

As part of the work carried out, the following papers were published.

- Tyacke, J. C. and Tucker, P. G. (2007). Unsteady CFD modelling for electronics cooling. In *International Conference on Thermal, Mechanical, and Multi-Physics Simulation and Experiments in Micro-Electronics and Micro-Systems (EUROSIME)*, pages 760–766
- Tyacke, J. C., Tucker, P. G., and Nithiarasu, P. (2008b). Strategies for modelling turbulent flows in electronics. In *Semiconductor Thermal Measurement and Management Symposium (SEMI-THERM)*, pages 39–46
- Tyacke, J., Tucker, P. G., and Nithiarasu, P. (2008a). Unsteady CFD modelling of turbulent flows for electronics. In *2nd Electronics System Integration Technology Conference (ESTC)*, pages 1157–1163

---

## Acknowledgments

I would first like to thank Paul Tucker for his continued supervision, sometimes he has been far away from Swansea. Without constant encouragement and consultation I would not have had the patience to pursue this to the end. I would like to thank the EPSRC and Mentor Graphics Corporation (previously Flomerics Group PLC) for funding my PhD. I would also like to express my appreciation to Prof. Nithiarasu for taking over some of my supervision and for signing so many forms for me.

Thanks also to John Parry for his many discussions and ideas and Dave Carswell for helping me with code problems. I am sure I have missed out many people who have helped me but there are too many to mention.

Finally I would like to thank Gwen for putting up with me for four years through the highs and the lows. She has tried her best to get me out of bed on time to debug code day after day and has always been there for me along with my family and friends. Thanks to everyone.



# List of Tables

1.1	Comparison of heat flux between a light bulb and a BGA Package . . . . .	2
3.1	Comparison of CFD modelling approaches (Liu 2004). . . . .	22
4.1	Weighting constants for east cell face interpolation on a uniform grid. . . . .	51
6.1	Discretisation scheme errors using non-uniform polynomial coefficients. . . . .	80
7.1	Ribbed channel parameters. . . . .	90
7.2	Ribbed channel grid details. . . . .	91
7.3	Ribbed channel average profile errors (%) ( $121 \times 112 \times 67$ grid). . . . .	94
7.4	Ribbed channel average profile errors (%) ( $121 \times 112 \times 33$ grid). . . . .	95
7.5	Ribbed channel average profile errors (%) ( $62 \times 57 \times 17$ grid). . . . .	96
7.6	Cube flow parameters. . . . .	108
7.7	Air and epoxy properties. . . . .	109
7.8	Heated cube grid details. . . . .	110

---

7.9	Cube array average profile errors (%) (109 × 109 × 109 grid).	113
7.10	Cube array average profile errors (%) (75 × 75 × 75 grid).	114
7.11	Cube array average profile errors (%) (53 × 51 × 53 grid).	115
7.12	Cube array average profile errors (%) (41 × 45 × 41 grid).	116
7.13	Constants for fan momentum sources.	130
7.14	CPU case grid details.	131
7.15	CPU case average profile errors (%) for all variables and grids.	134
7.16	Comparison of computation time for each model.	139
8.1	Approximate ratios and corresponding Reynolds numbers using RANS and geometric length-scales.	144

# List of Figures

1.1	Major causes of electronics failure . . . . .	3
2.1	Nusselt number results using various RANS models. . . . .	10
4.1	Geographical notation as used by Patankar (1980). . . . .	49
4.2	Different stencils used for cell-face interpolation. . . . .	52
5.1	Succession of finer grids for CPU case. . . . .	61
5.2	Illustration of OpenMP domain decomposition. . . . .	63
5.3	OpenMP NEAT code speedup compared to ideal linear speedup. . .	64
5.4	Frequency-Amplitude plot for ribbed channel data samples. . . . .	71
6.1	1D temperature function. . . . .	75
6.2	Error reduction for 1D temperature function. . . . .	76
6.3	TS wave computational domain. . . . .	77
6.4	Comparison of discretisation schemes. . . . .	79

---

6.5	Vorticity magnitude contours. . . . .	83
6.6	Vorticity profile taken through the center of the convected vortex. . .	84
6.7	Reduction of maximum vorticity error with grid refinement. . . . .	85
7.1	Ribbed channel. . . . .	90
7.2	Rib stream traces, mid- $z$ -plane. . . . .	93
7.3	Mean streamwise velocity distributions. . . . .	97
7.4	Mean cross-stream velocity distributions. . . . .	97
7.5	$\overline{u'u'}$ ditributions. . . . .	99
7.6	$\overline{v'v'}$ ditributions. . . . .	99
7.7	$\overline{u'v'}$ ditributions. . . . .	100
7.8	$Nu$ along the channel floor. . . . .	103
7.9	Absolute errors for $Nu$ using all SGS models. . . . .	105
7.10	Epoxy layer and stretched grid. . . . .	107
7.11	Cube array. . . . .	108
7.12	Heat transfer coefficient and surface temperature profiles. . . . .	109
7.13	Cube streamlines at $y/h = 0.25$ . . . . .	111
7.14	Mean $U$ velocity profiles at various $x/H$ -locations. . . . .	117
7.15	Mean $U$ velocity profiles at various $x/H$ -locations. . . . .	118
7.16	$u'u'$ profiles at various $x/H$ -locations. . . . .	120

---

7.17	$w'w'$ profiles at various $x/H$ -locations. . . . .	121
7.18	$Nu$ along heat transfer profiles. . . . .	123
7.19	Absolute errors for $Nu$ using all SGS models. . . . .	125
7.20	CPU case schematic. . . . .	129
7.21	CPU profile paths. . . . .	129
7.22	Mean $U$ velocity profiles (1-6). . . . .	135
7.23	Turbulence intensity (%) profiles (1-6). . . . .	136
7.24	$Nu_x$ along the heater element . . . . .	138
8.1	$R_{k-\varepsilon}$ and $L_{k-\varepsilon}$ contours for the electronics test cases. . . . .	143
8.2	Energy spectra for different length-scale ratios. . . . .	145
A.1	Mean $U$ velocity profiles at various $x/h$ -locations ( $121 \times 112 \times 67$ ). . . . .	163
A.2	Mean $V$ velocity profiles at various $x/h$ -locations ( $121 \times 112 \times 67$ ). . . . .	163
A.3	$\overline{u'u'}$ profiles at various $x/h$ -locations ( $121 \times 112 \times 67$ ). . . . .	164
A.4	$\overline{v'v'}$ profiles at various $x/h$ -locations ( $121 \times 112 \times 67$ ). . . . .	164
A.5	$\overline{u'v'}$ profiles at various $x/h$ -locations ( $121 \times 112 \times 67$ ). . . . .	165
A.6	$Nu$ profile along channel ( $121 \times 112 \times 67$ ). . . . .	165
A.7	Mean $U$ velocity profiles at various $x/h$ -locations ( $121 \times 112 \times 33$ ). . . . .	166
A.8	Mean $V$ velocity profiles at various $x/h$ -locations ( $121 \times 112 \times 33$ ). . . . .	166

---

A.9	$\overline{u'u'}$ profiles at various $x/h$ -locations ( $121 \times 112 \times 33$ ).	167
A.10	$\overline{v'v'}$ profiles at various $x/h$ -locations ( $121 \times 112 \times 33$ ).	167
A.11	$\overline{u'v'}$ profiles at various $x/h$ -locations ( $121 \times 112 \times 33$ ).	168
A.12	$Nu$ profile along channel ( $121 \times 112 \times 33$ ).	168
A.13	Mean $U$ velocity profiles at various $x/h$ -locations ( $62 \times 57 \times 17$ ).	169
A.14	Mean $V$ velocity profiles at various $x/h$ -locations ( $62 \times 57 \times 17$ ).	169
A.15	$\overline{u'u'}$ profiles at various $x/h$ -locations ( $62 \times 57 \times 17$ ).	170
A.16	$\overline{v'v'}$ profiles at various $x/h$ -locations ( $62 \times 57 \times 17$ ).	170
A.17	$\overline{u'v'}$ profiles at various $x/h$ -locations ( $62 \times 57 \times 17$ ).	171
A.18	$Nu$ profile along channel ( $62 \times 57 \times 17$ ).	171
A.19	Mean $U$ velocity profiles at various $x/h$ -locations ( $121 \times 112 \times 67$ ).	172
A.20	Mean $V$ velocity profiles at various $x/h$ -locations ( $121 \times 112 \times 67$ ).	172
A.21	$\overline{u'u'}$ profiles at various $x/h$ -locations ( $121 \times 112 \times 67$ ).	173
A.22	$\overline{v'v'}$ profiles at various $x/h$ -locations ( $121 \times 112 \times 67$ ).	173
A.23	$\overline{u'v'}$ profiles at various $x/h$ -locations ( $121 \times 112 \times 67$ ).	174
A.24	$Nu$ profile along channel ( $121 \times 112 \times 67$ ).	174
A.25	Mean $U$ velocity profiles at various $x/h$ -locations ( $121 \times 112 \times 33$ ).	175
A.26	Mean $V$ velocity profiles at various $x/h$ -locations ( $121 \times 112 \times 33$ ).	175
A.27	$\overline{u'u'}$ profiles at various $x/h$ -locations ( $121 \times 112 \times 33$ ).	176

---

A.28 $\overline{v'v'}$ profiles at various $x/h$ -locations ( $121 \times 112 \times 33$ ).	176
A.29 $\overline{u'v'}$ profiles at various $x/h$ -locations ( $121 \times 112 \times 33$ ).	177
A.30 $Nu$ profile along channel ( $121 \times 112 \times 33$ ).	177
A.31 Mean $U$ velocity profiles at various $x/h$ -locations ( $62 \times 57 \times 17$ ).	178
A.32 Mean $V$ velocity profiles at various $x/h$ -locations ( $62 \times 57 \times 17$ ).	178
A.33 $\overline{u'u'}$ profiles at various $x/h$ -locations ( $62 \times 57 \times 17$ ).	179
A.34 $\overline{v'v'}$ profiles at various $x/h$ -locations ( $62 \times 57 \times 17$ ).	179
A.35 $\overline{u'v'}$ profiles at various $x/h$ -locations ( $62 \times 57 \times 17$ ).	180
A.36 $Nu$ profile along channel ( $62 \times 57 \times 17$ ).	180
A.37 Mean $U$ velocity profiles at various $x/h$ -locations ( $109 \times 109 \times 109$ ).	182
A.38 Mean $U$ velocity profiles at various $x/h$ -locations ( $109 \times 109 \times 109$ ).	183
A.39 Mean $u'u'$ profiles at various $x/h$ -locations ( $109 \times 109 \times 109$ ).	184
A.40 Mean $w'w'$ profiles at various $x/h$ -locations ( $109 \times 109 \times 109$ ).	185
A.41 $Nu$ profiles around the heated cube ( $109 \times 109 \times 109$ ).	186
A.42 Mean $U$ velocity profiles at various $x/h$ -locations ( $75 \times 75 \times 75$ ).	187
A.43 Mean $U$ velocity profiles at various $x/h$ -locations ( $75 \times 75 \times 75$ ).	188
A.44 Mean $u'u'$ profiles at various $x/h$ -locations ( $75 \times 75 \times 75$ ).	189
A.45 Mean $w'w'$ profiles at various $x/h$ -locations ( $75 \times 75 \times 75$ ).	190
A.46 $Nu$ profiles around the heated cube ( $75 \times 75 \times 75$ ).	191

---

A.47 Mean $U$ velocity profiles at various $x/h$ -locations ( $53 \times 51 \times 53$ ). . . . .	192
A.48 Mean $U$ velocity profiles at various $x/h$ -locations ( $53 \times 51 \times 53$ ). . . . .	193
A.49 Mean $u'u'$ profiles at various $x/h$ -locations ( $53 \times 51 \times 53$ ). . . . .	194
A.50 Mean $w'w'$ profiles at various $x/h$ -locations ( $53 \times 51 \times 53$ ). . . . .	195
A.51 $Nu$ profiles around the heated cube ( $53 \times 51 \times 53$ ). . . . .	196
A.52 Mean $U$ velocity profiles at various $x/h$ -locations ( $41 \times 45 \times 41$ ). . . . .	197
A.53 Mean $U$ velocity profiles at various $x/h$ -locations ( $41 \times 45 \times 41$ ). . . . .	198
A.54 Mean $u'u'$ profiles at various $x/h$ -locations ( $41 \times 45 \times 41$ ). . . . .	199
A.55 Mean $w'w'$ profiles at various $x/h$ -locations ( $41 \times 45 \times 41$ ). . . . .	200
A.56 $Nu$ profiles around the heated cube ( $41 \times 45 \times 41$ ). . . . .	201
A.57 Mean $U$ velocity profiles at various $x/h$ -locations ( $109 \times 109 \times 109$ ). . . . .	202
A.58 Mean $U$ velocity profiles at various $x/h$ -locations ( $109 \times 109 \times 109$ ). . . . .	203
A.59 Mean $u'u'$ profiles at various $x/h$ -locations ( $109 \times 109 \times 109$ ). . . . .	204
A.60 Mean $w'w'$ profiles at various $x/h$ -locations ( $109 \times 109 \times 109$ ). . . . .	205
A.61 $Nu$ profiles around the heated cube ( $109 \times 109 \times 109$ ). . . . .	206
A.62 Mean $U$ velocity profiles at various $x/h$ -locations ( $75 \times 75 \times 75$ ). . . . .	207
A.63 Mean $U$ velocity profiles at various $x/h$ -locations ( $75 \times 75 \times 75$ ). . . . .	208
A.64 Mean $u'u'$ profiles at various $x/h$ -locations ( $75 \times 75 \times 75$ ). . . . .	209
A.65 Mean $w'w'$ profiles at various $x/h$ -locations ( $75 \times 75 \times 75$ ). . . . .	210



---

A.66	$Nu$ profiles around the heated cube ( $75 \times 75 \times 75$ ).	211
A.67	Mean $U$ velocity profiles at various $x/h$ -locations ( $53 \times 51 \times 53$ ).	212
A.68	Mean $U$ velocity profiles at various $x/h$ -locations ( $53 \times 51 \times 53$ ).	213
A.69	Mean $u'u'$ profiles at various $x/h$ -locations ( $53 \times 51 \times 53$ ).	214
A.70	Mean $w'w'$ profiles at various $x/h$ -locations ( $53 \times 51 \times 53$ ).	215
A.71	$Nu$ profiles around the heated cube ( $53 \times 51 \times 53$ ).	216
A.72	Mean $U$ velocity profiles at various $x/h$ -locations ( $41 \times 45 \times 41$ ).	217
A.73	Mean $U$ velocity profiles at various $x/h$ -locations ( $41 \times 45 \times 41$ ).	218
A.74	Mean $u'u'$ profiles at various $x/h$ -locations ( $41 \times 45 \times 41$ ).	219
A.75	Mean $w'w'$ profiles at various $x/h$ -locations ( $41 \times 45 \times 41$ ).	220
A.76	$Nu$ profiles around the heated cube ( $41 \times 45 \times 41$ ).	221
A.77	Mean $U$ velocity profiles (1-6).	223
A.78	Turbulence intensity (%) profiles (1-6).	224
A.79	$Nu_x$ along the heater element.	225
B.1	Cell diagram for variable $v$ , staggered in the $j$ -direction.	227

# Nomenclature

$p^*$	Guessed pressure for SIMPLE algorithm
$u^*$	Guessed velocity for SIMPLE algorithm
$\alpha$	Mean temperature gradient
$\alpha_I$	Decay rate constant
$\alpha_R$	Phase constant
$\alpha_{NB}$	Neighbour weights for calculation of cell face values
$\bar{p}$	Modified filtered pressure
$\bar{S}_{ij}$	Mean rate of strain tensor
$\beta$	Mean pressure gradient, truncation error constant
$\Delta$	Filter width
$\Delta_S$	Smagorinsky filter width
$\delta_{ij}$	Kronecker delta
$\eta$	Kolmogorov microscale
$\Gamma$	Diffusion coefficient
$\kappa$	Wavenumber, von-Karman constant

---

$\kappa_c$	Cut-off wavenumber
$\mathbf{G}$	Filter function
$\mathbf{n}$	Outward facing vector normal to cell face
$\mathbf{r}$	Filter radius
$\mu$	Dynamic viscosity
$\mu_T$	Turbulent (eddy) viscosity
$\nu$	Laminar kinematic viscosity
$\nu_T$	Eddy viscosity
$\omega$	Vorticity
$\omega_R$	Real frequency
$\bar{p}$	Filtered pressure
$\bar{T}$	Filtered temperature
$\bar{u}$	Filtered velocity
$\phi$	General flow variable
$\rho$	Density
$\sigma$	Variance
$\tau_{ij}^R$	Residual stress tensor
$\tau_{ij}^r$	Anisotropic part of residual stress tensor
$\tau_0$	Largest time scale
$\tau_\eta$	Kolmogorov time scale

---

$\tau_{ij}$	Turbulent stress tensor
$\theta$	Momentum thickness
$\tilde{p}$	Periodically reduced static pressure
$\tilde{T}$	Periodic temperature
$\varepsilon$	Dissipation rate
$\varepsilon_T$	Destruction of turbulent kinetic energy
$A$	Amplitude
$A_0$	FFT amplitude
$C$	Convective term
$C_\varepsilon, C_1, C_2, C_S$	Kosović model constants
$C_S$	Smagorinsky constant
$C_\mu$	$k-l$ model constant
$C_\varepsilon$	$k-l$ model constant
$C_{ij}$	Cross stresses
$D$	Diffusive term
$D_h$	Hydraulic diameter
$DFT$	Discrete Fourier Transform
$E(\kappa)$	Energy Spectrum
$E, W, N, S, F, B$	Neighbouring node locations
$e, w, n, s, f, b$	Cell face locations

---

$E_i$	Energy input or loss for fans and grills
$E_\phi$	Error in $\phi$
$F$	Serial code fraction, convective flux
$f$	Frequency
$f(k)$	Frequency
$f(x)$	Function
$H$	Cube height
$h$	Heat transfer coefficient, rib height, cube channel height
$h_j$	Residual heat flux tensor
$i, j, k$	Cartesian directions
$K$	Grill loss coefficient
$k$	Turbulent kinetic energy, thermal conductivity, discretisation order
$k_r$	Residual kinetic energy
$l$	Lengthscale
$l_0$	Pseudo integral lengthscale
$L_h$	Pseudo integral scale based on obstacle height, $h$
$L_k(x)$	Lagrangian interpolation coefficient
$l_\mu$	$k - l$ Lengthscale
$l_\varepsilon$	$k - l$ lengthscale
$L_{ij}$	Leonard stresses

---

$L_{k-\varepsilon}$	Pseudo integral scale based on RANS
$l_{SGS}$	LES SGS lengthscale
$N$	Number of processors
$N_z$	Number of zero samples
$N_{ds}$	Number of data samples
$N_{FFT}$	Number of Fast Fourier Transform points
$NS$	Navier-Stokes
$Nu$	Nusselt number
$O$	Order of
$P$	Time mean pressure
$p$	Pressure
$p'$	Turbulent pressure fluctuation
$P_r$	Rate of residual kinetic energy production
$P_{kT}$	Production of turbulent kinetic energy
$Pr$	Prandtl number
$q$	Convective heat flux
$q''$	Convective heat flux per unit area
$Q_0$	Volume flow rate
$R$	Ratio of integral to Kolmogorov microscale, vortex radius
$r$	Ratio of filter width to grid spacing

---

$R_h$  Ratio of lengthscales based on obstacle height,  $h$

$R_\phi$  Residual of variable  $\phi$

$R_{ij}$  Subgrid Reynolds stresses

$R_{k-\varepsilon}$  Ratio of lengthscales based on RANS

$Re$  Reynolds number

$RMS_\phi$  RMS change in variable  $\phi$

$S$  Source term

$S_{ij}$  Rate of Strain tensor

$St$  Strouhal number

$T$  Time mean temperature

$t$  Time, temperature

$t'$  Turbulent temperature fluctuation

$T_{core}$  Cube core temperature

$TFLOPS$  Tera FLoating point Operations Per Second

$U$  Time mean velocity

$u', v', w'$  Turbulent velocity fluctuations

$u, v, w$  Cartesian velocity componenets

$U_0$  Bulk velocity

$u_0$  Largest velocity scale

$u_\eta$  Kolmogorov velocity scale

---

$W_N^{kn}$  Phase factor

$X(k), x(n)$  Discrete Fourier Transform

$x, y, z$  Cartesian coordinates

$x^+, y^+, z^+$  Distances in wall units

$x_c, y_c$  Vortex center coordinates

(I)LES (Implicit) Large Eddy Simulation

(U)RANS (Unsteady) Reynolds-Averaged Navier-Stokes

2/3D Two/Three Dimensional

2UP Second order upwind

BGA Ball grid array

CD2 Second order central difference

CD4 Fourth order central difference

CFD Computational Fluid Dynamics

CMOS Complimentary metal-oxide-semiconductor

CV Control volume

DES Detached Eddy Simulation

DNS Direct Numerical Simulation

EASM Explicit Algebraic Stress Model

FD Finite difference

FFT Fast Fourier Transform



---

FV Finite volume

IC Integrated circuit

LES Large Eddy Simulation

PCB Printed Circuit Board

Q QUICK

RANS Reynolds-Averaged Navier-Stokes

SGS Subgrid scale

# Chapter 1

## Introduction

### 1.1 Background

#### 1.1.1 Historical challenges of electronics cooling

The reliability of high-performance electronics systems and devices has always been correlated to the underlying thermal management design. Therefore thermal management has always been linked to product success. In the past few decades, being able to predict and control the thermal characteristics of electronics has become increasingly important as heat flux density has risen. For performance electronics, such as telecommunications racks/servers, forced convection has always dominated the market since the required cooling system fans became reliable enough and in the 1960s large ventilation rooms were required for the cooling of vacuum tubes. When the CMOS (Complementary metal-oxide-semiconductor) was introduced, thermally related problems were reduced for some time. However the market demand for faster, smaller electronics devices soon caused heat related issues to return. Use of heatsinks to enlarge cooling surface

	Light Bulb	BGA Package
Power dissipation	100 W	25 W
Surface area	106 cm <sup>2</sup>	1.96 cm <sup>2</sup>
Heat flux	0.9 W/cm <sup>2</sup>	12.5 W/cm <sup>2</sup>

Table 1.1: Comparison of heat flux between a light bulb and a BGA Package

areas did not solve the underlying problems of heat density and reliability problems soon arose again.

Reliability prediction methods used in the 1950-60s relied on poor and old data that could not keep up with advances in technology. A new design process was required to improve reliability predictions. Today the heat flux density is still increasing rapidly and the market desire to shrink devices and push towards system-on-chip technologies compounds problems, by placing increasing numbers of transistors onto ever shrinking areas. The generally accepted Moores law predicts that the number of transistors on an integrated circuit (IC) will approximately double every two years. In the '70s and '80s there was much disbelief, as transistor densities were converted into power dissipation, heat fluxes began to rival space vehicle re-entry temperatures (Azar 2000). An example of this increase in heat flux comes from the telecommunications segment, where there has been an increase from 0.5 – 10W/cm<sup>2</sup> (a factor of 20) in ten years! Another heat flux density comparison is tabulated in Table 1.1 showing that a small BGA (Ball Grid Array) chip has a 13 times higher heat flux density than a light bulb.

Reliability testing has now become based on Physics of Failure, which aims to make critical design decisions based on mechanical, electrical and thermal modes of failure (Parry et al. 2002; Pecht 1996). Computational methods are now used to assist in the exploration of designs and fix problems early in the design process preventing them occurring in the final product.

### 1.1.2 Use of numerical modelling

Computational Fluid Dynamics (CFD) has been used in the electronics industry to aid in the rapid design of electronics components and systems for many years. The main aim of this is to accurately predict heat transfer processes in the product so that a design can be optimised and reliability can be assured. The continuing trend towards smaller devices and increasing power densities fuels the need to make the correct design choices early in the design cycle. Therefore, accurate thermal predictions are now more important than ever. As is depicted in Figure 1.1, thermal failure accounts for 55% of all electronics failures, 74% if humidity (which is related to thermal diffusion) is taken into account (Reynell 1990). The turbulence encountered in electronics system flows is useful for increasing heat transfer but makes accurate modelling difficult. Areas adversely affecting the accurate modelling of electronics systems and the challenges faced by thermal engineers are discussed by Joshi et al. (2001); Lasance (2001, 2005, 2007); Parry et al. (2002), whilst an overview of the tools available and their use is given by Dhinsa et al. (2005); Rodgers and Evely (2004); Tucker (1997).

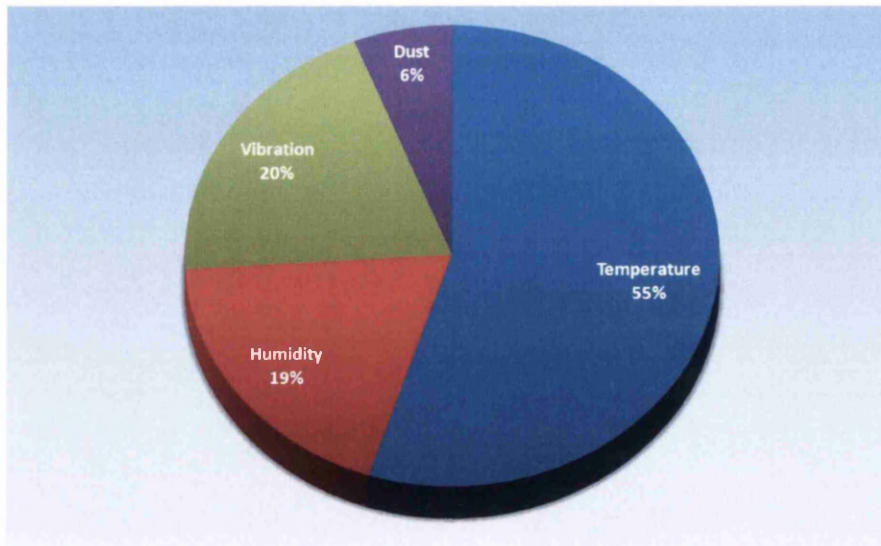


Figure 1.1: Major causes of electronics failure

The typical CFD methods used in the electronics design process are based on simple RANS turbulence models. Originally designed for use in the aerospace industry, statistical RANS models were never meant for use with complex geometries and time dependent flows such as those found at off design conditions in aerospace (for example, aerofoils at high angles of attack, or aircraft landing gear). Similar flow conditions are often found in electronics systems, as these generally contain bluff bodies, sharp corners, bends, fans and grills, creating strong streamline curvature and time dependent flow features. Use of RANS models for these complex time dependent flows is unsuitable (Shur et al. 1999; Tucker 2006) due to the time averaging nature of the RANS equations and the fact that RANS models were typically developed for high Reynolds number flows over streamlined geometries. The way in which aerospace and electronics type flows can be related is discussed by Tucker and Liu (2005b). Because RANS simulations are heavily dependent on the turbulence model employed, empirical constants and wall functions (Dhinsa et al. (2004); Roknaldin (2004)), results can be misleading or unreliable. In the aerospace industry there is a tendency to make ad-hoc adjustments to models to fix known problems, which further complicates the modelling of various types of flows and is not conducive to an efficient design process. It seems unlikely that any RANS model will be able to overcome these difficulties as much of the problem is inherited from the RANS formulation. For complex or bluff geometries, a more universal method capable of resolving time dependent flow features such as separation, reattachment, recirculation and vortex shedding is required.

LES has been used in the aerospace industry on problematic flows with limited success due to the high near wall grid demands and computational expense. To alleviate some of the computational overhead, tremendous research has been carried out on hybrid RANS-(I)LES methods using economical RANS near walls and (I)LES elsewhere. One of the first hybrid approaches was Detached Eddy

Simulation (DES) suggested by Spalart et al. (1997) and has been used with some success, especially for external flows. An overview of RANS, LES and hybrid modelling approaches is also given by Spalart (2000). Whereas a RANS model controls the whole flow, only the unresolved subgrid scale (SGS) eddies (those smaller than the grid resolution and that are mostly dissipative) are modelled in (I)LES. Hence, solutions are much less dependent on the turbulence model used. ILES does not rely on an explicit SGS model but relies on numerical dissipation to remove the correct amount of energy from the flow. For the most common RANS and LES models, the typical Boussinesq approximation with only linear terms is used and the turbulent stresses (Reynolds stresses for RANS and residual stresses for LES) become notionally isotropic. Linear models are known to be inaccurate in describing the complex anisotropic stresses in a flow and nonlinear models have been developed for RANS (Craft et al. (1996); Gatski and Speziale (1993)) and LES (Geurts and Holm (2003); Kosović (1997)) to better capture the flow, although the added complexity increases computation time. There is therefore, a wealth of methods and models to choose from depending on problem type, time limitations and accuracy requirements.

## 1.2 Objectives of the study

Due to the fact that current CFD packages are unable to consistently give reliable thermal predictions, one key objective is to consistently provide a more accurate prediction of heat transfer within a system. Due to geometrical complexity, unsteady nature of flows in electronics systems and the failure of RANS models to capture important flow physics, methods based on (I)LES are analysed. An unsteady method would also have other uses in the physics of failure framework as thermal cycling (causing fatigue) has a great influence on the reliability of electronics systems (Cushing et al. 1993). The obvious drawback of unsteady

methods is that computation times may be increased substantially, hence there will be some emphasis on reducing simulation times and investigating what methods give the best trade-off between accuracy and computation time. Remembering the fact that these tools may be used in a design process, some thought is given to how the methods used may be applied in industry, bearing in mind that most simulations are based on RANS, with meager grids. The low Reynolds number of flows in electronics, typically,  $Re \leq 5000$  (Chung and Tucker 2003), also invites us to investigate the effects of various turbulence models, grid demands and near wall treatments compared to more widely studied high- $Re$  flows. RANS, (I)LES and hybrid RANS-(I)LES methods will be used to test flows of increasing complexity to find where limitations may lie. Due to sensitivity to numerical effects, discretisation schemes are also tested and used to some advantage for (I)LES based simulations.

### 1.3 Thesis outline

Chapter 2 provides a brief review of literature on electronics heat transfer modelling and some of the methods used. Further details on turbulence modelling and the models used are provided in Chapter 3. The numerical methods used are discussed in Chapter 4. Chapter 5 focuses attention on reducing run times and increasing efficiency. Chapter 6 is used to test any modifications to the code to check correctness and numerical traits. The cases used for testing heat transfer predictions can be found in Chapter 7 along with overall results. The validity of some modelling assumptions are assessed in Chapter 8. Conclusions and recommendations for further work are described in Chapter 9.

# Chapter 2

## Literature review

### 2.1 Introduction

Electronics cooling simulation has been used to reduce costs compared to the continual use of experimental setups and to reduce the length of product development cycles. These simulations allow virtual prototyping to test the performance and reliability of various components under different conditions. Numerical simulations often fall into the categories of chip/component, board/package and system level. In each case, certain details may be omitted to simplify the model and reduce computational cost, with the hope that no significant data is lost from the simulation. For example, chips may be treated as flat blocks with no wall roughness, however, this may be partially accounted for by altering the wall modelling of the turbulence model. Generally heat sources are treated as a uniform heat input or constant temperature regions. Fans are usually modelled as uniform momentum sources. The following sections will review recent attempts to understand modelling of simple and more complex flows found in electronics cooling simulation. These include channels with ribs, cubes, cylinders and other



geometries.

## 2.2 Ribbed channel and similar flows

The heated ribbed channel and array of cubes, used as test cases in this work, are intended to represent an idealised circuit board with integrated circuits. This simplification is similar to methods currently used in industry (Gupta 2002) and is therefore justified. The heated ribbed channel is based on the work of Acharya et al. (1993). In the original work of Acharya et al. (1993) the standard  $k - \varepsilon$  and nonlinear  $k - \varepsilon$  model of Speziale (1987) are compared with experimental data. The nonlinear model slightly improved turbulence intensities although results were similar in both cases. The behavior of turbulence models is dependent on the Reynolds number of the flow, with most electronics flows being at low and transitional Reynolds numbers. The majority of CFD calculations in this application area make use of the high Reynolds number form of the  $k - \varepsilon$  model (Dhinsa et al. (2004)), however, Iacovides and Raisee (1999) show that low Reynolds number eddy viscosity models are required for the prediction of flow around rib roughened turbine blades at  $Re = 20,000$ . Work on similar rib-roughened channels by Tafti (2005) showed the Dynamic Smagorinsky LES model seemed insensitive to grid resolution whereas the quasi-DNS (coarse Direct Numerical Simulation) showed clear differences and under-predicted heat transfer. Although insensitivity to grid resolution would be beneficial, stability and other issues surrounding the Dynamic Smagorinsky model make it cumbersome to use as a general purpose LES model. Viswanathan and Tafti (2005) revisit this case comparing DES and RANS. DES results compared well with experimental data, whereas RANS simulation failed to capture key flow features. This is not surprising given the fact that most of the transient flow features are resolved in DES. However, the RANS-LES interface of standard DES is based on the grid

spacing and results are sensitive to the grid topology and resolution. Tucker and Liu (2005a) demonstrate this applying DES to a complex electronics system, the irregular grid produced by the geometry making the flow impossible to converge.

Studying hybrid and coarse-grid LES, Breuer et al. (2005) show that mean flow and turbulence features are captured well on a grid of  $\approx 1$  million compared to an LES of  $\approx 13.6$  million cells. Chung and Tucker (2004a) show that periodicity may not be assumed until around five repetitions in the studied ribbed channel. A study of parallel boards with heat producing blocks similar to those found in telecommunications racks is studied by Furukawa and Yang (2003). Periodicity is not found even at the ninth cavity of this essentially ribbed channel. It was found that the point at which periodicity is found increases with  $Re$ .

Figure 2.1 shows that by choosing different RANS models, the predictive accuracy can vary dramatically and as mentioned, heat transfer ( $Nu$ ) is generally over predicted. Although more complex nonlinear RANS models such as the  $k - l$ /EASM and  $k - l$ /Cubic improve results, they can be problematic to converge. This is mentioned in relation to a similar heated ribbed channel by Bredberg and Davidson (1999) and has also been experienced in previous work related to this topic (Liu (2004); Tucker (2006)). For these reasons various modelling choices such as which RANS model to use, would be a burden to the end user. It is noted by Hutton (2009), with over 100 RANS models (or variants) available, much confusion exists in industry.

## 2.3 Flow around cubes and square cylinders

The heated cube case is based on the work of Meinders and Hanjalić (1999) which has also been studied by various groups numerically in the 8th ERCOF-TAC/IAHR/COST Workshop on Refined Turbulence Modelling (Hellsten and

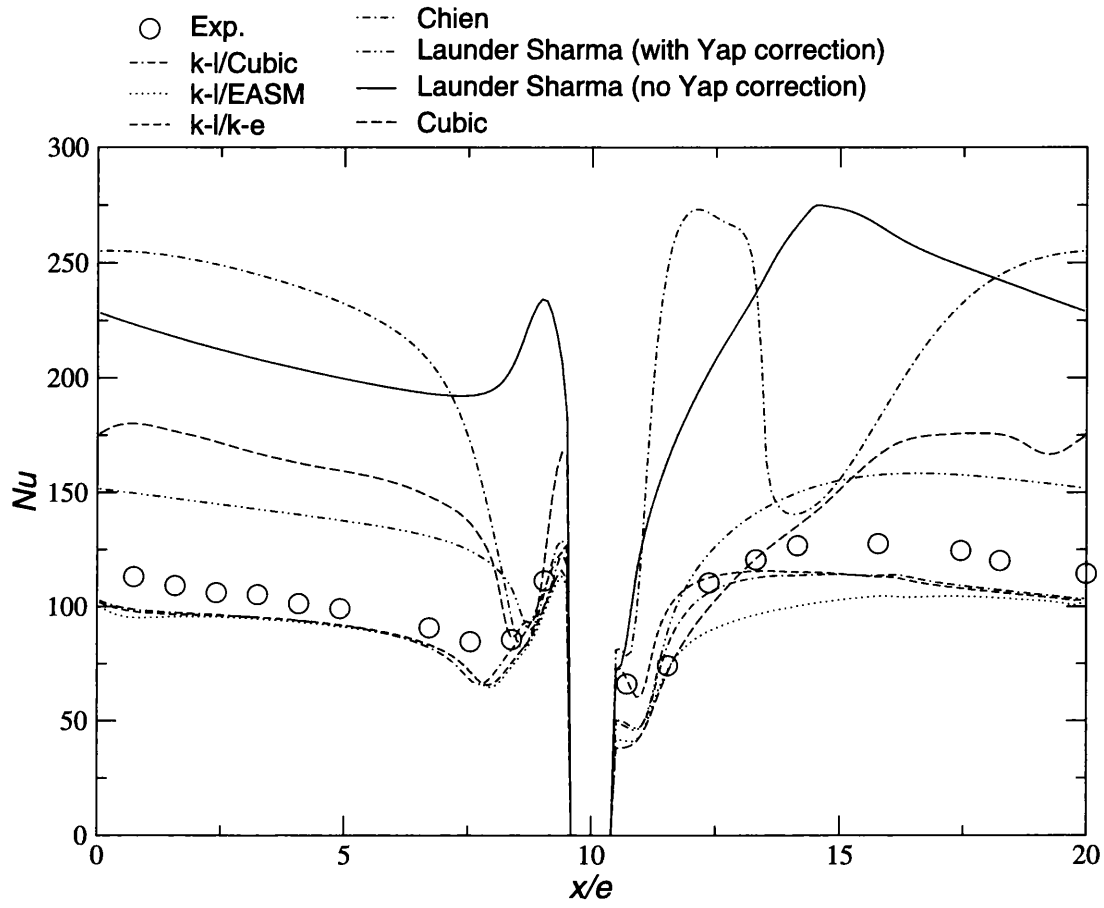


Figure 2.1: Nusselt number results using various RANS models.

Rautaheimo 1999). Generally RANS is shown to perform poorly compared to time dependent solutions such as LES or hybrid RANS-(I)LES. van der Velde et al. (1999) perform a kind of ILES (DNS on a grid too coarse to be called a true DNS) on a  $100 \times 100 \times 100$  grid with temperatures being predicted well. Similarly Mathey et al. (1999) also use a  $100 \times 100 \times 100$  grid to perform an LES simulation using the Smagorinsky model. Thermal predictions were good except for around the base of the cube, where temperatures were over predicted. Ničeno and Hanjalić (1999) use an unstructured grid of 418,760 cells to predict fluid flow (though no heat transfer was modelled) also matching well with experimental data. Following in this vein, Ničeno et al. (2002) perform an LES simulation using the Smagorinsky model with 425,000 cells. The temperature distribution on the cube surface was found to be rather nonuniform reflecting the complex nature of the flow and again the temperature near the lower wall was over predicted, thought to be due to discarding the experimentally detected heat loss through the base wall.

Dhinsa et al. (2003, 2004) studied flow over a cube and found no RANS model to consistently improve results. It was also found that the popular  $k - \varepsilon$  model struggled to perform well or accurately capture turbulent phenomenon even for simple geometries. Xie and Castro (2006) present RANS and LES data for flow over arrays of wall mounted obstacles. Grids that would normally be too coarse for LES simulations of flow over smooth bodies produced good results when applied to bluff bodies due to turbulence production being of a similar scale to the obstacle size. RANS solutions were inadequate and it was also found that dependence on  $Re$  was weak. Schmidt and Thiele (2002) study the cube of Meinders and Hanjalić (1999) using dynamic LES models, RANS and DES to test the differences between methods and grids. It was found that DES was a good compromise between RANS and LES, capturing most flow features well whereas RANS gave a poor representation of unsteady flow features. It was found that the most crucial part of the grid is that near the wall and that using a coarse RANS grid for DES will

give poor results due to the grid being too coarse in regions of high unsteadiness.

Vengadesan and Nakayama (2005) compare experimental data with the standard Smagorinsky, dynamic Smagorinsky and one-equation SGS models. It was found that the one-equation ( $k-l$ ) model was the best choice. Several RANS  $k-\varepsilon$  based models are tested on a square cylinder by Bosch and Rodi (1998) with various wall and turbulence model modifications. It was concluded that  $k-\varepsilon$  models can mostly capture the main quantities of interest but not all complex details. These details such as 3D motions leading to modulation of vortex shedding could not be accounted for in a 2D simulation. It should be noted that many CFD simulations are still performed in 2D, whereas all turbulence is three-dimensional. Modelling a flow past a square cylinder, Wienken et al. (2006) found that the  $k-\varepsilon$  and Reynolds Stress Model were not capable of capturing the large scale flow structures in the wake of the body, in contrast LES proved to perform well.

## 2.4 Full systems and other relevant geometries

Although relatively simple cases have been discussed so far, real systems are far more complex. Lasance (2007) uses an experiment and a steady CFD simulation to provide insight into the effects of multiple obstacles, effects from grills and cables and concludes mismatches of 20-30% in numerical and experimental temperatures may be expected, probably due to the unsteady character of the flow system. Flows may be sensitive to smaller geometrical aspects and Chung and Tucker (2004b) find that using a thin fin to trip a flow of  $Re = 500$  into turbulence, heat transfer can be increased dramatically (circa 500%) with a consequent reduction of reattachment length. This tripping also caused the flow to behave like a flow of  $Re = 700$ . This tripping or increase of turbulence production is also tested by Hemida and Krajnović (2007) by placing small rib structures around

a cube geometry, increasing heat transfer by about 14% further illustrating the impact small features can have. Although interesting, in this work we are only concerned with consistently and accurately predicting heat transfer, not increasing it. Flow features downstream of fans are hard to predict, further complicated by the use of grills, screens and filters. The surface roughness produced by smaller PCB components also affects the pressure drops around the system. Often only mean statistical data is available for boundary conditions, inadequate for unsteady simulations (Baelmans et al. 2003). The importance of a more physically correct turbulence modelling method for the accurate prediction of heat transfer is demonstrated by Chung et al. (2003) studying a sharp 180° bend in a channel flow. Here, heat transfer is increased by around six times after oscillatory flow ensues after increasing  $Re$  from 600 to 700. The reattachment length is correspondingly reduced. The particular type of flow is hard to predict *a priori* and it is evident that incorrect assumptions about the flow could have dramatic consequences.

Assuming a fully turbulent boundary layer over a whole surface and using a RANS model, generally over predicts the heat transfer coefficient, resulting in apparently lower surface temperatures (Roknaldin 2004). This could later lead to overheating and device failure. Use of wall functions can also over predict heat transfer and as pointed out by Roknaldin (2004), the extent of all logarithmic layers in a system cannot be estimated accurately *a priori* for wall functions to be accurate. Clearly removing the need for prior knowledge about a flow would be advantageous for industrial use.

## 2.5 LES modelling

High order Implicit-LES is studied by Drikakis et al. (2009). It is noted that LES may become sensitive to numerical errors especially when there is poor separation

of scales (low  $Re$  flows) and also that it is unknown to what extent anisotropies persist into the inertial subrange. This would affect the universality of various models. RANS-LES methods are discussed and issues raised when using such methods by Leschziner et al. (2009). Hutton (2009) discusses the application of LES to industrial flows. As is discussed, the transferal of LES to industry will require a large knowledge base and parallel algorithms to harness the power of advancing hardware technology.

## 2.6 Summary

Although CFD simulations are generally accepted as a design tool, various problems are still present, but not necessarily appreciated by the end user. The isolation of the user from the CFD code itself, imposes that the user has faith in the software to select a laminar or turbulent flow regime, the correct RANS model and to make various other (sometimes rather subjective) decisions like assuming periodicity in parts of the domain. In the current design environment, there is still quite some scope for modelling errors. The methods proposed here strive to reduce modelling dependence and to allow consistent, accurate thermal predictions.

# Chapter 3

## Turbulence Modelling

### 3.1 Introduction

In this chapter, an introduction to turbulence and the methods available to model it will be discussed. The RANS, (I)LES and hybrid RANS-(I)LES strategies employed will then be described.

### 3.2 Turbulence

Turbulence is three-dimensional and contains a range of length scales. Due to the increased mixing of fluid created by interacting eddying motions, heat, mass and momentum are effectively exchanged. This gives higher diffusion coefficients. Vortex stretching at the largest length scales provides energy to maintain the turbulence as shear from the mean flow stretches the largest invicid eddies. Since angular momentum is conserved, smaller eddies are produced. Energy is passed similarly from large to small scales, a process known as the energy cascade. As the



scales become smaller, viscosity effects drain energy from the flow as it is dissipated as heat. In electronics systems, large scales are highly anisotropic whereas the smaller scales are generally more isotropic due to the diffusive effect of viscosity. The smallest scales are generally known as the Kolmogorov scales quantified by Kolmogorov (1941) (for an English translation see Kolmogorov (1991)).

### 3.3 Kolmogorov hypotheses and turbulent scales

The largest turbulent scale is known as the integral length scale. This is determined by the dimensions of the geometry and boundary conditions. Energy is passed from the larger scales via the energy cascade until the smallest eddies determined by the viscosity of the fluid are reached and the energy is dissipated. The smallest eddies also have the smallest time scales and are often considered historically to be statistically independent of the mean flow. Between the extremes of the largest and smallest scales, a complete spectrum of scales is expected at high Reynolds numbers. Kolmogorov suggested that the directional information of the large scale motions is lost in the chaotic scale reduction process of the energy cascade. This leads to the hypothesis of local isotropy where the small scales (those smaller than the energy containing scales) are locally isotropic at *sufficiently high* Reynolds numbers. This statistically universal state depends on the rate at which energy is passed onto smaller scales and the viscous dissipation. Kolmogorov's first similarity hypothesis is that at *sufficiently high* Reynolds numbers, the small scale motions have a universal form defined by  $\nu$  and  $\varepsilon$ . It is also assumed that the energy dissipated by the smallest eddies is supplied by the larger energy containing eddies. The Kolmogorov scales for length, velocity and time can be obtained using dimensional analysis using the knowledge that the smallest scales depend upon the (kinematic) viscosity  $\nu$  and dissipation rate  $\varepsilon$ .

The resulting Kolmogorov scales for length, velocity and time are respectively

$$\eta = \left( \frac{\nu^3}{\varepsilon} \right)^{1/4} \quad (3.1)$$

$$u_\eta = (\varepsilon\nu)^{1/4} \quad (3.2)$$

and

$$\tau_\eta = \left( \frac{\nu}{\varepsilon} \right)^{1/2} \quad (3.3)$$

Basing the Reynolds number on these scales gives a Reynolds number of 1, showing that these are the scales where viscosity begins to dominate over inertia.

Kolmogorov's second similarity hypothesis states that scales between the energy containing and Kolmogorov scales (the inertial subrange) may be determined by  $\varepsilon$  independent of  $\nu$ .

The ratios of the smallest to largest scales can be found from the Kolmogorov scales and from the scaling  $\varepsilon \sim u_0^3/l_0$  resulting in Equations (3.4)-(3.6) (Pope 2000). The subscript '0' refers to the largest flow scale and characteristic velocity scales.

$$\eta/l_0 \sim Re^{-3/4} \quad (3.4)$$

$$u_\eta/u_0 \sim Re^{-1/4} \quad (3.5)$$

$$\tau_\eta/\tau_0 \sim Re^{-1/2} \quad (3.6)$$

The ideas and relations of the Kolmogorov hypotheses form the basis of many turbulence models. However the applicability of these theories and models based on simple flow dynamics is questionable for lower  $Re$  flows and is discussed later in Chapter 8.

## 3.4 Approaches to turbulence modelling

### 3.4.1 Direct numerical simulation (DNS)

DNS is perhaps the easiest method to understand as it basically involves the discretisation and solution of the Navier-Stokes (NS) equations while including suitable boundary conditions. Since the solution is not of the exact NS equations, but of the discretised NS equations, accurate discretisation schemes and an extremely fine grid is required to remove these errors so that all possible scales of motion (right down to the Kolmogorov scales) are resolved and the nearly exact solution to the NS equations is recovered. Since the range of scales is proportional to  $Re^{3/4}$ , in three dimensions, the number of grid points required is proportional to  $Re^{9/4}$ . Although the fine grid required makes the simulation of most flows impossible due to computational requirements, it has been useful for investigating the physics of more simple flows at low  $Re$ . It has been extremely useful in increasing the understanding of the fundamental properties of turbulence and has formed the basis from which many theoretical ideas have been proposed or proven. Although DNS is useful, computational limitations have forced us to find more economical approaches to simulation, often tailored for specific types of flow. This results in a trade off between computation time and solution accuracy, both of which vary depending on the modelling methods involved. Some average of turbulent quantities allows unresolved scales to be modelled in terms of the resolved scales.

### 3.4.2 Reynolds-averaged Navier-Stokes (RANS)

Taking a time average of the NS equations leads to the RANS equations, the solution of which produces a time averaged representation of the turbulent flow. The RANS equations give a generally smooth function in space (and time for URANS). This is in contrast to the actual NS equations, where the real function appears more chaotic, yet is certainly deterministic. In the derivation of the RANS equations, extra turbulent stress terms are produced forming the Reynolds stress tensor which must be modelled to close the set of equations. These are known as the Reynolds stresses and represent the turbulent fluctuations around the mean velocity. Many models have been developed, from simple mixing-length models through two-equation  $k - \varepsilon$  and  $k - \omega$ , to algebraic and full Reynolds stress models. Many models have been developed for specific applications because the equations themselves are not time dependent and cannot accurately capture important flow features such as separation, reattachment, recirculation and vortex shedding. Other drawbacks of the RANS approach are that there are often many constants in the models which are often empirical and used to calibrate the models to obtain better results. The lack of a universal model means that different flows and boundary conditions may require a different model choice. This is a drawback for industrial use. For URANS calculations, the averaging time must be much larger than the largest time scale of the flow, but smaller than any coherent unsteadiness, although generally, the RANS equations are not capable of accurately capturing unsteady phenomenon. Although RANS has various drawbacks, it has become popular for general CFD use since in most cases it has low grid resolution requirements.

### 3.4.3 Large eddy simulation (LES)

LES lies between the two extremes of the DNS and RANS methods. Instead of using a time average as in RANS, LES makes use of spatial filtering to obtain a filtered set of NS equations. Again, to close the equations, a turbulence model is required to give the turbulent stress tensor. Scales smaller than the grid width are modelled using a subgrid scale (SGS) model and larger eddies are resolved. Commonly the model is simply referred to as the SGS model. Scales larger than the filter width (be it explicit or the natural grid filter) are practically unaffected by the filter whereas features smaller than the filter width are suppressed. Benefits of this method are that most of the flow is resolved and only the smallest scales are modelled meaning that LES is much less dependent on the model chosen than RANS based models. Since the equations are not time-averaged, the equations remain time dependent, so many more physical phenomena can be accurately represented. Decomposing the velocity into filtered and residual (subgrid) scales means that the large unsteady motions are represented explicitly. This means that most of the energy containing anisotropic features of the flow are described in a relatively accurate manner. Fine structures near walls such as streaks (whose dimensions in viscous units are around 1000 viscous wall units long and 30-50 viscous wall units wide and high (Ferziger and Perić 2002)) mean that grids must be fine in these regions, increasing computation time. Using LES based methods, instabilities from the boundary layer will be more physically correct in triggering and maintaining turbulence. It is the opinion of many that since it is only the smaller more universal eddies that are modelled, simple models may be used to represent them. However, near walls the flow is highly anisotropic, suggesting a more complex model may be required. The Reynolds number and the choice and type of filter can greatly affect the performance of subgrid models. Compared with DNS, LES is economical and so higher  $Re$  flows may be simulated with this method. The SGS model allows some control over the dynamics of the flow but

mainly serves to accurately model the turbulent stresses in a range of different flows. When eddies contributing to the production of turbulent kinetic energy are well resolved, the role of the SGS model is to drain the appropriate amount of energy from the flow and the effects of the model are small or insignificant. Poorly resolved flows take a stronger influence from the SGS components, making the model more crucial to an accurate simulation. Scales similar in size to the grid spacing are poorly resolved, so errors are largest for these, whereas the largest eddies are resolved well. An SGS model is obtained from empirical knowledge and from the basic properties of the filtered NS equations, the aim being to represent the effects of the sub-filter scales on the larger scales.

#### 3.4.4 Hybrid RANS-(I)LES

Due to the high near wall grid demands of LES and the computational economy of RANS, it seems logical to use a hybrid approach where economical RANS is used near walls to capture boundary layers and LES elsewhere to capture the important time dependent flow features. This was first proposed by Spalart et al. (1997) for use in the aerospace industry, where pure LES will not be viable for some time due to the high- $Re$  flows involved. The method proposed by Spalart is known as Detached-Eddy Simulation (DES) (Spalart et al. 1997). Using RANS near walls and time dependent (I)LES elsewhere gives rise to some theoretical questions near the interface such as whether the RANS region is actually URANS (Unsteady-RANS) since the RANS layer is buffeted by unsteady structures, even though the time scale of these is well below the scale normally required for URANS.

Table 3.1 gives a comparison of RANS and LES as these are the two main feasible techniques.

	RANS	LES
Methodology	Model all eddies	Resolve large scales and model smaller SGS eddies
Empiricism	Strong, whole flow controlled by turbulence model	Weak, only 10-20% of flow modelled
Grid requirement (wall bounded flows)	Low, $y^+ < 1$ (low $Re$ ) or $y^+ > 30$ (high $Re$ )	High, $y^+ < 1$ $\Delta x^+ \approx 50 \sim 150$ $\Delta z^+ \approx 15 \sim 40$
Accuracy for complex flows	Low	High
Computational Cost	Low	High

Table 3.1: Comparison of CFD modelling approaches (Liu 2004).

### 3.5 Governing equations

The governing equations for (U)RANS and (I)LES for incompressible flows may be written in the same Cartesian conservative form:

$$\frac{\partial \tilde{u}_j}{\partial x_j} = 0 \quad (3.7)$$

$$\rho \frac{\partial \tilde{u}_i}{\partial t} + \rho \frac{\partial (\tilde{u}_i \tilde{u}_j)}{\partial x_j} = \delta_{1j} \beta - \frac{\partial \tilde{p}}{\partial x_i} + \frac{\partial}{\partial x_j} \left[ (\mu + \mu_T) \frac{\partial \tilde{u}_i}{\partial x_j} \right] - \frac{\partial \tau_{ij}}{\partial x_j} \quad (3.8)$$

$$\rho \frac{\partial \tilde{T}}{\partial t} + \rho \frac{\partial (\tilde{u}_j \tilde{T})}{\partial x_j} = -\rho \delta_{1j} \alpha \tilde{u}_j + \frac{\partial}{\partial x_j} \left[ \frac{\mu}{Pr} \frac{\partial \tilde{T}}{\partial x_j} \right] - \frac{\partial h_j}{\partial x_j} \quad (3.9)$$

In the above equations,  $\tilde{u}_i$  is a fluid velocity component ( $i, j=1-3$  representing streamwise, normal(vertical) and spanwise directions respectively,  $\rho$  the fluid density,  $\mu$  dynamic viscosity,  $\tilde{p}$  the periodically reduced static pressure,  $\tilde{T}$  periodic

temperature,  $t$  time and  $x_j$  ( $j=1-3$ ) the spatial coordinate. The tilde represents ensemble averaging or spatial filtering for (U)RANS and (I)LES respectively. The subscript  $T$  refers to the turbulent viscosity, whether it is derived from a RANS or LES model.  $\alpha$  and  $\beta$  represent the mean temperature and pressure gradients in the periodic streamwise direction. This is necessary for the ribbed channel case although  $\alpha$  is not required for the cube array. The CPU case is not periodic, and so neither  $\alpha$  nor  $\beta$  are required. The relations for  $\alpha$  and  $\beta$  are given in Section 7.2.1, as they are used for the ribbed channel.

## 3.6 Turbulence modelling - RANS

RANS has for a long time been the CFD method of choice for predictions in electronics cooling. This is mainly due to its computational economy. Stability and robustness have been improved for industrial use by imposing limitations on the user and using often rather crude generalisations to simplify and speed up computations.

### 3.6.1 Reynolds stresses

The concept behind the RANS approach is to decompose the flow variables into time mean and fluctuating components. This is known as *Reynolds decomposition*, giving

$$\begin{aligned}u_i &= U_i + u'_i \\p &= P + p' \\t &= T + t'\end{aligned}\tag{3.10}$$



where the capitalisation and *prime* represent the time mean and fluctuating components respectively. Substitution of these newly defined variables into the Navier-Stokes and energy equations produces the Reynolds-averaged Navier Stokes and energy equations below.

$$\frac{\partial U_j}{\partial x_j} = 0 \quad (3.11)$$

$$\rho \frac{\partial U_i}{\partial t} + \rho \frac{\partial (U_i U_j)}{\partial x_j} = -\frac{\partial P}{\partial x_i} + \frac{\partial}{\partial x_j} \left[ \mu \frac{\partial U_i}{\partial x_j} \right] + \frac{\partial \tau_{ij}}{\partial x_j} \quad (3.12)$$

$$\rho \frac{\partial T}{\partial t} + \rho \frac{\partial (U_j T)}{\partial x_j} = +\frac{\partial}{\partial x_j} \left[ \frac{\mu}{Pr} \frac{\partial T}{\partial x_j} \right] + \frac{\partial (-\overline{\rho u'_j t'})}{\partial x_j} \quad (3.13)$$

The equations are closed by the extra terms on the right of each equation with  $\tau_{ij} = -\overline{\rho u'_i u'_j}$  being the Reynolds stress tensor and  $-\overline{\rho u'_j t'}$  being the turbulent heat flux tensor.

### 3.6.2 Eddy-viscosity models

The viscous stress of a Newtonian fluid can be expressed as

$$-(\tau_{ij} + P\delta_{ij})/\rho = 2\nu S_{ij} \quad (3.14)$$

where  $S_{ij}$  is the rate of strain tensor and  $P$  the pressure.

In analogy to this, Boussinesq in 1877 proposed the use of an artificial eddy viscosity to relate the deviatoric Reynolds stress to the mean rate of strain. This

leads to the Reynolds stresses arising from the RANS equations being modelled by simply adding the eddy viscosity to the fluids molecular viscosity.

In analogy to (3.14), the anisotropic turbulent stresses can be written

$$\overline{u'_i u'_j} - \frac{2}{3}k\delta_{ij} = -2\nu_T \bar{S}_{ij} \quad (3.15)$$

where  $\bar{S}_{ij}$  is the mean rate of strain tensor,  $k$  the turbulent kinetic energy and  $\nu_T$  the eddy viscosity. On the right hand side of each is the anisotropic part of the stress. Thus there is the intrinsic assumption that the anisotropic part is related to the local mean rate of strain, although this assumption does not account for anisotropies arising from prior strain. It is also assumed how the isotropic stress should be stated. The subtraction of  $\frac{2}{3}k\delta_{ij}$  is required to ensure that  $-\rho(\overline{u'^2} + \overline{v'^2} + \overline{w'^2}) = -2\rho k$ . The task of the turbulence model is then, to determine  $\nu_T$ . Linear turbulence models are also unable to model complex flow structures, for example, swirling flow from fans, due to the scalar eddy viscosity. This produces a notionally isotropic turbulence closure.

### 3.6.2.1 Wolfshtein $k-l$

This RANS model is used in the hybrid simulations. To calculate the eddy viscosity for this  $k-l$  model, the transport equation for the kinetic energy is required. This is given by Equation 3.16.

$$\frac{\partial k_T}{\partial t} + \frac{\partial U_j k_T}{\partial x_j} = \frac{1}{\rho} \frac{\partial}{\partial x_j} \left[ \left( \mu + \frac{\mu_T}{\sigma_k} \right) \left( \frac{\partial k_T}{\partial x_j} \right) \right] + P_{k_T} - \varepsilon_T \quad (3.16)$$

The turbulent Prandtl number for kinetic energy,  $\sigma_k = 1$  (Pope 2000) and the turbulence production and dissipation terms are given by  $P_{k_T}$  and  $\varepsilon_T$ , shown

below.

$$P_{k_T} = 2 \frac{\mu_T}{\rho} \bar{S}_{ij} \bar{S}_{ij} \quad (3.17)$$

$$\varepsilon_T = C_\varepsilon k_T^{3/2} / l_\varepsilon \quad (3.18)$$

The turbulent viscosity is given by Equation 3.19

$$\mu_T = \rho C_\mu l_\mu k^{1/2} \quad (3.19)$$

The constants are defined as  $C_\varepsilon=1$  and  $C_\mu=0.09$ .

The RANS length scales for this  $k-l$  based model are given by Equations (3.20) and (3.21) (Zhong and Tucker 2004).

$$l_{\varepsilon,RANS} = 2.4y(1 - e^{-0.263y^*}) \quad (3.20)$$

$$l_{\mu,RANS} = 2.4y(1 - e^{-0.016y^*}) \quad (3.21)$$

where  $y^* = y\rho k_T^{1/2} / \mu$ .

Due to the magnitude of a RANS model eddy viscosity being much larger than a SGS viscosity, the discretisation scheme has a less pronounced effect on the solutions outcome and so, discretisation is not discussed with respect to RANS modelling.

## 3.7 Turbulence modelling - (I)LES

Instead of splitting the components into time mean and fluctuating parts as in RANS, LES makes use of a spatial filter leaving resolved filtered and unresolved sub-filter scales. Despite LES being superior to (U)RANS through only modelling a small portion of flow, it too has some drawbacks. One of these is the computational cost for wall bounded flows, where the grid spacings required to resolve fine anisotropic streak structures are around  $y_{wall}^+ \approx 1$ ,  $\Delta x^+ \approx 100$ ,  $\Delta z^+ \approx 20$  in the wall normal, streamwise and spanwise directions respectively (Davidson and Peng 2003; Zhong and Tucker 2004). Away from walls, grid requirements are lower due to larger and less intricate structures and much higher accuracy can be obtained compared to (U)RANS simulations. Being more numerically sensitive, LES may introduce additional frequencies or an implied filter and subgrid model due to numerical effects.

For aerospace flows, it may be at least 2045 until LES can be used successfully (Spalart 2000). However, due to lower Reynolds numbers (here, less than 15000) and a more consistent reduction in predictive error compared to RANS solutions, (I)LES methods are a more viable option for electronics cooling simulation.

### 3.7.1 Residual/Subgrid stresses

By applying a spatial filter to the NS equations, the following continuity, momentum and energy equations can be obtained.

$$\frac{\partial \bar{u}_j}{\partial x_j} = 0 \tag{3.22}$$

$$\rho \frac{\partial \bar{u}_i}{\partial t} + \rho \frac{\partial (\bar{u}_i \bar{u}_j)}{\partial x_j} = -\frac{\partial \bar{p}}{\partial x_j} + \frac{\partial}{\partial x_j} \left[ \mu \frac{\partial \bar{u}_i}{\partial x_j} \right] \quad (3.23)$$

$$\rho \frac{\partial \bar{T}}{\partial t} + \rho \frac{\partial (\bar{u}_j \bar{t})}{\partial x_j} = \frac{\partial}{\partial x_j} \left[ \frac{\mu}{Pr} \frac{\partial \bar{T}}{\partial x_j} \right] \quad (3.24)$$

Because of the unknown nonlinear convective term  $\bar{u}_i \bar{u}_j$  instead of a term similar to that in the original NS equations ( $\bar{u}_i \bar{u}_j$ ) appearing in Equation 3.23, the difference between the two is defined by the residual stress tensor:

$$\tau_{ij}^R = \rho (\overline{u_i u_j} - \bar{u}_i \bar{u}_j) = \frac{\tau_{kk}}{3} \delta_{ij} + \rho \tau_{ij}^r \quad (3.25)$$

In (3.25),  $\tau_{ij}^r$  is the anisotropic part (trace) of the total  $\tau_{ij}^R/\rho$ .

The residual kinetic energy is

$$k_r = \frac{1}{2} \tau_{ii}^R \quad (3.26)$$

The anisotropic (deviatoric) part of the residual stress tensor is given by

$$\tau_{ij}^r = \tau_{ij}^R - \frac{2}{3} k_r \delta_{ij} \quad (3.27)$$

The isotropic part may be included in the modified filtered pressure

$$\bar{p} = \bar{p} + \frac{2}{3} \rho k_r \quad (3.28)$$

The filtered momentum equation may now be expressed using these new definitions

$$\rho \frac{\partial \bar{u}_i}{\partial t} + \rho \frac{\partial (\bar{u}_i \bar{u}_j)}{\partial x_j} = -\frac{\partial \bar{p}}{\partial x_i} + \frac{\partial}{\partial x_j} \left[ \mu \frac{\partial \bar{u}_i}{\partial x_j} \right] - \frac{\partial \tau_{ij}^r}{\partial x_j} \quad (3.29)$$

The above equation is not closed until we can model the residual stress tensor  $\tau_{ij}^R$  (or  $\tau_{ij}^r$  if the isotropic part is included in the modified filtered pressure). It is interesting to look at the decomposition of the residual stress. Applying this decomposition to the term  $\overline{u_i u_j}$  in Equation (3.23), the nonlinear term can be expressed as below (Leonard 1974).

$$\begin{aligned} \overline{u_i u_j} &= \overline{(\bar{u}_i + u'_i)(\bar{u}_j + u'_j)} \\ &= \overline{\bar{u}_i \bar{u}_j} + \overline{\bar{u}_i u'_j} + \overline{\bar{u}_j u'_i} + \overline{u'_i u'_j} \\ &= \underbrace{(\overline{\bar{u}_i \bar{u}_j} - \bar{u}_i \bar{u}_j)}_{L_{ij}} + \bar{u}_i \bar{u}_j + \underbrace{\overline{\bar{u}_i u'_j} + \overline{\bar{u}_j u'_i}}_{C_{ij}} + \underbrace{\overline{u'_i u'_j}}_{R_{ij}} \end{aligned} \quad (3.30)$$

The *Leonard*, *Cross* and *subgrid Reynolds* stresses denoted by  $L_{ij}$ ,  $C_{ij}$  and  $R_{ij}$  each describe different interactions within the flow. The Leonard stresses describe interaction between the larger motions of the fluid. The cross stresses relate to the large and small scale motions, whereas the subgrid Reynolds stresses relate to the smallest turbulent features at the subfilter level. This is known as the Leonard or triple decomposition and can be stated more neatly as

$$\tau_{ij}^R = L_{ij} + C_{ij} + R_{ij} = \overline{u_i u_j} - \bar{u}_i \bar{u}_j \quad (3.31)$$

In a similar manner to the above momentum equations, the residual heat flux tensor can be defined as

$$h_j = \overline{u_j t} - \bar{u}_j \bar{T} \quad (3.32)$$

Using (3.32) the final governing temperature equation can be obtained

$$\rho \frac{\partial \bar{T}}{\partial t} + \rho \frac{\partial (\bar{u}_j \bar{T})}{\partial x_j} = \frac{\partial}{\partial x_j} \left[ \frac{\mu}{Pr} \frac{\partial \bar{T}}{\partial x_j} \right] - \rho \frac{\partial h_j}{\partial x_j} \quad (3.33)$$

### 3.7.2 Filtering

For LES, the NS equations are spatially filtered, it is therefore useful to familiarise oneself with some common filters used in LES. The filtering operation for velocity  $u$  can be given by,

$$\bar{\mathbf{u}}(\mathbf{x}, t) = \int G(\mathbf{r}, \mathbf{x}) \mathbf{u}(\mathbf{x} - \mathbf{r}, t) d\mathbf{r} \quad (3.34)$$

with the normalisation condition

$$\int \mathbf{G}(\mathbf{r}, \mathbf{x}) d\mathbf{r} = 1 \quad (3.35)$$

Applying a filter to the velocity  $u_i$  for example, gives

$$u_i = \bar{u}_i + u'_i \quad (3.36)$$

or

$$u'_i = u_i - \bar{u}_i \quad (3.37)$$

This is similar to the Reynolds decomposition although the filtered residual is not equal to zero. (The time mean of  $u'$  is zero in RANS.)

To resolve the larger scales well, the filter width should be chosen to be considerably smaller than the smallest energy containing motions. Various filters exist, the most common being the Box, Gaussian and Spectral cut-off filters. These may be expressed in physical and wavenumber forms.

For the box filter,  $\bar{u}$  becomes the average of  $u(x')$  for  $x - \frac{1}{2}\Delta < x' < x + \frac{1}{2}\Delta$ . In physical space it is positive and there is a cut-off of scales. In spectral space effects from various wavenumbers are present. The Box filter is not effective at attenuating high wave-numbers. The grid itself acts like an implicit box filter (this is also known as natural or grid filtering) and the box filter is equivalent to the Gaussian filter to second order accuracy (Sagaut 2006). Use of an explicit filter greater than the grid size results in a sub-filter scale (SFS) as well as the SGS scale.

The Gaussian filter is compact, generally local, of a similar form in both physical and spectral space and is positive. This filter is a Gaussian distribution with zero mean and a variance  $\sigma^2 = \frac{1}{12}\Delta^2$ . This value was chosen by Leonard (1974) to match the second moments  $\int_{-\infty}^{\infty} r^2 \mathbf{G}(r) dr$  of the box filter. Modes of higher wavenumber than the cutoff frequency are still represented as it is a smooth function in both physical and frequency space.

The spectral cut-off filter is non-local in physical space. As the name suggests, there is a sharp cut-off of wave-numbers above the cut-off frequency (cut-off wavenumber= $\kappa_c$ ). Since it only removes wave-numbers above the cut-off, it is possible to represent the large scales exactly.

In a typical application  $\kappa_c = \frac{1}{8}\kappa_{DNS}$  and  $\kappa_{LES} = 2\kappa_c = \frac{1}{4}\kappa_{DNS}$  (Pope 2000). Therefore, in 3D, LES requires 64 times fewer nodes. This saving comes at the cost of the uncertainties involved in modelling the unresolved modes. It may also be noted that spatial filtering also gives rise to implicit time filtering (Sagaut 2006).



### 3.7.3 Grid independence of LES

In traditional LES, implicit filters arising from the grid and discretisation methods are often used instead of an explicit filter. This divides the solution into the resolved and unresolved subgrid scales that must be modelled in some way. Use of an explicit filter on the other hand, further separates the solution into the resolved filtered scales (RFS), resolved subfilter-scales (RSFS) and the unresolved subfilter scales (USFS). This distinction between the explicit filter and the subgrid scales would allow a grid independent LES to be performed. Upon refinement, the explicit filter would still be effective, even though the subgrid scale could be much smaller than the filter width. The USFS motions then consist of both subgrid and partially resolved scales of similar size to the explicit filter. Although at first this seems attractive, it introduces many other aspects into the simulation such as explicit filter width, grid resolution requirements (as the explicit filter needs enough grid points to resolve the larger scales), filter choice, numerical interactions and commutation errors. For example high order numerical schemes require the filter functions to be commutative to at least the same order as the numerical scheme (Gullbrand 2002). For these reasons, the natural grid filter is used here. This may make it easier to conclude what modelling method is most suitable by reducing the number of variables under study. The use of the grid filter means that the grid can be made so fine that a DNS is approached because, as the filter width is reduced, so too is the SGS contribution. Therefore grid independence will never be obtained. This does not mean that use of different grid resolutions is not helpful in revealing which scales of motion are important. As will later be seen, grid resolution is only part of the overall modelling procedure and other important effects must be taken into account.

### 3.7.4 Linear eddy-viscosity models (LEVMs)

To relate the smaller scales (the SGS stresses) to the larger scales (via the strain rate tensor  $\bar{S}_{ij}$ ), the eddy viscosity model may be used. We use the term *linear model* as the SGS tensor is related to the strain rate tensor with an eddy viscosity as a proportionality parameter. This assumption is perhaps justified by the fact that the SGS stresses have little influence on the large scales and only need to model the net energy transfer from the large to the dissipative scales. The idea of local isotropy means that the small scales can be described by a characteristic velocity and time scale whilst being independent of time. It is also assumed that energy equilibrium is instantaneously maintained with the large scales and that the filter is inside a substantial inertial subrange. The LES turbulent stress tensor is given by Equation 3.25. For linear eddy-viscosity models such as the Smagorinsky (Smagorinsky 1963) or Yoshizawa (Yoshizawa 1993) models,  $\tau_{ij}^r$  is given by

$$\tau_{ij}^r = -2\mu_T \bar{S}_{ij} / \rho \quad (3.38)$$

where the filtered rate of strain tensor is

$$\bar{S}_{ij} = \frac{1}{2} \left( \frac{\partial \bar{u}_i}{\partial x_j} + \frac{\partial \bar{u}_j}{\partial x_i} \right). \quad (3.39)$$

For more complex nonlinear models, extra terms are added in order to try and better represent anisotropies in the SGS stress tensor.

Similar to the RANS formulation of the eddy viscosity model, the kinematic eddy viscosity can be related as

$$\nu_T \propto v_{SGS} \ell_{SGS} \quad (3.40)$$

where  $v_{SGS}$  and  $l_{SGS}$  are the velocity and length scales of the SGS motions respectively. Generally the length scale is related to the filter width  $\Delta$  which is usually taken from the grid spacings as  $(\Delta_x \Delta_y \Delta_z)^{1/3}$ . However, there are various ways of defining the filter width.

The transfer of energy to the unresolved motions is specified by the rate of residual kinetic energy production

$$P_r = -\tau_{ij}^r \overline{S}_{ij} = 2\nu_T \overline{S}_{ij} \overline{S}_{ij} = \nu_T \overline{S}^2 \quad (3.41)$$

This defines the local equilibrium hypothesis that energy does not accumulate at any frequency and the energy balance is instantaneously restored. This acts to continuously dissipate energy that is cascaded down through the assumed inertial range.

#### 3.7.4.1 Smagorinsky

Perhaps the most well known LES model is that proposed by Smagorinsky (Smagorinsky 1963). This is the LES equivalent to the mixing-length model of Prandtl. The eddy viscosity for this model may be written as

$$\mu_T = \rho(C_S \Delta_S)^2 \overline{S} \quad (3.42)$$

where

$$\Delta_S = 2 \min \left[ \kappa y_{min}, (\Delta_x \Delta_y \Delta_z)^{\frac{1}{3}} \right] \quad (3.43a)$$

$$\bar{S} = \sqrt{2S_{ij}S_{ij}} \quad (3.43b)$$

For all simulations  $C_S = 0.1$  and as per Equation 3.43a, a simple mixing length model is used near walls, naturally blending to the LES volumetric lengthscale  $\Delta$ . This reduces  $\mu_T$  at walls where the Smagorinsky model is generally too dissipative. Note that the factor of two is often omitted from (3.43a) by some resulting in apparently higher constants.

The value of  $\mu_T$  remains positive meaning that only the forward scatter of energy from the large scales to the residual (subgrid) scales is possible. The choice of the Smagorinsky constant  $C_S$  is one of the models main downfalls. The original value obtained by Lilly (1967) (from isotropic turbulence and other assumptions) of 0.17 was supposed to be a universal constant, not a “tuning” constant. However, this value is generally too large, especially for wall-bounded flows like plane channels (Sagaut 2006) and can even prevent transition into turbulent flow (the viscosity remains too high near walls suppressing the instabilities required to generate turbulence). This large constant causes too much dissipation as the mean shear rate is increased (compared to the isotropic homogeneous case), so the constant is often reduced for different cases. To reduce dissipation specifically near walls, damping functions may also be employed such as the Van Driest damping function (Driest 1956). Although this does bring benefits, it is hard to justify in the background of LES.

Despite its drawbacks ( $\mu_T$  does not even reduce to zero in laminar flow), the Smagorinsky model has become popular due to its simplicity and provides theoretical insight, on which, many other LES models are built. With some experimentation and tuning, simulations can be reasonably accurate, although for industrial use this would not be an acceptable practice. When referring to this model in the results, the label “Smag” will be used followed by the grid resolution

label. Only second order central differencing is used for this model.

### 3.7.4.2 Yoshizawa $k$ - $l$

To introduce history and non-local effects into the SGS model, an extra transport equation for the turbulent kinetic energy  $k_T$  can be introduced. This slightly modified model of the Yoshizawa (1993) model is used as described in Davidson and Peng (2003). Relating the eddy viscosity to  $k_T$  helps to more realistically account for areas of flow where there is little shear yet the eddy viscosity is not zero.

$$\frac{\partial k_T}{\partial t} + \frac{\partial \bar{u}_j k_T}{\partial x_j} = \frac{1}{\rho} \frac{\partial}{\partial x_j} \left[ \left( \mu + \frac{\mu_T}{\sigma_k} \right) \left( \frac{\partial k_T}{\partial x_j} \right) \right] + P_{k_T} - \varepsilon_T \quad (3.44)$$

Basing the SGS/turbulent viscosity on the kinetic energy gives the isotropic relation

$$\mu_T = \rho C_\mu l_\mu k_T^{1/2} \quad (3.45)$$

The turbulent Prandtl number for kinetic energy,  $\sigma_k = 1$  (Pope 2000) and the turbulence production and dissipation terms are given by  $P_{k_T}$  and  $\varepsilon_T$ , shown below.

$$P_{k_T} = 2 \frac{\mu_T}{\rho} \bar{S}_{ij} \bar{S}_{ij} \quad (3.46)$$

$$\varepsilon_T = C_\varepsilon k_T^{3/2} / l_\varepsilon \quad (3.47)$$

Because this model is so similar to the RANS model of Wolfshtein (1969), only the length scales and constants need to be changed. The LES length scales for this  $k-l$  based model are given by (3.48).

$$l_{\epsilon,LES} = l_{\mu,LES} = (\Delta_x \Delta_y \Delta_z)^{1/3} \quad (3.48)$$

This relates the smallest resolved scales with the largest unresolved scales with the constants for relations (3.47) and (3.45) being  $C_\epsilon = 1.05$  and  $C_\mu = 0.07$ . Similarly to the Smagorinsky model, the minimum of the RANS (3.20–3.21) and LES length scales (3.48) are taken to ensure sensible behaviour near walls giving  $l_\epsilon$  and  $l_\mu$  in (3.45) and (3.47).

Although another model by Yoshizawa introduces another transport equation to compute further parameters for use in this type of model (Sagaut 2006), the above constants are used, consistent with Zhong and Tucker (2004). When referring to this model in the results, the label “Yosh” will be used followed by the grid resolution label. Only second order central differencing is used for this model.

### 3.7.5 Mixed nonlinear models

One main feature of nonlinear SGS models is that they are able to model local energy backscatter from the small scales to the larger scales. This may occur where large coherent structures develop in the flow field and has been confirmed using DNS (Domaradzki et al. 1993). Unless negative eddy viscosities are allowed by the model, linear models are purely dissipative. Theoretically it is thought that backscatter is not related to negative values of SGS viscosity. Events known as ejections have been studied in low- $Re$  wall bounded flows, where the events were found to be deterministic (Piomelli et al. 1996). Therefore stochastic models

for this process may be insufficient. These models are also better able to model the anisotropy found in shear flows. Generally these models do not dissipate enough energy from the flow and so a mixed form is chosen in which dissipation is achieved using the Yoshizawa model described earlier (see Section 3.7.4.2), to calculate the subgrid viscosity. Other nonlinear terms are then added via source terms. Capturing of anisotropic flow features at the smaller scales is hoped to be improved using these models, which may be beneficial when using coarser grids, although they are more sensitive to numerical effects.

Of the models studied here, two are based on the concept of regularisation of the NS equations and were not originally intended as LES models. In the NS equations, very intermittent vorticity bursts can inject kinetic energy at scales much smaller than the Kolmogorov scales creating problematic singularities. Regularisation of the NS equations causes a disappearance of these as it tends to damp the smallest scales. This may be interpreted as a smoothing operation and can be cast in the LES context. Both the Leray and LANS- $\alpha$  LES models are based on regularisation principles. Although they are similar in final form, they stem from different ideas and concepts. The Leray model is based on a *smoothed transport velocity* whereas the LANS- $\alpha$  formulation is created from the *filtered Kelvin circulation theorem* which incorporates the smoothed transport velocity. These principles imply closures to the LES equations.

### 3.7.5.1 Leray regularisation

Altering the convective flux of the NS equations into  $\bar{u}_j \partial u_i / \partial x_j$  gives the equations where the solution  $\mathbf{u}$  is convected by the smoothed velocity  $\bar{\mathbf{u}}$ .

$$\frac{\partial u_i}{\partial t} + \bar{u}_j \frac{\partial u_i}{\partial x_j} + \frac{\partial p}{\partial x_i} - \nu \frac{\partial^2 u_i}{\partial x_j \partial x_j} = 0 \quad (3.49)$$

To state this in terms of filtered variables only we make use of the filter  $\mathbf{G}$  and its inverse  $\mathbf{G}^{-1}$ . Thus, replacing quantities using  $\bar{\mathbf{u}} = \mathbf{G}(\mathbf{u})$  and  $\mathbf{u} = \mathbf{G}^{-1}(\bar{\mathbf{u}})$  Equation 3.49 may be expressed as

$$\mathbf{G}^{-1} \left( \frac{\partial \bar{u}_i}{\partial t} + \frac{\bar{u}_j \partial \bar{u}_i}{\partial x_j} + \frac{\partial \bar{p}}{\partial x_i} - \nu \frac{\partial^2 \bar{u}_i}{\partial x_j \partial x_j} \right) = - \frac{\partial (\bar{u}_j \mathbf{G}^{-1}(\bar{u}_i) - \mathbf{G}^{-1}(\bar{u}_j \bar{u}_i))}{\partial x_j} \quad (3.50)$$

The bracketed left hand side of Equation 3.50 is the standard LES form of the equations. Applying the filter  $\mathbf{G}$  to both sides, we can write the bracketed right hand side of Equation 3.50 as the Leray stress tensor below.

$$\tau_{ij}^{Leray} = \mathbf{G} (\bar{u}_j \mathbf{G}^{-1}(\bar{u}_i)) - \bar{u}_j \bar{u}_i = \overline{\bar{u}_j \bar{u}_i} - \bar{u}_j \bar{u}_i \quad (3.51)$$

This tensor is not symmetric unlike most other subgrid tensors.

For the Leray model, the anisotropic part is given by Equation 3.52.

$$\tau_{ij}^r = (-2\mu_T \bar{S}_{ij}) / \rho - C_L l_{SGS}^2 N_L \quad (3.52)$$

where  $C_L = 1/24$  and

$$N_L = \frac{\partial u_i}{\partial x_k} \frac{\partial u_k}{\partial x_j} + \frac{\partial u_i}{\partial x_k} \frac{\partial u_j}{\partial x_k} \quad (3.53)$$

When calculating  $\mu_T$  using (3.45),  $C_\mu = 0.05$ . The right term of (3.52) is limited to the magnitude of the linear Yoshizawa terms.

Since the Taylor expansion at quadratic order of the box and Gaussian filters is the same (Geurts 2005; Sagaut 2006), the velocities for the NL term are



smoothed using a second order approximation to the Gaussian filter and the resolved variables are grid filtered. When referring to this model in the results, the label “Ler” will be used followed by the discretisation scheme and grid resolution label. Where no discretisation scheme is given, second order central differencing is used.

### 3.7.5.2 LANS- $\alpha$ regularisation

The LANS- $\alpha$  model used is similar to the Leray model but with extra terms to relate it to the Kelvin recirculation theorem. For the LANS- $\alpha$  model, in Equation 3.52  $N_L$  and  $l_{SGS}$  may be replaced by  $N_\alpha$  and  $\alpha$  with  $N_\alpha$  given below

$$N_\alpha = \frac{\partial u_i}{\partial x_k} \frac{\partial u_k}{\partial x_j} + \frac{\partial u_i}{\partial x_k} \frac{\partial u_j}{\partial x_k} + \frac{\partial u_k}{\partial x_i} \frac{\partial u_k}{\partial x_j} \quad (3.54)$$

The best results are thought to be obtained when using a length scale  $\alpha$  close to the grid spacing (Geurts 2005). This justifies the use of  $(\Delta_x \Delta_y \Delta_z)^{1/3}$  as a representative LES length-scale. It can be shown that when applied to fully developed three-dimensional turbulence, the  $\alpha$ -model exhibits the  $\kappa^{-5/3}$  behaviour for scales larger than  $\alpha$  and  $\kappa^{-3}$  for scales smaller than  $\alpha$  (Sagaut 2006). When referring to this model in the results, the label “ $\alpha$ ” or Alpha (or Alp) will be used followed by the discretisation scheme and grid resolution label. Where no discretisation scheme is given, second order central differencing is used.

### 3.7.5.3 Kosović

The Kosović model is a phenomenological closure. It is hoped it will provide better results in shearing flows (Liu et al. 2007).

$$\tau_{ij}^r = -(2\mu_{SGS}S_{ij})/\rho - C_e l_{SGS}^2 \left(\frac{27}{8\pi}\right)^{1/3} C_S^{2/3} N_K \quad (3.55)$$

$$N_K = \left[ C_1 \left( S_{ik}S_{kj} - \frac{1}{3}S_{mn}S_{nm}\delta_{ij} \right) + C_2 (S_{ik}\Omega_{kj} - \Omega_{ik}S_{kj}) \right] \quad (3.56)$$

or in a similar form to Equation 3.53

$$N_K = 0.5 \frac{\partial u_i}{\partial x_k} \frac{\partial u_k}{\partial x_j} + 1.5 \frac{\partial u_i}{\partial x_k} \frac{\partial u_j}{\partial x_k} - 0.5 \frac{\partial u_k}{\partial x_i} \frac{\partial u_k}{\partial x_j} \quad (3.57)$$

The constants are defined as  $C_S = 0.202$ ,  $C_1 = C_2 = 1.53$  and  $C_e = 0.11$ . Also when calculating  $\mu_{SGS}$ ,  $C_\mu = 0.11$ . When referring to this model in the results, the label ‘‘Kos’’ will be used followed by the discretisation scheme and grid resolution label. Where no discretisation scheme is given, second order central differencing is used.

### 3.7.6 ILES

The sensitivity of typical LES based solutions to discretisation truncations errors and phenomena such as false diffusion, which is akin to the use of an eddy viscosity, allows the numerical details of the procedure to be used to provide dissipation in place of an explicit SGS model. In ILES there is no assumed form of the subgrid scales and the implied subgrid model is determined only by the structure of the resolved flow (Drikakis et al. 2009) and the numerical aspects of the solver. Specially designed numerical schemes can be formulated to give more formal closures, though the subgrid scales are still determined by the structure of the resolved flow.

Various discretisation schemes may be used, each with their own benefits and drawbacks. Two common choices for spatial discretisation are the first order upwind (only suitable for RANS) and second order central difference schemes. Other schemes have been proposed to address the restrictions of the schemes above, all of which have some drawbacks such as computational expense or difficulty of implementation. Many are also inelegant making them hard to interpret. Restrictions may be placed on the discretisation to ensure stability or monotonicity, important for compressible flows, though some conditions may be relaxed for incompressible flows. Investigated in this work are the second order central difference, second order upwind, QUICK and 4<sup>th</sup> order central difference schemes for the convective terms (the diffusive terms are left second order accurate since based on  $Re$  the effects will be comparatively small). ILES modelling is here only tested in a hybrid RANS-ILES framework (see Section 3.8.2).

## 3.8 Turbulence modelling - hybrid RANS-(I)LES

### 3.8.1 $k-l$ based RANS-LES

As discussed earlier, this model makes use of a (U)RANS layer near walls to model the streak structures which would otherwise require a high resolution grid at walls for LES to be used. This layer is then blended into the LES region where larger time dependent motions are captured. The interface between the two regions is either based on turbulence properties (for example  $y^+$  values) or set at a given distance from walls. For LES regions, the single equation  $k-l$  based Yoshizawa model is used. Since the form of this model is nearly identical to  $k-l$  RANS models, only the length scales and constants need be changed between the two regions. The constants from the Wolfstein RANS model and the required length scales used in the RANS regions are as given in Section 3.6.2.1 and for the LES

region in Section 3.7.4.2.

Because of the large difference in length scales at the interface, smoothing is required to avoid an abrupt change in turbulent viscosity. This is achieved by using a multigrid restriction operator. The lengthscales for the RANS and LES regions are given by equations (3.20)–(3.21) and (3.48) respectively. The location of the interface between the RANS and LES regions is given later for each test case. (See Sections 7.2–7.4).

Due to the variation of  $Pr$  or  $\Gamma$  at RANS-LES interfaces (or thermally different interfaces for the cube test case), the harmonic mean based on the assumption that cell faces lie halfway between nodes is used (Patankar 1980):

$$\Gamma = 2 \frac{\Gamma_{i,j,k} \Gamma_{i,j+1,k}}{\Gamma_{i,j,k} + \Gamma_{i,j+1,k}} \quad (3.58)$$

When referring to the  $k-l$ -based RANS-LES model in the results, the label “RL” will be used followed by the grid resolution label. This method is only tested with second order central differences.

### 3.8.2 $k-l$ based RANS-ILES

This method is very similar to the RANS-LES method described except that a Hamilton-Jacobi equation is used to smoothly set length scales to zero for the ILES region. Therefore smoothing is not required. The technique is described in Tucker and Liu (2005a). The turbulent Prandtl number need only be specified for the RANS region since the turbulent viscosity becomes zero in the ILES region. When referring to this model in the results, the label “RI” will be used followed by the discretisation scheme (CD2/CD4, 2UP and Q for second/fourth-order central

difference, second order upwind and QUICK respectively) and grid resolution label.

### **3.9 Summary**

This chapter has introduced some details of turbulence theory and the RANS and LES formulations were introduced. The RANS and a range of linear and nonlinear LES models have also been described along with reasoning for their use. The hybrid methods used were also detailed.

# Chapter 4

## NEAT code details and numerical methods

### 4.1 Introduction

LES is much more sensitive to discretisation schemes than (U)RANS simulations, this is due to the relatively small turbulent (eddy) viscosity. This diffusion coefficient is large in RANS simulations damping out smaller scale unsteadiness. In LES, only the unresolved turbulence needs to be modelled and the SGS model (eddy viscosity for simple models) can become over powered by discretisation error as shown by Chow and Moin (2003); Ghosal (1999); Kravchenko and Moin (1997); Meyers et al. (2007). In fact, the numerical contribution to the overall residual stresses can be much larger than that of the SGS stresses. Due to the meager grids encountered in commercial CFD applications, discretisation errors are likely to be large. This is often viewed as a disadvantage at first when considering LES models, where one would usually want to minimise discretisation errors. However, these discretisation errors can be put to some use using ILES, where it has been shown

that the truncation and other numerical errors can be shown to be equivalent to residual stresses.

Previous work on the cases in the introduction provide considerable motivation to investigate reductions in mesh size and different discretisation schemes using hybrid RANS-(I)LES methods. One reason to use ILES is to reduce computation time through removing the need for a SGS model, another is that using (I)LES relies on suitable discretisation. The more complex nonlinear LES models are more sensitive to discretisation errors and may also benefit from higher numerical fidelity. Nonlinear LES models require a smaller discretisation error to prevent the influence of the more refined turbulence model being masked by numerical errors. However, use of a fine grid reduces the proportion of modelled turbulence, potentially making the effects of these advanced models insignificant. The use of more modest grids and perhaps higher order methods to reduce numerical noise may allow a particular nonlinear model to prove useful. Squires et al. (2005) apply URANS, DES and laminar models to a separated flow over a rounded corner square to investigate grid refinement, domain size and other modelling aspects. It was found that 5-10 cells were sufficient to capture streamwise vortices and higher order methods may allow accuracy to be retained using fewer cells. van der Velde et al. (1999) make use of a fourth order numerical scheme to perform DNS using fewer grid nodes. Using a channel flow, fourth order numerical scheme results were improved over those using a second order scheme. Relevant to the (I)LES regions of the present solutions is the work of Nakayama and Vengadesan (2002). It was found that noticeable improvements can be observed through use of higher order difference schemes although it is noted that on conservative grids, these may introduce stability problems. It was found that some upwinding may be required to prevent solution divergence. This prompts us to look at the effects of different discretisation schemes including the order and stencil type.

## 4.2 NEAT code details

The NEAT code is a Finite Volume, structured Cartesian coordinate system, incompressible flow solver. The code makes use of cell faces centered between computational nodes. Due to this boundaries lie on cell faces and using second order central differences for spatial terms, stretched grids have no effect on the neighbour coefficients. The pressure and velocity fields are iteratively solved using the SIMPLE algorithm (Patankar 1980). To remove possible checker-board pressure effects, the velocity fields are staggered with respect to the pressure field. The basic discretisation and SIMPLE algorithm is described by Patankar (1980), though an outline is given here.

Each electronics cooling test case (as described in Chapter 7) had various differences in the source code, due to boundary conditions and contributions from previous users. Therefore the source code had to be modified to incorporate any required changes such as the inclusion of any missing turbulence models or editing routines, for example, to add or remove periodicity or the spatial discretisations described later. The code for the CPU case was parallelised using OpenMP to speed up computation time. Modifications to the code will be described in more detail in the following sections.

## 4.3 Finite volume method overview

The general transport equation for any quantity  $\phi$ , is given in the Cartesian-tensor form by Equation 4.1

$$\frac{\partial}{\partial t}(\rho\phi) + \frac{\partial}{\partial x_j}(\rho u_j \phi) = \frac{\partial}{\partial x_j} \left( \Gamma \frac{\partial \phi}{\partial x_j} \right) + S \quad (4.1)$$



and mass conservation is expressed as

$$\frac{\partial \rho}{\partial t} + \frac{\partial}{\partial x_j}(\rho u_j) = 0 \quad (4.2)$$

where  $\Gamma$  is the diffusion coefficient,  $S$  is the source term of the relevant quantity  $\phi$  and  $j$  takes the values of 1, 2 and 3 denoting the  $x$ ,  $y$  and  $z$  directions. Following Einstein summation, repeated subscripts are summed.

The Finite Volume method uses the integral form of the conservation equation. Rather than directly approximating the derivatives in the Navier-Stokes equations as in the Finite Difference method, quantities are integrated over each cell and the value stored is the cell-average. The Finite Difference method on the other hand only deals with point values. Integration over each control volume (CV) can be replaced using the Gauss divergence theorem (Spiegel 1959) so that we need only integrate over each CV surface. Here,  $\mathbf{n}$  represents the outward facing vector normal to the CV face.

$$\int_S \rho \phi \mathbf{u} \cdot \mathbf{n} dS = \int_S \Gamma \text{grad} \phi \cdot \mathbf{n} dS + \int_{\Omega} q_{\phi} d\Omega \quad (4.3)$$

One of the key advantages to the FV method is that for each CV and hence the entire domain, conservation of mass (Equation 4.2) and energy is satisfied.

## 4.4 Spatial discretisation

Now that we have the equations for the variable  $\phi$ , we must discretise it in some way so that each CV can be solved. This is done by approximating all exact terms in Equation 4.1. Using the geographical notation of Patankar (1980), we define

CV faces as  $e, w, n, s, f, b$ . For simplicity we shall only consider one dimension as each direction can be treated similarly for the purpose of this work. The notation used can be interpreted using the diagram in Figure 4.1.

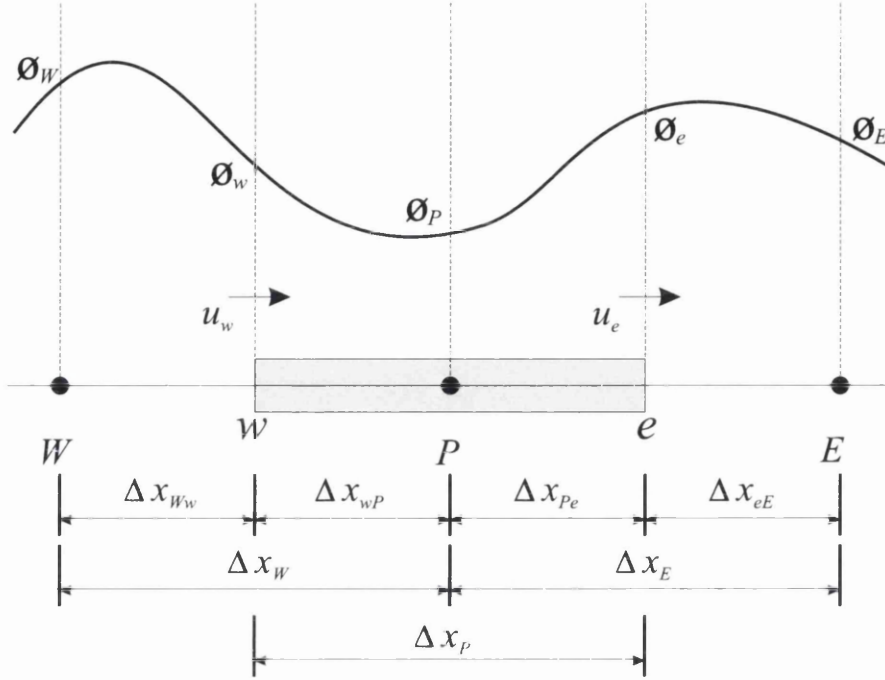


Figure 4.1: Geographical notation as used by Patankar (1980).

Given a grid spacing  $\Delta x$ , the unsteady transport equation (Equation 4.1) can be written as

$$\frac{\partial \rho}{\partial t} + (\rho u_i \phi)_e - (\rho u_i \phi)_w = \left( \Gamma \frac{\partial \phi}{\partial x} \right)_e - \left( \Gamma \frac{\partial \phi}{\partial x} \right)_w \quad (4.4)$$

The diffusion terms can be expressed as

$$\left( \Gamma \frac{\partial \phi}{\partial x} \right)_e - \left( \Gamma \frac{\partial \phi}{\partial x} \right)_w = \Gamma_e \frac{(\phi_E - \phi_P)}{\Delta x_e} - \Gamma_w \frac{(\phi_P - \phi_W)}{\Delta x_w} \quad (4.5)$$

Defining  $D = \Gamma/\Delta x$  and  $C = \rho u$ , the general equation can be written as

$$C_e\phi_e - C_w\phi_w = D_e(\phi_E - \phi_P) - D_w(\phi_P - \phi_W) \quad (4.6)$$

Although Finite Difference derivatives can be formulated in a similar way, Finite Volume and Finite Difference discretisations are only the same up to second order. Therefore the error decreases as second order but the errors are different. Since the cell-average values are available only at the nodal locations, interpolations are required to obtain the cell face values of variables where required. Here we will use polynomials of different orders and nature using both central difference and upwind stencils. If the same interpolation polynomial coefficients were to be used for both FD and FV, there would always be an  $O\Delta x^2$  error between the two methods as shown by Leonard (1994). The stencils used will now be introduced and discussed. Uniform grids are used for discussion, but the polynomial coefficients are weighted by the grid spacings using the Lagrangian formula (Equation 4.7 where  $L_k(x)$  is given by Equation 4.8) for use on non-uniform structured grids.

$$f(x) = L_0(x)f_0 + L_1(x)f_1 + L_2(x)f_2 + \dots + L_n(x)f_n \quad (4.7)$$

$$L_k(x) = \frac{(x - x_0)(x - x_1)(x - x_2) \dots (x - x_{k-1})(x - x_{k+1}) \dots (x - x_n)}{(x_k - x_0)(x_k - x_1)(x_k - x_2) \dots (x_k - x_{k-1})(x_k - x_{k+1}) \dots (x_k - x_n)} \quad (4.8)$$

On a uniform grid, the variable being interpolated to the east cell face is weighted as shown in Table 4.1 with weights  $\alpha_W - \alpha_{EE}$  as in Equation 4.9. For the west face, indices are shifted to the west by one node. The corresponding interpolation functions are depicted in Figure 4.2 where an arbitrary curve (solid line) is approximated with the mentioned stencils at the east (dashed line) and west (dotted line) 1D cell faces.

$$\phi_e = \alpha_W \phi_W + \alpha_P \phi_P + \alpha_E \phi_E + \alpha_{EE} \phi_{EE} \quad (4.9)$$

Scheme	$\alpha_W$	$\alpha_P$	$\alpha_E$	$\alpha_{EE}$
CD2	-	$\frac{1}{2}$	$\frac{1}{2}$	-
2UP	$-\frac{1}{2}$	$\frac{3}{2}$	-	-
QUICK	$-\frac{1}{8}$	$\frac{6}{8}$	$\frac{3}{8}$	-
CD4	$-\frac{1}{16}$	$\frac{9}{16}$	$\frac{9}{16}$	$-\frac{1}{16}$

Table 4.1: Weighting constants for east cell face interpolation on a uniform grid.

The coefficients for central difference schemes are not directional and so the stencils shown in Figure 4.2(a) and 4.2(d) apply for positive and negative flow directions.

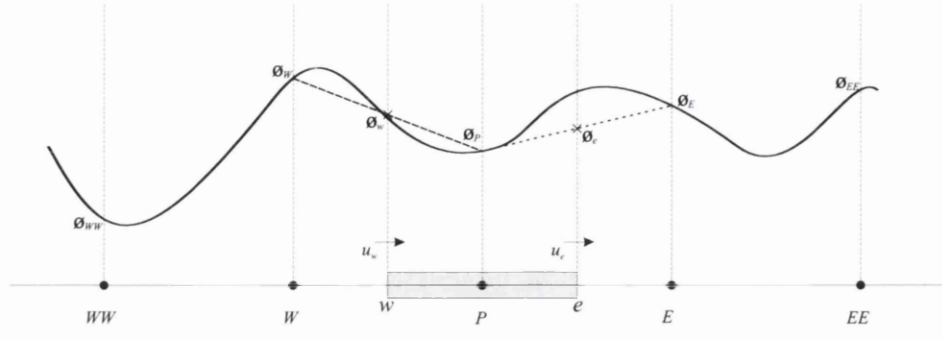
Schemes are implemented using a deferred-correction approach (Ferziger and Perić 2002). For the east convective flux,  $F_e$ , we correct the first order upwind scheme via the source term by adding the difference between the required higher order flux  $F_e^H$  and the lower order flux  $F_e^L$ . This gives the relationship

$$F_e = F_e^L + (F_e^H - F_e^L) \quad (4.10)$$

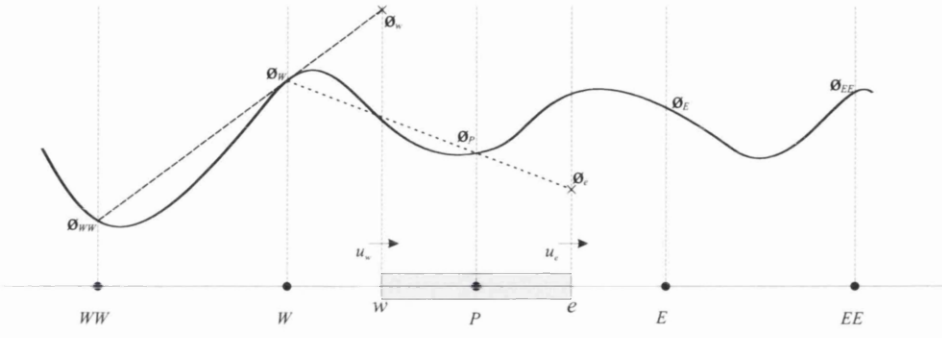
Only adding the difference between the two schemes to the source is thought not to have a large effect on convergence since the first order upwinding gives diagonal dominance.

#### 4.4.1 False diffusion

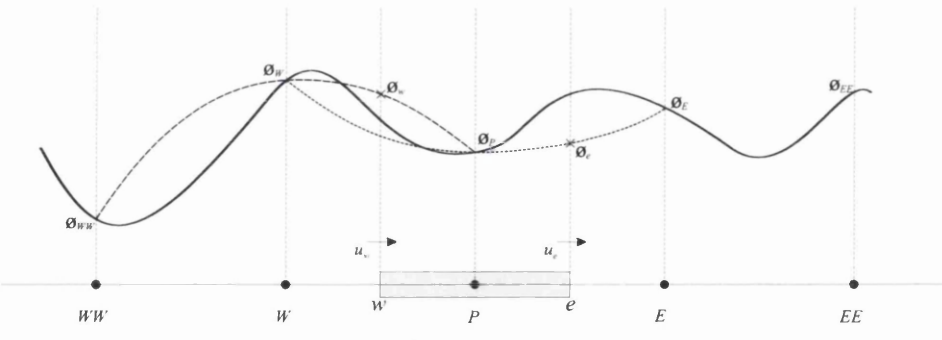
False diffusion is a multidimensional phenomenon caused by treating each cell face one-dimensionally and is not the same as truncation error. It occurs because the flow direction is not taken into account, for example, assuming flow from the west, when the flow is entering the cell from the southwest. For any one dimensional



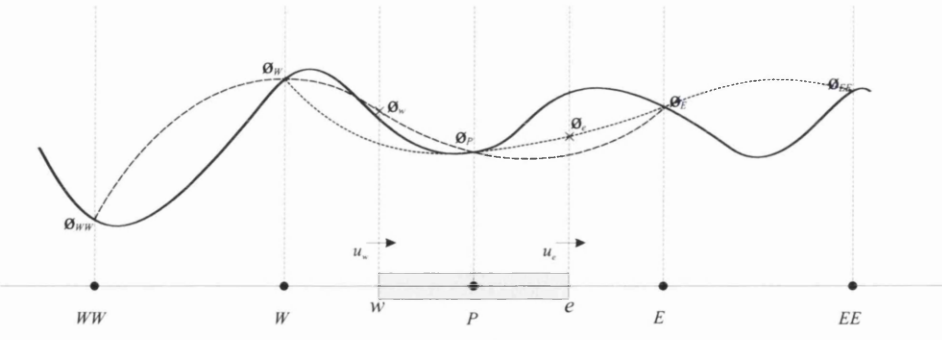
(a) CD2



(b) 2UP



(c) QUICK



(d) CD4

Figure 4.2: Different stencils used for cell-face interpolation.

stencil, if the flow is not normal to the cell face, some false diffusion will be generated.

### 4.4.2 Second order central difference

One of the most obvious and widely used schemes is the second order central difference scheme. This is a linear interpolation of the two nearest nodes surrounding the cell face to be approximated (see Figure 4.2(a)). It can be shown using Taylor expansion that this has a leading truncation error of  $O\Delta x^2$  and is dispersive. It is common to assume that a higher order truncation error term leads to a more accurate solution. However this is only the case at sufficiently small grid spacings. For example CD2 is often considered to be more accurate than first order upwinding due to considerable false diffusion of the latter scheme, yet this is true only for small Peclet numbers. If  $Pe$  becomes greater than 2, the neighbour coefficients can become negative creating spurious oscillations in the solution. These over- and under-shoots can affect stability and produce physically unrealistic results such as negative kinetic energy. Although this formal restriction on  $Pe$  seems to limit the applicability of this scheme, it has still been adopted widely due to its simplicity and the fact that satisfactory results are often obtained.

### 4.4.3 Second order upwind

Second order upwinding is an extension of first order upwinding involving two nodes upstream of the cell face. Again a second order linear interpolation is used, though the cell face value is more of a projection than an average as in the CD2 scheme. This can be seen in Figure 4.2(b). Table 4.1 gives the stencil for a positive flow direction and therefore if the flow is in the opposite direction, the stencil must be reversed so that the interpolation nodes are on the upstream side. Although

of higher order accuracy than the first order upwind scheme, the extra upwind node produces more false diffusion than the CD2 scheme if the flow is diagonal to the grid. Overall the scheme is less diffusive than first order upwinding however. A derivation of this scheme maintaining positive neighbour coefficients is given in Appendix B.1.

#### 4.4.4 QUICK

The QUICK scheme is in many ways similar to both the CD2 and second order upwind schemes. It has two upstream nodes and one downstream node, it is like the CD2 scheme with a 1 node upwind bias. This scheme fits a quadratic profile through the three points and can be more accurate as a result of being better able to fit curves (see figure 4.2(c)). A third order leading truncation error is found on Taylor expansion. Being similar to both CD2 and second order upwinding, it inherits traits from both these schemes. Due to being of order of accuracy greater than 1, the scheme will produce over- and under-shoots similar to the CD2 scheme. The upwind bias also produces some false diffusion as with the second order upwind scheme. A derivation of the QUICK scheme maintaining positive neighbour coefficients is given in Appendix B.2.

#### 4.4.5 Fourth order central difference

The CD4 scheme further increases the order of the polynomial used to interpolate the variable to 3 and makes use of two nodes either side of the cell face (see Figure 4.2(d)). This gives a fourth order leading truncation error term. CD4 is used to reduce numerical errors for the nonlinear LES models. Oscillations are expected to be small due to general lack of discontinuities in the flows under study, however large gradients will exist near boundaries and larger errors are to be expected here.

Generally use of higher order CD schemes would imply dispersion errors of higher frequency and lower amplitude with increasing order.

## 4.5 Basic solution procedure

The NEAT code solves a set of linearised equations formulated in a tri-diagonal matrix with the variable  $\phi$ , neighbouring coefficients  $a_{nb}$  and a source term  $S$ . Each differential equation is discretised so that equations of the form

$$a_p\phi_P = a_e\phi_E + a_w\phi_W + a_n\phi_N + a_s\phi_S + S \quad (4.11)$$

or

$$\begin{bmatrix} 1 & 0 & 0 & 0 & \cdots & 0 & 0 \\ -a_{w,2} & a_{p,2} & -a_{e,2} & 0 & \cdots & 0 & 0 \\ 0 & -a_{w,3} & a_{p,3} & -a_{e,3} & \cdots & 0 & 0 \\ \vdots & \vdots & \ddots & \ddots & \ddots & \vdots & \vdots \\ \vdots & \vdots & \vdots & \ddots & \ddots & \ddots & \vdots \\ 0 & 0 & 0 & 0 & a_{w,n-1} & a_{p,n-1} & -a_{e,n-1} \\ 0 & 0 & 0 & 0 & 0 & 0 & 1 \end{bmatrix} \begin{bmatrix} \phi_1 \\ \phi_2 \\ \phi_3 \\ \vdots \\ \vdots \\ \phi_{n-1} \\ \phi_n \end{bmatrix} = \begin{bmatrix} S_1 \\ S_2 \\ S_3 \\ \vdots \\ \vdots \\ S_{n-1} \\ S_n \end{bmatrix} \quad (4.12)$$

can be solved by either the iterative Gauss-Seidel or direct TDMA (Tri-Diagonal Matrix Algorithm) methods by rearranging into the form of Equation 4.12. With reference to Figure 4.1, the locations of the variable  $\phi$  can be understood. Details of these solution procedures can be found in Versteeg and Malalasekera (1995).



To solve the Navier-Stokes equations or any scheme derived from them, the pressure and velocity fields must be linked in some way. The pressure field and velocities are intimately related and must be solved either simultaneously or iteratively to overcome the nonlinear relationship between them. In the NEAT code, the SIMPLE (Semi-Implicit Method for Pressure-Linked Equations) algorithm of Patankar and Spalding (1972) is employed. Essentially this method is a guess-and-correct procedure. The pressure field  $p^*$  is guessed, the momentum equations are solved using this guessed pressure field resulting in  $u^*$ . The differences between the guessed and true pressure and velocity fields allow an equation to be solved iteratively to correct the pressure and velocity fields. The procedure and corrections can be iterated until convergence is reached, giving both the correct pressure and velocity fields.

## 4.6 Changes made to the NEAT code

The NEAT code originally included the first order upwind (Courant et al. 1952), hybrid (Spalding 1972), second order central difference and the CONDIF scheme of Runchal (1987). The described cell face approximations were added to the NEAT code using a generalised method capable of computing polynomials of  $n^{\text{th}}$  order in either a central difference or (partially and fully) upwinded stencil type. The included derivations of the second order upwind and QUICK schemes are included in Appendices B.1 and B.2 as these were initially used before the more general approach was developed. Inkeeping with the rest of the NEAT code, care was taken to include 2D and 3D terms with and without periodic boundaries so that high order could be maintained wherever possible. Automatic reduction of the stencil size (and generally order) near solid surfaces was also included. Therefore the only changes to be made by the user are two numbers in the input file to define the stencil.

## 4.7 Summary

This chapter has provided an overview of the numerical methods, spatial discretisation and code used in this work. An understanding of this gives some foresight into what may or may not be useful strategies.

# Chapter 5

## Performance optimisation

### 5.1 Introduction

Although it is known that LES-based techniques allow for higher solution accuracy and offer more insight into flow physics than RANS-based solutions, there is a large increase in computational demand due to the solution being time dependent. It is therefore of great importance, especially for non-academic applications, that solution times be reduced as much as possible to make unsteady methods commercially viable. All areas that comprise the simulation have influence on the total time to solution. These include pre-processing, boundary conditions and economical use of resources at runtime.

### 5.2 Starting conditions

It is always important to provide starting conditions as close to the solution as possible to minimise the amount of work the solver has to do in order to

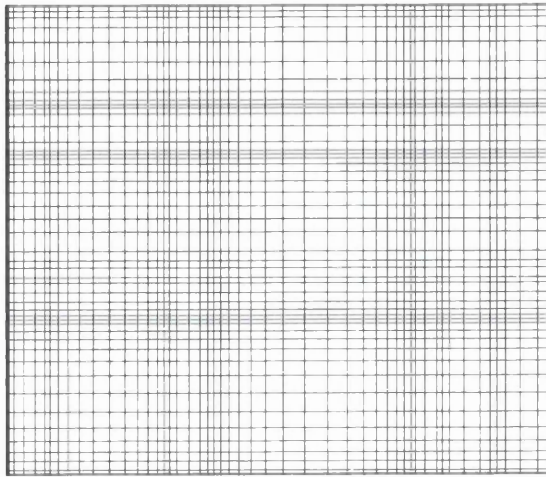
converge the solution. Matters can be exacerbated on a per case basis when for example there is a large difference in time scales between part of the domain. This is exemplified by the cube channel test case where the difference in thermal conductivity and heat capacity between the epoxy layer and the surrounding air flow generates a thermal time constant ( $= \rho c_p h^2 / k$ ) ratio of  $\approx 187$  (i.e. the epoxy reaches a quasi-steady state much slower than the air reacts to any change in the surface temperature of the epoxy). This means that although the flow around the cube may have matured to a physically realistic state, the temperature in the epoxy would still be rising and it would take much longer to perform the simulation. This numerical stiffness was found by Tucker and Keogh (1996). To help resolve issues such as this, it is useful to return to (U)RANS methods to obtain a good estimate of the quasi-steady temperature field in the epoxy in a relatively short period of time, or to solve the pure conduction problem in the cube epoxy only. This can then be used as the starting point for the thermal field as the velocity-pressure field is then solved.

One key problem with unsteady simulations is providing realistic boundary conditions. Real life systems are seldom steady and the successful introduction of realistic synthetic turbulence (it is most likely that experimental data is not available to provide time dependent boundary conditions) at unsteady boundaries has generally proved illusive. One problem is that instabilities introduced through the boundary conditions can amplify causing solution divergence, or stochastic forcing for example, may have only a small effect (Tucker and Liu 2005a), making the use of such methods questionable.

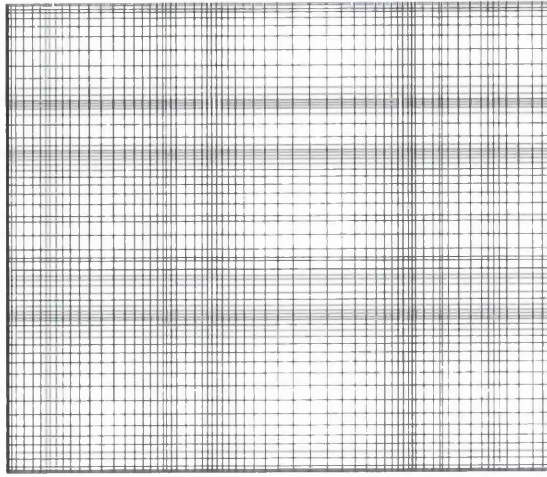
### 5.3 Successive grid refinement

Starting a simulation from scratch makes the time to complete a simulation much longer. This is largely due to the flow having to mature in time from the starting conditions (for example,  $\mathbf{U} = 0$ ) to a physically realistic solution. Using the finest grid required tends to waste a lot of time because the largest scales dominate the solution, which itself is defined by large scale geometrical features. It is therefore useful to start the solution on a low-resolution grid to obtain the larger scales and characteristic flow structures. This also allows a larger time step to be used, further reducing the computation time. Once the flow has matured, the solution can be interpolated onto a finer grid. This is a step by step process and is not the same as the multigrid method (see Tucker (2001)). Progressively, this enables smaller and smaller details to be resolved. This grid refinement can be seen in Figure 5.1 for a plane in the CPU case.

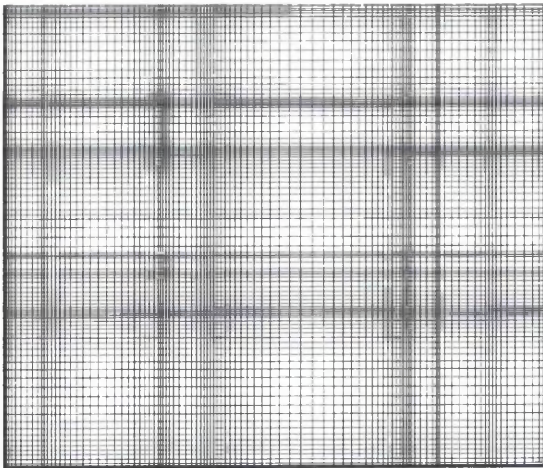
It is possible that lower resolution in both time and space could be obtained using higher order discretisations. Assuming no large computational overhead for higher order schemes, a similar accuracy to a real flow could be obtained in less time. Further grid refinements could also be made through the actual topology of the grid used. In the current work, many nodes are packed close together in regions of low turbulent activity due to using a structured Cartesian grid. The total number of cells could therefore be reduced in some regions if an unstructured or multi-block grid was used. Successive refinement may also help to measure what the time and length-scales of motion are. This would help with creating a higher quality grid and the determining the size of the LES filter to use. Using successive grid refinement for the ribbed channel flow, computation time was reduced by a factor of seven. This could probably be improved by introducing some convergence criteria, so that the refinement process can be automated.



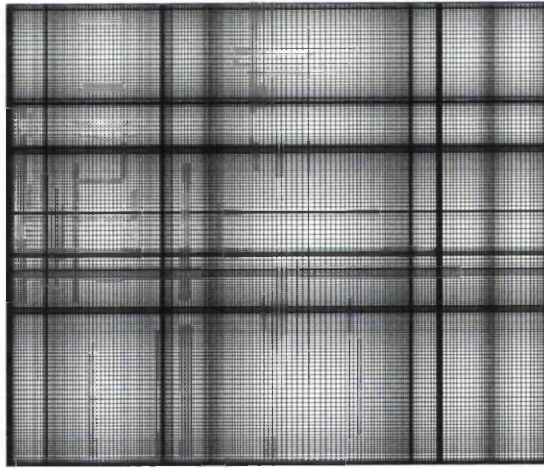
(a) resolution 1



(b) resolution 2



(c) resolution 3



(d) resolution 4

Figure 5.1: Succession of finer grids for CPU case.

## 5.4 Parallel computation

Due to the large grid used for the CPU case, it was necessary to reduce computation time dramatically to run several simulations. Due to the use of structured Cartesian grids, the NEAT code lends itself well to the parallelisation method of OpenMP, where the domain is split in one direction. Using OpenMP, only do-loops can be parallelised always leaving serial portions of the code untouched. This in theory is relatively straight forward however setting *all* variables in the code with the correct access permissions (private or shared) was laborious and time consuming. Some attention will be given to the process that involved considerable effort.

The computational domain is split into sub-domains (see Figure 5.2), each one to be processed by one thread (a fork of a containing process/executable). Typically one thread per CPU core is used, though multi-core CPUs and CPUs that can process more than one thread per core allow more threads to be processed per physical CPU. This however is dependant on computer architecture/hardware.

To avoid data dependencies (where different threads may try to read and write data to or from the same position in memory), the solver for example, was altered to use the Gauss-Seidel solver and the do-loops were split using the red-black method (Ferziger 1998). After debugging, the serial and parallel codes produced the same answers after several hundred time steps. One problem that arose was the default stack memory size. The OpenMP method is prone to this problem due to many threads requiring the same data to be copied to memory. Fortunately, most compilers and computing systems allow the stack size to be changed to circumvent this problem.

Using OpenMP to parallelise the NEAT code realised a speedup of about 12 times using 16 processors. Amdahl's law defines the maximum speedup obtained when

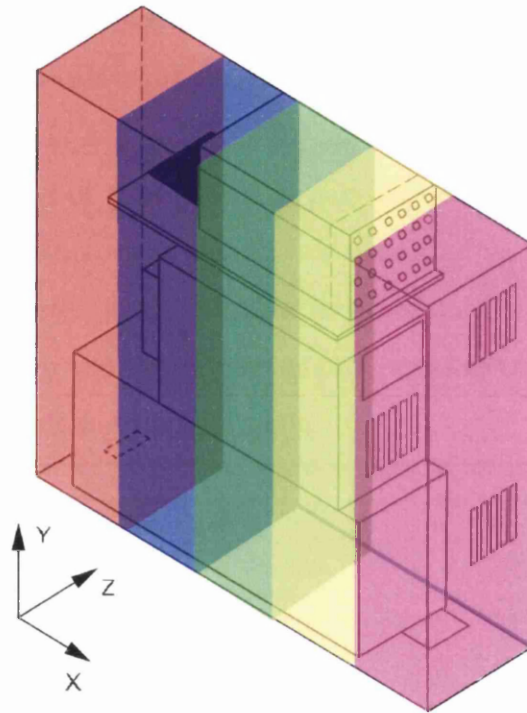


Figure 5.2: Illustration of OpenMP domain decomposition.



only a portion of a code is made parallel and is given by Equation 5.1

$$\text{Max. speedup} \leq \frac{1}{F + (1 - F)/N} \quad (5.1)$$

where  $F$  is the fraction of serial code that cannot be parallelised and  $N$ , the number of processors.

From the above speedup it seems that around 5% of the runtime is serial or computational overhead (for example, call statements and thread creation). This serial portion of the code is a constant for any number of threads. However for larger grids, the portion of time spent in parallel do-loops increases. Although the gains are quite satisfactory, Amdahls law is related to the law of diminishing returns and for an increase in the number of processors, departs from the linear relation between speedup and the number of processors as can be seen in Figure 5.3 with data from the parallellised NEAT code.

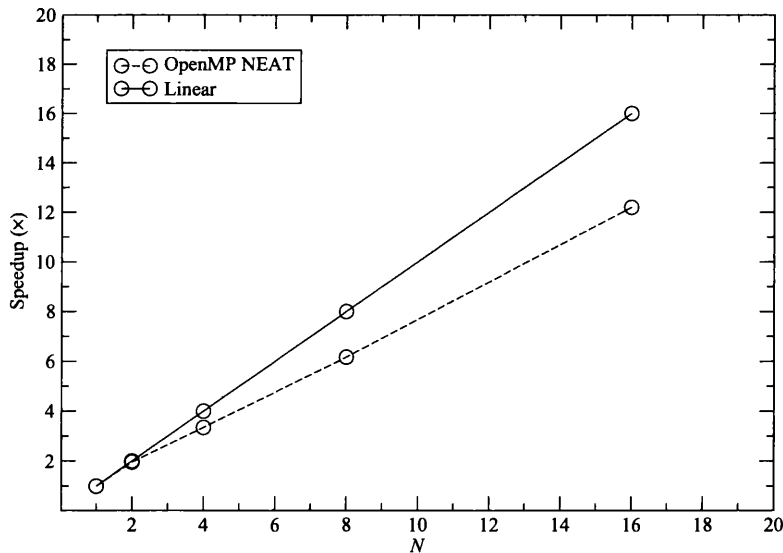


Figure 5.3: OpenMP NEAT code speedup compared to ideal linear speedup.

Although the gains with increasing the number of processors are not linear, other CFD codes are able to obtain a nearly linear relationship. With increasing

parallelism at the hardware level, continuing gains are expected. Due to the frequency at which CPUs operate no longer increasing substantially (as a consequence of thermal limitations), they have instead turned to a more parallel architecture. Although past super-computers linked many single-core CPUs together, common desktop CPUs can process 2-8 threads. Another growing area offering cheap highly parallel computation is the Graphics Processing Unit (GPU). Recently it has become easier to make more general purpose computations on the GPU known as GPGPU (Brandvik and Pullan 2008; Hagen et al. 2006; Harris 2004). One of the latest GPUs contains 1600 simple processors running at 850 MHz (offering up to 2.72 TFLOPS) allowing massively parallel problems to be solved for a few hundred pounds. Compared to a super-computer, this gives a high price to performance ratio. Generally, the use of a structured solver also improves computational efficiency when compared to unstructured codes. Brandvik and Pullan (2008) show an order of magnitude improvement in computation time when an existing code was run on a GPU compared to being run on a CPU. The square geometry of electronics systems also makes parallel structured Cartesian solvers an attractive method.

## 5.5 Convergence criteria

### 5.5.1 Typical residual and RMS monitoring

Typical convergence criteria is based on changes or final values of residuals ( $R_\phi$ ) (error in the general discretised equation  $a_p = \sum a_{nb}\phi_{nb} + S$ ) and/or RMS changes in each variable. The expressions for the residual and RMS changes in the variable

$\phi$  are given in Equations 5.2a and 5.2b.

$$R_\phi = \sum_{i=1}^M \left| \left( \sum_{nb} a_{nb} \phi_{nb} \right)_i + S_i - (a_p \phi_p)_i \right| \quad (5.2a)$$

$$\text{RMS}_\phi = \sqrt{\frac{\sum_{\Omega} (\phi^{\text{new}} - \phi^{\text{old}})^2}{\sum_{\Omega} (\phi^{\text{new}})^2}} \quad (5.2b)$$

where  $M$  is the total number of cells in the domain.

It is common to monitor residuals for a decrease of magnitude (Ferziger and Perić 2002). This however is not entirely reliable as a sole judgment of convergence, especially for unsteady computations. For unsteady computations, the residual will oscillate around a range of values as at each timestep, the solution is equivalent to a *steady* state iterative procedure. Therefore each time step, the *steady* state changes slightly and the solution must converge to it. Normally the change between time steps is small enough that only a few iterations are required for convergence, as the previous time step is a good estimate of the solution at the new time step. Depending on the underlying low frequency unsteadiness, the changes in residual and RMS errors can be relatively large or small. The magnitude of the variable being considered also needs to be accounted for, hence residuals are usually normalised by a suitable factor to account for the variance in variable magnitudes. Using RMS changes also has its pitfalls. A flow that changes slowly in time or that has strong under-relaxation will only ever change slightly at each iteration. Therefore the RMS change will be small but the solution not fully converged. As shown by Tucker (2001), convergence errors will result in phase errors. Global quantities of interest to the thermal designer will generally be time average quantities, less sensitive to phase errors. In this study the guidelines of Tucker (2001) are followed with normalised residuals and RMS changes below  $2 \times 10^{-2}$  and  $5 \times 10^{-5}$  respectively. It can be seen that there is no definite way of

telling whether an unsteady simulation has converged and matured to the point where useful data can be collected. Following from this, a method of testing for such conditions using Fourier Analysis is now assessed.

### 5.5.2 Fourier analysis

The periodic nature of many flows in electronics systems and many other flows implies that some characteristic frequencies may be detected and used as a gauge for convergence as the solution matures in time. This periodicity may be due to large time scale features of the domain, such as the repetition of geometry in the rib and cube test cases, or higher frequency vortex shedding from sharp edges and bluff bodies. Frequencies within the flow can be extracted through data sampling and it is possible, following Ahmed and Barber (2005), that the development of these characteristic frequencies as the solution progresses in time may be used as an unsteady convergence criterion. In an attempt to define a point in time where a given solution has developed far enough for meaningful data to be collected or to interpolate to a finer grid as described previously, Fourier analysis is applied to the ribbed channel as it is the most simple representative electronics flow in this study.

The Fast Fourier Transform (FFT) is an efficient method to calculate the more computationally expensive Discrete Fourier Transform (DFT), changing the sample signal values from the time domain to the frequency-amplitude domain. If a sequence  $x(n)$  is defined in the interval 0 to  $N - 1$  the DFT  $X(k)$  or  $x(n)$  is defined over the same interval as

$$X(k) = \sum_{n=0}^{N-1} x(n)e^{ik\omega_0 n}, 0 \leq k \leq N - 1 \quad (5.3)$$

where  $i = \sqrt{-1}$ ,  $\omega_0 = 2\pi/N$  (radians) and  $k$  is the frequency index. This may be written as

$$X(k) = \sum_{n=0}^{N-1} x(n)W_N^{kn}, 0 \leq k \leq N-1 \quad (5.4)$$

where the phase factor  $W_N = e^{2\pi i/N}$ .

The FFT method only works if the number of FFT points ( $N_{FFT}$ ) points is a power of 2. Therefore, if the number of samples ( $N_{ds}$ ) is not a power of 2, zero padding is used where  $N_z$  is the number of zero samples added to the original samples. One advantage of zero padding is that it provides a better display of the Fourier transform since all the samples are closer together, their spacing given by  $2\pi/(N_{ds} + N_z)$ . In the frequency domain, the amplitude is a function of both the original amplitude of the signal ( $A_0$ ) and the number of FFT points giving  $A = A_0 N_{FFT}/2$ . The frequency is calculated as

$$f_k = k/N_{FFT}\Delta t \quad (5.5)$$

Of course the maximum frequency that can be captured through time sampling depends on the sampling frequency and using a sampling interval of  $\Delta t$  can be defined as

$$f_{max} = 1/2\Delta t \quad (5.6)$$

The minimum (cutoff) frequency also depends on the sampling rate and the number of data samples  $N_{ds}$ .

$$f_{min} = 1/N_{ds}\Delta t \quad (5.7)$$

The cutoff region is defined by having a maximum frequency of  $f_{min}$ . The difference between two consecutive frequencies depends on the number of FFT points and is found from

$$f_{sp} = 1/N_{FFT}\Delta t \quad (5.8)$$

As eddies are shed from the rear face of the rib, it should be possible to detect frequency peaks related to the dominant frequencies in the flow. Using the details of the ribbed channel, the sampling frequency (10 000 Hz) and the number of data samples (5000), the previous relations may be used to obtain the limiting detectable frequencies and frequencies that are likely to be of interest.

$$f_{min} = 1/N_{ds}\Delta t = 1/(5000 \times 0.0001) = 2.0 \text{ Hz} \quad (5.9)$$

$$f_{max} = 1/2\Delta t = 1/0.0002 = 5000 \text{ Hz} \quad (5.10)$$

Given 5000 data samples, the next power of 2 is  $2^{13} = 8192$ , giving an error bound of

$$f_{eb} = \frac{1}{2}(1/N_{FFT}\Delta t) = 1/0.0002 * 8192 = 0.61 \text{ Hz} \quad (5.11)$$

To accurately resolve any frequency, it is suggested by Shur et al. (2003) that 5–10 periods at least 4 grid cells are required. This essentially restricts the maximum

and minimum frequencies that can be accurately detected so that  $10 \leq f_{min} \leq 20$  Hz. It is important that  $f_{min}$  is less than the physical frequencies of the flow variable. For the highest frequencies,  $f_{max} \leq U_0/(4\Delta)$ , where  $\Delta = 0.002$  m is the maximum grid spacing of the medium grid and  $U_0 = 3.6 \text{ ms}^{-1}$  giving  $f_{max} = 450$  Hz. Therefore the detectable frequency range will be  $10 < f < 450$  Hz.

It is important to try and estimate the frequencies of interest in the flow so that they may be detected and compared using Fourier analysis. On the largest scale, using the bulk velocity  $U_0$ , the time taken for fluid to travel the full length of the domain is 0.0353 s giving a lower frequency of  $f_{min,rib} = 28.35$  Hz. The main frequency of interest is probably the rate of vortex shedding from the rear of the rib. Typical Strouhal numbers for vortex shedding off a cylinder are  $0.1 < St < 0.3$  and for a rib in a free stream  $0.12 < St < 0.2$  (Panigrahi 2001). Basing the Strouhal number on the rib height and  $U_0$ , this results in the highest frequency of interest  $57 < f_{max,rib} < 170$  Hz. Both frequencies are well within the detectable frequency range. Studying a ribbed channel case similar to that of Acharya et al. (1993), Panigrahi (2001) also suggests that  $St$  should be based on the momentum thickness  $\theta$  giving  $St = 0.012$  as the rib is not in a free steam but wall-bounded. Using  $\theta = 0.48$  mm, (obtained from Panigrahi (2001)), this results in a frequency of 90 Hz. Although this is in the range of frequencies given above, it demonstrates some disagreement about what frequencies to expect depending on the flow type.

Data samples were taken in the shear layer at  $2h$  downstream of the rib and  $y/h = 1.404$  where evidence of vortex shedding is likely to be found. Figure 5.4 shows the obtained frequency spectrum for two consecutive data sets. Both sets match in frequency and have similar amplitude at frequencies of 8.5, 17.1 and 75.8 Hz. The Fourier method does not accurately predict the amplitude in noisy data sets. It is thought that the random nature of turbulence and the transformation and rotation of eddies caused by this makes frequencies hard to detect unless much more data is recorded. Using experiments Meinders and Hanjalić (1999) needed

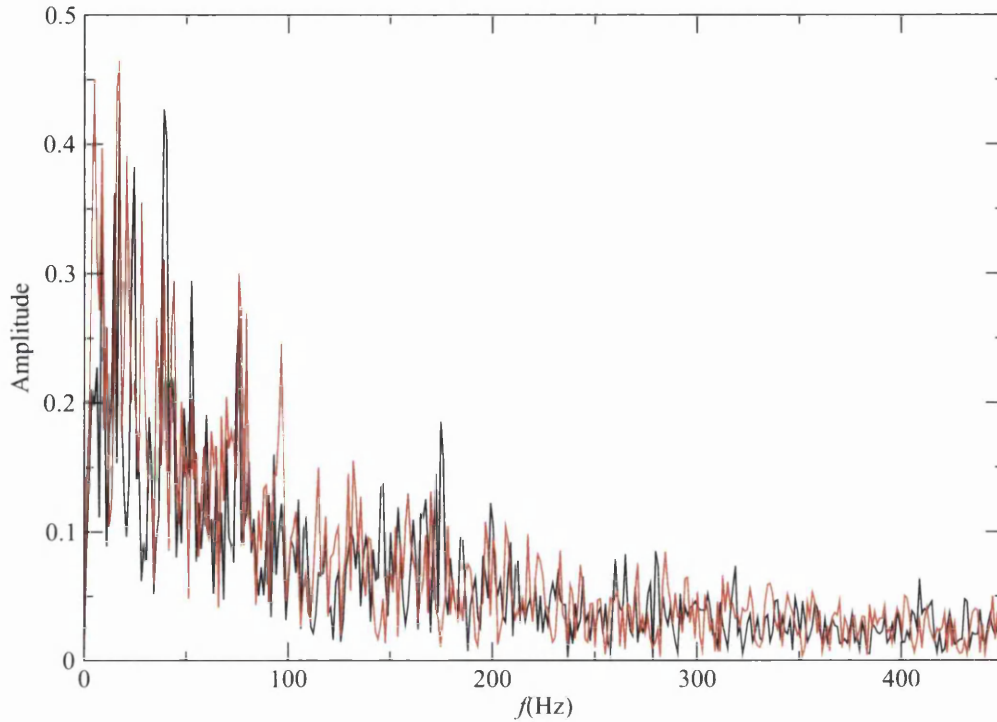


Figure 5.4: Frequency-Amplitude plot for ribbed channel data samples.

to use 500,000 data points to accurately obtain a power density spectrum for flow over a cube. This was equivalent to 20,000-40,000 vortex shedding cycles with a Strouhal number of 0.109.

Although more than enough data was theoretically collected it proved impractical to reliably detect key frequencies in the flow using this method due to the extra runtime required. This precludes its widespread use as a convergence criterion for (I)LES based solutions.

The previous work of Ahmed and Barber (2005) applies the method to URANS, where only the largest scales producing unsteadiness will be detectable. Even applied to URANS, the method requires that unsteadiness is certain to occur, which is not always the case when using RANS based methods, due to increased damping. An example of this is a study by Bosch and Rodi (1998) on vortex shedding past square cylinders. Comparisons are made with their own and other



URANS simulations, highlighting the fact that for example, the placement of boundary conditions can have a strong influence on the solution and that similar simulations may or maynot establish vortex shedding.

A more general application of this method to other geometries would require knowledge of where to place sampling points in the flow and what frequencies are expected. Given that the ribbed channel is the simplest electronics test case in this study, it seemed unproductive to proceed further with this method given that a geometry such as the CPU case contains many different dominant frequencies depending on which region of flow is studied. Based on the conclusions and suggestions of Hellsten and Rautahimo (1999), where predictions of periodic vortex shedding using time-accurate methods was inadequate, it would seem such methods or applications require more investigation. Instead of using Fourier analysis it may prove more useful to compare mean velocity profiles at different times throughout the solution, each time averaged for a relatively short period of time. Mean velocity profiles are normally captured easily by most simulations. This should require substantially less data than trying to detect various frequencies as only data used in progressing the solution in time is required. The question would still remain however, what tolerance to use for the comparison of two consecutive profiles? This, or the use of other convergence criteria would require further study on a variety of industrially relevant flows with the consideration of commercially viable constraints, such as overall computation time and computational resources.

## 5.6 Recommendations

To obtain the most accurate solution in the shortest possible time it is important to gather as much information as possible prior to running the simulation. This

would enable the best starting conditions to be applied. Steady simulations or previous data may be used to provide a starting point for numerically stiff thermal simulations. Unfortunately, URANS cannot be used to obtain a rough estimate of an LES flow. Once the RANS eddy viscosity is replaced by the SGS viscosity, there is too little dissipation to maintain a stable solution. Once the balance of forces from the increased shear stresses is removed, a highly unstable flow field exists, invalid for LES simulation. Fortunately, the geometries studied here will run on low-resolution grids, so the flow field can be matured quickly. Using successive grid refinement allows smaller and smaller scales to be incorporated and could be easily introduced commercially based on current multigrid routines. An automated method for this process is required, naturally requiring a criterion for interpolating to the next finest grid. The use of parallel computing at every stage would provide a substantial speedup and the square geometries lend themselves well to domain decomposition and efficient structured solvers. Future increases in computing power such as GPGPU processing, will naturally reduce computation times to more acceptable levels.

# Chapter 6

## High order validation and verification

### 6.1 Introduction

The addition of new convective term discretisations to the previous code required that the code was tested in various ways to ensure it was correct. A simple 1D test and two 2D cases were used to verify and validate the code and also used to investigate the behaviour of each scheme in more than one dimension. To investigate numerical effects of the different spatial discretisations used, a Tollmein-Schlichting wave and a convected vortex were chosen.

### 6.2 1D cell face interpolation test

To check that the 1D cell face values were approximated correctly using various interpolations, the known temperature function below was used as a reference.

$$T(x) = \sum_{n=1}^9 \frac{\sin((2n-1)x)}{2n-1} \quad (6.1)$$

This function gives an approximation to a step function using the summation of several sine functions. This results in a steep gradient (though not so steep that under/over-shoots are found) as shown in Figure 6.1.

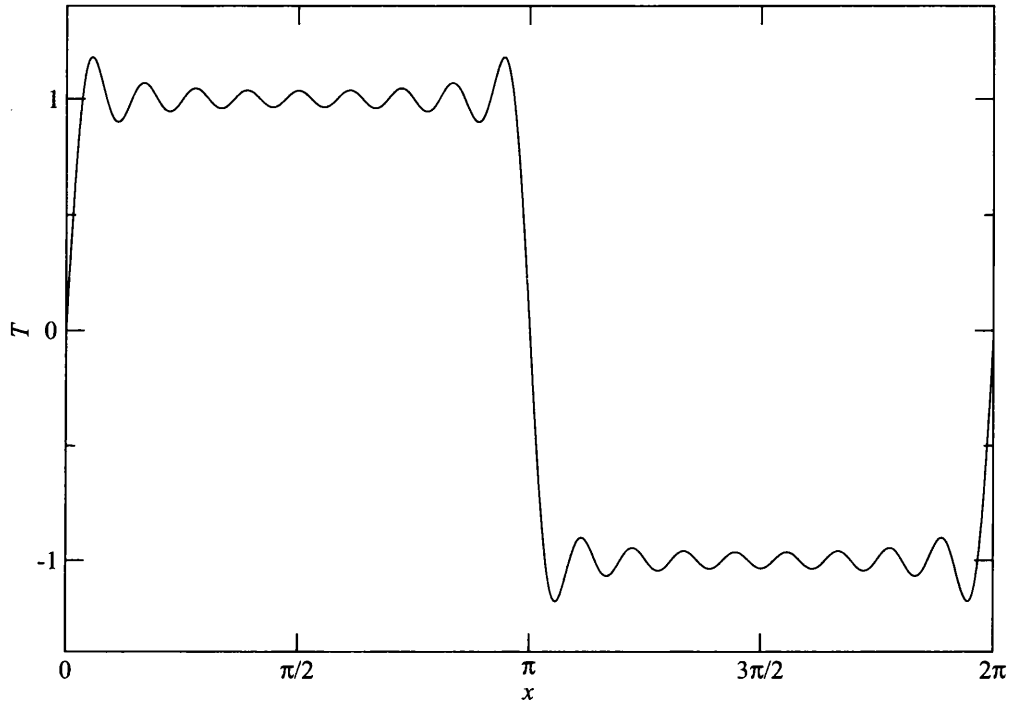


Figure 6.1: 1D temperature function.

From Equation 6.1 nodal values were calculated and east/west cell face values approximated using different order cell-face interpolations. Although central difference stencils for orders greater than four are not discussed, the stencils and behaviour are similar to those of the second and fourth order stencils.

For any nonlinear interpolation there is a range of expected behaviour between a grid density high enough to be in the radius of convergence but coarse enough for there to be significant differences between different orders of interpolation. A higher order scheme will reach maximum accuracy (for example machine round-off

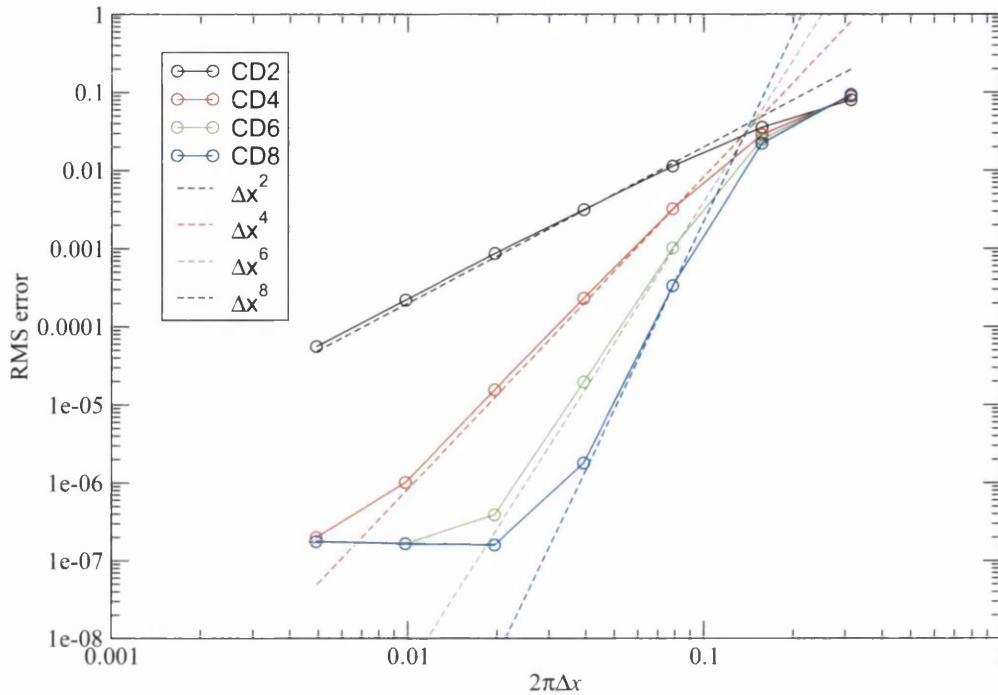


Figure 6.2: Error reduction for 1D temperature function.

error or another more dominant limiting factor) before a lower order scheme. A linear interpolation will reduce the error continuously (as it will never perfectly fit a curve) until machine round off error. These effects can be seen in Figure 6.2 where the gradients nearly match the expected  $\Delta x^n$  relationship for a range of  $\Delta x$ . Using deferred correction (Ferziger and Perić 2002) each scheme has been implemented in the neat code. Except when stated, *CD2* refers to the standard CD2 scheme in the NEAT code.

### 6.3 Tollmien-Schlichting wave propagation

The study of a Tollmien-Schlichting (T-S)-wave perturbing a channel flow is studied to assess basic properties of various numerical discretisation schemes as studied by Chung and Tucker (2004b). The properties of each scheme are important to know for both LES and ILES based computations. LES solutions

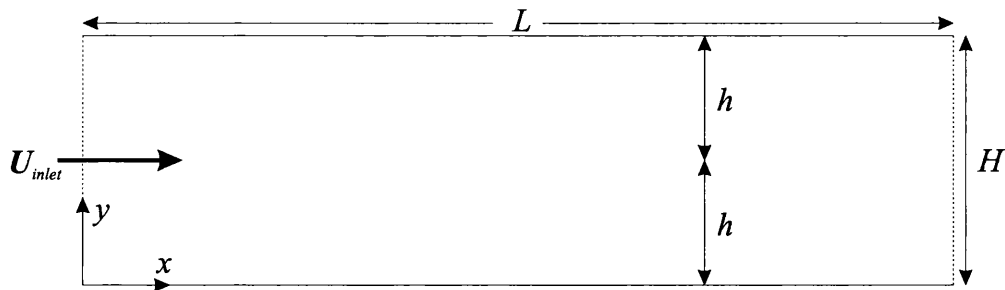


Figure 6.3: TS wave computational domain.

may tolerate a scheme that is less diffusive, with oscillations stemming from high order discretisation becoming damped by the explicit SGS viscosity. In this case it is possible a higher order scheme may be used to reduce numerical diffusion whilst maintaining stability. ILES on the other hand relies solely on the numerical schemes and discretisation applied to the flow. Therefore, a more dissipative scheme perhaps containing some upwinding may become more appropriate. The current case will help to clarify what traits, order of accuracy and type of stencil will be most appropriate for use in further calculations.

A T-S-wave is used to disturb the typical laminar parabolic inlet profile found in plane channel flows. Based on the center-line velocity  $U_c$  and the channel half height  $h$ , the subcritical Reynolds number of 5000 is tested. This ensures that the T-S-wave decays downstream of the inlet. Details of the simulation can be seen in Figure 6.3.

For the inlet profile  $\mathbf{u}_{inlet}$ , the two-dimensional TS wave superimposed on the laminar parabolic profile ( $U_0(y) = y(2h - y)$ ) is given by

$$u'_i(x = 0, y, t) = A_{TS} \Re [\hat{u}_i(y) e^{-i\omega_R t}] \quad (6.2)$$

where  $A_{TS}$  is the amplitude of the perturbation at the inlet,  $\omega_R$  the real frequency and  $u'_i(y)$  is the complex velocity vector obtained from the spatial eigenfunctions

of the Orr-Sommerfeld equation.  $\Re$  shows the real part is taken of the complex number and  $i = \sqrt{-1}$ .

Assuming a wavelike solution of the form

$$u'_i(x, y, t) = A_{TS} \Re [\hat{u}_i(y) e^{i(\alpha x - \omega_R t)}] \quad (6.3)$$

the governing equation for the linear stability of parallel shear flow, after linearisation with respect to  $(U, V)$ , can be expressed by the resulting Orr-Sommerfeld equation (Equation 6.4).

$$\left[ \left( U_0 - \frac{\omega_R}{\alpha} \right) \left( \frac{d^2}{dy^2} - \alpha^2 \right) - \frac{d^2}{dy^2} U_0 + \frac{i}{\alpha Re} \left( \frac{d^2}{dy^2} - \alpha^2 \right)^2 \right] \hat{v} = 0 \quad (6.4)$$

In the above equations, the complex wavenumber  $\alpha$  is defined as  $\alpha = \alpha_R + \alpha_I$  where  $\alpha_R$  will reflect dispersion errors and  $\alpha_I$  represents the decay rate constant.  $U_0$  is the base flow of the form  $U_0(y) = y(2 - y)$  and  $\alpha_R$  and  $\omega_R$  are related by  $c = \omega_R/\alpha_R$ . After  $\hat{v}$  is obtained through solution of Equation 6.4,  $\hat{u}$  is calculated from the continuity equation  $\hat{u} = i\hat{v}_y/\alpha$ .

$$u'_i = u_i - U_i \quad (6.5)$$

To obtain the perturbation field  $(u', v')$ , the unperturbed flow may be subtracted from the perturbed one as per Equation 6.5

A 2D grid of  $512 \times 129$  is used with a time step of 0.05 s following Chung and Tucker (2004b). The grid is uniform in the  $x$ -direction and stretched in the  $y$ -direction using a  $\tanh$  function towards the upper and lower walls. The simulation was run for 201.5 seconds before quantifying errors for the amplitude decay rate,  $\alpha_I$

and wave number,  $\alpha_R$ . The vertical perturbation is depicted along  $x$  at  $y = 0$  in Figure 6.4.

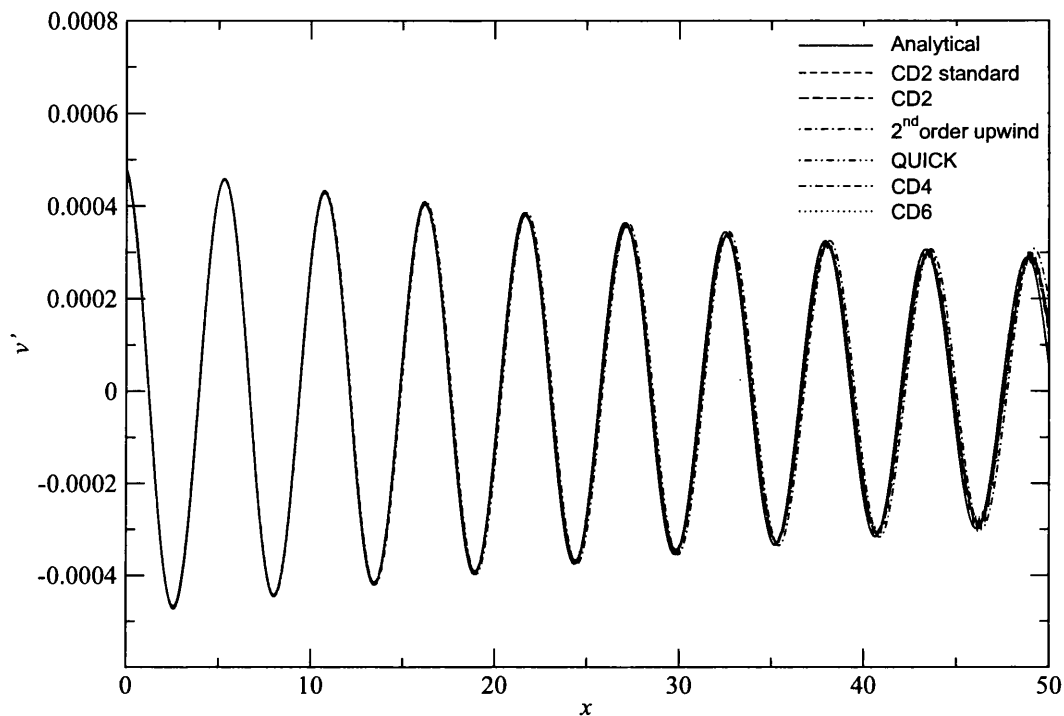


Figure 6.4: Comparison of discretisation schemes.

The amplitude decay rate error is taken from the error between peaks/troughs and the average error in wave number is taken at the center of the channel. The maximum peak was compared for several peaks in the center of the domain and averaged to obtain an estimate of the decay rate error. These errors are presented in Table 6.1. It is useful to compare the two methods of implementing the CD2 scheme to check that they match (i.e. that the extra code is equivalent to standard CD2). All polynomial coefficients are calculated before the main solver begins iterating so no performance penalty is suffered.

$$\text{Here } E(\phi) = (\phi - \phi_{exact}) / \phi_{exact} \times 100$$

From the given figures and tables it can be seen that 2UP is the most dispersive with larger overshoots than any other scheme. CD2 is more dissipative than the



Scheme	$E(\alpha_R)$	$E(\alpha_I)$
CD2 standard	-0.29	-2.0
CD2	-0.29	-2.0
2UP	-0.68	2.2
QUICK	-0.37	-1.3
CD4	-0.37	-1.1
CD6	-0.39	0.1

Table 6.1: Discretisation scheme errors using non-uniform polynomial coefficients.

higher order schemes due to its lower order terms having a stronger effect on the solution. Both QUICK and CD4/6 have similar dispersion errors although the more oscillatory CD4/6 schemes show a less dissipative nature. The second order upwind scheme is the most dispersive of all the schemes though the upwinded stencil tends to form smooth over/under-shoots, this effect is also present in the QUICK scheme. The oscillatory behaviour of high order schemes is also reflected in the decay rate error of the CD6 scheme which does not remove enough energy, leaving a small positive error. These results are expected of each scheme and help to prove the code is indeed correct.

## 6.4 Convection of a vortex

To test for any improvements found through a higher order face approximation, a vortex being convected by a uniform velocity field was chosen. This 2D inviscid case was selected as it allowed only the convective terms to be studied, with well defined boundary conditions and analytical solutions. The convected vortex is in an otherwise uniform flow of  $U_\infty = 34 \text{ ms}^{-1}$ . The initial flow conditions for  $u$ ,  $v$  and  $p$  were set using Equations 6.6a–6.6d

$$u = U_{\text{inf}} - \left( \frac{C}{R^2} \right) (y - y_c) e^{-\frac{r^2}{2}} \quad (6.6a)$$

$$v = \left( \frac{C}{R^2} \right) (x - x_c) e^{-\frac{r^2}{2}} \quad (6.6b)$$

$$p_\infty - p = \frac{\rho C^2}{2R^2} e^{-r^2} \quad (6.6c)$$

$$r^2 = \frac{(x - x_c)^2 + (y - y_c)^2}{R^2} \quad (6.6d)$$

where  $p_\infty = 0$ .  $R$  denotes the vortex core radius chosen as 2, and the non-dimensional vortex strength parameter  $C/(U_\infty R) = 0.02$  following Visbal and Gaitonde (1999). Similar grid spacings ( $\Delta x/R = \Delta y/R = 0.375; 0.1875; 0.125; 0.09375$ ) and suitably small time steps were used following Visbal and Gaitonde (1999) to be confident that the temporal resolution ( $CFL < 0.04$ ) was high enough. To remove any possible lower order error from the pressure field the analytical pressure gradient was derived from differentiating the analytical pressure (Equation 6.6c) and set at each time step.

Taking  $C_1 = \frac{\rho C^2}{2R^2}$

$$-p = C_1 e^{-r^2} = C_1 e^{-\frac{(x-x_c)^2}{R^2}} e^{-\frac{(y-y_c)^2}{R^2}} \quad (6.7)$$

on differentiating with respect to  $y$  we obtain

$$\frac{\partial p}{\partial y} = C_1 e^{-\frac{(x-x_c)^2}{R^2}} \frac{(-2y + 2y_c) e^{-\frac{(y-y_c)^2}{R^2}}}{R^2} \quad (6.8)$$

A similar expression is found for  $\frac{\partial p}{\partial x}$ .

Near boundaries, ghost nodes were set using the analytical solutions at each time

step to allow the whole domain to be treated using a higher order stencil. The vortex was convected for a distance of  $x/R = 8.5$ .

To assess solution errors associated with the schemes, the numerical solution was compared to that of the analytical solution. To calculate the analytical vorticity  $\omega = \left( \frac{\partial u}{\partial y} - \frac{\partial v}{\partial x} \right)$  the gradients  $\frac{\partial u}{\partial y}$  and  $\frac{\partial v}{\partial x}$  were required.

After differentiation of  $u$  with respect to  $y$

$$\frac{\partial u}{\partial y} = \left( 1 + \frac{-y + y_c}{R^2} \right) e^{-\frac{(y-y_c)^2}{2R^2}} \quad (6.9)$$

A similar expression is found for  $\frac{\partial v}{\partial x}$ .

Taking a linear interpolation for the numerical gradients would introduce a second order error term into the numerical vorticity. A general leading order truncation error term can be expressed as  $E_\phi = \beta \Delta x^k$  where  $\beta$  and  $k$  are the truncation error constants and order of the interpolation respectively and  $E_\phi$  the error. To prevent post-processing errors contaminating results, numerical gradients were obtained using finite differences of relevant order. For  $\frac{\partial u}{\partial y}$ , the following finite differences were used for 2<sup>nd</sup>, 4<sup>th</sup> and 6<sup>th</sup> order schemes respectively.

For example,

$$\frac{\partial u}{\partial y}_{2nd} = \frac{u_{i,j+1} - u_{i,j-1}}{2\Delta y} \quad (6.10a)$$

$$\frac{\partial u}{\partial y}_{4th} = \frac{-u_{i,j+2} + 8u_{i,j+1} - 8u_{i,j-1} + u_{i,j-2}}{12\Delta y} \quad (6.10b)$$

$$\frac{\partial u}{\partial y}_{6th} = \frac{u_{i,j+3} - 9u_{i,j+2} + 45u_{i,j+1} - 45u_{i,j-1} + 9u_{i,j-2} - u_{i,j-3}}{60\Delta y} \quad (6.10c)$$

Contours of the different CD FV schemes are shown in Figure 6.5 and the profile used for error analysis, taken through the center of the vortex is shown for the different interpolations in Figure 6.6. It can be seen that the contours are symmetrical from top to bottom, owing to the symmetry of the stencil and its coefficients. Also, the higher order schemes introduce smaller amplitude, higher frequency errors into the solution. This is to be expected. The CD4 and CD6 schemes are both almost identical approximations to the vortex function in Figure 6.5, this suggests that CD6 is not worth the extra computational effort over the CD4 scheme.

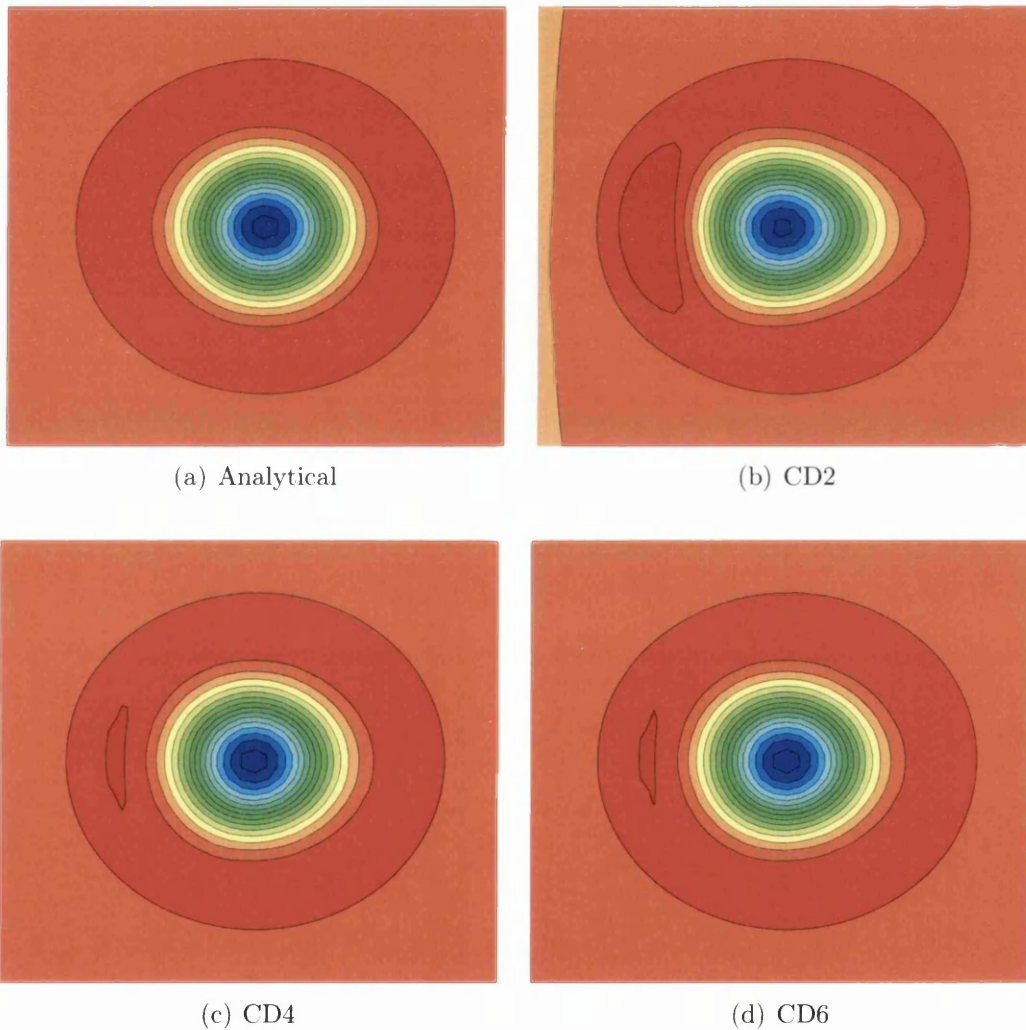


Figure 6.5: Vorticity magnitude contours.

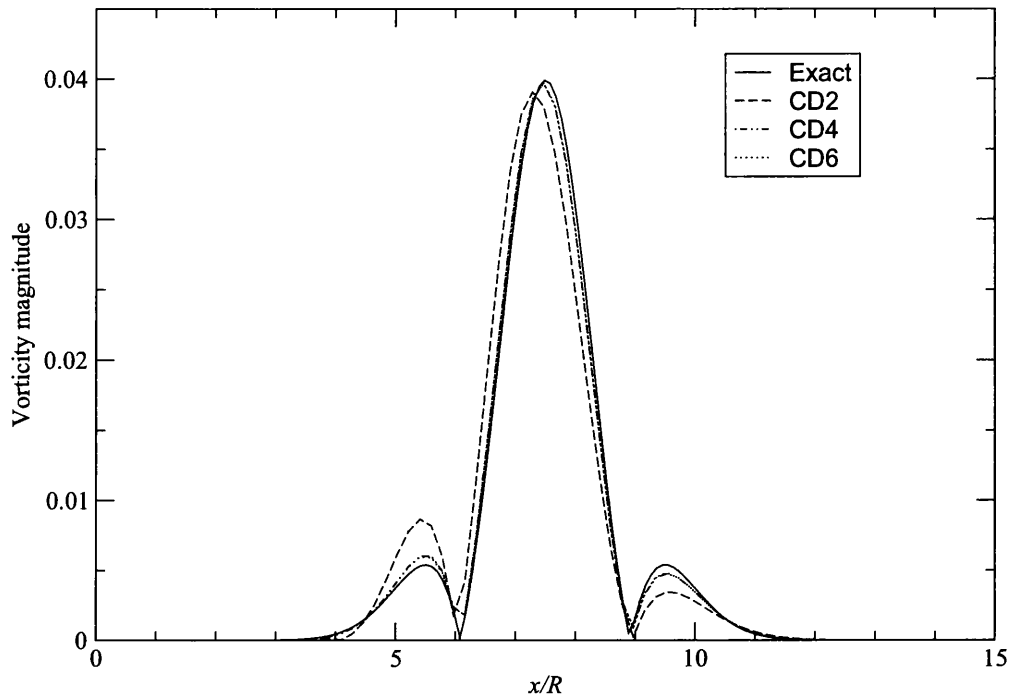


Figure 6.6: Vorticity profile taken through the center of the convected vortex.

Returning back to the cell face interpolations required for the FV method, the maximum errors between the analytical vorticity and numerical solutions are presented in Figure 6.7. Fits to the numerical sample runs can be compared to the expected gradients for error reduction. It can be seen that the higher order interpolations have reduced the errors, but only at a second order rate. There are various reasons for this and these will be discussed in the next section. Although the CD4 and CD6 schemes are strictly second order as implemented here, a significant improvement can be seen from using them. The horizontal dotted lines highlight that around half the grid density is required than CD2 to get the same accuracy. Alternatively a greater accuracy may be obtained using the same grid. As can be seen, the error is reduced nearly an order of magnitude from approximately 3–0.5%.

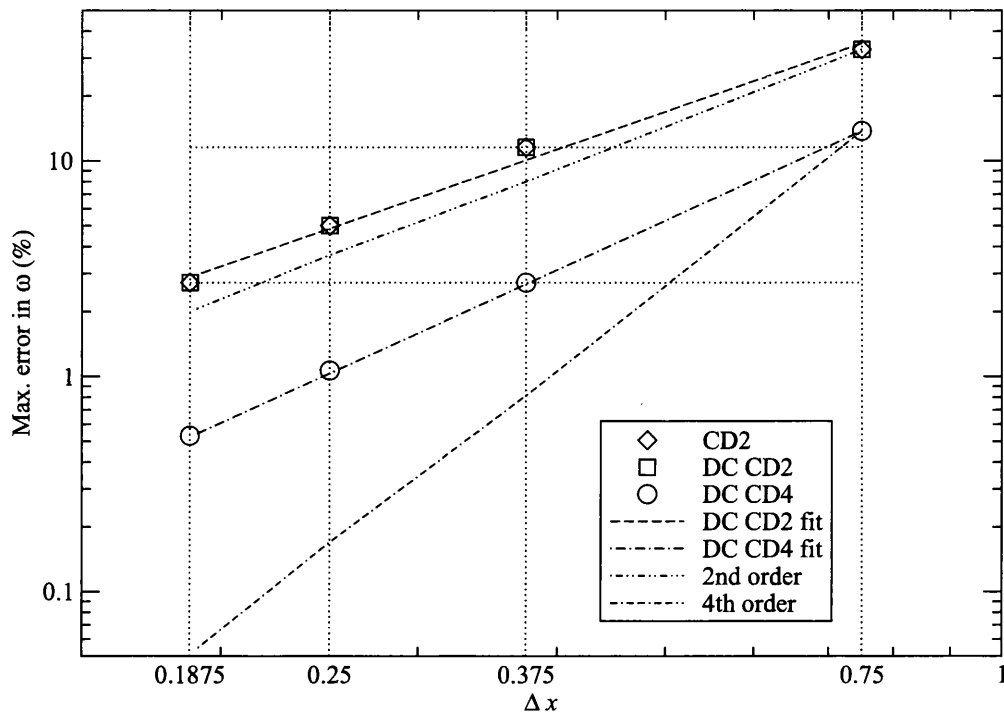


Figure 6.7: Reduction of maximum vorticity error with grid refinement.

## 6.5 Sources of second order errors

Although it may seem strange that applying a higher order discretisation should give a second order error trait as per Figure 6.7, there are several causes that may contribute to this behaviour.

### 6.5.1 Cell topology

Through the use of a face centered grid arrangement, the computational node is not at the cell center so the cell average used in the FV formulation is not as good an approximation of the cell integral although moderate stretching of the grid probably does not have much influence on solution accuracy. The assumption of a uniform value of quantities at cell faces is also likely to degrade accuracy, although higher order representations over the cell face surface often

introduce more interpolation operations to obtain the required data points for the approximation.

### 6.5.2 Staggered grid

The staggered grid used to rectify the pressure field felt by the velocity field implies a pressure gradient correct to only second order. This is due to the pressure nodes lying on the velocity control volume cell faces. No information is given on how the pressure field varies within each cell as the SIMPLE procedure used, iteratively corrects the pressure and velocity field to satisfy the continuity equation. This implies an assumed linear variation over the cell between the pressure nodes lying on the cell faces, resulting in a second order approximation. To remove this second order behaviour, a collocated technique could be used although this would require significant portions of the NEAT code to be re-written. If a collocated grid was to be used, some other technique would be required to correct problems associated with the checker board pressure effect such as Rhie-Chow interpolation (Rhie and Chow 1983).

### 6.5.3 Surface quadrature

Another less obvious assumption made is that of the surface integrals appearing in Equation 4.3. The net flux through the CV boundary is the sum of the surface integrals. To exactly evaluate the correct surface integral, we would need to know the value of all variables everywhere on the surface. To approximate the surface integrals, we must make two approximations. The first being the cell face interpolation from cell values, the second being the approximation of the integral using one or more data samples on the cell face. The midpoint rule used here takes the cell face center value as a representative value for the whole cell face surface,

therefore multiplying it by the cell face surface area gives an approximation to the surface integral. However, this is only second order accurate. For 2D simulations a more complex but higher order surface integral approximation is Simpson's rule giving fourth order accuracy (Ferziger and Perić 2002), though it is not used here due to the increased complexity introduced. Use of higher order methods generally creates much larger computational molecules and more conditional statements in the CFD code.

#### **6.5.4 Time integration**

Although the Crank-Nicolson scheme is used for time discretisation, a one legged formulation is used (Tucker and Liu 2005a) leaving a small implicit, dissipative element in the solved equations, which aids stability. For all simulations the CFL number is kept low ( $CFL < 0.2$ ), so time errors are not thought to have a heavy influence. Other errors may stem from the reduction of the order of the convective scheme near boundaries and filter commutation errors.

### **6.6 Summary**

In this chapter the additional numerical schemes added to the code were tested in both 1D and 2D. It was found that there are several second order errors sources other than the cell face interpolation. Using CD4, a significant improvement in accuracy was obtained on these particular cases. The expected behaviour of each scheme was found showing that the code was correct and could be applied to more useful cases such as those representing electronics systems.



# Chapter 7

## Electronics heat transfer test cases

### 7.1 Introduction

To test the various modelling approaches employed, three main test cases were used. The first two, a heated ribbed channel and an array of wall mounted cubes represent simplified integrated circuits. The third is a simplified CPU case representing a more complex electronics system (with boards removed). Flows found in electronics systems are typically of a low Reynolds number ( $100 < Re < 5000$ ), therefore the test cases chosen are also of a relatively low Reynolds number ( $Re < 15000$  limited by the available experimental data). All test cases have been studied in previous literature though details are provided here for convenience. This chapter also provides the results obtained for the three cases. Due to the wide variety of geometries and scales found in electronics systems, this section provides insight into the capabilities and limitations of the methods. Figures will be used where deemed appropriate, to highlight details that are most

interesting and useful. A full set of results may be found in the appendices.

## 7.2 Heated ribbed channel

### 7.2.1 Case description

The first and most simple test case is a rib in a heated channel. This could represent a simplified board in an electronics system. This was first studied by Acharya et al. (1993) and later work on this particular case has also been performed by Liu et al. (2006). This is the most basic test case studied here, in time being essentially a two-dimensional flow. However complex time dependent flow features generated include separation, reattachment, recirculation and vortex shedding.

This flow has a Reynolds number of 14,200 based on the bulk velocity,  $U_0$  and the channel height,  $H$ . The ribbed channel is shown in Figure 7.1. In the stream-wise and span-wise directions ( $x$  and  $z$  respectively), periodic boundary conditions are applied for both the flow and temperature fields. Either side of the rib, a constant heat flux is applied to the channel floor, whilst the rib is adiabatic. Impermeability and no-slip conditions are applied at walls. Surfaces not pertaining to heat transfer are treated as adiabatic.

The mean pressure gradient used to drive the flow and the temperature gradient are given by Equations (7.1) and (7.2) respectively. The mean temperature gradient is used to remove heat from the streamwise direction to prevent heat build up in the system via the constant heat flux  $q_w''$ .

$$\beta_{new} = \beta_{old} - \rho \left( \frac{(Q_{new} - Q_0) - 0.5(Q_{old} - Q_0)}{0.5\Delta t H z_{max}} \right) \quad (7.1)$$

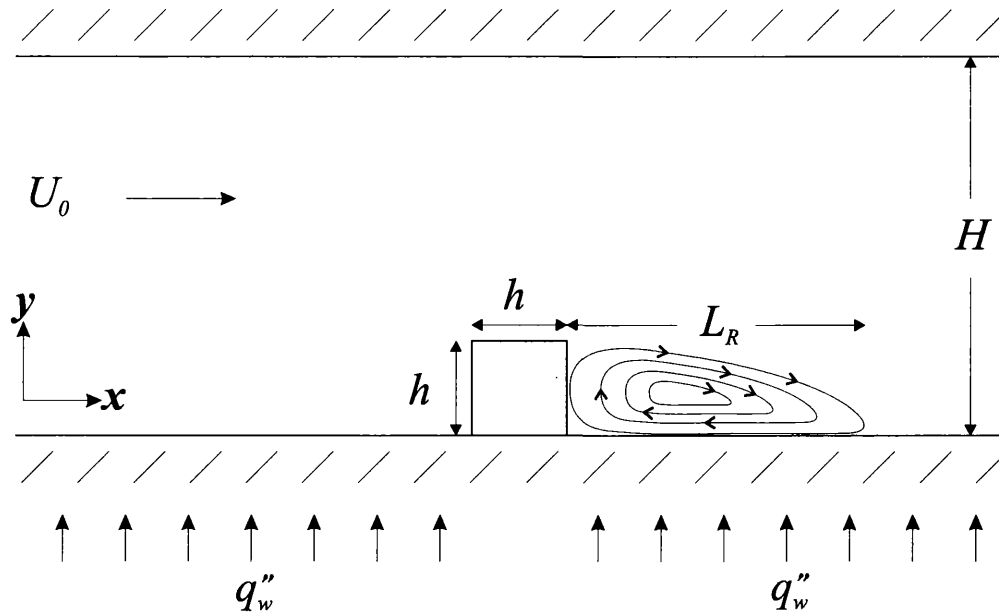


Figure 7.1: Ribbed channel.

Here,  $Q_0$  is the volume flow rate with  $H z_{max}$  giving the cross sectional area of the channel. The subscripts 'new' and 'old' represent new and old time levels.

$$\alpha = \frac{q''_w}{\rho c_p H U_0} \quad (7.2)$$

Flow parameters for the ribbed channel are shown in Table 7.1

Rib Height, (m)	0.00635	$Re$	14,200
Channel Height, (m)	0.061	$U_0$ , ( $\text{ms}^{-1}$ )	3.6
Channel Width, (m)	0.06	$q''_w$ , ( $\text{Wm}^{-2}$ )	280
Channel Length, (m)	0.127	$Pr$	0.7
Hydraulic diameter $D_h$ , (m)	0.1016		

Table 7.1: Ribbed channel parameters.

For this case, the turbulent Prandtl number,  $Pr_T$  is taken as 0.9 for RANS regions and 0.4 for LES regions following the work of Tucker and Davidson (2004). Because of this change in  $Pr_T$  in hybrid simulations, Equation 3.58 is used to provide the

harmonic mean.

To study heat transfer, the local Nusselt number at the wall is calculated using Equation 7.3.

$$Nu = \frac{q_w'' D_h}{k(T_w(x) - T_b(x))} \quad (7.3)$$

Here,  $T_w(x)$  and  $T_b(x)$  are the wall and bulk temperatures in the  $x$ -direction,  $D_h$  is the hydraulic diameter and the thermal conductivity  $k$ , is given by  $\mu C_p / Pr$ . The spanwise average is taken for the bulk and wall temperatures.

The grids are stretched towards all boundaries in the  $x - y$  directions, whilst a uniform grid is used in the homogeneous  $z$ -direction. Although this flow is nearly two-dimensional in time, it is important to include three-dimensional terms so that important processes such as vortex stretching may be captured. A two parameter *tanh* function (Chung and Tucker 2003) was used to generate the stretched grids. Three resolution grids have been used and are tabulated in Table 7.2.

Label	$x \times y \times z$	Total cells	$y_{wall}^+$	$\Delta x^+$	$\Delta y^+$	$\Delta z^+$
A	$121 \times 112 \times 67$	907984	2	5-40	2-30	20
B	$121 \times 112 \times 33$	447216	2	5-40	2-30	40
C	$62 \times 57 \times 17$	60078	3.5	10-80	3.5-60	80

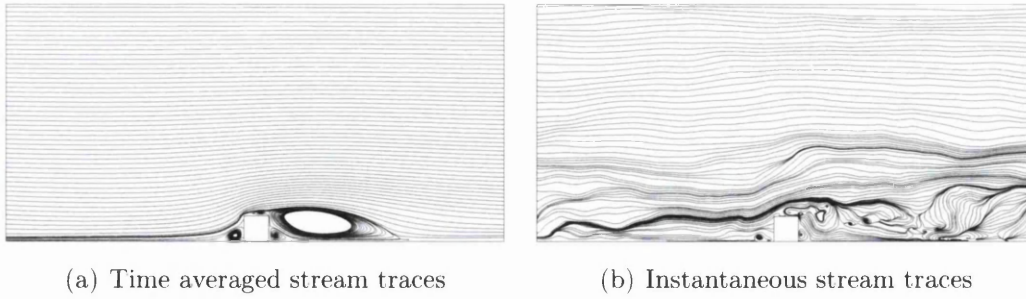
Table 7.2: Ribbed channel grid details.

Use of stretched grids allows higher resolution near walls where the turbulent scales are smallest and to allow a more accurate representation of the heat transfer around the channel floor. A fine grid near the walls and corners of this geometry allows the high velocity and temperature gradients to be resolved more accurately. (I)LES has similar grid requirements in the  $y$ -direction to those of RANS, however, in channel flows, streak structures typically have a size of  $\Delta z^+ \approx 100$  and therefore requires a grid spacing of at around  $\Delta x^+ \approx 100$  and  $\Delta z^+ \approx 20$  (Davidson and

Peng 2003). According to Davidson and Peng (2003), using URANS near walls allows increases of grid spacing to  $100 < \Delta x^+ < 600$  and  $100 < \Delta z^+ < 300$ . Grids A and B also compare well to the resolutions given in Table 3.1. Given the above definitions we can be sure that the grids have adequate resolution for (I)LES.

### 7.2.2 Flow structure

Figure 7.2(a) shows the time averaged flow over the rib. From this we can see the general features of the flow. After separation from the top of the rib, a large recirculation bubble is formed, after which the flow reattaches on the heated floor of the channel. Smaller recirculation regions can be seen around the bottom corners of the rib and a shallow one on top of the rib. From the instantaneous Figure 7.2(b), the top half of the channel can be seen to display an almost laminar flow, indicating a fine grid is not required here. The similar results obtained using different resolution grids indicates this is not due to additional damping introduced by the coarsening of the grid towards the center of the channel. Use of stretched grids reflects the less influential flow regions through grid coarsening. Also in this figure, vortices can be seen shedding from the rib and travelling downstream. Panigrahi (2001) notes from experimental data that eddies do not break up in the reattachment region as is traditionally believed and vortices can be seen to persist for some distance downstream. The instantaneous (time dependent) flow is much more complex than the time averaged flow which is similar to what one would expect from a RANS model. It is these complex time dependent eddies which increase the turbulent heat transfer through the physical effects of turbulent mixing and subsequent transport of heat away from the heat source.

Figure 7.2: Rib stream traces, mid- $z$ -plane.

### 7.2.3 Average errors

To be able to get an overview of each models performance, errors are averaged for the profiles at different locations. Where experimental data does not coincide with numerical nodes, a stiff quadratic spline is used to acquire an interpolated value. Full plots of all profiles can be found in the Appendices. The average errors of each variable over all profile locations is presented in Tables 7.3-7.5. The following equation is used to calculate the errors, where the subscripts  $exp$  and  $num$  refer to experimental and numerical data respectively.

$$\text{Error}_\phi = \frac{\sum_{i=1}^m |\phi_{exp} - \phi_{num}|}{\sum_{i=1}^m \phi_{exp}} \quad (7.4)$$

The resulting absolute errors give no indication of the overall effect of each model. Therefore, a ‘+’ or ‘-’ is prefixed to show whether the error is mostly positive or negative respectively. The following discussions will focus on some details of the obtained results.

Variable	← Model →											
	Smag	Yosh	Ler	$\alpha$	Kos	RL	RICD2	R12U	RIQ	LerCD4	$\alpha$ CD4	KosCD4
$U/U_0$	-22.1	-21.6	-21.7	-21.6	-21.4	-19.6	-19.6	-17.2	-20.7	-16.4	-17.9	-20.9
$V/U_0$	-43.2	-42.1	-41.3	-42.7	-43.6	-42.6	-42.4	-38.0	-44.0	-44.1	-43.5	-46.0
$\overline{w'u'}^{1/2}/U_0$	-23.3	-22.3	-21.4	-21.0	-22.5	-22.2	-21.4	-20.9	-21.7	-20.0	-21.0	-22.4
$\overline{v'v'}^{1/2}/U_0$	-20.3	-20.7	-19.7	-20.2	-21.1	-20.5	-18.4	-25.0	-16.7	-18.0	-19.3	-21.1
$-\overline{u'v'}^{1/2}/U_0 \times 1000$	-57.6	-58.9	-56.4	-58.1	-59.0	-57.5	-57.1	-63.8	-58.4	-51.3	-53.6	-59.3
$dp/dx^e$	6.1	5.9	6.6	7.0	6.4	6.0	5.9	7.0	6.1	6.9	6.7	7.0
$L_R$	5.7	5.7	5.6	5.8	5.7	5.6	5.6	5.6	5.0	5.1	5.3	5.5
$Nu$	-9.4	-13.7	-14.0	-13.6	-12.0	-10.7	-13.3	-12.5	-13.4	-12.1	-12.7	-10.6

Table 7.3: Ribbed channel average profile errors (%) ( $121 \times 112 \times 67$  grid).

<sup>e</sup>Entries for  $dp/dx$  and  $L_R$  are not the percentage error but the actual values.

Variable	←— Model —→											
	Smag	Yosh	Ler	$\alpha$	Kos	RL	RICD2	RI2U	RIQ	LerCD4	$\alpha$ CD4	KosCD4
$U/U_0$	-21.4	-27.2	-25.3	-24.2	-24.8	-21.9	-27.4	-21.9	-21.2	-19.6	-20.6	-22.2
$V/U_0$	-45.4	-50.5	-49.5	-45.0	-48.6	-40.4	-47.8	-47.0	-43.3	-41.9	-44.4	-47.5
$\overline{u'u'}^{1/2}/U_0$	-24.1	-23.5	-21.7	-20.9	-21.6	-22.7	-23.5	-22.4	-21.7	-19.9	-19.6	-22.7
$\overline{v'v'}^{1/2}/U_0$	-24.3	-24.0	-22.1	-22.0	-24.0	-23.2	-22.6	-28.4	-20.4	-18.3	-19.3	-23.6
$-\overline{u'v'}^{1/2}/U_0 \times 1000$	-55.7	-59.6	-55.2	-54.9	-58.3	-55.2	-59.1	-71.1	-65.9	-54.3	-54.5	-58.1
$dp/dx^a$	6.1	5.9	6.0	5.8	7.0	6.0	6.2	6.3	6.0	6.2	6.2	7.0
$L_R$	5.7	5.7	5.7	5.7	5.7	5.6	6.6	6.6	6.5	5.2	5.0	5.4
$Nu$	-11.2	-13.1	-14.7	-14.7	-9.7	-11.5	-15.9	-11.9	-11.8	-9.4	-9.5	-8.3

Table 7.4: Ribbed channel average profile errors (%) ( $121 \times 112 \times 33$  grid).<sup>a</sup>Entries for  $dp/dx$  and  $L_R$  are not the percentage error but the actual values.



Variable	← Model →											
	Smag	Yosh	Ler	$\alpha$	Kos	RL	RICD2	RI2U	RIQ	LerCD4	$\alpha$ CD4	KosCD4
$U/U_0$	-24.8	-26.7	-24.6	-26.4	-22.5	-25.9	-26.9	-23.6	-22.7	-23.9	-26.4	-21.1
$V/U_0$	-44.4	-49.8	-46.2	-47.0	-44.0	-46.4	-50.8	-54.0	-40.2	-40.1	-48.0	-45.1
$\overline{u'u'}^{1/2}/U_0$	-21.8	-22.8	-21.3	-21.8	-22.5	-21.9	-22.6	-28.6	-22.8	-20.5	-22.6	-23.7
$\overline{v'v'}^{1/2}/U_0$	-29.7	-23.9	-21.4	-26.5	-32.3	-29.6	-24.0	-33.3	-30.9	-22.7	-24.4	-31.1
$-\overline{u'v'}^{1/2}/U_0 \times 1000$	-64.8	-62.5	-57.2	-62.2	-63.1	-63.4	-62.5	-83.5	-74.3	-60.5	-63.1	-63.6
$dp/dx^a$	6.6	4.4	6.2	5.7	7.4	6.5	4.4	6.1	5.6	6.3	5.8	7.4
$L_R$	5.8	5.4	6.0	6.1	6.2	6.0	6.8	7.5	6.8	6.0	6.1	6.2
$Nu$	-7.2	-24.7	-12.3	-17.7	-8.7	-16.1	-24.7	-23.5	-21.2	-11.7	-15.0	-9.0

Table 7.5: Ribbed channel average profile errors (%) ( $62 \times 57 \times 17$  grid).<sup>a</sup>Entries for  $dp/dx$  and  $L_R$  are not the percentage error but the actual values.

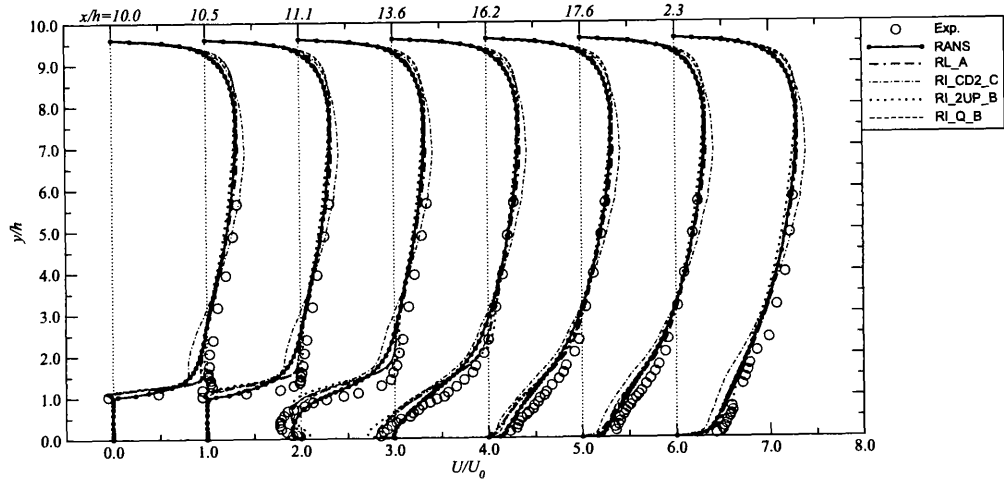


Figure 7.3: Mean streamwise velocity distributions.

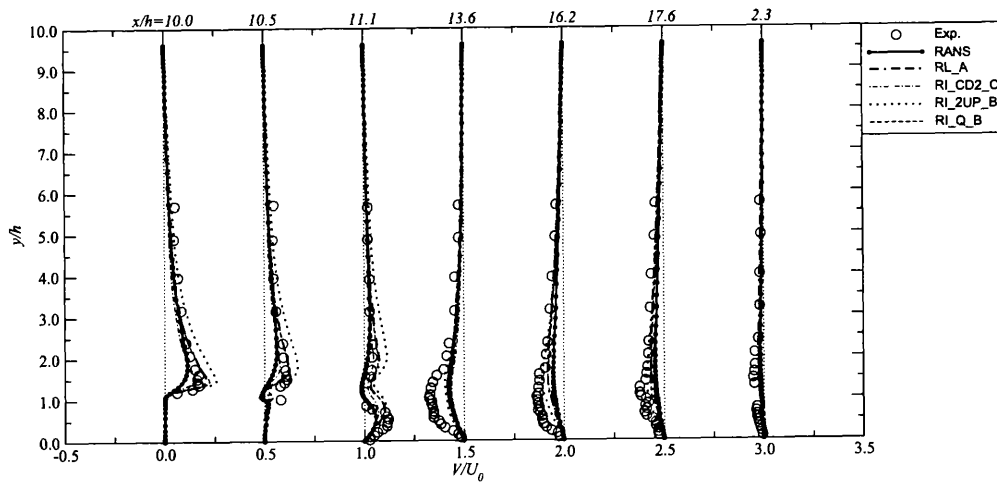


Figure 7.4: Mean cross-stream velocity distributions.

### 7.2.4 Mean velocity distributions

Mean streamwise velocity distributions are shown for several axial locations of the ribbed channel in Figure 7.3. Locations at  $x/h = 10, 10.5$  and  $11.1$  correspond to the center of the rib, the east face and a small distance downstream respectively. Apart from  $x/h = 2.3$ , all other locations are downstream. Towards the center of the channel, agreement among each model and with experimental data is good. Below  $y/h = 2$ , velocities are under predicted downstream of the rib. The RI\_Q and RI\_2UP schemes both show excellent agreement with the other numerical and experimental data. An incorrect distribution of velocity can be seen for RI\_CD2 at different  $y/h$  locations on grid C, where the mean velocity is under-predicted around the wake. This may be due to lack of resolution near the rib surface to capture the separating shear layer. For mean  $V$  distributions (Figure 7.4), RI\_2U\_B over predicts velocities until just downstream of the rib. Other less dispersive models do not show this trend to the same extent. In the recirculation regions, all models under-predict  $V$ . No model captures the correct position and amplitude of the peak in the recirculation region. This may imply levels of dissipation that are too high or failure to accurately capture the strong anisotropy in this region. Overall agreement between different models and grid densities is satisfactory.

### 7.2.5 Higher order statistics

Normal turbulent stresses for the streamwise and cross-stream directions of the ribbed channel are shown in Figures 7.5 and 7.6. Downstream of the rib, RI\_2UP over-predicts the streamwise velocity fluctuations  $\overline{u'u'}^{1/2}$  around  $y/h = 2$ . This is around the vortex shedding region, where an upwind stencil may not be suitable. Except for the profiles immediately downstream of the rib (after  $x/h = 11.1$ )

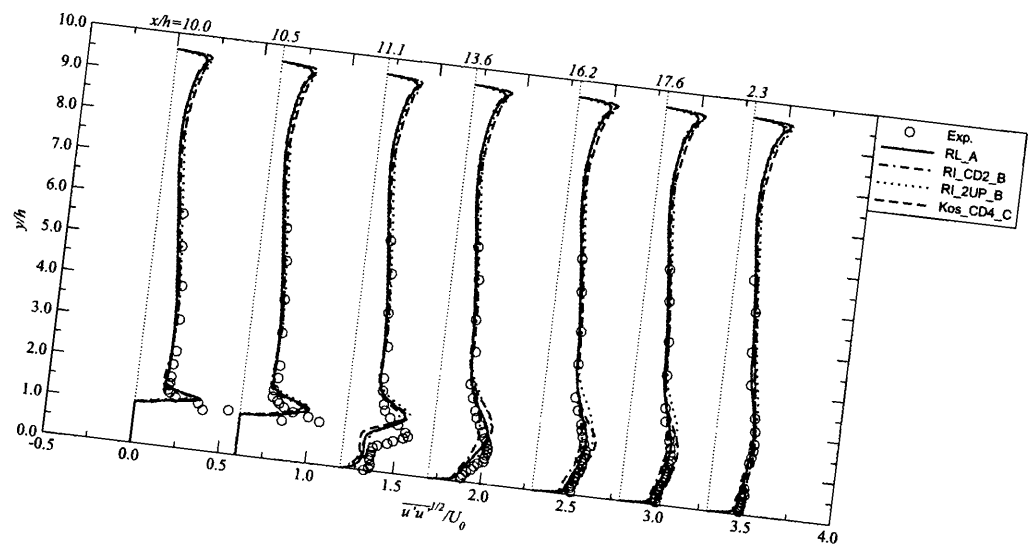


Figure 7.5:  $\overline{u'u'}$  distributions.

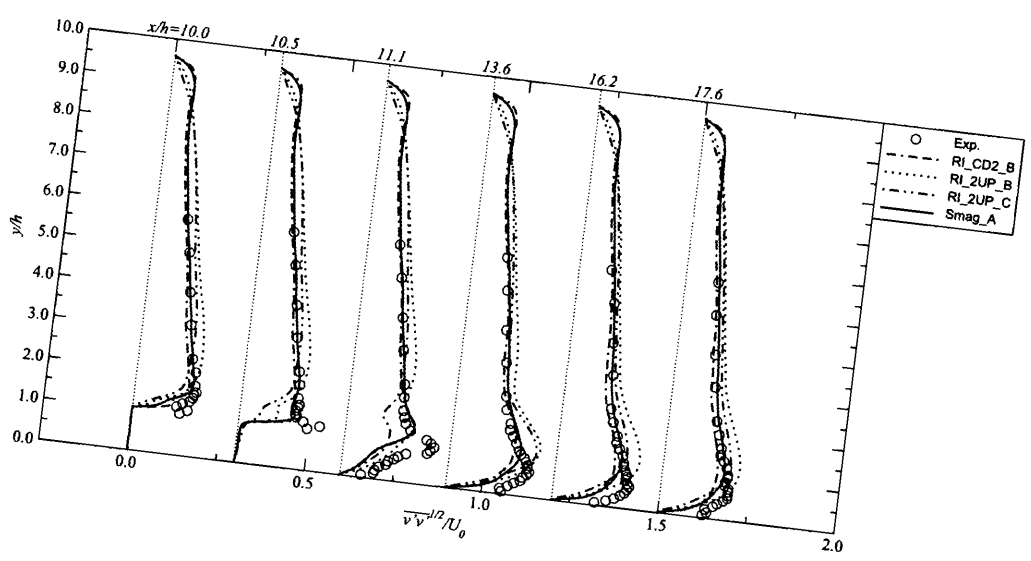
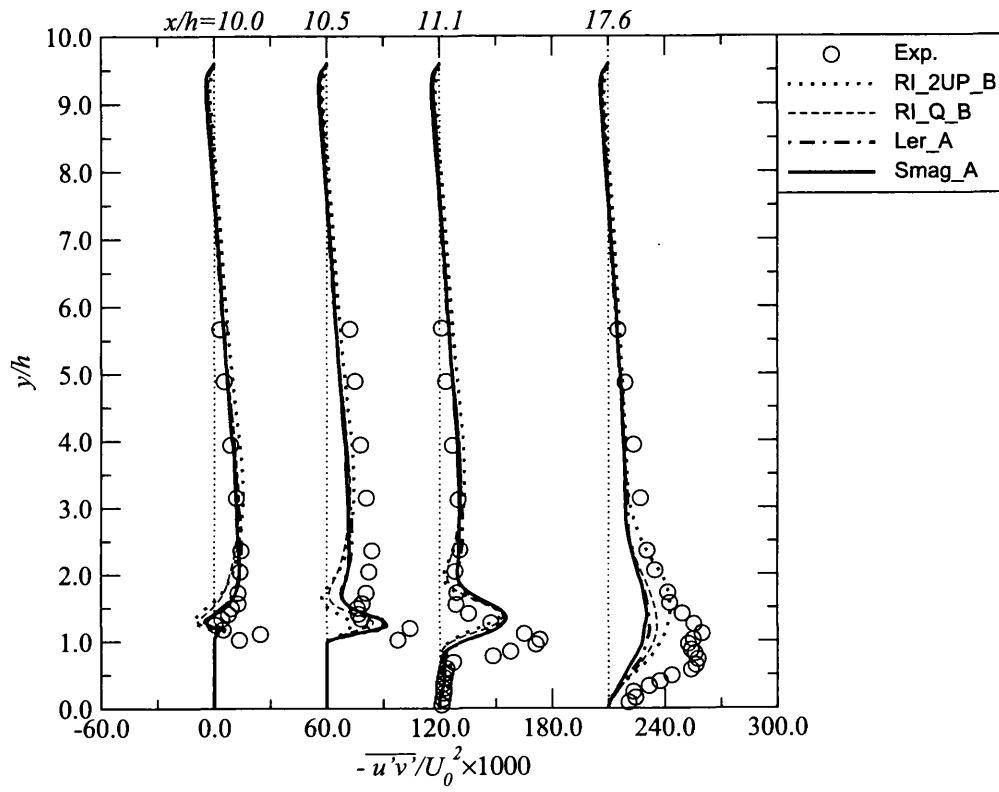


Figure 7.6:  $\overline{v'v'}$  distributions.

Figure 7.7:  $\overline{u'v'}$  distributions.

where the shear layer from the top rib surface produces sharp peaks, streamwise velocity fluctuations are well predicted, all models showing similar results to those of RI\_CD2 and the Kosović model on grids B and C respectively. Except for the RI\_2UP model, Figure 7.6 shows good agreement between all models in the core region. The over-prediction of  $\overline{v'v'}^{1/2}$  by this model is reduced moving to a coarser grid producing more diffusion but has a degrading effect near the rib where the velocity field is much less smooth. Profiles for  $10 \leq x/h \leq 11.1$  are not captured well below  $y/h = 2$  using RI\_2UP possibly due to the changing direction of the flow causing the stencil to switch directions regularly or the introduction of increased false diffusion or dispersion errors. This is another drawback of upwinded schemes and can produce unpredictable results. Most models under-predict the fluctuations in the recirculation region. This may to a large extent explain the under-prediction of heat transfer in this region. Until further downstream of the rib, the RI\_CD2 model performs almost identically to the Smagorinsky model, even downstream, the shape is similar. Outside of regions of high anisotropy the linear Smagorinsky model is able to make a more reasonable approximation to the residual stresses. As can be seen in Figure 7.7, the normalised shear stresses are mostly under-predicted, the peaks being effected by discretisation scheme in the RANS-ILES models. The greatest peak is found at  $x/h = 17.6$ , where RI\_2UP and RI\_Q show the greatest magnitudes, though peak positions are again incorrect. Both the Leray and Smagorinsky models are almost identical and greatly under-predict the stresses far downstream of the rib. The nonlinear Leray model is expected to be less dissipative than the Smagorinsky model, as is evidenced by the slightly improved profile at  $x/h = 17.6$



### 7.2.6 Reattachment length

As a measure of the predictive capabilities of the models, the dimensionless reattachment length is compared to the experimental value in Tables 7.3-7.5. It should be noted that these are dimensionless values, not percentage errors as in the rest of the table. The experimental value of the dimensionless reattachment length is  $L_R = 6.0 \pm 0.7$  (Acharya et al. 1993). This is made dimensionless by dividing by the rib height. The LES models generally produce a shorter reattachment length than the RANS-ILES cases, except for the finest grid. The most dissipative models (Smagorinsky and Yoshizawa) show less sensitivity to grid resolution effects. For ILES, numerical dissipation is 100% of the effective turbulent viscosity, whereas this is a lower percentage for a more dissipative model. However, the interaction of numerical and explicitly added SGS models is rarely clear *a priori*. For the lowest resolution grid, the RANS-ILES models using the QUICK and second order upwind schemes predict a reattachment length outside the experimental range, possibly due to greater diffusion introduced by this grid.

### 7.2.7 Heat transfer

The local Nusselt number for the ribbed channel is plotted for several models in Figure 7.8. On the lower resolution grids, RI2UP over-predicts  $Nu$  just east of the rib. This may be due to the poor modelling of turbulent stresses in the small recirculation bubble at the south-east corner of the rib. The more diffusive nature of the QUICK and second order upwind schemes may be seen to form the smoother profiles of the lowest resolution results. The lowest resolution grid is not able to capture high gradients in the flow accurately, yet as expected on grid refinement, most models converge to a similar solution due to lowered SGS model influence.

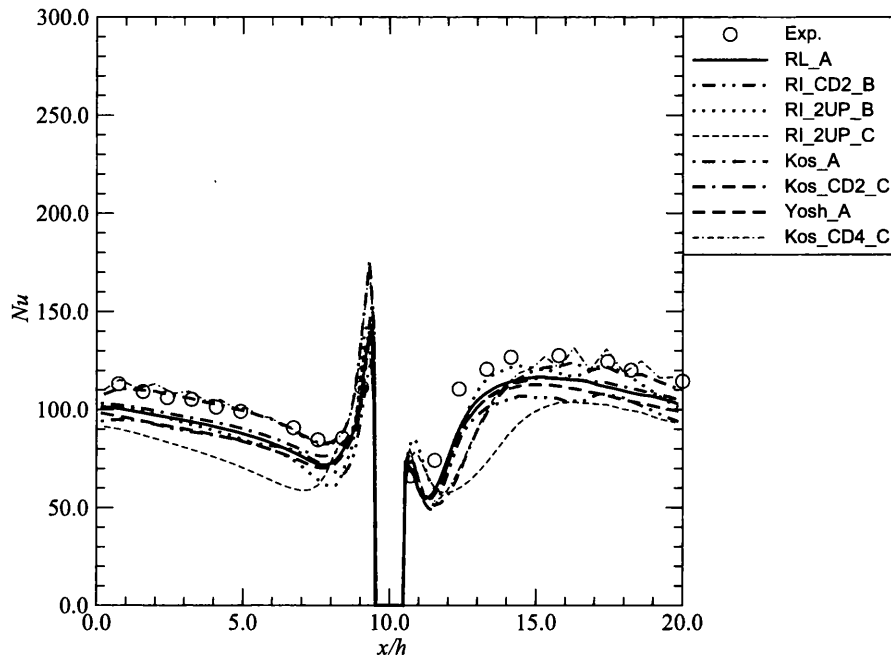


Figure 7.8:  $Nu$  along the channel floor.

Using Tables 7.3-7.5, it can be seen that generally, average errors are similar. On the finest grid, most models perform similarly to each other with the Smagorinsky model performing the best. The reduced filter width may move the filter into a more universal isotropic range of scales where simple models are more applicable. Using a natural grid-filter, this similarity on the finer grid is expected. On the medium resolution grid, the Kosović nonlinear model performs well for both CD2 and CD4 spatial schemes. Here CD4 provides an average improvement in  $Nu$  prediction of 4% over using the CD2 scheme. Both the RI.2UP and RI.Q improve heat transfer prediction compared to RI.CD2 here, possibly because of a strong streamwise flow direction, where an upwind biased stencil draws information from upstream whilst introducing some false diffusion in the reattachment and recirculation region, raising the rate of heat transfer to the mainstream. For all grids, the Smagorinsky model predicts  $Nu$  fairly well amongst the variety of SGS models.

On the coarsest grid, the nonlinear models based on the  $k-l$  Yoshizawa model,



show a marked improvement to the linear Yoshizawa model. Due to effectively increasing the filter width, it is possible that larger anisotropic turbulent scales are modelled much better using the nonlinear models. Moving to a CD4 scheme only brings an average of 1% improvement. On this grid, the Kosović model gives the lowest error for  $Nu$ . The RANS-ILES based solutions improve using 2UP and QUICK discretisations by about 2%, where as a reduction of 4% was found on grid B. As shown earlier the CD4 scheme reduces errors much faster than CD2. Even though there are still second order terms in the solution limiting the effects of the higher order scheme some improvement can be obtained. This is likely to be case dependent however.

Although using the CD4 convective discretisation, results using nonlinear models are improved slightly, the increase in computation time does not seem reasonable for this gain. Use of CD4 on the coarsest grid also introduces wiggles where the grid coarsens (away from the rib), this may be expected from higher order discretisation and can be seen clearly in Figure 7.8 (Kos\_CD4\_C). The lower resolution grid may interfere more with the SGS model contribution and become less stable if over- and under-shoots become too large. Varying the resolution in the  $z$ -direction had little influence on results, probably due to the 2D nature of the flow in time. The experimental error for the local Nusselt number is  $\pm 5\%$  (Acharya et al. 1993), showing most results to be within or near experimental accuracy.

Tafti (2005) investigates ribbed ducts for turbine cooling blades and using the dynamic Smagorinsky LES and quasi-DNS (ILES) models on two different grids, similar results were obtained to those presented here. For two grids of  $96^3$  and  $128^3$  nodes, heat transfer was underpredicted by 20-30% and 15-20% respectively. It was also found that by increasing turbulence intensities, the dynamic model improved heat transfer predictions to within 10%. Reassuringly, in this study, similar and improved accuracies have been achieved, with the same low sensitivity to the grid resolution.

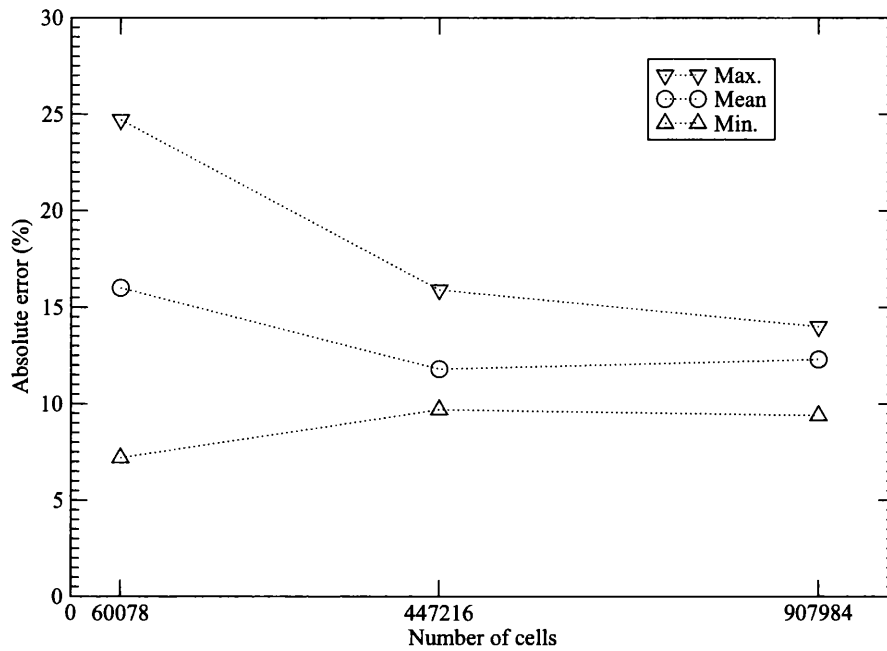


Figure 7.9: Absolute errors for  $Nu$  using all SGS models.

Figure 7.9 shows the mean absolute errors for  $Nu$  (averaged over all SGS models for each grid to give an impression of grid effects using an “average” SGS model). The mean, along with the maximum and minimum errors for the range of SGS models are shown. The mean shows the general trend and the maximum and minimum errors obtained with any SGS model show the maximum range in errors. As can be seen, there is a variation between SGS models on the coarsest grid of 20%, yet the average does not change much between grids. The doubling of the grid in the  $z$ -direction barely influences the errors. Generally although the SGS model seemed to have more influence in this case than the grid, the average variation is only about 10 percent.

## 7.2.8 Pressure differentials

Aside from heat transfer, another useful design element would be obtaining the correct pressure differential. This would allow an engineer to specify the correct

fan at minimum cost. Over all simulations there is a range of  $dp/dx = 4.4 - 7.4$ . A higher pressure differential would imply a more dissipative model. This occurs on the coarsest grid. On the finer grids, the lowest value of  $dp/dx$  is only 15% lower than the maximum showing greater consistency in this respect.

### 7.2.9 Conclusions

Although a simple geometry, the flow created around the rib is complex. However, using time dependent methods, excellent agreement is obtained with experimental data and amongst SGS models. The RANS-ILES models employing the second order upwind scheme (and to some extent the QUICK scheme) showed some unpredictability when compared to other flow profiles, with most other models performing similarly. Lowering grid resolution increased the role of the SGS model causing a slightly wider spread of results, though on average, little degradation was detected given the change in resolution. This would indicate the large vortices generated by the rib are the dominant structures in the flow and not the boundary layer region. The results would certainly be informative as part of the electronics design process for investigating gross flow features before refinement. The boundary layer region is probably of less importance as it is continually buffeted by large scale vortices, destroying the typical form of turbulence and assumptions that much turbulence modelling is based upon. This *top-down* type of flow is the most likely to occur in electronics flows as the square components are normally tightly packed and the results are therefore promising.

## 7.3 Array of wall mounted cubes

### 7.3.1 Case description

The second test case is an array of wall mounted cubes in a channel, one of which has a copper core maintained at a constant temperature ( $T_{core}$ ). This represents idealised integrated circuits in a more complex system. This case has been studied experimentally by Meinders et al. (1999) and modelled by various groups (see Hellsten and Rautahaimo (1999)). This flow is more challenging than the ribbed channel creating more 3D turbulence effects. Similar to the ribbed channel, the flow includes separation, recirculation and vortex shedding at various points around the cube(s). Additional complexity is introduced via an epoxy layer surrounding the constant temperature heat source requiring conjugate heat transfer to be solved (See Figure 7.10). Therefore conduction is solved within the epoxy layer and convection in the air flowing around it.

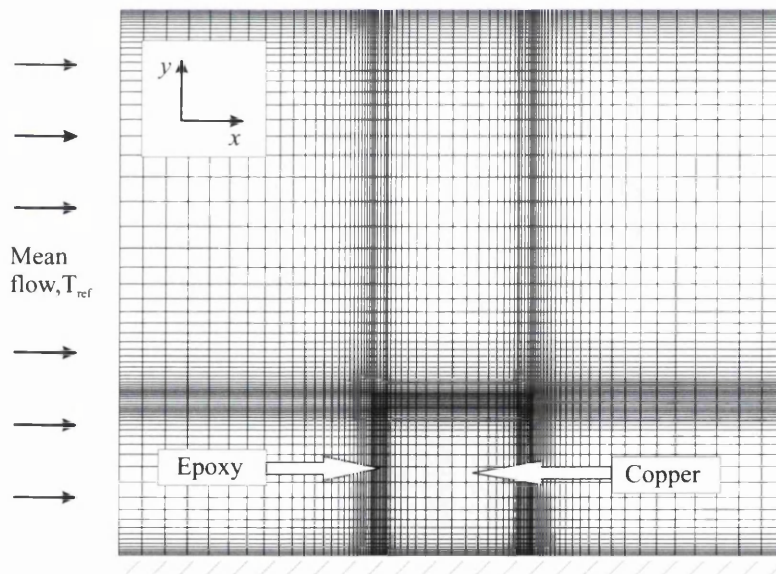


Figure 7.10: Epoxy layer and stretched grid.

Because the cube is surrounded by other cubes (see Figure 7.11), the flow field

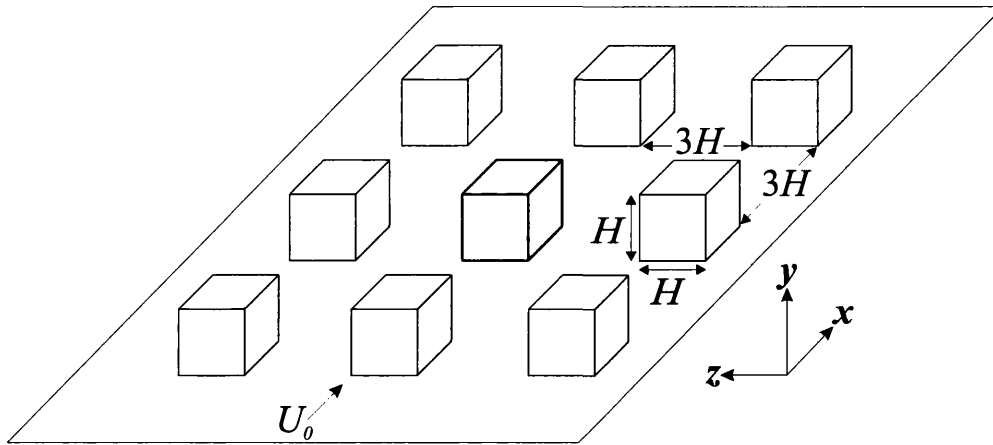


Figure 7.11: Cube array.

is periodic in the stream-wise and span-wise directions. Since only one cube is heated, the inlet temperature of the flow is maintained at a fixed reference temperature ( $T_{ref}$ ) and so is not periodic. No slip and impermeability conditions are applied at walls and adiabatic conditions are applied to surfaces other than the cube. The epoxy at the base of the cube is maintained at  $46^\circ\text{C}$ . Since only one cube is heated and modelled, for brevity, this case may also be referred to as the heated cube or cube.

Flow parameters for this case are shown in Table 7.6 and material properties of the air and epoxy are given in Table 7.7

Cube Height $H$ , (m)	0.015	$Re$	13,000
Epoxy thickness, (m)	0.0015	$U_0$ , ( $\text{ms}^{-1}$ )	3.86
Channel Height, (m)	0.051	$\dot{m}$ , ( $\text{kgs}^{-1}$ )	$13.70 \times 10^{-3}$
Channel Width, (m)	0.06	$T_{ref}$ , ( $^\circ\text{C}$ )	20
Channel Length, (m)	0.06	$T_{core}$ , ( $^\circ\text{C}$ )	75

Table 7.6: Cube flow parameters.

The mean pressure gradient used to drive the flow is given by Equation 7.1.

For this case, the turbulent Prandtl number,  $Pr_T$  is taken as 0.9 for RANS regions and 0.6 for LES regions. The turbulent Prandtl number can be obtained through

Property	Air	Epoxy
Density $\rho$ , (kg/m <sup>3</sup> )	1.16	1150.0
Viscosity $\mu$ , (m <sup>2</sup> /s)	$4.1818 \times 10^{-6}$	–
Thermal conductivity $k$ , (kgm/s <sup>3</sup> K)	0.0257	0.236
Specific heat $C_p$ , (m <sup>2</sup> /s <sup>2</sup> K)	1007.0	1668.5

Table 7.7: Air and epoxy properties.

experimental studies, chosen through other simulations or by more analytical means. The value of  $Pr_T = 0.6$  is chosen here instead of 0.4 as for the ribbed channel following the previous studies of Hemida and Krajnović (2007); Mathey et al. (1999); Zhong and Tucker (2004). As in the ribbed channel the harmonic mean is taken for the diffusion coefficients.

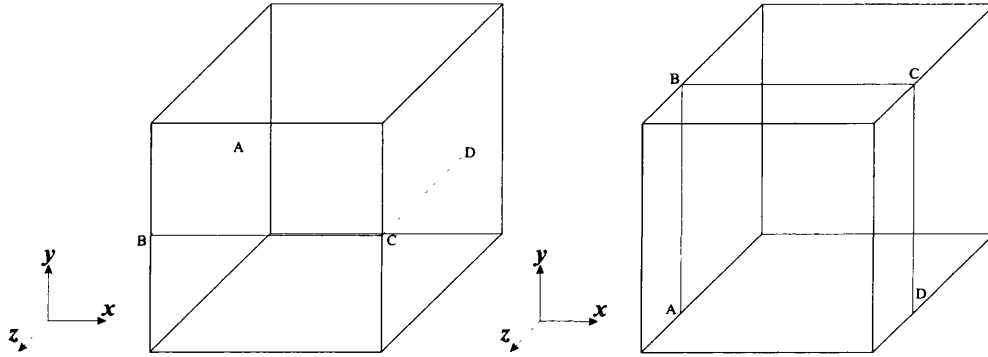


Figure 7.12: Heat transfer coefficient and surface temperature profiles.

To study heat transfer, the Nusselt number (dimensionless heat transfer coefficient)  $Nu$ , is calculated using Equation (7.5) around the profiles shown in Figure 7.12.

$$Nu = \frac{H \left( \frac{dT}{dx_i} \right)_s}{T_s - T_\infty} \quad (7.5)$$

The subscript ‘s’ represents the surface value by taking the harmonic mean of the air and epoxy conductivities similar to Equation (3.58). Hence  $k_s$  and  $T_s$  are the

surface conductivity and temperatures respectively.  $(dT/dx_i)_s$  is the temperature gradient across the epoxy-air interface, with  $i$  depending on the direction of the profile path.

The grids are stretched towards all boundaries in all directions and are detailed in Table 7.8. Use of stretched grids allows higher resolution near walls where the turbulent scales are smallest and to allow a more even distribution of errors. A finer grid near the walls and corners of this geometry allows the high velocity and temperature gradients to be captured more accurately.

Label	$x \times y \times z$	Total cells	$y_{wall}^+$	$\Delta x^+$	$\Delta y^+$	$\Delta z^+$
A	$109 \times 109 \times 109$	1295029	2	2.5-30	2-30	2.5-30
B	$75 \times 75 \times 75$	421875	2	2.5-50	2-60	2.5-50
C	$53 \times 51 \times 53$	143259	3	7-60	4-80	7-60
D	$41 \times 45 \times 41$	75645	4	10-70	7-100	10-70

Table 7.8: Heated cube grid details.

Although the first off wall node distances are a little large compared to a typical boundary layer dominated simulation, the grids were purposely coarsened to aid in finding the region where grid resolution becomes too poor for meaningful results to be obtained. Studying the same case, Rautaheimo and Siikonen (1999) use a grid with the first off wall grid distance of around  $1 < y^+ < 5$ . A further comparison can be made with the grid used by van der Velde et al. (1999). This group used a stretched grid of  $100^3$  to perform a kind of DNS (though not a fully resolved DNS). Using a grid of  $100^3$  and a first off wall node distance of  $y^+ = 3$ , Mathey et al. (1999) note through previous work that results are not so sensitive to the near-wall grid resolution or SGS model. It is considered that it is the geometrical features that are dominant here and that it is not as important to highly resolve the near wall region as it is to capture the dominant large vortices that are responsible for increasing heat transfer. The capability of LES using lower resolution grids is useful for its application in industry, where computational

economy is of great importance. Grids A and B compare well to the resolutions given in Table 3.1 and show the grids tested cover a wide range of resolution.

### 7.3.2 Flow structure

Time averaged streamtraces are shown for grids B and C in Figure 7.13. For both grids, gross flow features such as the horse shoe vortex are present with contra-rotating vortices found to the rear of the cube (right). Outside the vicinity of the cube, both flows are almost identical. Recirculation near the cube faces is not well captured using grid C due to lower resolution. Since main flow features are well captured, it is possible grid nodes may be better distributed, with a higher density near the cube faces. Various separation and reattachment points generate three-dimensional vortices around each cube. These flow features are a time dependent phenomenon and a typical RANS model could never be expected to accurately capture such flows. A more physically realistic method based on (I)LES is a more obvious choice for accurate thermal predictions.

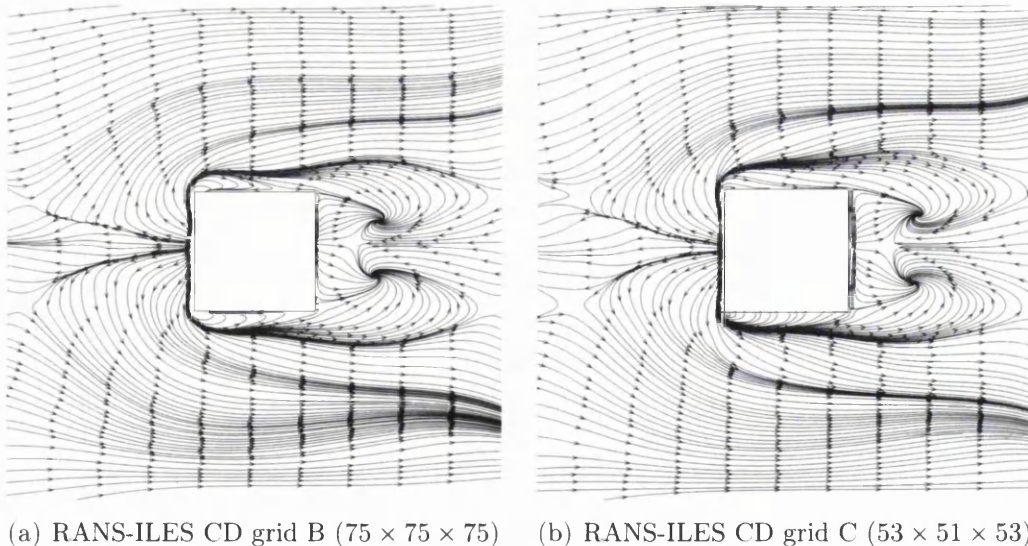


Figure 7.13: Cube streamlines at  $y/h = 0.25$ .



Castro et al. (2006) study staggered cube arrays experimentally and their results support the notion that eddy structures near walls differ significantly from those in regular smooth wall flows. They found that the dominant scales of turbulence are of the same order of magnitude as the obstacle height. This is precisely the trend found in the current work.

### 7.3.3 Average errors

The average errors of each variable over all profile locations is presented in Tables 7.9-7.12. As for the ribbed channel the absolute error values are given with the sign representing whether the overall error is positive or negative. Full plots of all profiles can be found in the Appendices. In the following subsections, results will be discussed in more detail.

### 7.3.4 Mean velocity distributions

For the cube, mean velocity profiles in the  $y$ - and  $z$ -directions are shown in Figures 7.14 and 7.15 respectively. All profiles at  $x/H = 1.2$  do not show the correct shape using RANS. The RI-CD2 model on grids B and D show good overall agreement with experimental data although lack of resolution shows more error creeping into the recirculation regions at  $x/H = 1.2$  and 3.8. On grid D, RI-2UP underpredicts the core velocity at all  $x/H$  locations but matches well up until  $y/H = 1$  for some locations (e.g.  $x/H = 1.2$  and 2.8). This could be due to dispersion errors, yet any improvements predicting the correct velocity profile around the cube may help to improve heat transfer predictions. The Leray and Yoshizawa models overpredict  $U$  above the cube in the core region leaving the velocity around the cube underpredicted. For profiles in the  $z$ -direction (Figure 7.15), the second order upwind RANS-ILES causes  $U$  to be too high and at  $x/H = 1.8$ , relatively

Variable (profile direction)	Average direction	←— Model —→									
		Smag	Yosh	Ler	$\alpha$	Kos	RL	RICD2	RI2U	RIQ	
$U/U_0$ ( $y/H$ )	$x/H$	-7.0	-4.9	-6.2	-7.8	-5.5	-5.6	-4.7	-6.8	-9.3	
$U/U_0$ ( $z/H$ )	$x/H$	-19.0	-20.0	-24.0	-27.3	-21.4	-14.3	-16.7	-17.5	-24.6	
$\overline{w'v'}/U_0U_0$ ( $y/H$ )	$x/H$	-17.3	17.4	16.7	-15.4	-16.7	-17.0	-16.6	24.5	-19.2	
$\overline{w'w'}/U_0U_0$ ( $y/H$ )	$x/H$	-32.3	-28.3	-28.3	-28.1	-31.8	-33.4	-31.3	-22.1	-22.9	
$dp/dx^c$	-	6.8	8.0	6.4	7.0	7.6	6.8	7.1	8.9	8.2	
$Nu$	$y/H$	28.8	-27.3	-22.2	-24.4	-22.2	-22.9	-23.8	-26.9	-31.3	
	$z/H$	23.5	-22.7	-16.1	-19.1	-17.8	-19.2	-19.8	-24.5	-29.6	

Table 7.9: Cube array average profile errors (%) ( $109 \times 109 \times 109$  grid).

<sup>a</sup>Entries for  $dp/dx$  are not the percentage error but the actual values.

Variable (profile direction)	Average direction	← Model →											
		Smag	Yosh	Ler	$\alpha$	Kos	RL	RICD2	RI2U	RIQ	LerCD4	$\alpha$ CD4	KosCD4
$U/U_0$ ( $y/H$ )	$x/H$	-5.8	-5.4	-7.5	-5.0	4.2	-5.0	-6.8	-5.3	-7.4	-4.2	-7.2	-5.3
$U/U_0$ ( $z/H$ )	$x/H$	-10.9	-6.5	-16.3	-12.8	-8.6	-5.4	-8.2	8.0	-8.2	-8.9	-12.8	-5.0
$\overline{u'u'}/U_0U_0$ ( $y/H$ )	$x/H$	24.9	27.9	21.6	19.2	20.1	25.7	19.9	35.9	29.5	-18.4	18.4	19.1
$\overline{w'w'}/U_0U_0$ ( $y/H$ )	$x/H$	-27.5	-29.9	-30.1	-28.2	-26.0	-29.8	-30.8	24.2	-18.1	-29.5	-28.4	-28.7
$dp/dx^a$	-	8.0	8.6	7.7	7.4	8.3	6.8	7.7	8.4	7.6	9.1	7.4	7.9
$Nu$	$y/H$	-22.9	-15.8	-19.8	-19.9	-19.0	-19.0	-18.4	-29.0	-30.2	-18.4	-21.5	-20.6
	$z/H$	-16.5	13.1	-14.1	-13.7	-12.6	-13.4	-14.0	-23.0	-25.4	-12.9	-15.6	-15.5

Table 7.10: Cube array average profile errors (%) ( $75 \times 75 \times 75$  grid).

<sup>a</sup>Entries for  $dp/dx$  are not the percentage error but the actual values.

Variable (profile direction)	Average direction	← Model →											
		Smag	Yosh	Ler	$\alpha$	Kos	RL	RICD2	RI2U	RIQ	LerCD4	$\alpha$ CD4	KosCD4
$U/U_0$ ( $y/H$ )	$x/H$	-7.6	8.5	-6.6	-6.9	-5.7	-8.5	-6.1	-10.8	9.4	5.6	6.7	-5.9
$U/U_0$ ( $z/H$ )	$x/H$	-8.5	-10.8	-8.6	-10.0	-10.4	-8.0	-11.0	-6.4	-8.4	-15.0	-12.6	12.9
$\overline{w'w'}/U_0U_0$ ( $y/H$ )	$x/H$	25.2	41.1	30.7	30.4	30.6	31.5	20.7	49.4	27.0	20.8	25.3	31.4
$\overline{w'w'}/U_0U_0$ ( $y/H$ )	$x/H$	-30.0	-32.0	-26.3	-29.2	-29.9	-34.9	-33.9	-30.8	-22.6	-22.7	-24.6	-25.9
$dp/dx^a$	-	8.5	8.5	7.7	7.3	8.3	7.2	6.8	7.8	7.0	7.5	7.5	9.2
$Nu$	$y/H$	-41.4	-40.6	-36.1	-36.4	-34.8	-36.5	-40.4	-45.7	-46.6	-39.0	-38.3	-34.9
	$z/H$	-32.0	-30.8	-24.6	-25.2	-24.2	-26.6	-29.5	-37.8	-39.1	-28.2	-28.2	-24.4

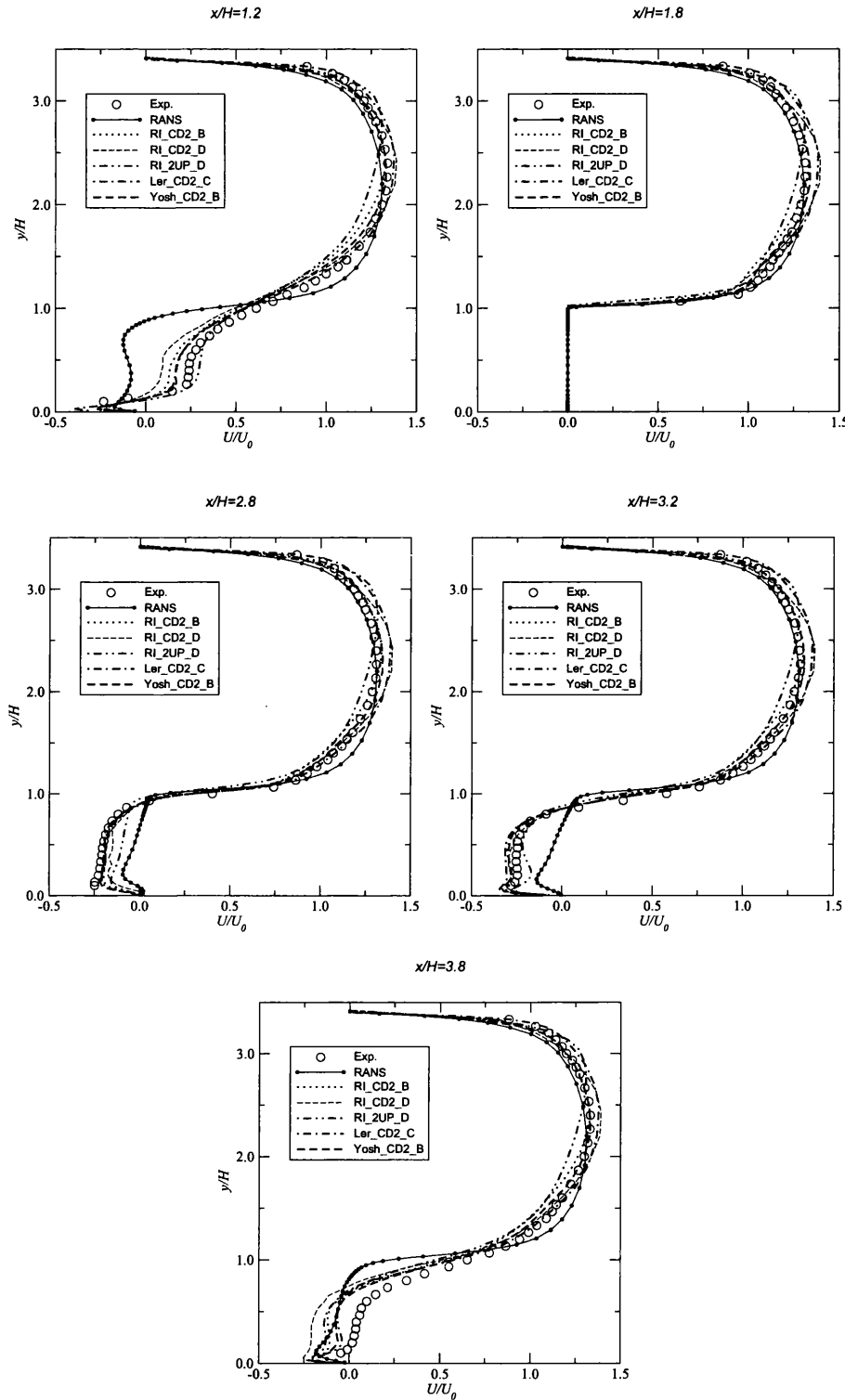
Table 7.11: Cube array average profile errors (%) ( $53 \times 51 \times 53$  grid).

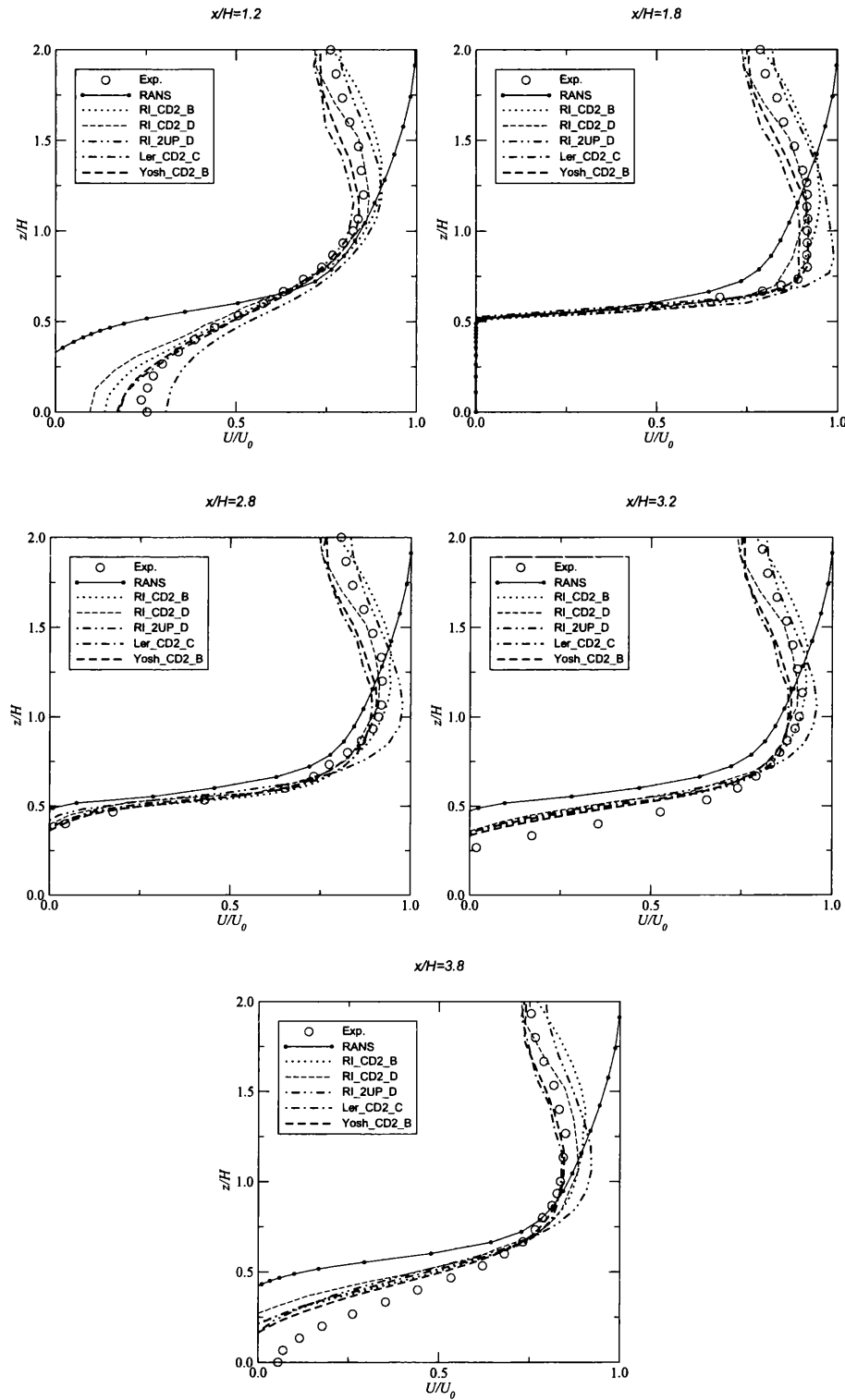
<sup>a</sup>Entries for  $dp/dx$  are not the percentage error but the actual values.

Variable (profile direction)	← Model →													
	Average direction	Smag	Yosh	Ler	$\alpha$	Kos	RL	RICD2	RI2U	RIQ	LerCD4	$\alpha$ CD4	KosCD4	
$U/U_0$ ( $y/H$ )	$x/H$	-10.6	-11.3	-9.3	-9.2	-11.5	-10.5	-8.1	-9.3	-9.8	-6.9	-7.0	-8.2	
$U/U_0$ ( $z/H$ )	$x/H$	-11.4	-11.6	-9.3	-9.8	14.4	16.5	-9.6	10.7	-9.8	-9.3	-13.5	15.0	
$\overline{w'w'}/U_0U_0$ ( $y/H$ )	$x/H$	45.3	42.5	33.7	40.9	45.8	50.1	32.1	60.7	43.9	29.0	26.7	45.1	
$\overline{w'w'}/U_0U_0$ ( $y/H$ )	$x/H$	-32.3	-37.3	-30.5	-28.4	-29.5	-33.0	-35.1	-29.4	-31.0	-23.6	-24.5	-28.3	
$dp/dx^a$	-	7.9	8.6	7.5	7.5	9.8	7.5	6.9	7.7	7.2	7.7	7.6	9.4	
$Nu$	$y/H$	-41.8	-41.3	-35.6	-35.7	-34.3	-36.0	-34.2	-38.9	-40.7	-37.7	-38.7	-35.6	
	$z/H$	-36.2	-35.3	-28.6	-28.9	-27.8	-30.2	-30.0	-33.2	-36.4	-29.9	-31.2	-28.5	

Table 7.12: Cube array average profile errors (%) ( $41 \times 45 \times 41$  grid).

<sup>a</sup>Entries for  $dp/dx$  are not the percentage error but the actual values.

Figure 7.14: Mean  $U$  velocity profiles at various  $x/H$ -locations.

Figure 7.15: Mean  $U$  velocity profiles at various  $x/H$ -locations.

large errors in  $U$  can be seen near the side of the cube ( $z/H \approx 0.75$ ). Again RANS fails to capture the right profile. In contrast, the Leray and Yoshizawa LES models tend to under-predict  $U$ . For grids B and D, RI\_CD2 seems to perform well in most profiles.

### 7.3.5 Higher order statistics

For the cube, the streamwise and spanwise turbulent stresses are plotted in Figures 7.16 and 7.17. For the normal stresses  $\overline{u'u'}$ , errors are generally reduced with a finer grid (Table 7.9-7.12). The RI\_Q and RI\_CD2 schemes also performed considerably better than the RI\_2UP scheme. For  $\overline{w'w'}$ , RI\_2UP performs similarly to the other RI schemes, where  $\overline{u'u'}$  is generally over-predicted. Significant errors exist between the RI\_2UP\_D model and experimental data (Figure 7.16). Visually other models show good agreement. The flow created around the cube in the spanwise direction proves more problematic for most models on grids A and B, though the situation is reversed for grids C and D where  $\overline{w'w'}$  is improved over  $\overline{u'u'}$ . This may explain to a large extent why heat transfer is not predicted as well on the lower resolution grids, as the dominant direction of flow is the streamwise direction. It is important to capture the dominant flow features and failure to do so may indicate the anisotropic flow is poorly modelled. Below  $y/H = 1.5$ , there are more random differences between models for  $\overline{u'u'}$  and  $\overline{w'w'}$  profiles and the peaks are not captured correctly. This demonstrates how, even when using (I)LES based methods, the modelling of turbulent stresses can have a complicated influence on the solution and it is not clear from the plotted results which model is optimal. Again in the core region of the flow, RI\_2UP\_D over predicts  $\overline{w'w'}$ . Some degradation is apparent from coarsening of the grid. It is evident however, that problematic regions of high turbulence are not consistently captured. This could also indicate failures of the (I)LES models themselves or the breakdown of



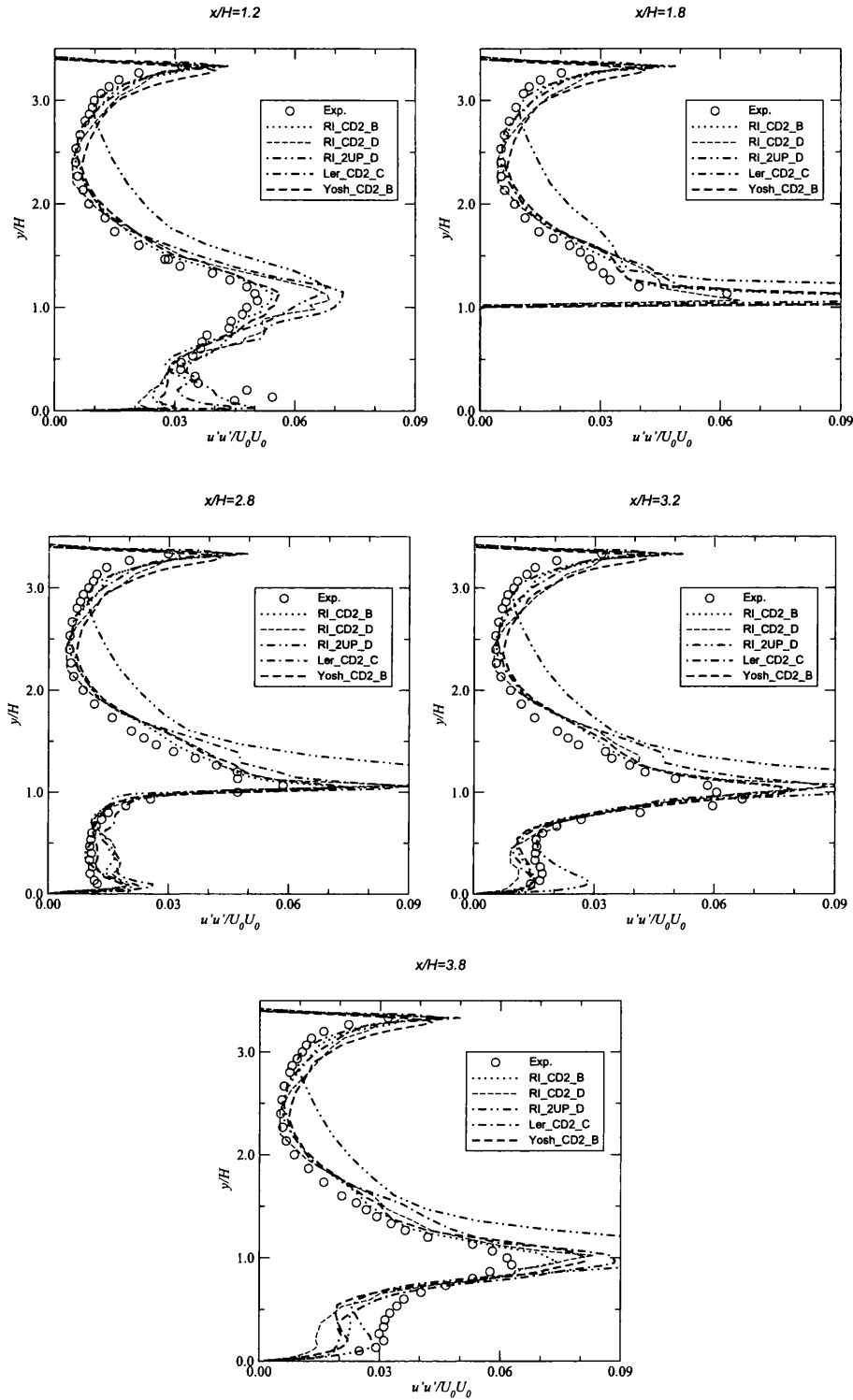


Figure 7.16:  $u'u'$  profiles at various  $x/H$ -locations.

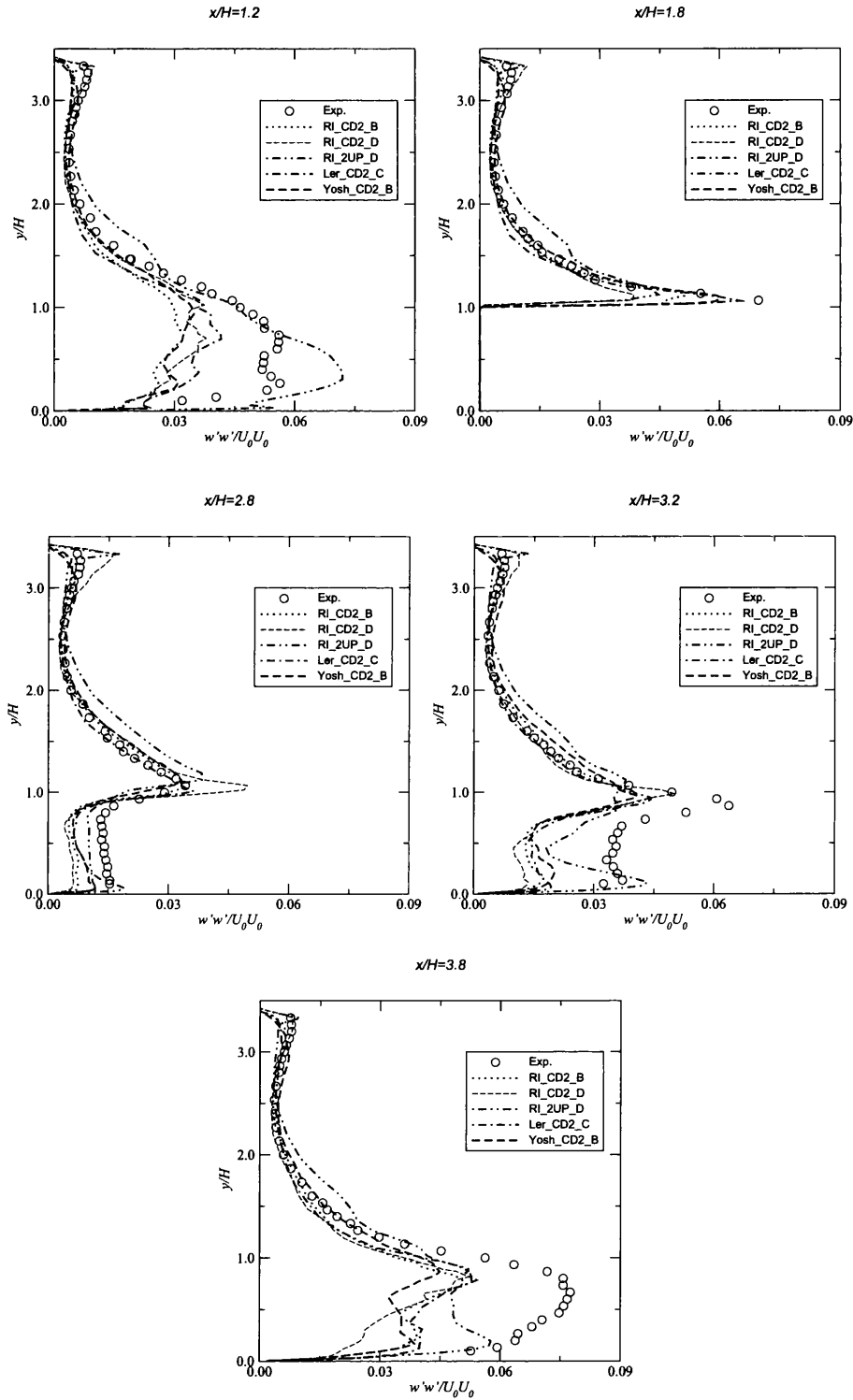


Figure 7.17:  $w'w'$  profiles at various  $x/H$ -locations.

any assumptions made.

### 7.3.6 Heat transfer

In Figure 7.18, the Nusselt number is plotted along the profiles given in Figure 7.12. Comparison is also made with the LES of Mathey et al. (1999) since this has a similar resolution ( $100^3$ ), yet uses the Smagorinsky model.

At all three locations in the  $y$ -direction RI\_CD2\_B and Yosh\_B maintain a shape similar to that of the experimental data. On lower resolution grids, models fail to show the correct shape and there is an accompanying drop in accuracy. On grid D, the RI\_CD2 scheme shows some improvement over the second order upwind scheme. A similar trend can be found in the  $z$ -direction profiles. The Yoshizawa model on grid B seems to perform particularly well though seems fortuitous given other results (see Tables 7.9-7.12), where all models show some variance in performance. Using the Smagorinsky model and a grid of 425,000 cells, Ničeno et al. (2002) obtained accurate thermal and flow predictions. The Yoshizawa LES model using grid B is almost identical to the LES of Mathey et al. (1999) at all  $y$ -locations, only differing along the path A-B. Except for at the base of the cube, the RI\_CD2\_B model also performs similarly. These results are encouraging given the LES of Mathey et al. (1999) was performed on a finer grid and that the grid of a similar size to grid B (Ničeno et al. 2002) also produced similar results.

The profiles for different  $z$ -locations show good agreement between the experimental data and each other, even though there are significant differences between the SGS modelling method. Qualitatively speaking, lowering resolution from grid B has significant impact on the  $Nu$  profiles, around corners and on the faces of the cube. This may be due to poor resolution of important scales and gradients and increased damping from the coarser grid.

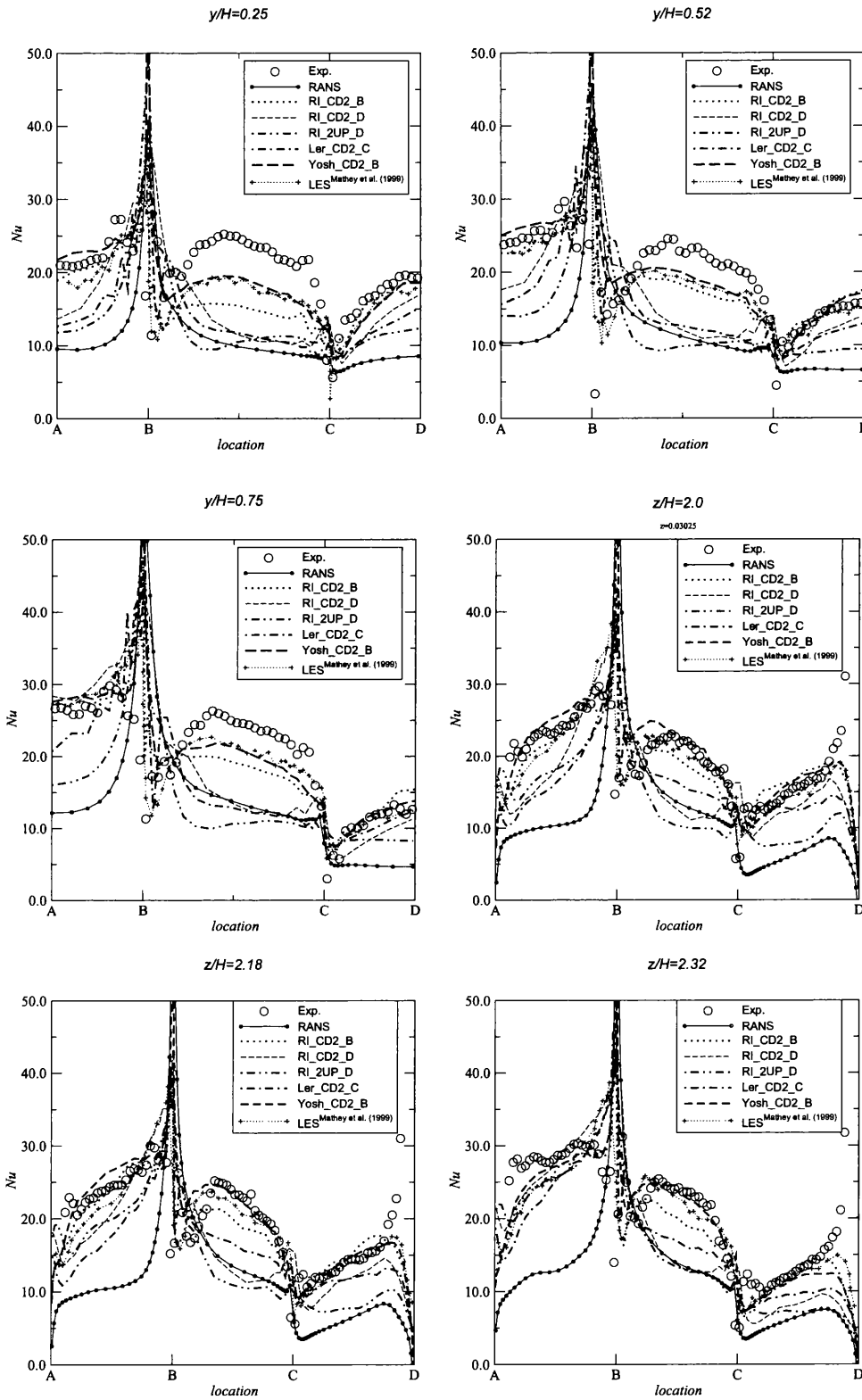


Figure 7.18:  $Nu$  along heat transfer profiles.

For both sets of profiles, it is the area after the leading edges of the cube (B–C for the  $y$  profiles in Figure 7.12) that is poorly represented. This is a region of separation from the front face and recirculation on the side and top of the cube. As can be seen in Figure 7.13, there lies a small recirculation bubble on the side of the cube, poorly captured by the coarser grid. On the finer grid (Figure 7.13(a)) it can be seen that the flow is drawn towards the cube surface by this recirculation, the impingement increasing heat transfer. From the heat transfer profiles it would appear this part of the flow structure is too weak, as was mentioned in section 7.3.5. Overall, profiles for the Nusselt number are rather mixed, making a qualitative interpretation of each model's performance difficult, although errors are lower for different  $z$  locations than different  $y$  locations.

On grids A and B, changing the model from RL\_CD2 to RL\_2UP or RL\_Q worsens heat transfer predictions yet improves predictions on grids C and D. It is possible the 3<sup>rd</sup> order QUICK scheme better retains accuracy on coarser grids or that the 2UP scheme artificially raises heat transfer even though the flow is not captured well. This may be because there is more rotation in the flow, making the use of an upwinded stencil less appropriate. Although the mean flow is in the streamwise direction, there are considerable 3D flow features causing high gradients in all directions near the cube. Due to this three-dimensional flow with strong streamline curvature and anisotropy, the nonlinear SGS models perform better by around 5% than the linear models on grids C and D. This may be due to the filter becoming larger and the subgrid scales becoming more anisotropic instead of universal and isotropic, as assumed in more simple linear models. On grids A and B, RL\_CD2 predicts  $Nu$  to within 14–24% with experimental error for the heat transfer coefficient being 5–10% (Meinders et al. 1997).

All models seem to show some sensitivity to the grid. This could be due to poor resolution near boundaries with coarsening grids and the interaction (summation or cancelling) of modelling and discretisation errors. These are always intimately

linked in a second order solver with  $\Delta \mathbf{x}_i^2$  truncation error terms and will interact with the SGS model, for example, the Smagorinsky model  $\mu_{SGS} = \rho(C_s \Delta_s)^2 \bar{S}$  term.

Having more heat transfer surfaces, conjugate heat transfer and a complex flow, predictive accuracy on average is expectedly a little worse than that of the ribbed channel. Given the additional complexity and uncertainty in boundary conditions (inescapable for all CFD methods), heat transfer is predicted relatively well on low resolution grids. Increasing resolution between grids C and B shows a marked improvement and further refinement to grid A shows no benefit. It appears the large energetic scales are well resolved on grid B but are lost to some extent on grids C and D. Given the low Reynolds number flow, a small change in grid resolution can have a large effect on which scales are resolved or modelled. This lack of scale separation will be discussed further in Chapter 8.

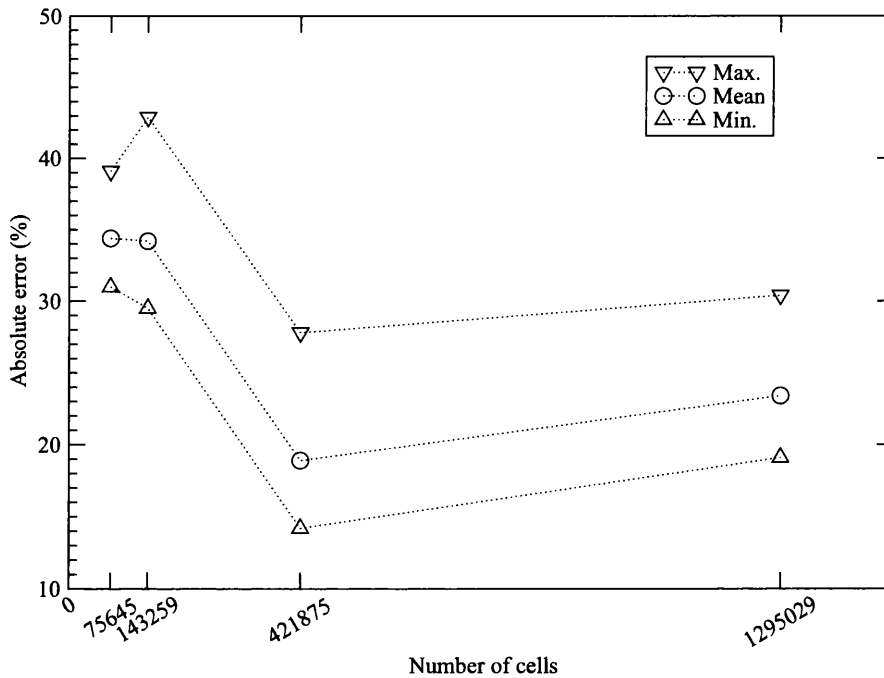


Figure 7.19: Absolute errors for  $Nu$  using all SGS models.

Figure 7.19 shows the mean absolute errors for  $Nu$  (averaged over all SGS models

for each grid to give an impression of grid effects using an “average” SGS model). The mean, along with the maximum and minimum errors for the range of SGS models are shown. The mean shows the general trend and the maximum and minimum errors obtained with any SGS model show the maximum range in errors. Contrasting with the ribbed channel case, the maximum variation between SGS models is on the second finest grid. This is largely due to a very small error from the Yoshizawa model and a large error from the RI\_2UP and RI\_Q models. As can be seen, the average line is nearer the minimum line, showing most models tend towards more accurate modelling of heat transfer. The average error decreases with increasing grid density except for the finest grid. This may be due to numerical errors interacting with the SGS models though the error is only slightly larger than for grid B. In general the SGS model changes the error between 10-15%, the grid having a similar effect. That these effects are of a similar magnitude would also indicate the problem of separating SGS and discretisation errors.

### 7.3.7 Pressure differentials

The pressure gradient,  $dp/dx$  shows a wider range of results for this case. On grid B the variation is only 20% of the maximum value, increasing to 30% for grid D. As expected,  $dp/dx$  rises as the grid gets coarser, the numerical errors dissipating energy. This shows up as a higher mean resistance to flow, hence  $dp/dx$  must increase. It seems that there is less scatter of  $dp/dx$  with grid than other variables making fan choice an easier decision based on any given simulation.

### 7.3.8 Conclusions

The heated cube is a significantly more complex flow than that of the ribbed channel. The flow from each cube in the array influences cubes (or generally any

other feature) downstream, so accurate modelling of the flow is challenging in itself. Though it is hard to see any particular trend, the results are still useful. This case shows a high dependency on grid resolution and it is considered that the correct grid distribution is important. The numerous edges and corners create high gradients in both velocity and temperature. Due to the large coherent structures produced, relatively coarse grids can be used to obtain fair results in a short time, yet it would seem that once the largest scales are not resolved well, the flow is not captured correctly. Increasing the grid resolution from grid B to A did not improve results, indicating that the most important, larger scales, have been resolved. The change of resolution would also have reduced the filter width and discretisation errors, accounting for the small change in results. This makes the filter size an important aspect that also affects the ability to separate numerical and modelling errors. Using a higher order convective term discretisation did not improve matters and in general degraded thermal predictive accuracy. This could be attributed to additional oscillations (over- and under-shoots) from the higher order terms. The RANS-ILES model using CD2 performed well compared to other models, possibly due to CD2 being insensitive to grid quality (Chung and Tucker 2003) and that no SGS model is used. This would affect the interplay of numerical and SGS modelling errors on different grids.

Uncertainties in the boundary conditions, for example at the base of the cube, introduce a potentially large source of error. The confined geometry of the cube makes each region highly dependent on other regions of flow and accurate SGS modelling is important yet difficult to achieve. Using ILES seems attractive in this sense as numerical influences can be used to implicitly generate the SGS terms without explicit assumptions about the flow, for example, whether the flow is isotropic or highly anisotropic as in channel flows or assumptions based on boundary layer theories, which may not be particularly important here.



## 7.4 Complex CPU case

### 7.4.1 Case description

The most challenging test case is a simplified CPU case. Much of the challenge lies in defining the boundary conditions on the many details of this system including several inlet/outlets, grills and fans. By electronics standards the fans are relatively large and so produce correspondingly higher Reynolds number flows. In the upper channel a heater element is modelled to study heat transfer just after the flow undergoes a  $180^\circ$  turn. Studies similar to this have shown heat transfer to be sensitive to upstream disturbances such as a thin fin trip (Tucker and Liu 2005a) or oscillatory flows (Chung et al. 2003). Therefore, this complex flow must be modelled well for the conditions around the upper channel and heat transfer zone to be correct. Also interesting is the possibility of different flow regimes appearing due to the inlet/outlets being passive i.e. air may enter or exit depending on the flow conditions. Air is circulated around the inside of the case via two fans, one in the middle section and one at the end of the upper channel. The abundance of grills, blocks and surfaces generates a highly complex flow including flow features such as separation, reattachment, localised and non-local circulation regions of strong streamline curvature and impingement with the possibility of transition from laminar to turbulent flow. The geometry consequently makes grid generation a challenge.

Non-slip and impermeability conditions are set at all walls and the ratio of Grashof and Reynolds numbers  $Gr/Re^2$  is low ( $< 0.01$ ) so bouyancy effects can be ignored (Tucker and Liu 2005a). At inlets/outlets, the total pressure is fixed and the normal velocity set to conserve mass, while other velocity components are set to zero. At each iteration the above boundary conditions are set as the flow directions are not known initially.

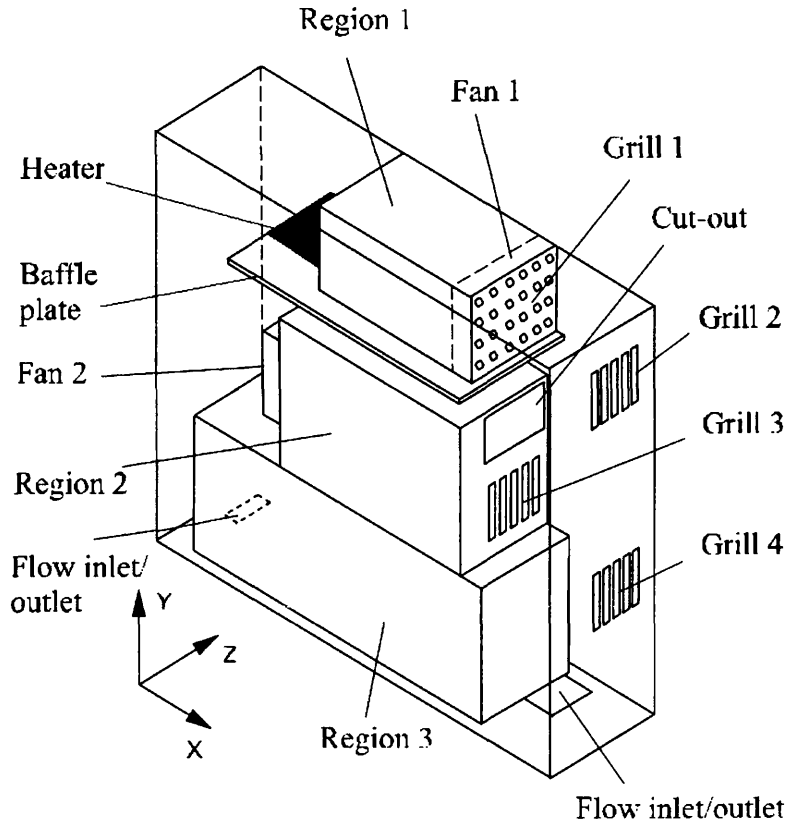


Figure 7.20: CPU case schematic.

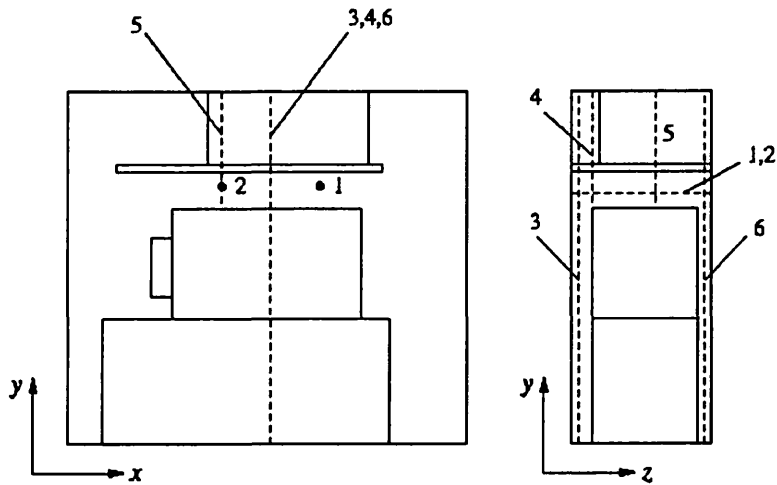


Figure 7.21: CPU profile paths.

The slotted grills are modelled using loss coefficients as

$$E_1 = \frac{1}{2}K\rho U_j^2 \quad (7.6)$$

where  $E_1$  is the loss of energy per unit volume of fluid with a local (not the lower approach velocity)  $U_j$  passing through the grill. Standard design guides values of  $K$  are taken for grills of these kind with  $K = 2$  for grill 1 and  $K = 1$  for the other grills.

Fans 1 and 2 are modelled using quadratic momentum sources as follows

$$E_i = C_0 + C_1U_j + C_2U_j^2 \quad (7.7)$$

where  $E_j$  is the energy input per unit volume and  $U_j$  is the local normal velocity.

The constants are given in table 7.13.

	$C_0(\text{J}/\text{m}^3)$	$C_1 (\text{Js}/\text{m}^4)$	$C_2 (\text{Js}^2/\text{m}^5)$
Fan1	59.0	-12.0	1.1
Fan2	59.5	-12.5	1.0

Table 7.13: Constants for fan momentum sources.

These values were previously obtained using least square fits to manufacturers data. To account for a 50% obstruction of fan 2 a value of  $K = 1$  is used as per the manufacturers tests. Stochastic forcing for fans was previously found to have little influence on results (Tucker and Liu 2005a) and so is not considered here.

The CPU case shown in figure 7.20 has dimensions of  $0.75 \times 0.64 \times 0.2\text{m}$  in the  $x \times y \times z$  directions. Similarly a  $209 \times 193 \times 101$  and a  $105 \times 99 \times 51$  stretched grid is used to contrast grid density. This may help determine minimum grid requirements for use in industry as the lower resolution grid has 530145 cells

versus the finer grids 4074037 cells, a factor of nearly 8. Details of the grids used can be found in Table 7.14

Label	$x \times y \times z$	Total cells	$y_{wall}^+$	$\Delta x^+$	$\Delta y^+$	$\Delta z^+$
A	$209 \times 193 \times 101$	4074037	1	2-32	2-28	2-32
B	$105 \times 99 \times 51$	530145	2	3-64	2-57	4-64

Table 7.14: CPU case grid details.

The interface between the RANS and (I)LES regions is set at  $y^+ = 30$  and smoothed using a multi-grid restriction operator. This is due to the changes in geometrical scales in various regions of the case making a flow-based interface more sensible. Here an average of the wall shear stress obtained from previous URANS simulations was used to set a fixed RANS-(I)LES interface.

The local Nusselt number obtained at the heater element is defined as

$$Nu_x = \frac{q(x - x_0)}{k(T_s - T_{ref})} \quad (7.8)$$

where  $q$  is the measured convective heat flux,  $T_s$  and  $T_{ref}$  are the surface and reference temperatures respectively and  $k$  is the thermal conductivity of air. More specific details concerning these values can be found in Liu (2004).

## 7.4.2 Flow structure

Although this case is simplified, a real CPU case may have stacks of circuit boards inside. This could generate some kind of periodic flow within the system. Studying rows of heated blocks (as in a telecommunications rack) Furukawa and Yang (2003) found that periodic flow takes an increasing number of blocks to become periodic as  $Re$  increases. This periodicity would be hard to predict and model effectively, and a physically realistic method such as (I)LES becomes attractive. Both the array

of cubes and the ribbed channel are modelled with periodic boundary conditions. The inflow and outflow boundaries therefore settle to a quasi periodic flow regime driven by a pressure gradient (to maintain the prescribed mass flow). For a non-periodic system, such as the CPU case, some boundary conditions must be set manually, while the inlets/outlets adapt to flow direction. Unknown or ill-defined boundary conditions could have a heavy influence on the final solution, yet in this case, the flow structure developed partly defines the boundary conditions, making the correct flow structure important.

Lasance (2007) notes that modelling ventilation grills by merely increasing the flow resistance may be too simple and that it is simply impossible to capture all details of the flow affecting heat transfer. A previous study has shown the inlet turbulent intensity did not have significant effect on the profiles presented (Tucker and Liu 2005a). This may be due to elements of interest (for example the heater element) are not near the fans or grills. This may be explained by the coherent jet structures breaking down to a more homogeneous state, supported by the data of Baelmans et al. (2003) showing that local flow phenomena are only important around grills/screens if components are placed within 5-10 times the diameter of the holes.

The geometrical complexity of the CPU case makes description of the resultant flow rather difficult. The main feature of interest in this flow however is the heated plate in the upper channel of the case. This causes the airflow to make a 180° turn over a short distance. This causes large vortices to be convected along the upper channel. Due to the number of fans and flow paths, there are many recirculation regions and areas of high and low turbulent activity. The nature of the boundary conditions means that the flow inlets/outlets can have positive or negative mass transfer, meaning that it is possible for the flow to change its general characteristics.

### 7.4.3 Average errors

For quantities of interest, profiles are taken along lines shown in Figure 7.21. The average errors of each variable over all profile locations are presented in Table 7.15. Full plots of all profiles can be found in the Appendices. In the following subsections, results will be discussed in more detail.

### 7.4.4 Mean velocity profiles

Mean velocity profiles (Figure 7.22) in the spanwise direction show similar shapes, though they do not follow the correct shape of the experimental data, the profiles are too flat. Profiles 3 and 4 show that the flow is underpredicted in the lower half of the upper channel, elsewhere a flat profile is again obtained. Profile 5 near the center (in  $z$ ) of the upper channel, shows the mean flow is predicted well up until the upper half of the channel. The Yoshizawa model under-predicts velocity in the upper channel. This indicates poor modelling of anisotropy near the channel wall or increased dissipation compared to the nonlinear LES models. Profile 6 remains too flat. This is similar to profiles 3 and 4 which are also near the case walls. This may indicate the walls presence damps out some of the large scale structures giving a more uniform velocity profile. Mean velocities are generally under predicted as can be seen in Table 7.15.

Variable (profile direction)	Averaged profiles	← Model →									
		Smag_A	Yosh_A	Ler_A	$\alpha_A$	Kos_A	RL_A	RL_CD2_A	$\alpha_B$	RL_CD2_B	
$U/U_0$	1-6	-15.4	-19.4	-17.8	-17.7	-16.3	-17.7	-14.8	-13.8	-15.5	
$T_i$	1-6	-23.4	-25.6	-22.9	-20.8	-26.1	-21.6	-18.4	-25.0	26.4	
$Nu_x$	-	38.2	36.2	19.	23.4	37.6	28.3	-16.6	269.0	85.1	

Table 7.15: CPU case average profile errors (%) for all variables and grids.

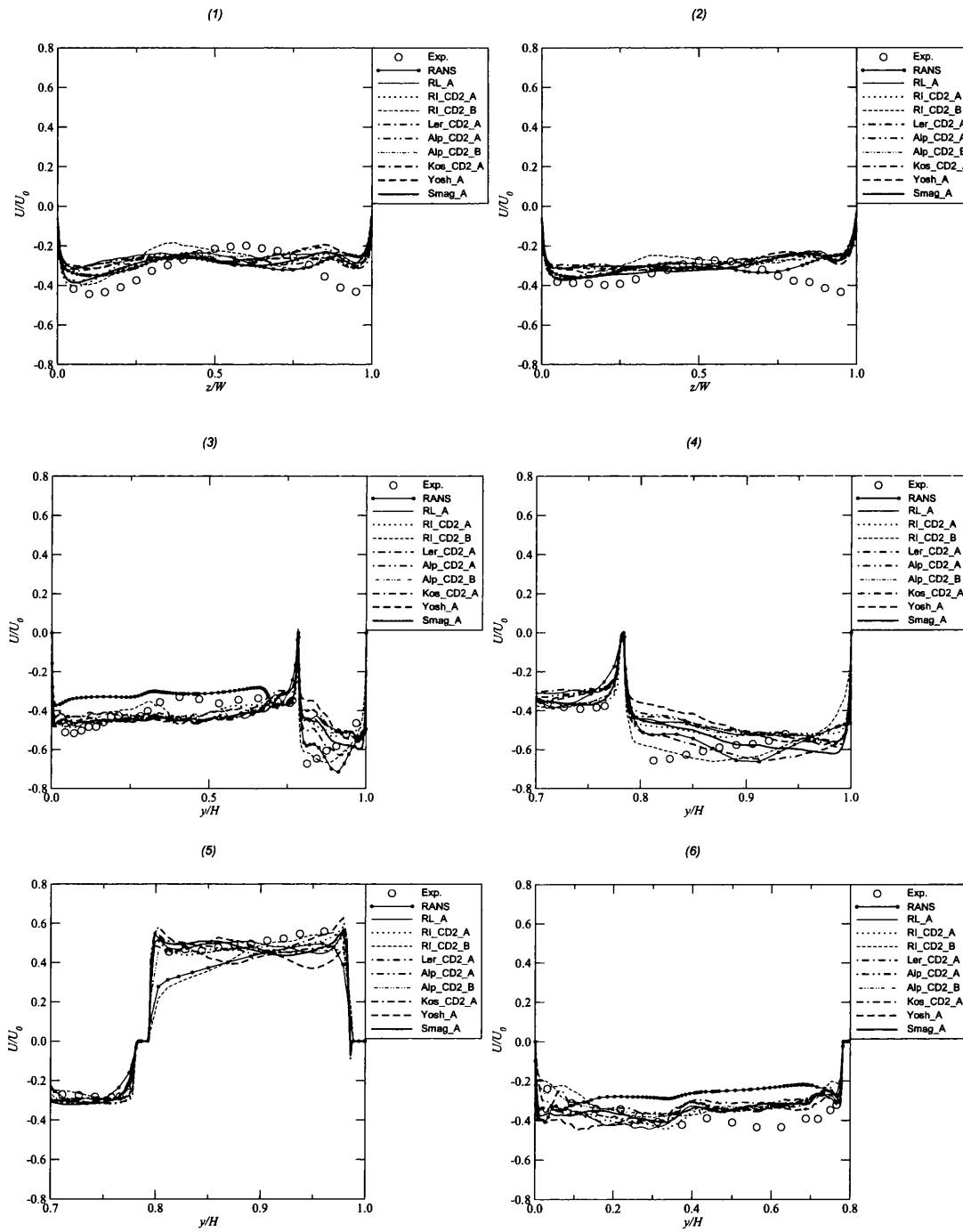


Figure 7.22: Mean  $U$  velocity profiles (1-6).



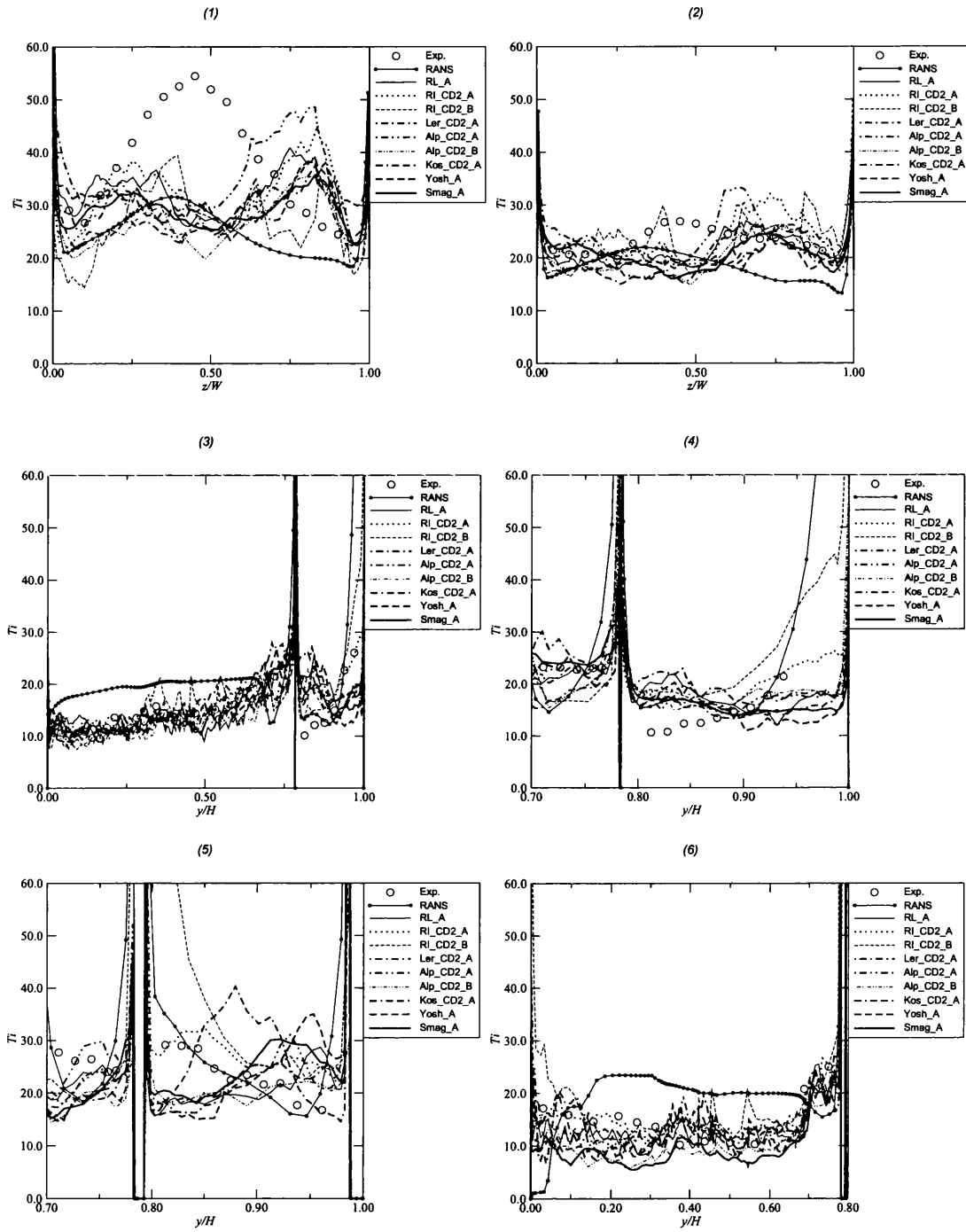


Figure 7.23: Turbulence intensity (%) profiles (1-6).

### 7.4.5 Turbulence intensity profiles

Experimental data for profile 1 (Figure 7.23) shows that the flow returning from Fan 1 and the cut-out of Region 2 gives a turbulence intensity of about 55%. Most models seem to predict the highest  $Ti$  at a greater  $z/W$  location, the highest peak coming from the Alpha\_CD2\_A model at just under 50%. The same trait is found further downstream of the flow at profile 2. Again the peaks are at a greater  $z/W$  location with the Alpha\_CD2\_A and RI\_CD2\_A models over predicting the maximum  $Ti$  by around 5%.  $Ti$  predictions for profile 3 are rather good up until the upper channel. Here  $Ti$  is over predicted in the lower half and under predicted in the upper half, this is also the case for profile 4. The Kosović model over predicts  $Ti$  in the center of the channel by 10–20% along with RI\_CD2\_A to a lesser extent. For this profile, nearer the heater element,  $Ti$  is under predicted in the lower half of the channel and overpredicted in the upper half, contrary to further downstream (profiles 3,4 and 6). Average errors in  $Ti$  are tabulated in Table 7.15, where it can be seen that  $Ti$  is underpredicted except for the RI\_CD2\_A model.

### 7.4.6 Heat transfer

From Table 7.15 and the turbulent intensity profiles 3 and 4, it can be seen that there is a correlation between the accuracy of turbulence intensity and the error in  $Nu$ . As the error in  $Ti$  is reduced, so is the error in  $Nu$ . When  $Ti$  is over predicted, so is  $Nu$ . The more dissipative models have smaller turbulent fluctuations. This added diffusivity also increases the diffusion coefficient for the temperature equation ( $k = C_p \mu_t / Pr_t$ ), increasing heat transfer. This is why the RI\_CD2\_A model under predicts  $Nu$  yet allows turbulent motions to persist through lower dissipation. The lowest positive error in  $Nu$  is from the Ler\_CD2\_A model. The Alpha model is normally less diffusive than the Leray model (Geurts 2005), though

they do give similar thermal predictions. The experimental uncertainty in  $Nu$  is around  $\pm 5\%$  (Liu 2004) and the obtained results quite reasonable given the complexity of the system.

Running the Alpha and RI\_CD2 models on grid B show suprisingly good results for around  $\frac{1}{8}^{th}$  of the grid. The errors are still high though, perhaps because some of the larger, dominant scales are not as well resolved with the additional diffusion raising  $Nu$ . This again shows there is scope for finding a more appropriate grid that will give both accuracy and reduced computational expense and also that anisotropic SGS models could be useful for these types of flows. It seems however that although the nonlinear SGS models can improve thermal predictions, the extra computational expense could be reduced by using the RI\_CD2 model on the same grid with potentially better results.

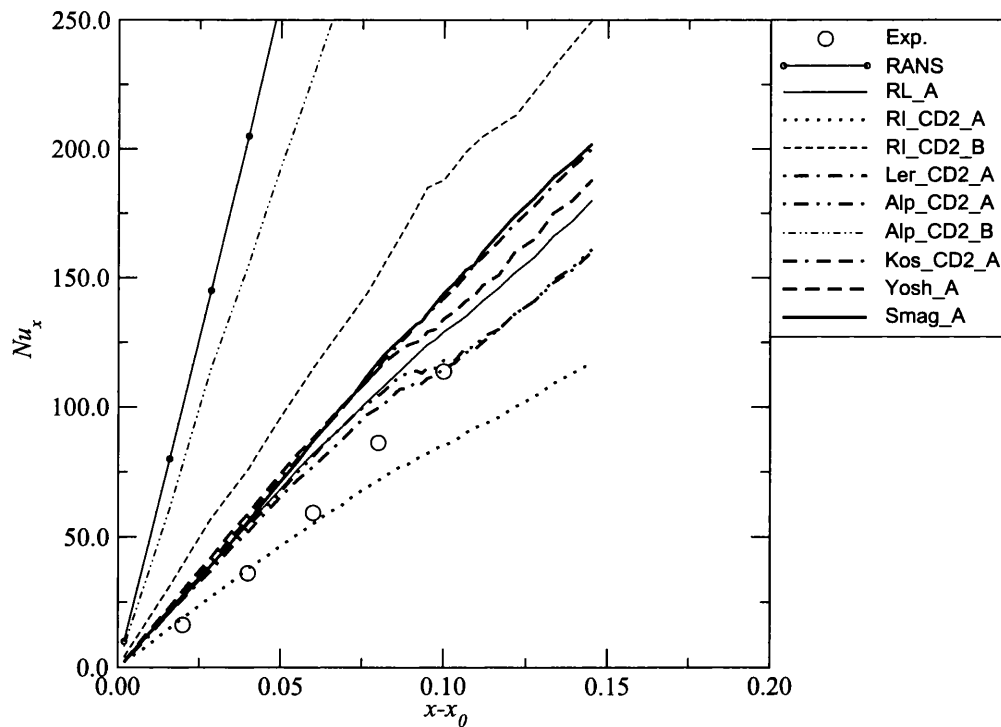


Figure 7.24:  $Nu_x$  along the heater element

Most models have over-predicted the values of  $Nu$ . This could be dangerous

in a design context, as this would imply lower component temperatures. From Table 7.15 it is clear that both the Leray and Alpha nonlinear SGS models have greatly improved heat transfer accuracy compared to the inferior linear Smagorinsky and Yoshizawa models. The nonlinear Kosović model does not compare so well due to additional dissipation, partly due to a higher value of  $C_\mu = 0.11$  rather than  $C_\mu = 0.05$  for the Leray model. Referring to Figure 7.24, the Smagorinsky and Kosović models are nearly identical. This means that the Kosović model would not be worth the extra computational effort in the current form. Perhaps lowering the value of  $C_\mu$  would align the model more with the other nonlinear models. Liu et al. (2007) studies the nonlinear terms' influence leaving  $C_\mu$  the same for each model, however, no nonlinear model clearly stood out.

#### 7.4.7 Conclusions

Given the complexity of this flow, the various models applied generate a wider range of results than the previous two cases. The best over all  $Nu$  profile is from the RI\_CD2\_A model. Bearing in mind the other models over-predicted  $Nu$ , the lack of additional dissipation from the ILES region actually benefited the final result leaving a margin of error between the experimental data.

Table 7.16 compares the modelling methods and computational effort. For this table, L=linear, NL=nonlinear and  $\Delta t$  is the time per iteration.

Model	LES(L)	LES(NL)	Hybrid(CD2)	Hybrid(2UP/Q)	LES(NL CD4)
$\Delta t$	1.0	1.6	1.2	1.3	1.9

Table 7.16: Comparison of computation time for each model.

As can be seen in Table 7.16, the nonlinear LES models carry substantial increases in computational effort. The most expensive models include nonlinear LES and the

CD4 scheme. Using the CD4 scheme also required around 50% more iterations per time step to converge. Bearing in mind effects on both accuracy and computational effort, the hybrid methods seem attractive, especially the RI-CD2 model. Though this is not always the most accurate model, it has shown comparable accuracy to the variety of other models tested at a reduced computational cost for three different flows.

# Chapter 8

## LES model applicability

### 8.1 Introduction

The assumption of smaller eddies being universal is contradicted by the array of results obtained using different subgrid closures. Although not wildly varying as with different RANS models applied to bluff geometries, it does bring into question whether various assumptions about turbulent flows are valid in certain scenarios. Empirical knowledge for modelling the SGS tensor  $\tau_{ij}$  is essential but incomplete, hence, most models presume some dissipative component or make use of similarity properties in an inertial range. Some of these ideas are explored and discussed.

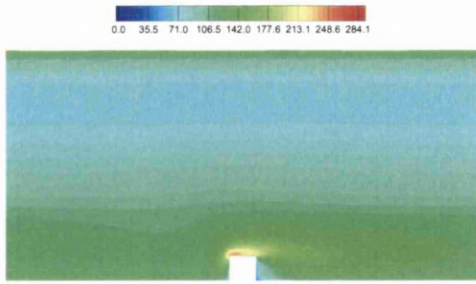
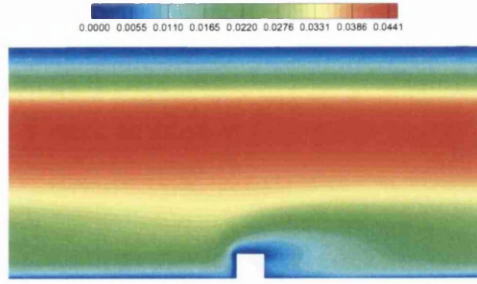
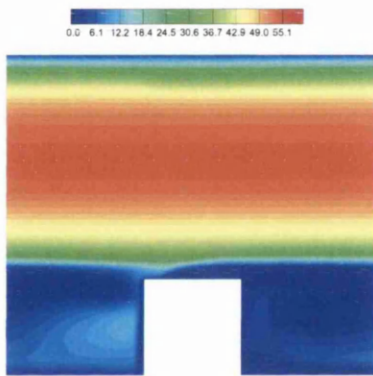
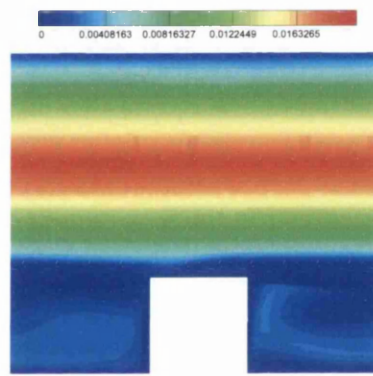
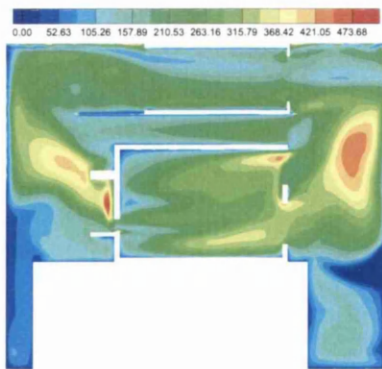
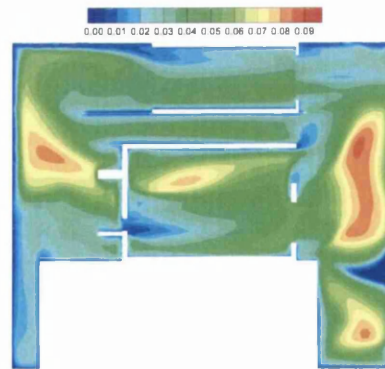
### 8.2 Assumption of a long inertial subrange

For low Reynolds number flows, there is a considerable overlap of energy containing and dissipative scales, increasing the likelihood of the filter being in the overlap region. This is in contrast to Kolmogorov's theories, on which many LES model

assumptions are based. The applicability of the assumption that there is a long inertial subrange displaying a  $\kappa^{-5/3}$  law made in many SGS models is tested here using a model energy spectrum based on the work of Gamard and George (1999) and estimations made for the main test cases. The method used is based on the ratio of the integral length-scale ( $L$ ) and Kolmogorov microscale ( $\eta$ ),  $R = L/\eta$ , which may be related to the Reynolds number as  $R = Re_L^{3/4}$ .

To model the energy spectrum, one can estimate the size of the integral length-scale using a pseudo integral length-scale. To obtain approximations to  $L$ , a  $k - \varepsilon$  RANS model was employed giving  $L_{k-\varepsilon} = u^3/\varepsilon$ . Where  $u = k^{1/2}$  and  $\varepsilon$  is the dissipation rate. The ratio of scales based on the RANS length scale is then obtained as  $R_{k-\varepsilon} = L_{k-\varepsilon}/\eta$ . Alternatively, based on the geometric features of the rib and cube cases (the height of the rib and cube), length-scales  $L_{h,rib} = 0.00635$  and  $L_{h,cube} = 0.015$  can be defined respectively. It can be confirmed viewing instantaneous contour plots from these cases that the largest vortices are of a similar size to the rib or cube height. This also allowed insight into the predicted length-scales by this popular RANS model by comparison to the geometric scales. Using the RANS model to obtain  $\eta$  (averaged over the wake of the rib and cube where better agreement was found between geometric and RANS pseudo lengthscales) and the geometric obstacle heights, the ratio of scales based on the geometry ( $R_{h,rib} = L_{h,rib}/\eta$  and  $R_{h,cube} = L_{h,cube}/\eta$ ) are obtained. The above ratios are tabulated in Table 8.1 including only the RANS prediction for the CPU case due to the range of geometrical scales encountered. In this table  $R_{k-\varepsilon,max}$  represents the maximum ratio of scales based on  $L_{k-\varepsilon}$ ,  $R_{h,max}$  represents the maximum ratio of scales based on the rib or cube height and  $Re_{k-\varepsilon,max}$  and  $Re_h$  show the respective Reynolds number.

From Figure 8.1(a)–(c), it can be seen that the RANS model predicts a much larger ratio of  $R_{k-\varepsilon,max,rib} \approx 290$  with  $R_{k-\varepsilon,max,cube} \approx 60$ . This is partially due to the cube having a higher blocking ratio than that of the rib. Most of the flow

(a) Rib  $R_{k-\epsilon}$ (b) Rib  $L_{k-\epsilon}$ (c) Cube  $R_{k-\epsilon}$ (d) Cube  $L_{k-\epsilon}$ (e) CPU  $R_{k-\epsilon}$ (f) CPU  $L_{k-\epsilon}$ Figure 8.1:  $R_{k-\epsilon}$  and  $L_{k-\epsilon}$  contours for the electronics test cases.



	$R_{k-\varepsilon,max}$	$R_h$	$Re_{k-\varepsilon,max}$	$Re_h$
Rib	290	70	1920	290
Cube	60	140	235	730
CPU	520	-	4160	-

Table 8.1: Approximate ratios and corresponding Reynolds numbers using RANS and geometric length-scales.

in the ribbed channel is in reality fairly benign, yet the RANS model predicts a high ratio of scales in the core region. Figure 8.1(b) shows that the length-scales predicted around the rib are a similar size to  $L_{h,rib}$ . Therefore  $\eta$  is expected to be a better approximation in this region. For the CPU case, a maximum ratio of  $R_{k-\varepsilon} \approx 500$  and  $L_{k-\varepsilon} \approx 0.1$ . Considering the large recirculation regions, the depth of the case being 0.2 m and the upper channel being of a similar height, this value of  $L_{k-\varepsilon}$  seems reasonable. However, even the maximum ratio does not meet the minimum ratio ( $R = L/\eta = 1000$ ) stated by George and Tutkun (2009), for there to be a significant inertial subrange, though this is rather subjective.

Using the obtained ratios, a model spectrum<sup>1</sup> is used to determine to what extent assumptions based on the existence of a long inertial subrange are valid.

To create a full model spectrum, we first define a low wavenumber model using the von-Karman spectrum as presented in Gamard and George (1999):

$$\overline{E}(\overline{\kappa}) = \frac{E}{u^2 L} = \frac{C_p \overline{\kappa}^4}{[1 + (\overline{\kappa}/\overline{\kappa}_e)^2]^{17/6}} \quad (8.1)$$

where  $\overline{\kappa} = \kappa L$ ,  $C_p = 6.25$  and  $\overline{\kappa}_e = 0.747$ .

The high wavenumber end of the spectrum can be modelled using the Lin/Hill spectrum (Gamard and George 1999):

<sup>1</sup>Originally provided with thanks by William George and edited by the author

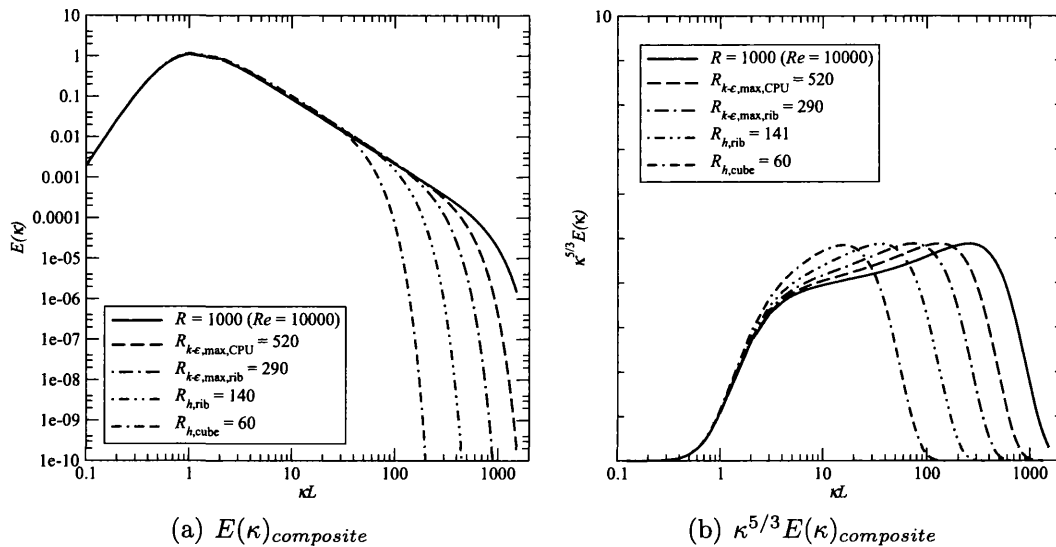


Figure 8.2: Energy spectra for different length-scale ratios.

$$E^+(\kappa^+) = \frac{E}{\nu^{5/4} \varepsilon^{1/4}} = \alpha_\kappa \kappa^{+5/3} \left[ 1 + \kappa^{+2/3} \right] \exp -\alpha_\kappa \left[ \frac{3}{2} \kappa^{+4/3} + \kappa^{+2} \right] \quad (8.2)$$

where  $\kappa^+ = \kappa\eta$  and  $\alpha_\kappa = 1.5$ .

To obtain the composite spectrum, we first change  $\kappa\eta$  to the  $\kappa L$  variable using the ratio  $L/\eta$ ; i.e.  $\kappa^+ = \kappa\eta = \kappa L \times \eta/L = \bar{\kappa} \times \eta/L$ . Multiplying the low and high wavenumber spectra together and dividing by the common part gives a composite spectrum applicable to all wavenumbers (Gamard and George 1999):

$$E_{composite} = \frac{(u^2 L) \bar{E}(\bar{\kappa}) (\varepsilon \nu^5)^{1/4} E^+(\kappa^+)}{(u^2 L) C_L(\bar{\kappa})^{-5/3}} \quad (8.3)$$

Using the length-scale ratios (obtained previously via the  $k - \varepsilon$  model or the obstacle height) to specify the wavenumber variables, the energy spectra are presented in Figure 8.2

As can be seen from Figure 8.2, there is little evidence of a  $\kappa^{-5.3}$  region for the smallest values of  $R$ . This is highlighted by the lack of a flat region on Figure 8.2(b). Even though the ratio of 1000 ( $Re = 10000$ ) is expected to be *stretching* the validity of the Kolmogorov theories (in that they require *very* high Reynolds numbers to be applicable) and there is some evidence of a flat region, all estimations of the range of length-scales present fall short of this ratio. It is therefore questionable whether such a range exists for the low- $Re$ , bluff geometry flows considered here. The hump at higher  $\kappa$  is due to the Lin/Hill model, which matches the trend found in experiential data. It appears closer to the low wavenumber end because the ratio of scales is small. For high- $Re$  flows a flat region appears betwween the two extremes of wavenumber (see pg. 239 Pope (2004)), however this seperation of scales is reduced as  $Re$  becomes low, as for the current test cases in Figure 8.2. Near walls where  $Re$  falls further, the energy spectrum may even be dominated a  $\kappa^{-1}$  region (William and Tutkun 2009). This indicates that large energy containing scales are interacting directly with the smaller dissipative scales, or that there is no clear distinction between the two. This implies that most scales are affected to some extent by turbulence production and destruction processes. This could explain the consistent performance of the Smagorinsky SGS model when applied to the ribbed channel. In this model, energy is removed at all scales and this simple model becomes more fitting for simple flows. In this respect, perhaps the most important aspect of the SGS model is merely to remove the correct amount of energy from the smallest scales so long as the SGS terms are fairly isotropic.

Referring to homogeneous isotropic turbulence, Hinze (1959) mentions that in the absence of any other effects for the subrange, only  $\varepsilon$  determines the region of energy containing eddies. This raises two important issues. Firstly, the flows studied are far from isotropic in nature, especially near surfaces, of which there are many. Secondly, the main generation of turbulence stems from the large scale

geometry, not from the natural growth of small instabilities as may be found in a developing channel flow. This means that by using common SGS models, we could be applying theory based on simple dynamics to something very different.

In light of the above problems, it may seem improper to make assumptions about the unresolved scales based on simple turbulence theory. Although ILES makes no explicit assumptions, it can be shown that numerical errors have the same form as an SGS model. It is noted by Drikakis et al. (2009) that the form of dissipation is not important for well resolved turbulence so long as there is adequate separation between the start of the inertial subrange and the dissipative scales. When this is not so, it is desirable to provide some dissipative influence on the larger scales as would be found in the energy spectrum. Both LES and ILES will encounter difficulties in this case as the simulation becomes sensitive to the form of the imposed subgrid model. Due to unknown scales and Reynolds number dependencies, a model that may be of future interest is that of Razafindralandy et al. (2007). This SGS model transforms and scales with the flow, preserving symmetries in the NS equations. Therefore the SGS model may adapt in a more realistic way to the resolved scales in these complex flows. One pitfall may be that the model relies on a chosen lengthscale. The choice of lengthscale may not be obvious but it may be that a method could be found so that the correct lengthscale could be generated for different geometries.

### 8.3 Filter choice

The narrow inertial subrange shown in the previous figures make filter choice an important topic. Normally, one would place the filter in the inertial subrange where the dynamics are dominated by convection. When the ratio  $r = \Delta/h$  ( $h$  being grid spacing) is small, numerical errors will have a stronger influence on

the solution. Using a larger filter with  $r = 4 - 6$  it has been found that the solution may become grid independent (Geurts 2005). This increased filter size gives some separation of the numerical and SGS modelling details. Reaching grid independence could be useful for use in industry to monitor changes in the solution upon grid refinement. Using successive grid refinement, the scales of motion could also be estimated and a suitable grid and filter width could be obtained. One of the drawbacks of using a larger filter could be that the filter would be placed nearer the largest scales. Considering there may be a narrow inertial subrange, this could mean that some of the most crucial scales are filtered.

## 8.4 Summary

It has been shown here that there is a high potential for the SGS models employed here to become inapplicable. In some cases, there is a very short inertial subrange meaning that dissipation affects most scales of turbulence. This also means that the correct placement of the filter in the assumed inertial subrange becomes difficult. Filter size and placement could also have a large effect on the interaction of numerical and other modelling errors.

# Chapter 9

## Conclusions and future work

This thesis has focused on the consistent prediction of heat transfer in relation to the types of flows found in and around electronics components and systems. Due to the wide variety of solutions obtained with different RANS models, LES based methods were investigated and compared with each other based on thermal predictive accuracy and computational efficiency. Using the three electronics heat transfer test cases the following conclusions can be drawn.

### 9.1 Conclusions

- The ribbed channel geometry is insensitive to grid resolution and SGS model. Although there were small differences in accuracy, the consistency between models is good.
- The flow around the heated cube (itself in an array of cubes), turned out to be much more challenging. This case showed much greater sensitivity to the grid resolution than the ribbed channel. Some evidence of improvement when using a nonlinear LES model was detected, yet compared to the RANS-

ILES model using second order central differences, the extra computational effort does not seem justifiable. Heat transfer errors ranged from around 10-30%, mostly under-predicting  $Nu$ . Possible other sources of error are the case setup, as the epoxy base boundary condition is not well known.

- The CPU case showed the greatest sensitivity to SGS model. A strong relation between the dissipative elements, turbulence intensity and thermal predictive accuracy was found. The Leray and Alpha LES models showed a marked improvement over the linear models, yet again, the RANS-ILES model using second order central differences performed well, with a relatively small error that under predicted heat transfer.
- The largest scales defined by geometry are the most important to resolve. This gives a top-down flow type where less emphasis may be placed on accurate wall modelling. This would imply the use of low resolution grids may be acceptable, but the potential of a narrow range of scales may make this problematic until further studies have been carried out. One would need reliable *a priori* estimates of the range of scales.
- Higher order convective term treatment did not show any consistent benefit but may be useful in some cases. Alternatively, a larger filter to separate numerical and modelling errors may be used. Use of a fully higher order discretisation may give rise to more accurate heat transfer but this would likely be outweighed by increased computation time.
- For almost any case, grid and SGS model, the heat transfer was predicted to within around 40%. Though this is not particularly accurate, given the uncertainty in problem definition and boundary conditions, variety in modelling methods and flow types, this is promising and more consistent than (U)RANS methods. There may still be significant errors due to problem definition and boundary conditions, yet the RANS-ILES model with second

order central differencing seemed to give reliable results overall.

- Results suggest boundary conditions and grid (indirectly, (I)LES filter width) requirements are areas of importance. The latter requirements could be addressed with better prior knowledge of the scales of motion. However, promising results have been obtained on grids that may be considered to be of low resolution.
- The assumptions of SGS models were brought into question and some effort was made to investigate the existence (or non-existence) of an inertial subrange. Some evidence of such a range was found, although it is probably rather short. This also raises the issue of how large the filter should be in relation to the grid and scales of motion in each system. The good performance of RANS-ILES may be attributable to the fact that no assumption is made about the SGS stresses as is done with an explicit model.
- Use of lower-resolution grids, successive grid refinement and parallel processing combine to bring significant time savings. This should make the use of (I)LES based methods more accessible in the near future for electronics design.

## 9.2 Recommendations for future work

- Further investigation into the structure and *a priori* estimation of scales of motion generated by bluff geometries. This would provide a more solid basis for grid generation and filtering.
- The development of convergence criteria to allow data to be collected as soon as a simulation is mature would be necessary to automate the successive grid refinement strategy to make it viable commercially. Such criteria could have wide spread application and allow more efficient simulations to be performed.



- Investigation of nonlinear models with different filter widths may be beneficial to separate the SGS model from numerical noise. However, bearing in mind the possibility of a narrow inertial range, filter placement and size estimation could be challenging, hence the need for further study of low Reynolds number flows around bluff geometries.
- The SGS model of Razafindralandy et al. (2007) could be explored to see if an SGS model that scales with local flow features is useful.

# Bibliography

- Acharya, S., Dutta, S., Myrum, T. A., and Baker, R. S. (1993). Periodically developed flow and heat transfer in a ribbed duct. *International Journal of Heat and Mass Transfer*, 36(8):2069–2082.
- Ahmed, M. H. and Barber, T. J. (2005). Fast Fourier transform convergence criterion for numerical simulations of periodic fluid flows. *AIAA Journal*, 43:1042–1052.
- Azar, K. (2000). The history of power dissipation. Technical report, Electronics Cooling Magazine.
- Baelmans, M., Meyers, J., and Nevelsteen, K. (2003). Flow modelling in air-cooled electronic enclosures. In *19th IEEE SEMI-THERM Symposium*.
- Bosch, G. and Rodi, W. (1998). Simulation of vortex shedding past a square cylinder with different turbulence models. *International Journal for Numerical Methods in Fluids*, 28:601–616.
- Brandvik, T. and Pullan, G. (2008). Acceleration of a 3D Euler solver using commodity graphics hardware. In *46th AIAA Aerospace Sciences Meeting and Exhibit*.
- Bredberg, J. and Davidson, L. (1999). Prediction of flow and heat transfer in a stationary two-dimensional rib roughened passage using low-Re turbulent models. In *Third European Conf. on Turbomachinery, IMech*.
- Breuer, M., Jaffrezic, B., Šarić, S., Jakirlić, S., Deng, G., Chikhaoui, O., Fröhlich, J., von Terzi, D., Manhart, M., and Peller, N. (2005). Issues in hybrid LES-RANS and coarse grid LES of separated flows. In *Euromech colloquium 469*.
- Castro, I. P., Cheng, H., and Reynolds, R. (2006). Turbulence over urban-type roughness: deductions from wind tunnel measurements. *Boundary-Layer Meteorology*, 118:109–131.
- Chow, F. K. and Moin, P. (2003). A further study of numerical errors in large-eddy simulations. *Journal of Computational Physics*, 184:366–380.
- Chung, Y. M. and Tucker, P. G. (2003). Accuracy of higher-order finite difference schemes on nonuniform grids. *AIAA journal*, 41(8):1609–1611.

- Chung, Y. M. and Tucker, P. G. (2004a). Assessment of periodic flow assumption for unsteady heat transfer in grooved channels. *Journal of Heat Transfer*, 126:1044–1047.
- Chung, Y. M. and Tucker, P. G. (2004b). Numerical studies of heat transfer enhancements in laminar separated flows. *International Journal of Heat and Fluid Flow*, 25:22–31.
- Chung, Y. M., Tucker, P. G., and Roychowdhury, D. G. (2003). Unsteady laminar flow and convective heat transfer in a sharp bend. *International Journal of Heat and Fluid Flow*, 24:67–76.
- Courant, R., Isaacson, E., and Rees, M. (1952). On the solution of non-linear hyperbolic differential equations by finite differences. *Comm. Pure Appl. Math.*, 5:243.
- Craft, T. J., Launder, B. E., and Suga, K. (1996). Development and application of a cubic eddy-viscosity model of turbulence. *International Journal of Heat and Fluid Flow*, 17:108–115.
- Cushing, M. J., Mortin, D. E., Stadterman, T. J., and Malhotra, A. (1993). Comparison of electronics-reliability assessment approaches. *IEEE Transactions on Reliability*, 42(4):542–546.
- Davidson, L. and Peng, S. H. (2003). Hybrid les-rans modelling: a one-equation sgs model combined with a  $k - \omega$  model for predicting recirculating flows. *International Journal for Numerical Methods in Fluids*, 43(9):1003–1018.
- Dhinsa, K., Bailey, C., and Pericleous, K. (2003). Accuracy of turbulence models and CFD for thermal characterisation of electronic systems. *Electronics Packaging Technology Conference*, pages 507–512.
- Dhinsa, K., Bailey, C., and Pericleous, K. (2005). Turbulence modelling for electronic cooling: A review. In *International Symposium on Electronics Materials and Packaging*, pages 275–281.
- Dhinsa, K. K., Bailey, C. J., and Pericleous, K. A. (2004). Turbulence modelling and its impact on CFD predictions for cooling of electronic components. In *Inter Society Conference on Thermal Phenomena*, pages 487–494.
- Domaradzki, J. A., Liu, W., and Brachet, M. E. (1993). An analysis of subgrid-scale interactions in numerically simulated isotropic turbulence. *Phys. Fluids*, 41:453–480.
- Driest, E. R. (1956). On turbulent flow near a wall. *J. Aerospace Sci.*, 23:1007–1011.
- Drikakis, D., Hahn, M., Mosedale, A., and Thornber, B. (2009). Large eddy simulation using high resolution and high order methods. *Phil. Trans. R. Soc. A*, 367:2985–2997.

- Ferziger, J. H. (1998). *Numerical Methods for Engineering Application*. John Wiley & Sons, Inc., 2<sup>nd</sup> edition.
- Ferziger, J. H. and Perić, M. (2002). *Computational Methods for Fluid Dynamics*. Springer, 3<sup>rd</sup> edition.
- Furukawa, T. and Yang, W. (2003). Thermal-fluid flow in parallel boards with heat generating blocks. *International Journal of Heat and Mass Transfer*, 46:5005–5015.
- Gamard, S. and George, W. (1999). Reynolds number dependence of energy spectra in the overlap region of isotropic turbulence. *Flow, Turbulence and Combustion*, 63:443–477.
- Gatski, T. B. and Speziale, C. G. (1993). On explicit algebraic stress models for complex turbulent flows. *J. Fluid Mech.*, 254:59–78.
- George, W. K. and Tutkun, M. (2009). Mind the gap: A guideline for LES. *Phil. Trans. R. Soc. A*, 367:2839–2847.
- Geurts, B. J. (2005). Leray and LANS- $\alpha$  modelling of turbulent mixing. *Journal of Turbulence*, 00(00):1–42.
- Geurts, B. J. and Holm, D. D. (2003). Regularization modelling for large-eddy simulation. *Physics of Fluids*, 15(1):13–16.
- Ghosal, S. (1999). Mathematical and physical constraints on large-eddy simulation of turbulence. *AIAA Journal*, 37:425–433.
- Gullbrand, J. (2002). Grid-independent large-eddy simulation in turbulent channel flow using three-dimensional explicit filtering. Technical report, Center for Turbulence Research.
- Gupta, A. (2002). Modeling large-scale electronic systems using computational fluid dynamics through a "zoom-in" approach. In *Inter Society Conference on Thermal Phenomena*.
- Hagen, T. R., Lie, K., and Natvig, J. R. (2006). Solving the Euler equations on graphics processing units. In *International Conference on Computational Science*.
- Harris, M. J. (2004). *GPU Gems*, chapter Fast Fluid Dynamics Simulation on the GPU, pages 637–665. Addison-Wesley.
- Hellsten, A. and Rautahaimo, P., editors (1999). *Proceedings of the 8th ERCOFTAC/IAHR/COST Workshop on Refined Turbulence Modelling*.
- Hemida, H. and Krajnović, S. (2007). LES study of the influence of the vortex generators on cooling of surface-mounted cubes. In *Thermal Issues in Emerging Technologies, THETA 1*.

- Hinze, J. O. (1959). *Turbulence: An introduction to Its Mechanism and Theory*. McGraw-Hill Series in Mechanical Engineering. McGraw-Hill Book Company, Inc.
- Hutton, A. (2009). The emerging role of large eddy simulation in industrial practice: challenges and opportunities. *Phil. Trans. R. Soc. A*, 367:2819–2826.
- Iacovides, H. and Raisee, M. (1999). Recent progress in the computation of flow and heat transfer in internal cooling passages of turbine blades. *International Journal of Heat and Fluid Flow*, 20:320–328.
- Joshi, Y., Baelmans, M., Copeland, D., Lasance, C. J. M., Parry, J., and Rantala, J. (2001). Challenges in thermal modeling of electronics at the system level: Summary of panel held at the thermic 2000. *IEEE transactions on components and packaging technologies*, 24(4):611–613.
- Kolmogorov, A. N. (1941). The local structure of turbulence in incompressible viscous fluid for very large reynolds numbers. *Dokl. Akad. Nauk SSSR*, 30:299–303.
- Kolmogorov, A. N. (1991). The local structure of turbulence in incompressible viscous fluid for very large reynolds numbers. *Proc. R. Soc. London Ser. A*, 434:9–13.
- Kosović, B. (1997). Subgrid-scale modelling for the large-eddy simulation of high-reynolds-number boundary layers. *J. Fluid Mech.*, 336:151–182.
- Kravchenko, A. G. and Moin, P. (1997). On the effect of numerical errors in large eddy simulations of turbulent flows. *Journal of Computational Physics*, 131:310–322.
- Lasance, C. J. M. (2001). The conceivable accuracy of experimental and numerical thermal analysis of electronic systems. *Seventeenth IEEE SEMI-THERM Symposium*.
- Lasance, C. J. M. (2005). CFD simulations in electronic systems: A lot of pitfalls and a few remedies. *Electronics Cooling Magazine*.
- Lasance, C. J. M. (2007). Accuracy comparison of a standard CFD code for the thermal analysis of non-simple geometries with baseline experiments. In *23rd IEEE SEMI-THERM Symposium*.
- Leonard (1974). Energy cascade in large-eddy simulation of turbulent fluid flows. *Adv. in Geophys*, 18:237–248.
- Leonard, B. P. (1994). Comparison of truncation error of finite-difference and finite-volume formulations of convection terms. *Appl. Math. Modelling*, 18:46–50.

- Leschziner, M., Li, N., and Tessicini, F. (2009). Simulating flow separation from continuous surfaces: Routes to overcoming the Reynolds number barrier. *Phil. Trans. R. Soc. A*, 367:2885–2903.
- Lilly, D. K. (1967). The representation of small scale turbulence in numerical simulation experiments. In Goldstine, H. H., editor, *IBM Sci. Computing Symp. On Environmental Sciences*, pages 195–210.
- Liu, Y. (2004). *Numerical simulations of unsteady complex geometry flows*. PhD thesis, School of Engineering, University of Wales, Swansea.
- Liu, Y., Tucker, P. G., and Kerr, R. M. (2007). Linear and nonlinear model large-eddy simulations of a plane jet. *Computers & Fluids*, 37:439–449.
- Liu, Y., Tucker, P. G., and Lo Iacono, G. (2006). Comparison of zonal RANS and LES for a non-isothermal ribbed channel flow. *International Journal of Heat and Fluid Flow*, 27:391–401.
- Mathey, F., Fröhlich, J., and Rodi, W. (1999). Description of numerical methodology for test case 6.2. In *Proceedings, 8th ERCOFTAC/IAHR/COST Workshop on Refined Turbulence Modelling. Report 127, June 17-18. Helsinki University of Technology, Helsinki, Finland*.
- Meinders, E., Hanjalić, K., and Martinuzzi, R. (1999). Experimental study of the local convection heat transfer from a wall-mounted cube in turbulent channel flow. *Journal of Heat Transfer-Transactions of the ASME*, 121(3):564–573.
- Meinders, E. R. and Hanjalić, K. (1999). Vortex structure and heat transfer in turbulent flow over a wall-mounted matrix of cubes. *International Journal of Heat and Fluid Flow*, 20:255–267.
- Meinders, E. R., van der Meer, T. H., and Lasance, C. J. M. (1997). Application of infrared thermography to the evaluation of local convective heat transfer on arrays of cubical protrusions. *Int. J. Heat and Fluid Flow*, 18(1):152–159.
- Meyers, J., Geurts, B. J., and Sagaut, P. (2007). A computational error-assessment of central finite-volume discretizations in large-eddy simulation using a smagorinsky model. *Journal of Computational Physics*, 227:156–172.
- Nakayama, A. and Vengadesan, S. N. (2002). On the influence of numerical schemes and subgrid-stress models on large eddy simulation of turbulent flow past a square cylinder. *International Journal for Numerical Methods in Fluids*, 38:227–253.
- Ničeno, A. D. T., Dronkers, K., and Hanjalić, K. (2002). Turbulent heat transfer from a multi-layered wall-mounted cube matrix: a large eddy simulation. *International Journal of Heat and Fluid Flow*, 23:173–185.

- Ničeno, B. and Hanjalić, K. (1999). Description of numerical methodology for test case 6.2. In *Proceedings, 8th ERCOFTAC/IAHR/COST Workshop on Refined Turbulence Modelling. Report 127, June 17-18. Helsinki University of Technology, Helsinki, Finland.*
- Panigrahi, P. K. (2001). Fundamentally excited flow past a surface-mounted rib. Part 1: Turbulent structure characterisation. *Sādanā*, 26:387–412.
- Parry, J. D., Rantala, J., and Lasance, C. J. M. (2002). Enhanced electronic system reliability – challenges for temperature prediction. *IEEE Transactions on Components and Packaging Technologies*, 25(4):533–538.
- Patankar, S. V. (1980). *Numerical Heat Transfer and Fluid Flow*. Series in computational methods in mechanics and thermal sciences. Taylor & Francis.
- Patankar, S. V. and Spalding, D. B. (1972). A calculation procedure for heat, mass and momentum transfer in three-dimensional parabolic flows. *Int. J. Heat Mass Transfer*, 15:1787.
- Pecht, M. (1996). Why the traditional reliability prediction models do not work - is there an alternative? Technical report, Electronics Cooling Magazine.
- Piomelli, U., Yunfang, Y., and Adrian, R. J. (1996). Subgrid-scale energy transfer and near-wall turbulence structure. *Phys. Fluids*, 8:215–224.
- Pope, S. B. (2000). *Turbulent Flows*. Cambridge University Press.
- Pope, S. B. (2004). Ten questions concerning the large-eddy simulation of turbulent flows. *New Journal of Physics*, 6(35).
- Rautaheimo, P. and Siikonen, T. (1999). Description of numerical methodology for test case 6.2. In *Proceedings, 8th ERCOFTAC/IAHR/COST Workshop on Refined Turbulence Modelling. Report 127, June 17-18. Helsinki University of Technology, Helsinki, Finland.*
- Razafindralandy, D., Hamdouni, A., and Béghein, C. (2007). A class of subgrid-scale models preserving the symmetry group of Navier-Stokes equations. *Communications in Nonlinear Science and Numerical Simulation*, 12:243–253.
- Reynell, M. (1990). Advanced thermal analysis of packaged electronic systems using computational fluid dynamics techniques. *Computer-Aided Engineering Journal*, pages 104–106.
- Rhie, C. M. and Chow, W. L. (1983). A numerical study of the turbulent flow past an isolated airfoil with trailing edge separation. *AIAA Journal*, 21:1525–1532.
- Rodgers, P. and Evely, V. (2004). CFD prediction of electronic component operational temperature on PCBs. *Electronics Cooling Magazine*.
- Roknaldin, F. (2004). Board level thermal analysis via large eddy simulation (LES) tool. In *Inter Society Conference on Thermal Phenomena*.

- Runchal, A. K. (1987). CONDIF: a modified central-difference scheme for convective flows. *Int. J. Numer. Meth. in Engrg.*, 24:1593–1608.
- Sagaut, P. (2006). *Large Eddy Simulation for Incompressible Flows: An Introduction*. Scientific Computation. Springer, 3<sup>rd</sup> edition.
- Schmidt, S. and Thiele, F. (2002). Comparison of numerical methods applied to the flow over wall-mounted cubes. *International Journal of Heat and Fluid Flow*, 23:330–339.
- Shur, M., Spalart, P. R., Strelets, M., and Travin, A. (1999). Detached-Eddy Simulation of an aerofoil at high angle of attack. In *Proceedings of the Fourth International Symposium on Engineering Turbulence Modelling and Measurements*, pages 669–678.
- Shur, M. L., Spalart, P. R., Strelets, M. K., and Travin, A. K. (2003). Towards the prediction of noise from jet engines. *International Journal of Heat and Fluid Flow*, 24:551–561.
- Smagorinsky, J. (1963). General circulation experiments with the primitive equations. I. The basic experiment. *Monthly Weather Review*, 91:99–165.
- Spalart, P. R. (2000). Strategies for turbulence modelling and simulations. *International Journal of Heat and Fluid Flow*, 21:252–263.
- Spalart, P. R., Jou, W., Strelets, M., and Allmaras, S. R. (1997). Comments on the feasibility of LES for wings, and on a hybrid RANS/LES approach. *First AFOSR International Conference on DNS/LES in Advances in DNS/LES*, pages 137–147.
- Spalding, D. B. (1972). A novel finite-difference formulation for differential expressions involving both first and second derivatives. *Int. J. Num. Methods Eng.*, 4:551.
- Speziale, C. G. (1987). On non-linear  $k-l$  and  $k-\varepsilon$  models of turbulence. *Journal of Fluid Mechanics*, 178:459–475.
- Spiegel, M. R. (1959). *Vector Analysis and an introduction to tensor analysis*. McGraw-Hill.
- Squires, K. D., Forsythe, J. R., and Spalart, P. R. (2005). Detached-eddy simulation of the separated flow over a rounded-corner square. *Journal of Fluids Engineering*, 127:959–966.
- Tafti, D. K. (2005). Evaluating the role of subgrid stress modeling in a ribbed duct for the internal cooling of turbine blades. *International Journal of Heat and Fluid Flow*, 26:92–104.
- Tucker, P. (1997). CFD applied to electronic systems: A review. *IEEE Transactions on Components, Packaging, and Manufacturing Technology-Part A*, 20(4).



- Tucker, P. G. (2001). *Computation of Unsteady Internal Flows*. Kluwer Academic Publishers.
- Tucker, P. G. (2006). Turbulence modelling of problem aerospace flows. *International Journal For Numerical Methods In Fluids*, 51:261–283.
- Tucker, P. G. and Davidson, L. (2004). Zonal k-l based large eddy simulations. *Computers and Fluids*, 33:267–287.
- Tucker, P. G. and Keogh, P. S. (1996). On the dynamic thermal state in a hydrodynamic bearing with a whirling journal using CFD techniques. *Journal of Tribology*, 118(2):356–363.
- Tucker, P. G. and Liu, Y. (2005a). Contrasting a novel temporally oriented Hamilton-Jacobi-equation-based ILES method with other approaches for a complex geometry flow. *International Journal for Numerical Methods in Fluids*, 48:1241–1257.
- Tucker, P. G. and Liu, Y. (2005b). Contrasting CFD for electronic systems modeling with that for aerospace. In *Int. Conf. on Thermal, Mechanical and Multiphysics Simulation and Experiments in Micro-Electronics and Micro-Systems, EuroSimE*.
- Tyacke, J., Tucker, P. G., and Nithiarasu, P. (2008a). Unsteady CFD modelling of turbulent flows for electronics. In *2nd Electronics System Integration Technology Conference (ESTC)*, pages 1157–1163.
- Tyacke, J. C. and Tucker, P. G. (2007). Unsteady CFD modelling for electronics cooling. In *International Conference on Thermal, Mechanical, and Multi-Physics Simulation and Experiments in Micro-Electronics and Micro-Systems (EUROSIME)*, pages 760–766.
- Tyacke, J. C., Tucker, P. G., and Nithiarasu, P. (2008b). Strategies for modelling turbulent flows in electronics. In *Semiconductor Thermal Measurement and Management Symposium (SEMI-THERM)*, pages 39–46.
- van der Velde, R. M., Verstappen, R. W. C. P., and Veldman, A. E. P. (1999). Description of numerical methodology for test case 6.2. In *Proceedings, 8th ERCOFTAC/IAHR/COST Workshop on Refined Turbulence Modelling. Report 127, June 17-18. Helsinki University of Technology, Helsinki, Finland*.
- Vengadesan, S. and Nakayama, A. (2005). Evaluation of LES models for flow over bluff body from engineering application perspective. *Sādhanā*, 30:11–20.
- Versteeg, H. K. and Malalasekera, W. (1995). *An introduction to Computational Fluid Dynamics The Finite Volume Method*. Pearson Education Ltd.
- Visbal, M. R. and Gaitonde, D. V. (1999). High-order-accurate methods for complex unsteady subsonic flows. *AIAA Journal*, 37(10):1231–1239.

- Viswanathan, A. K. and Tafti, D. K. (2005). Detached Eddy Simulation of turbulent flow and heat transfer in a ribbed duct. *J. Fluids Eng.*, 127:888–896.
- Wienken, W., Stiller, J., and Keller, A. (2006). A method to predict cavitation inception using large-eddy simulation and its application to the flow past a square cylinder. *J. Fluids Eng.*, 128:316–325.
- William, K. G. and Tutkun, M. (2009). The mesolayer and reynolds number dependencies of boundary layer turbulence.
- Wolfshtein, M. (1969). The velocity and temperature distribution in one-dimensional flow with turbulence augmentation and pressure gradient. *International Journal of Heat and Mass Transfer*, 12:301–318.
- Xie, Z. and Castro, I. P. (2006). LES and RANS for turbulent flow over arrays of wall-mounted obstacles. *Flow, Turbulence and Combustion*, 76(3):291–312.
- Yoshizawa, A. (1993). Bridging between eddy-viscosity-type and second-order models using a two-scale DIA. *In: Proceedings of the 9th International Symposium on Turbulent Shear Flow, Kyoto*, 23.1.1-6.
- Zhong, B. and Tucker, P. G. (2004). k-l based hybrid LES/RANS approach and its application to heat transfer simulation. *International Journal for Numerical Methods in Fluids*, 46:983–1005.

# Appendix A

## Full results

### A.1 Ribbed channel plots

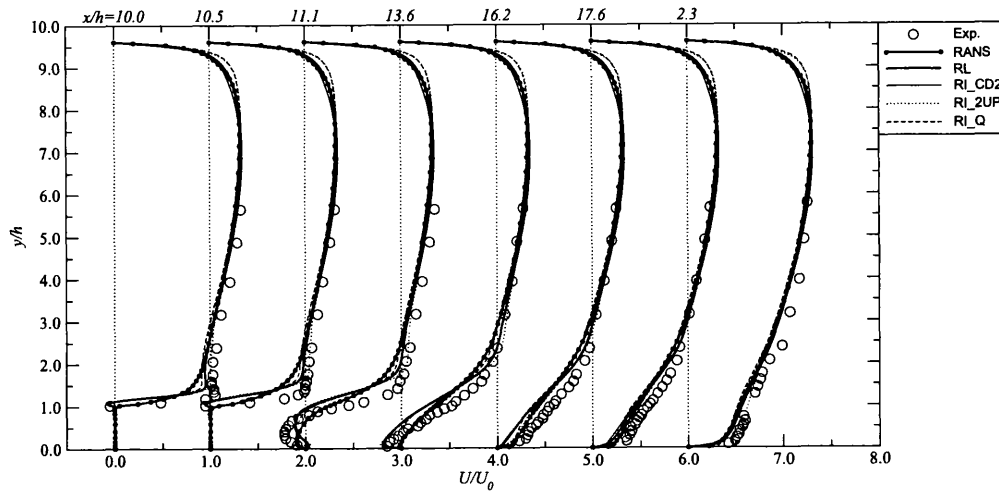


Figure A.1: Mean  $U$  velocity profiles at various  $x/h$ -locations ( $121 \times 112 \times 67$ ).

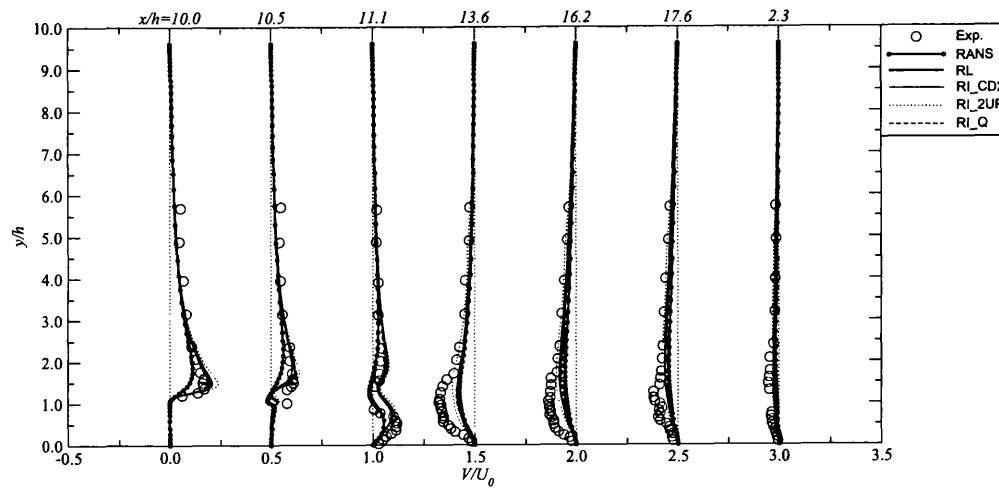


Figure A.2: Mean  $V$  velocity profiles at various  $x/h$ -locations ( $121 \times 112 \times 67$ ).

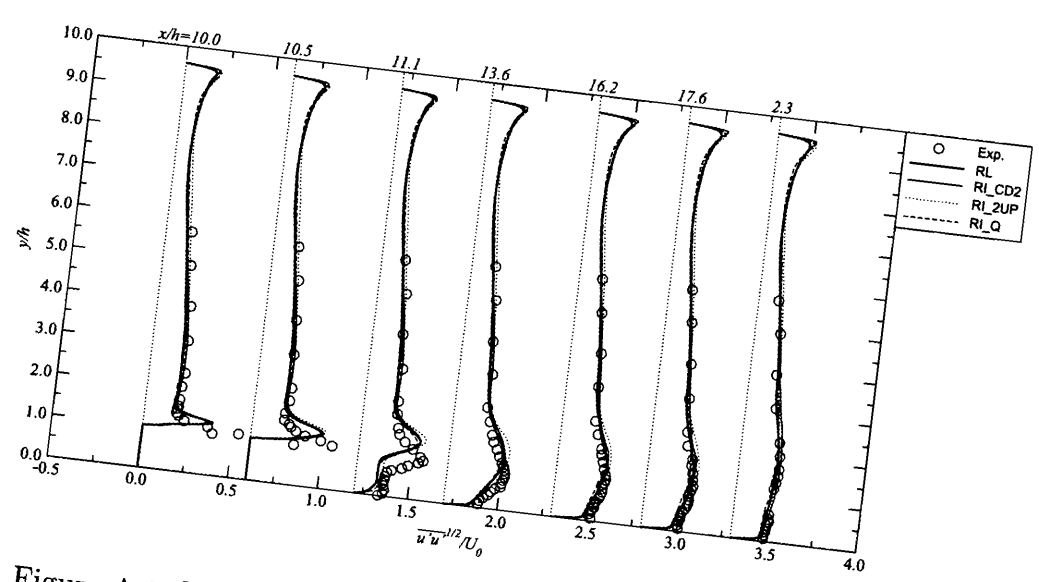


Figure A.3:  $\overline{u'u'}$  profiles at various  $x/h$ -locations ( $121 \times 112 \times 67$ ).

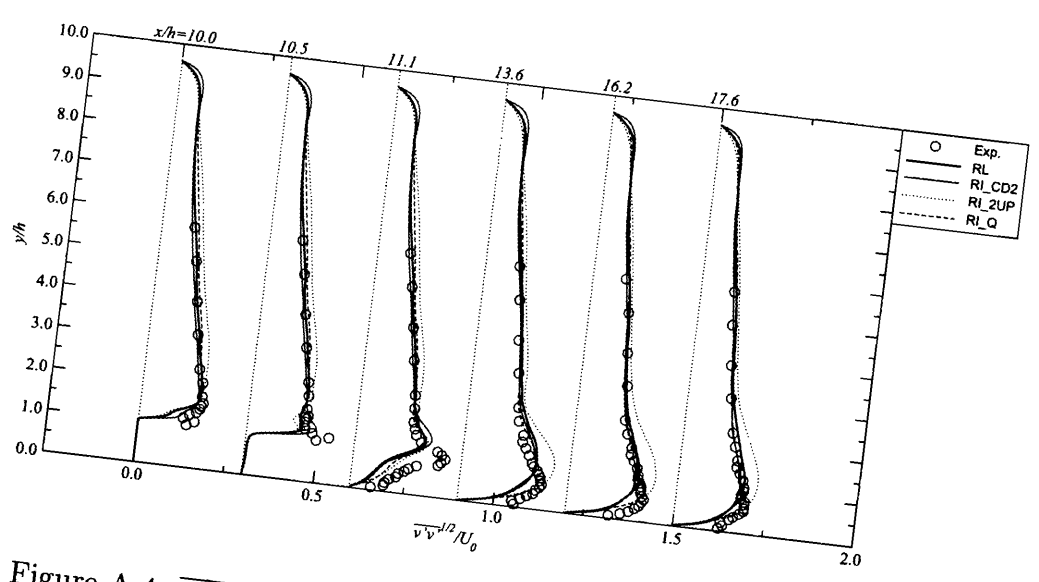


Figure A.4:  $\overline{v'v'}$  profiles at various  $x/h$ -locations ( $121 \times 112 \times 67$ ).

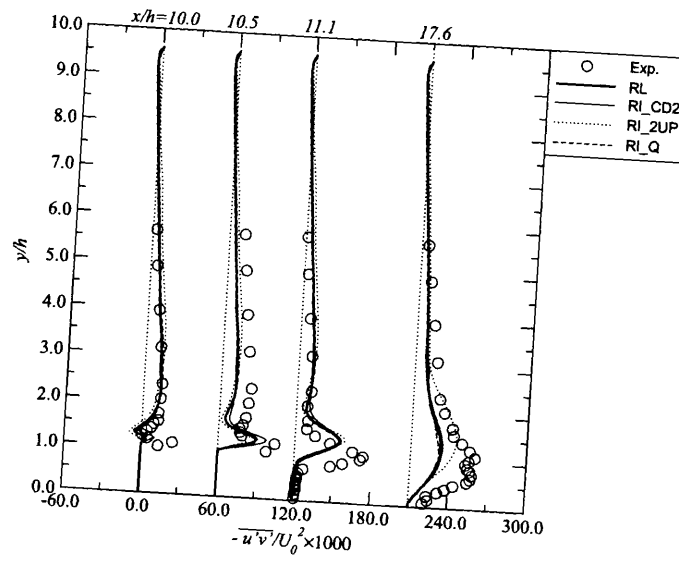


Figure A.5:  $\overline{u'v'}$  profiles at various  $x/h$ -locations ( $121 \times 112 \times 67$ ).

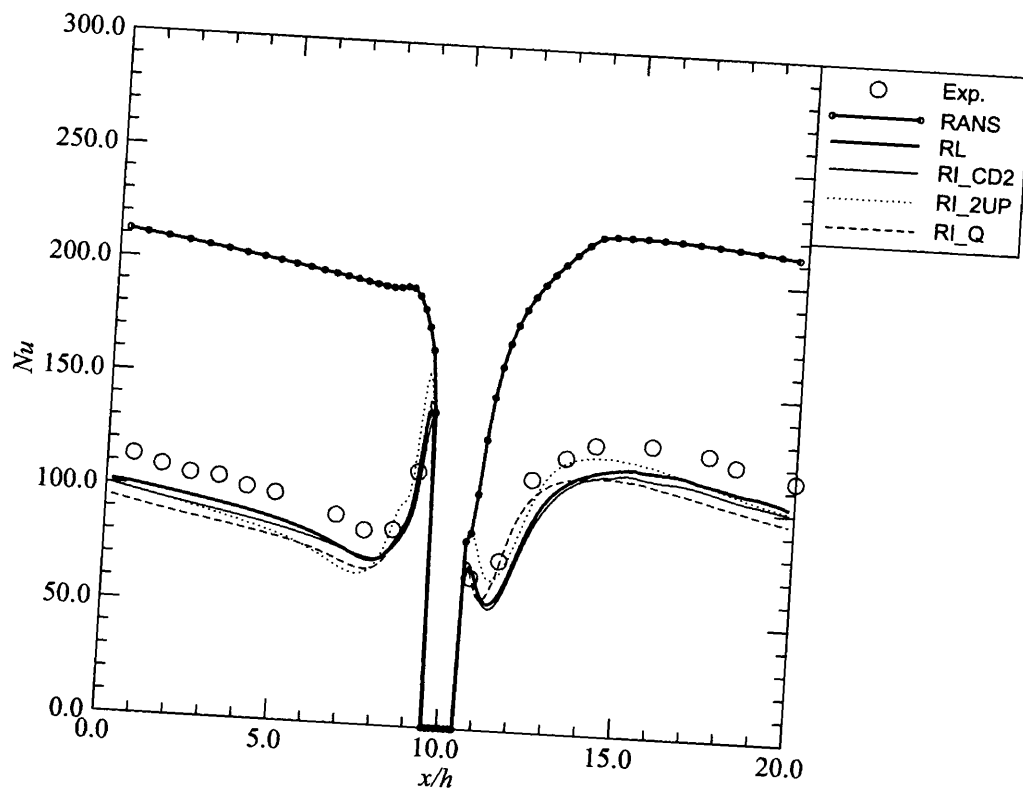


Figure A.6:  $Nu$  profile along channel ( $121 \times 112 \times 67$ ).

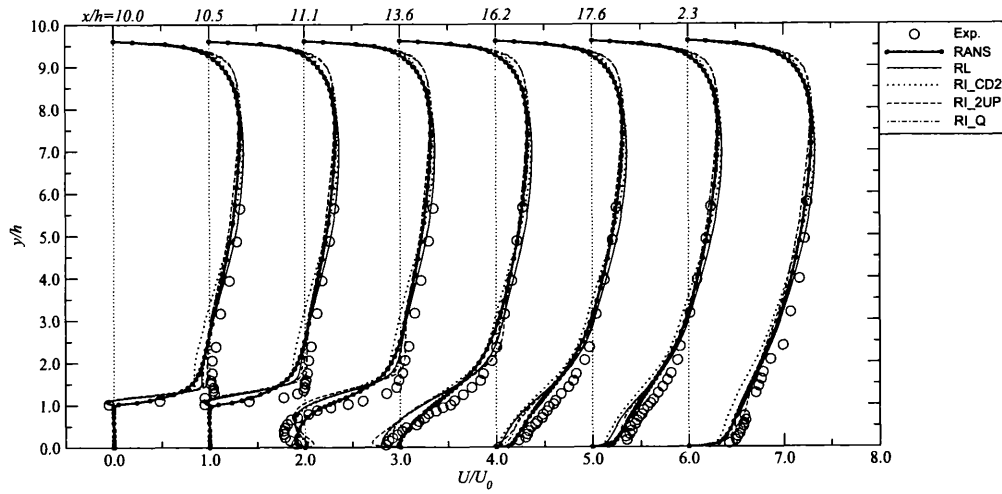


Figure A.7: Mean  $U$  velocity profiles at various  $x/h$ -locations ( $121 \times 112 \times 33$ ).

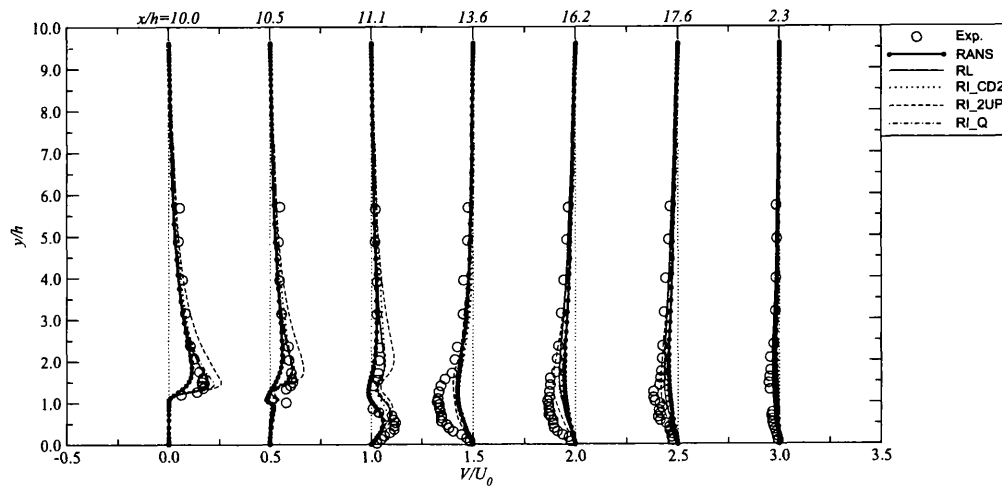


Figure A.8: Mean  $V$  velocity profiles at various  $x/h$ -locations ( $121 \times 112 \times 33$ ).

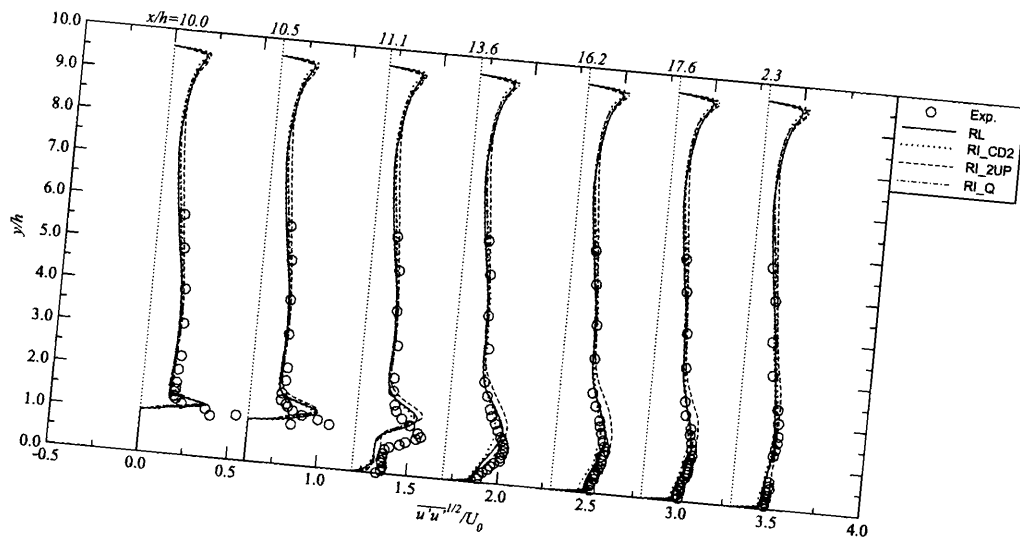


Figure A.9:  $\overline{u'u'}$  profiles at various  $x/h$ -locations ( $121 \times 112 \times 33$ ).

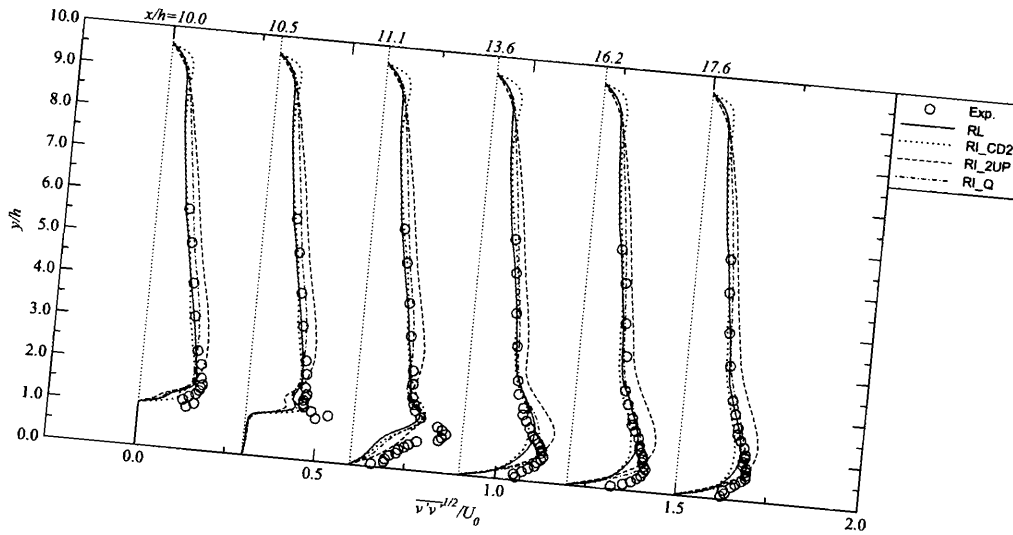


Figure A.10:  $\overline{v'v'}$  profiles at various  $x/h$ -locations ( $121 \times 112 \times 33$ ).



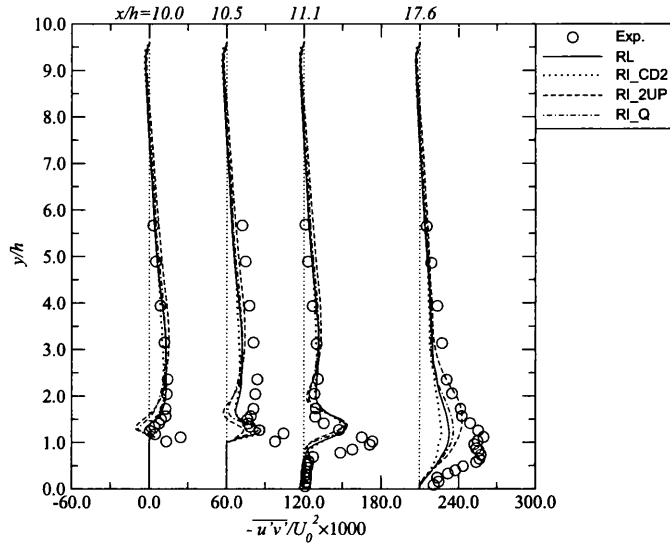


Figure A.11:  $\overline{u'v'}$  profiles at various  $x/h$ -locations ( $121 \times 112 \times 33$ ).

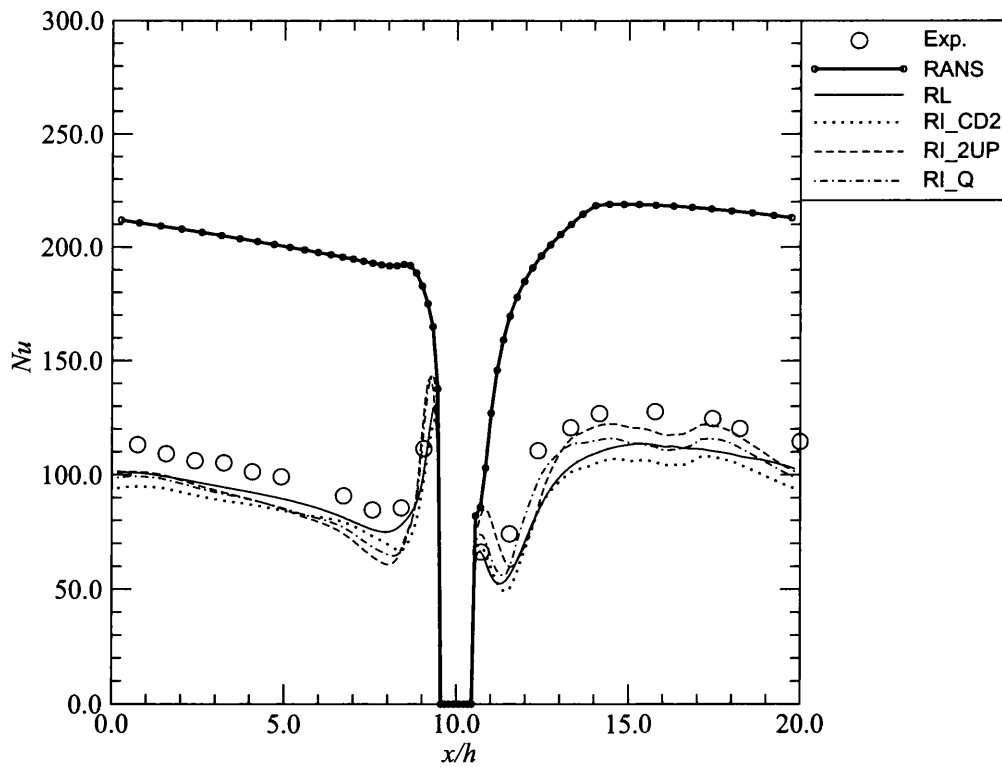


Figure A.12:  $Nu$  profile along channel ( $121 \times 112 \times 33$ ).

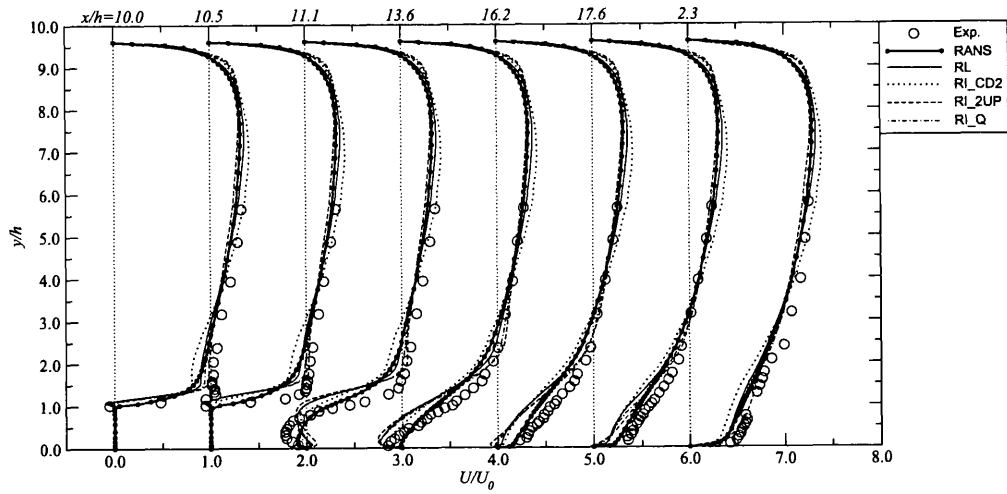


Figure A.13: Mean  $U$  velocity profiles at various  $x/h$ -locations ( $62 \times 57 \times 17$ ).

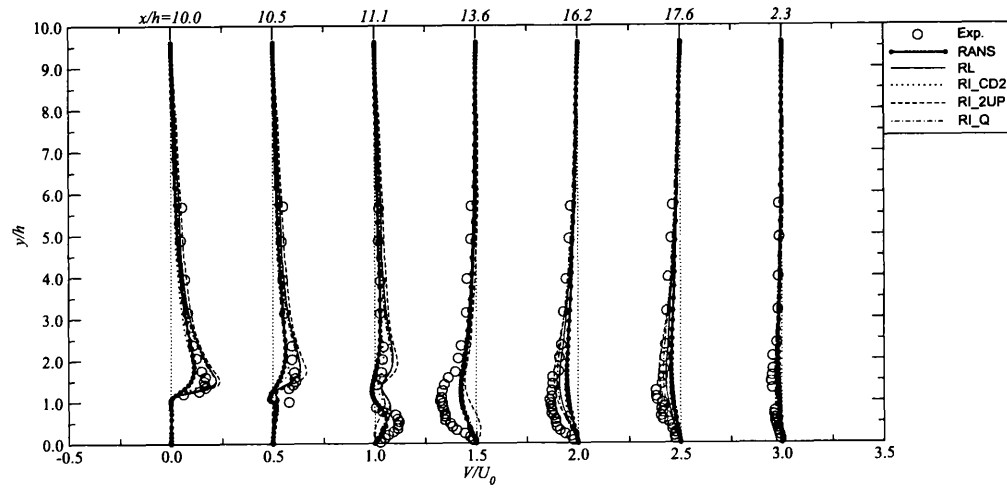


Figure A.14: Mean  $V$  velocity profiles at various  $x/h$ -locations ( $62 \times 57 \times 17$ ).

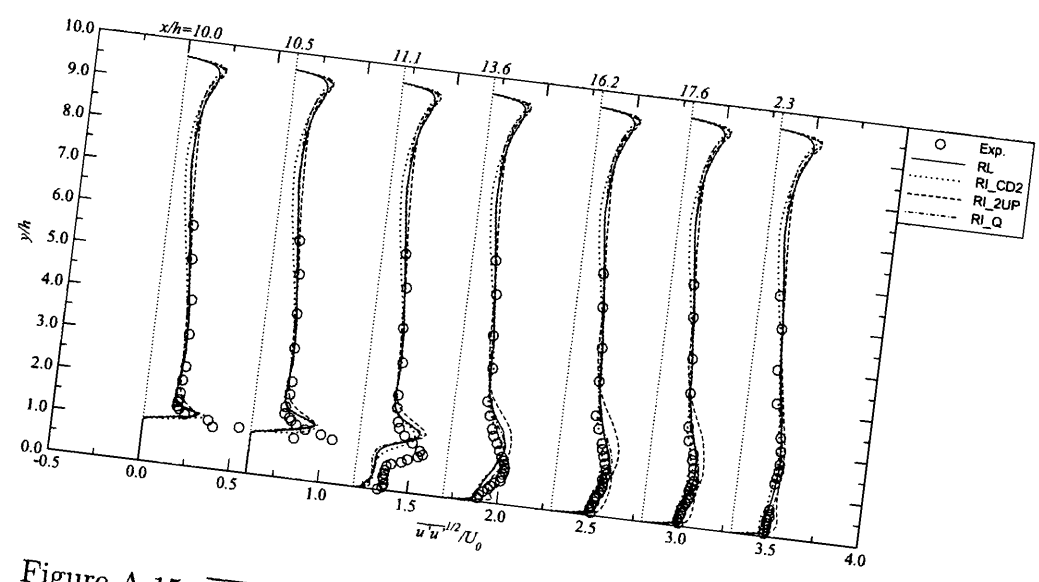


Figure A.15:  $\overline{u'u'}$  profiles at various  $x/h$ -locations ( $62 \times 57 \times 17$ ).

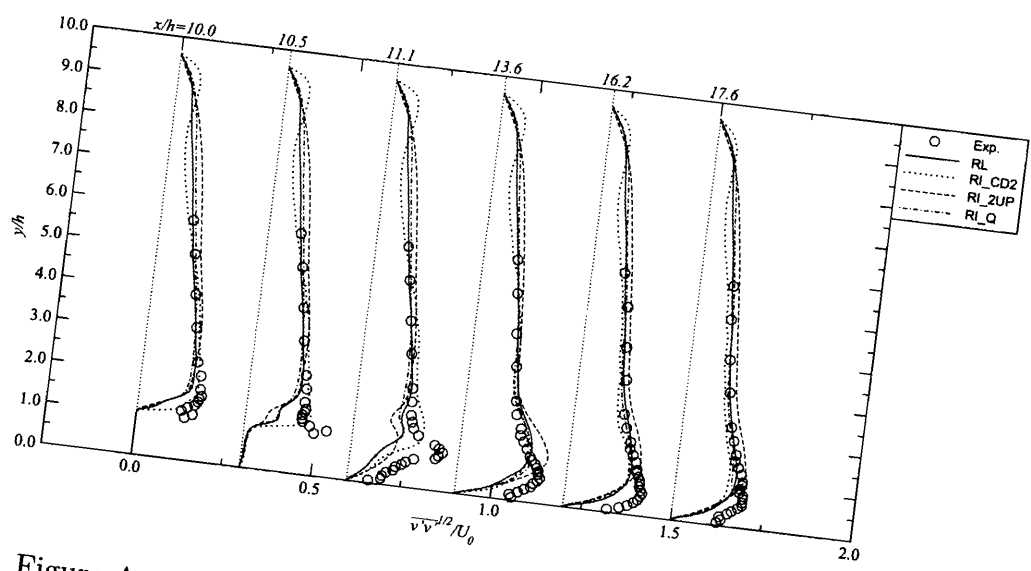


Figure A.16:  $\overline{v'v'}$  profiles at various  $x/h$ -locations ( $62 \times 57 \times 17$ ).

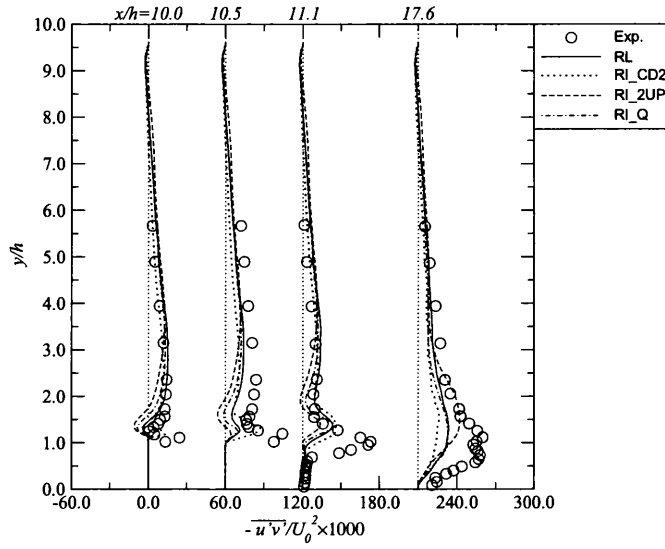


Figure A.17:  $\overline{u'v'}$  profiles at various  $x/h$ -locations ( $62 \times 57 \times 17$ ).

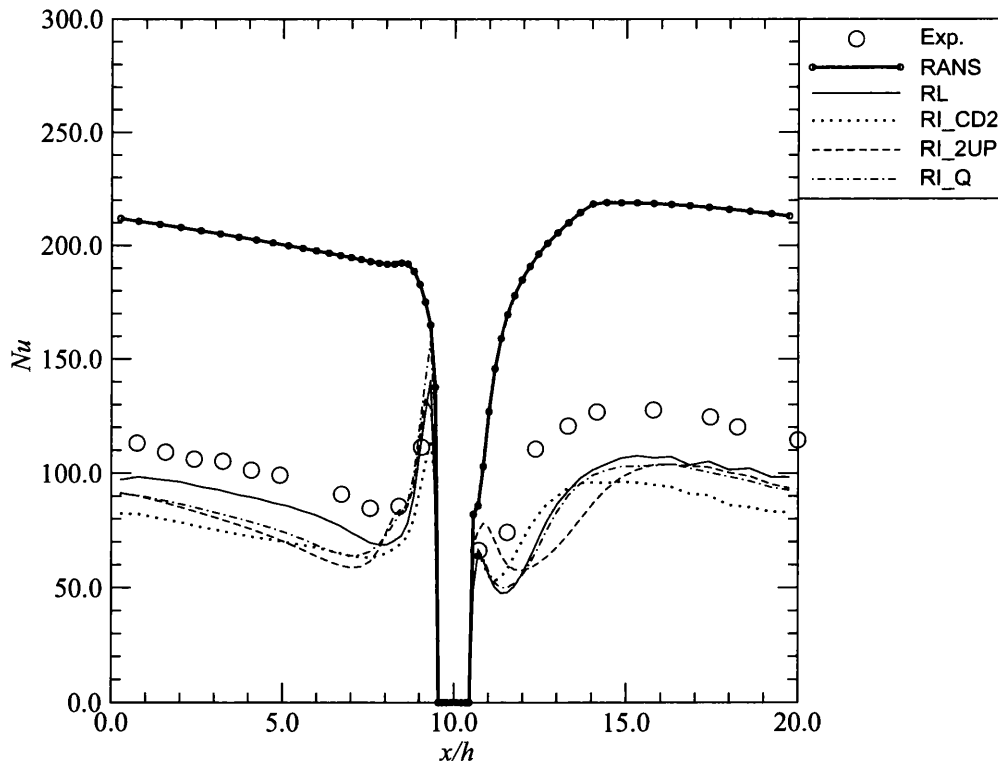


Figure A.18:  $Nu$  profile along channel ( $62 \times 57 \times 17$ ).

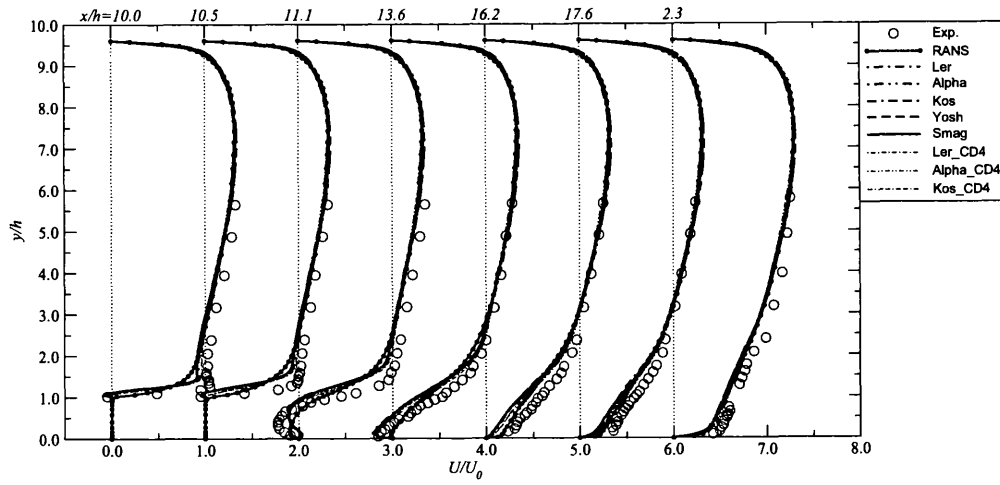


Figure A.19: Mean  $U$  velocity profiles at various  $x/h$ -locations ( $121 \times 112 \times 67$ ).

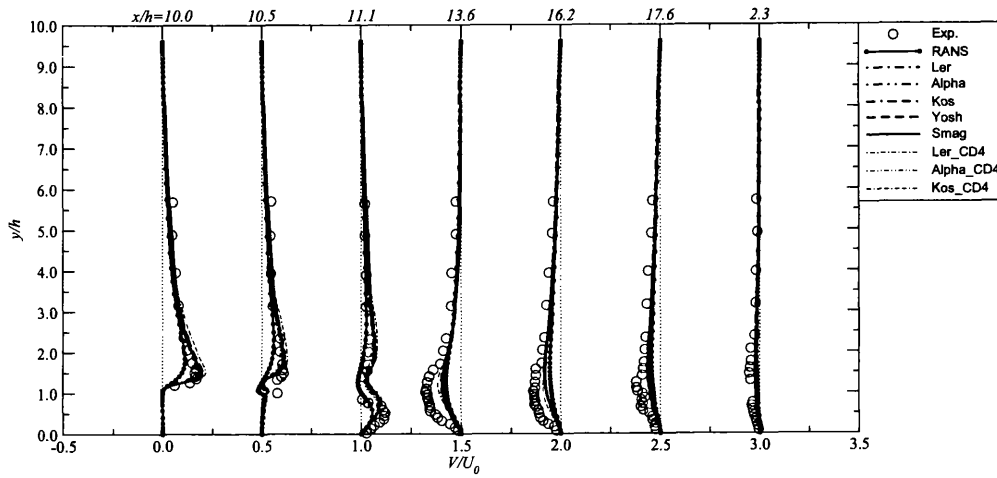


Figure A.20: Mean  $V$  velocity profiles at various  $x/h$ -locations ( $121 \times 112 \times 67$ ).

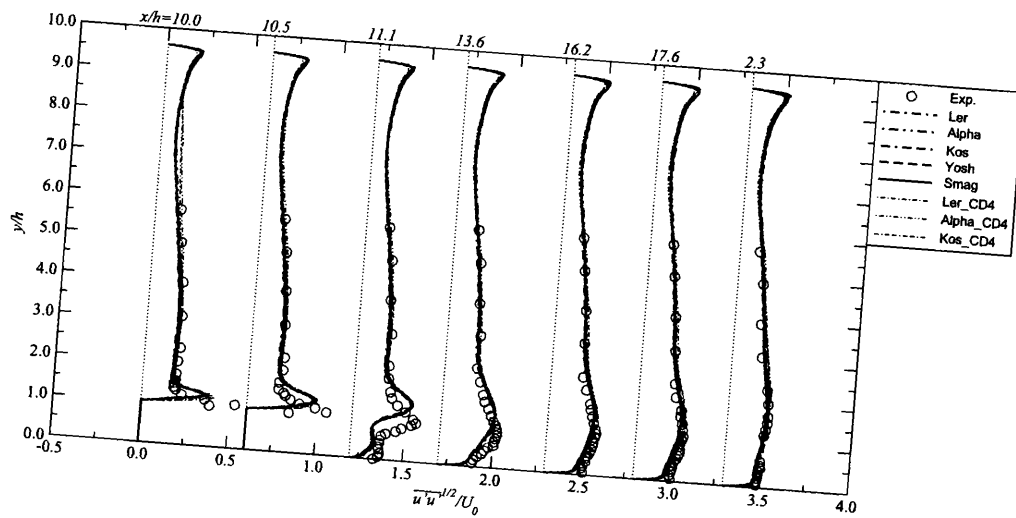


Figure A.21:  $\overline{u'u'}$  profiles at various  $x/h$ -locations ( $121 \times 112 \times 67$ ).

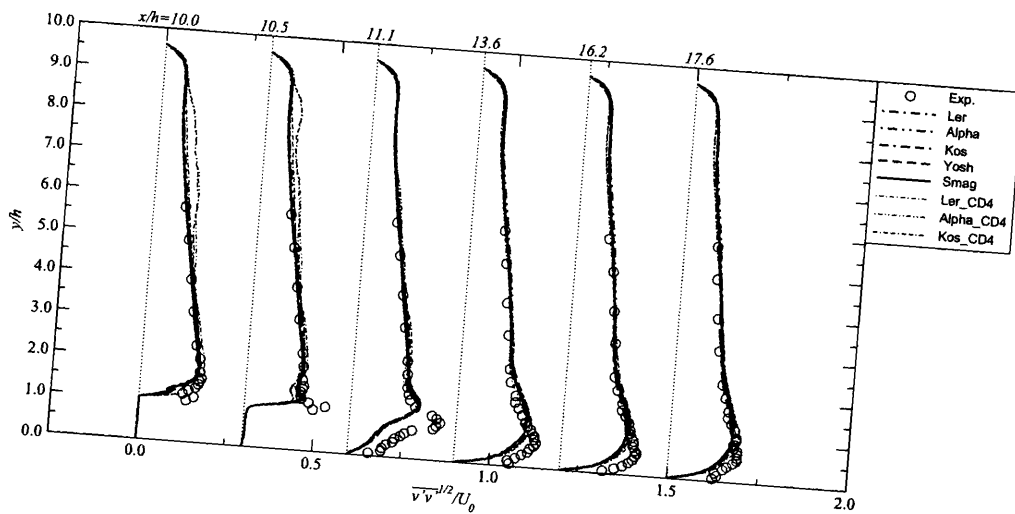


Figure A.22:  $\overline{v'v'}$  profiles at various  $x/h$ -locations ( $121 \times 112 \times 67$ ).

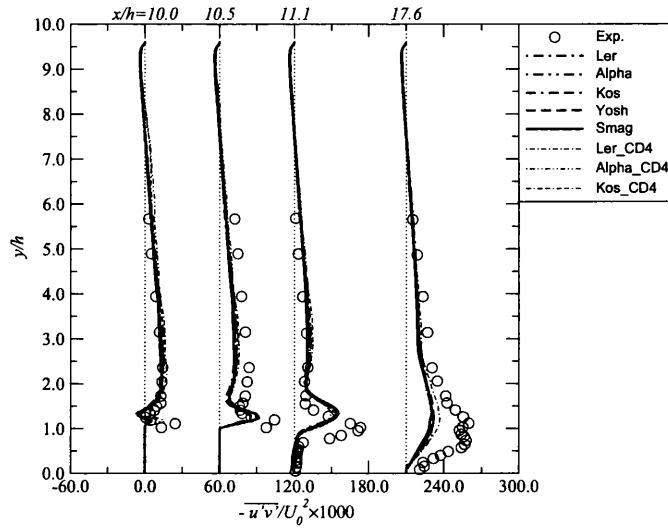


Figure A.23:  $\overline{u'v'}$  profiles at various  $x/h$ -locations ( $121 \times 112 \times 67$ ).

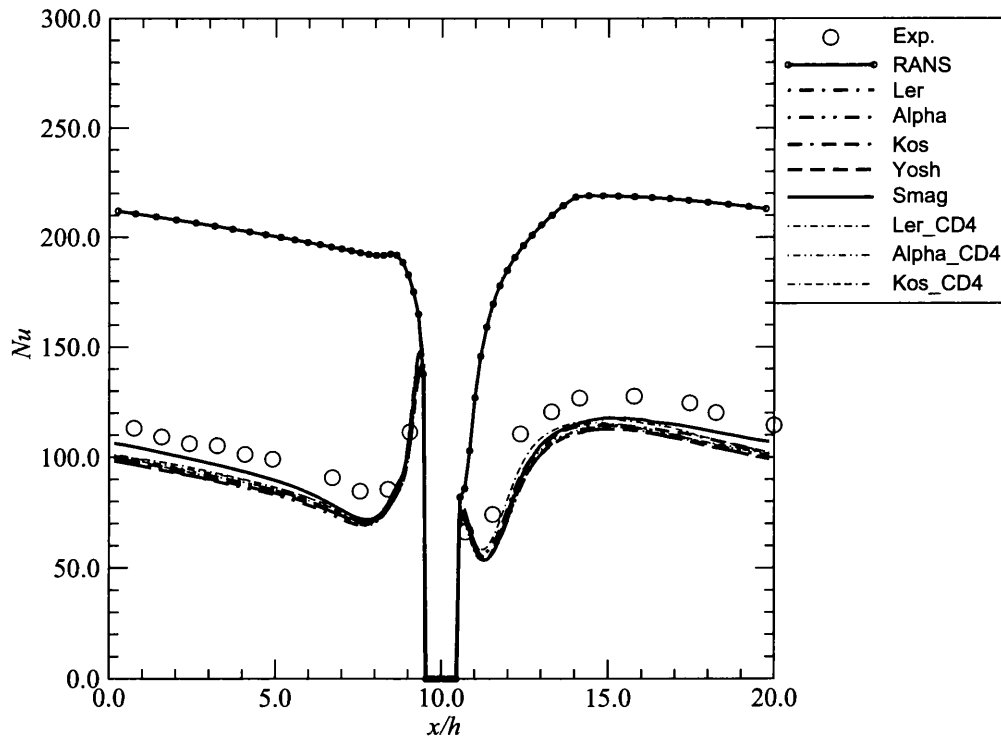


Figure A.24:  $Nu$  profile along channel ( $121 \times 112 \times 67$ ).

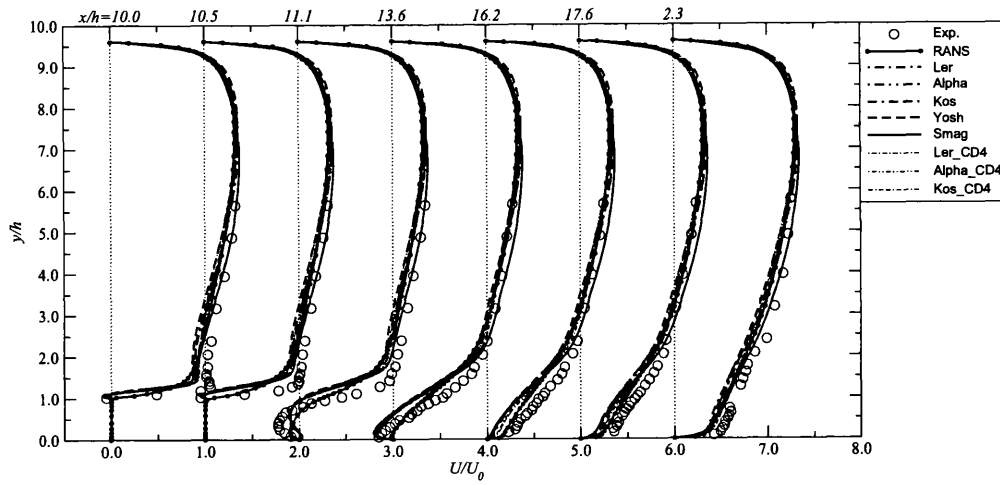


Figure A.25: Mean  $U$  velocity profiles at various  $x/h$ -locations ( $121 \times 112 \times 33$ ).

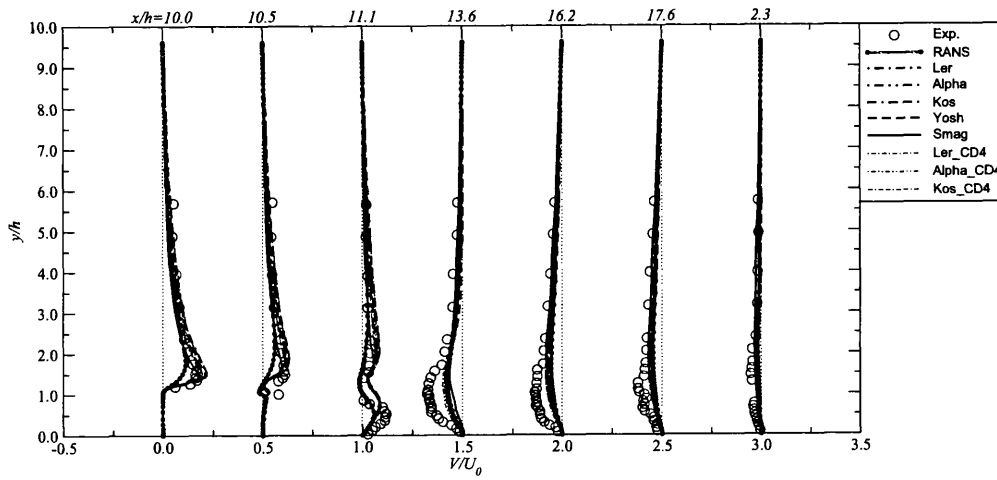


Figure A.26: Mean  $V$  velocity profiles at various  $x/h$ -locations ( $121 \times 112 \times 33$ ).



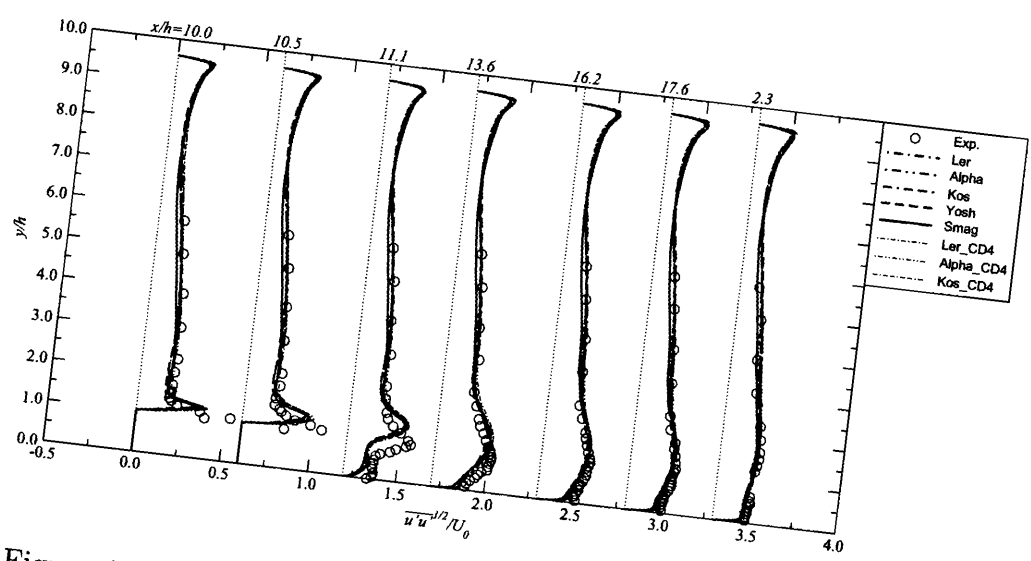


Figure A.27:  $\overline{u'u'}$  profiles at various  $x/h$ -locations ( $121 \times 112 \times 33$ ).

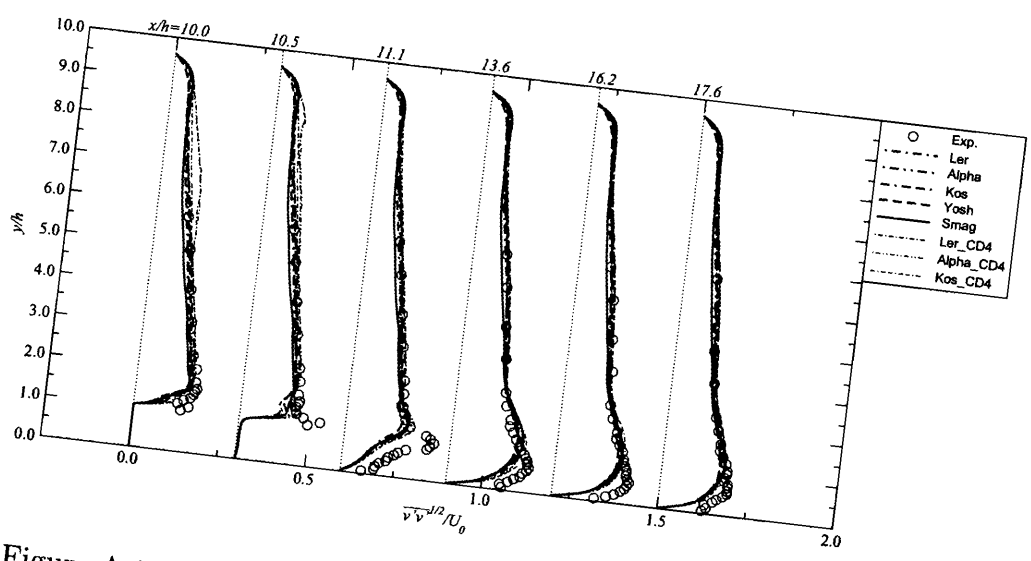


Figure A.28:  $\overline{v'v'}$  profiles at various  $x/h$ -locations ( $121 \times 112 \times 33$ ).

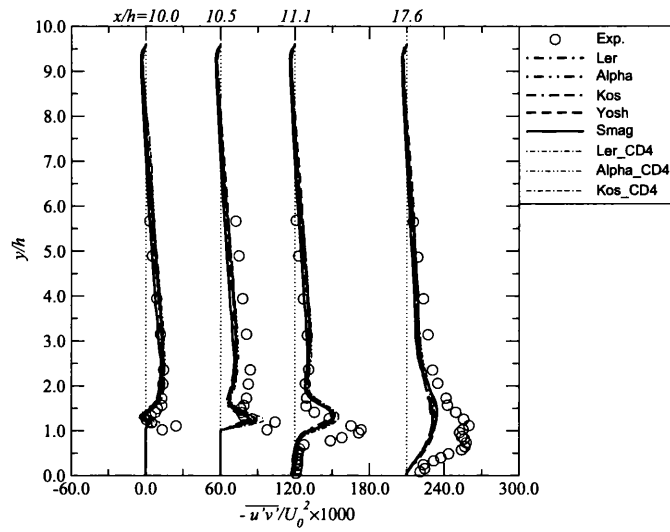


Figure A.29:  $\overline{u'v'}$  profiles at various  $x/h$ -locations ( $121 \times 112 \times 33$ ).

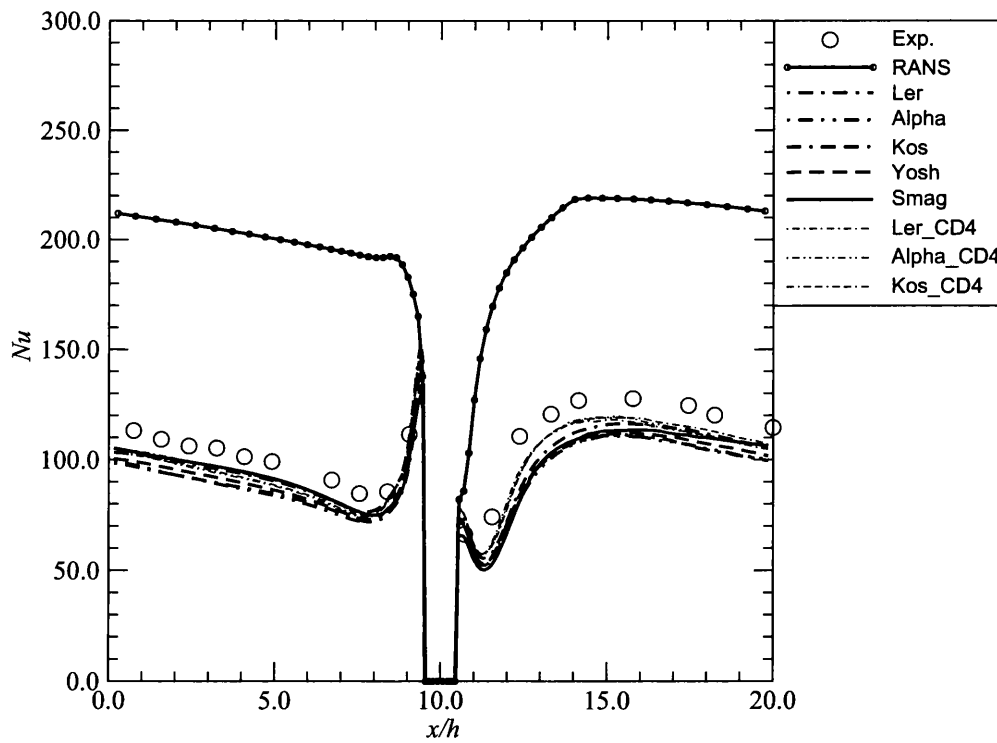


Figure A.30:  $Nu$  profile along channel ( $121 \times 112 \times 33$ ).

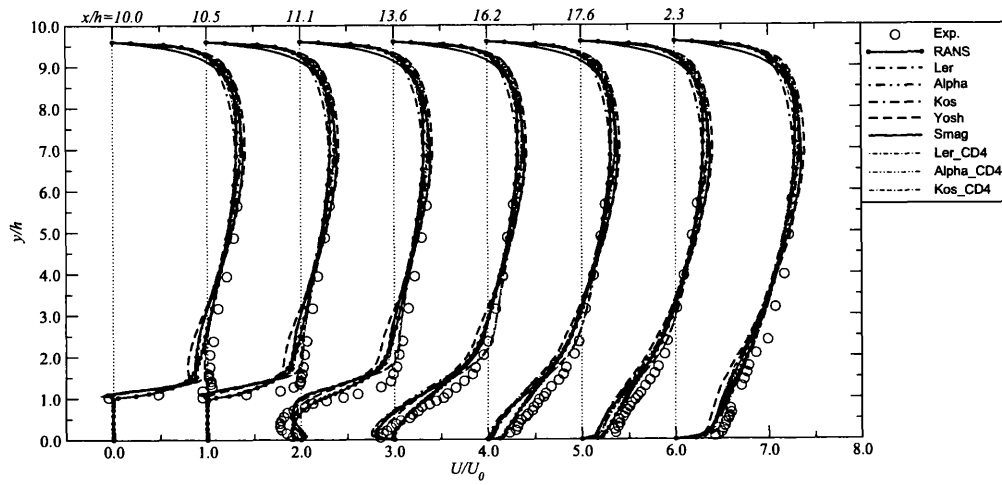


Figure A.31: Mean  $U$  velocity profiles at various  $x/h$ -locations ( $62 \times 57 \times 17$ ).

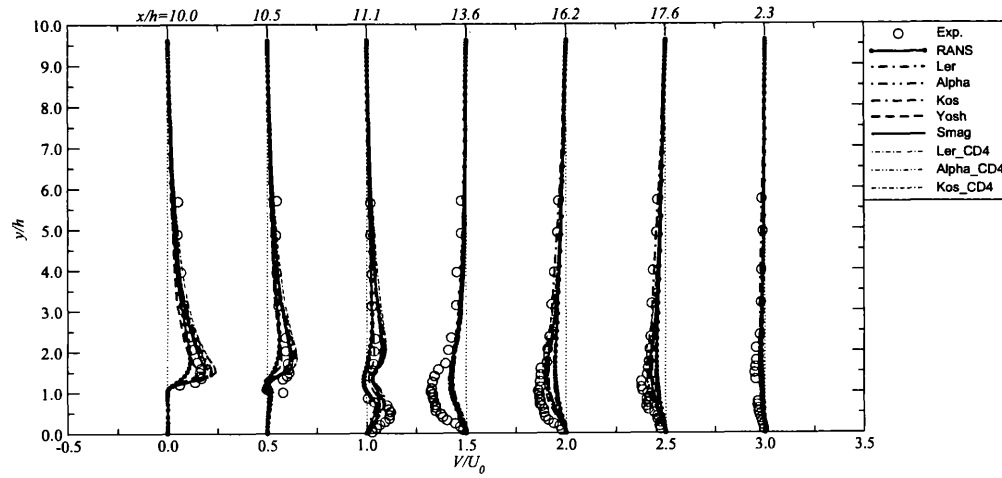


Figure A.32: Mean  $V$  velocity profiles at various  $x/h$ -locations ( $62 \times 57 \times 17$ ).

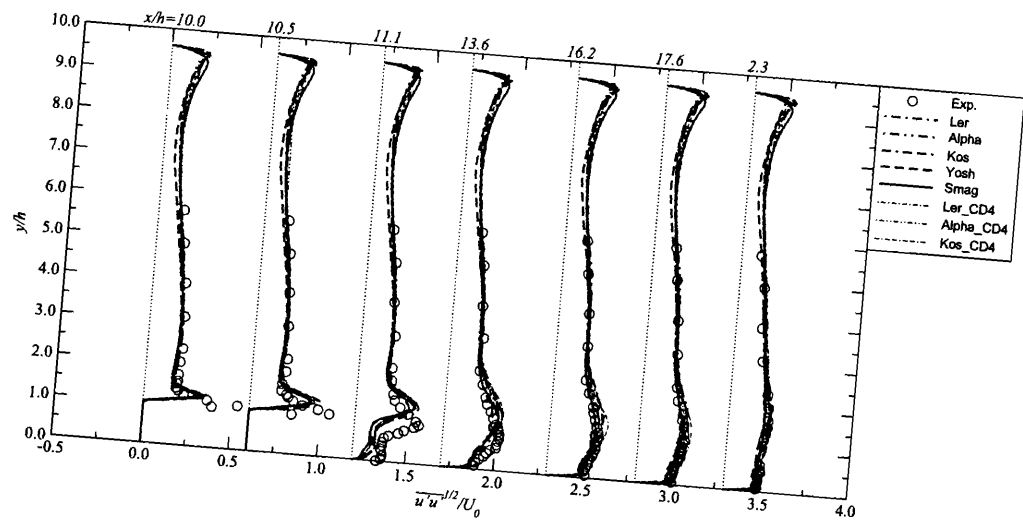


Figure A.33:  $\overline{u'u'}$  profiles at various  $x/h$ -locations ( $62 \times 57 \times 17$ ).

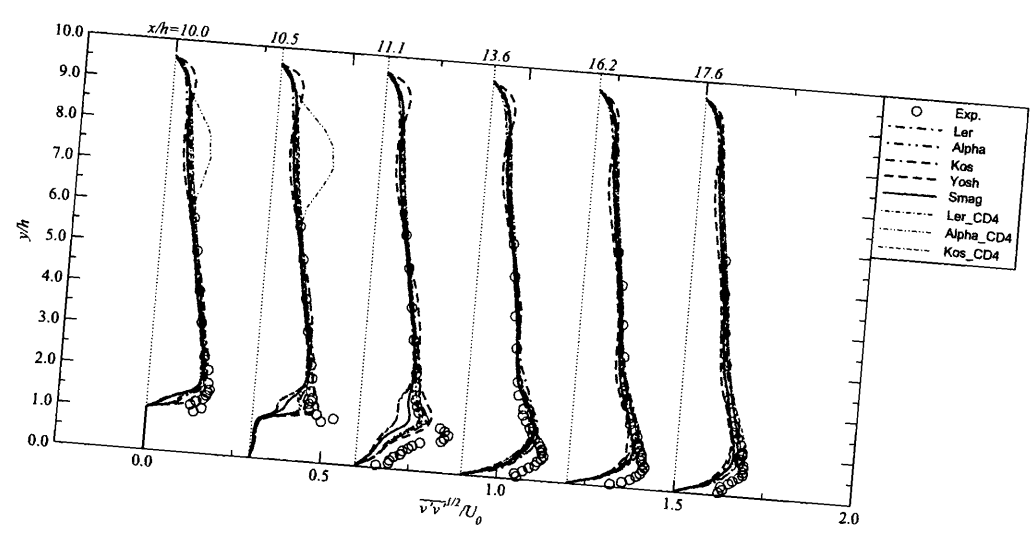


Figure A.34:  $\overline{v'v'}$  profiles at various  $x/h$ -locations ( $62 \times 57 \times 17$ ).

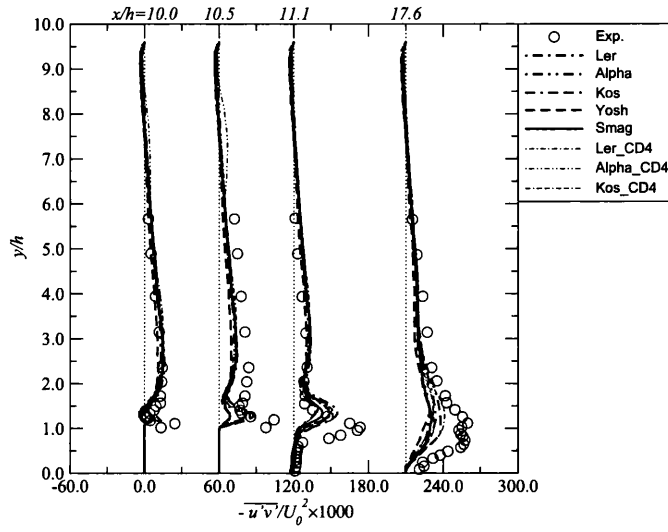


Figure A.35:  $\overline{u'v'}$  profiles at various  $x/h$ -locations ( $62 \times 57 \times 17$ ).

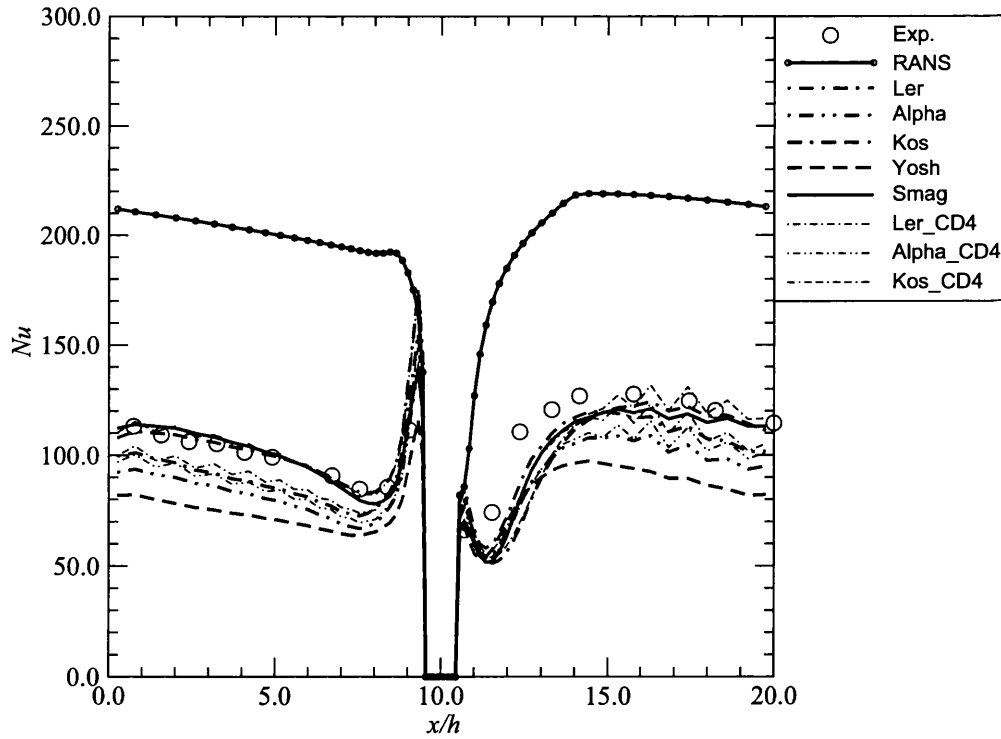
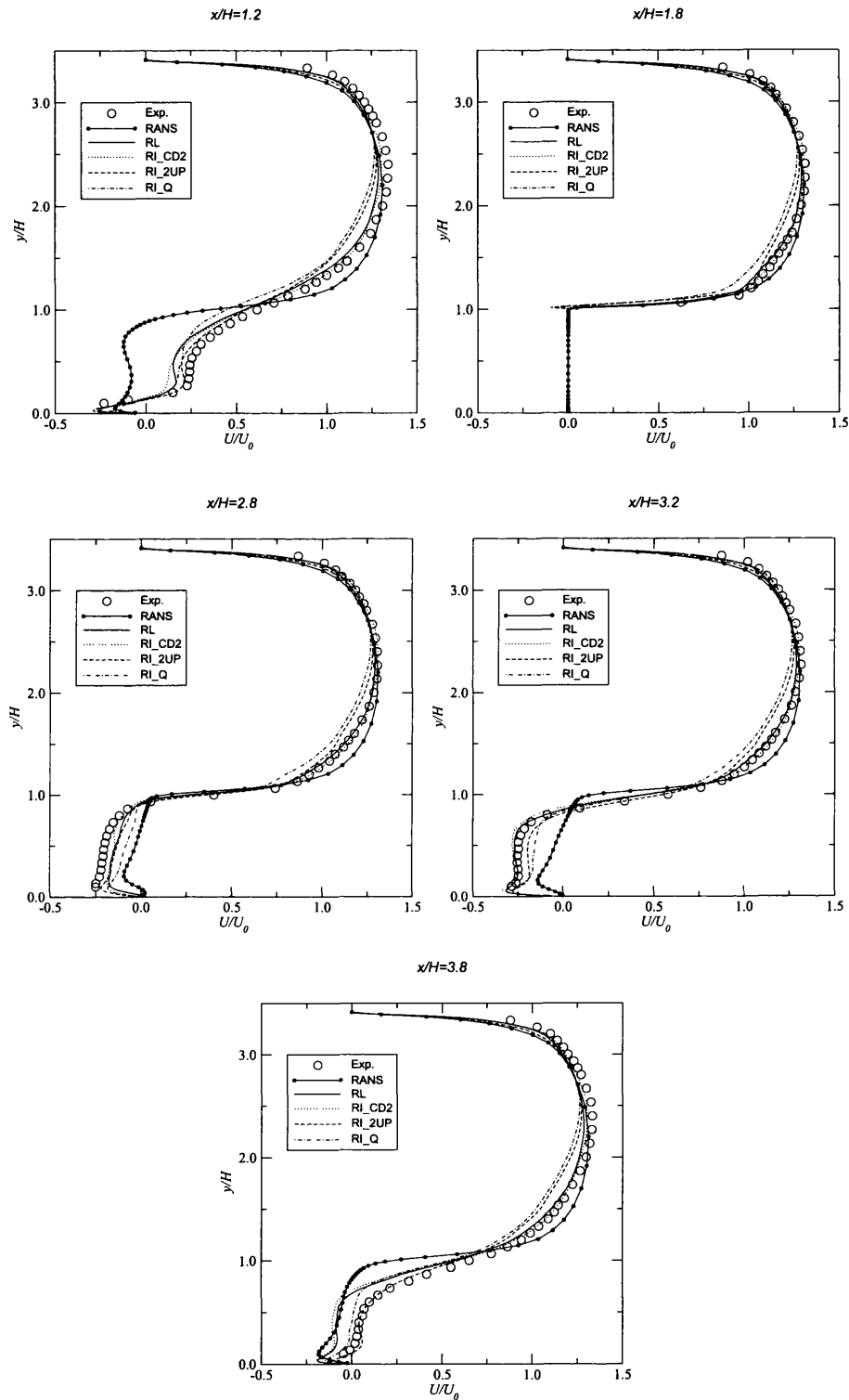


Figure A.36:  $Nu$  profile along channel ( $62 \times 57 \times 17$ ).

## A.2 Array of cubes plots

Figure A.37: Mean  $U$  velocity profiles at various  $x/h$ -locations ( $109 \times 109 \times 109$ ).

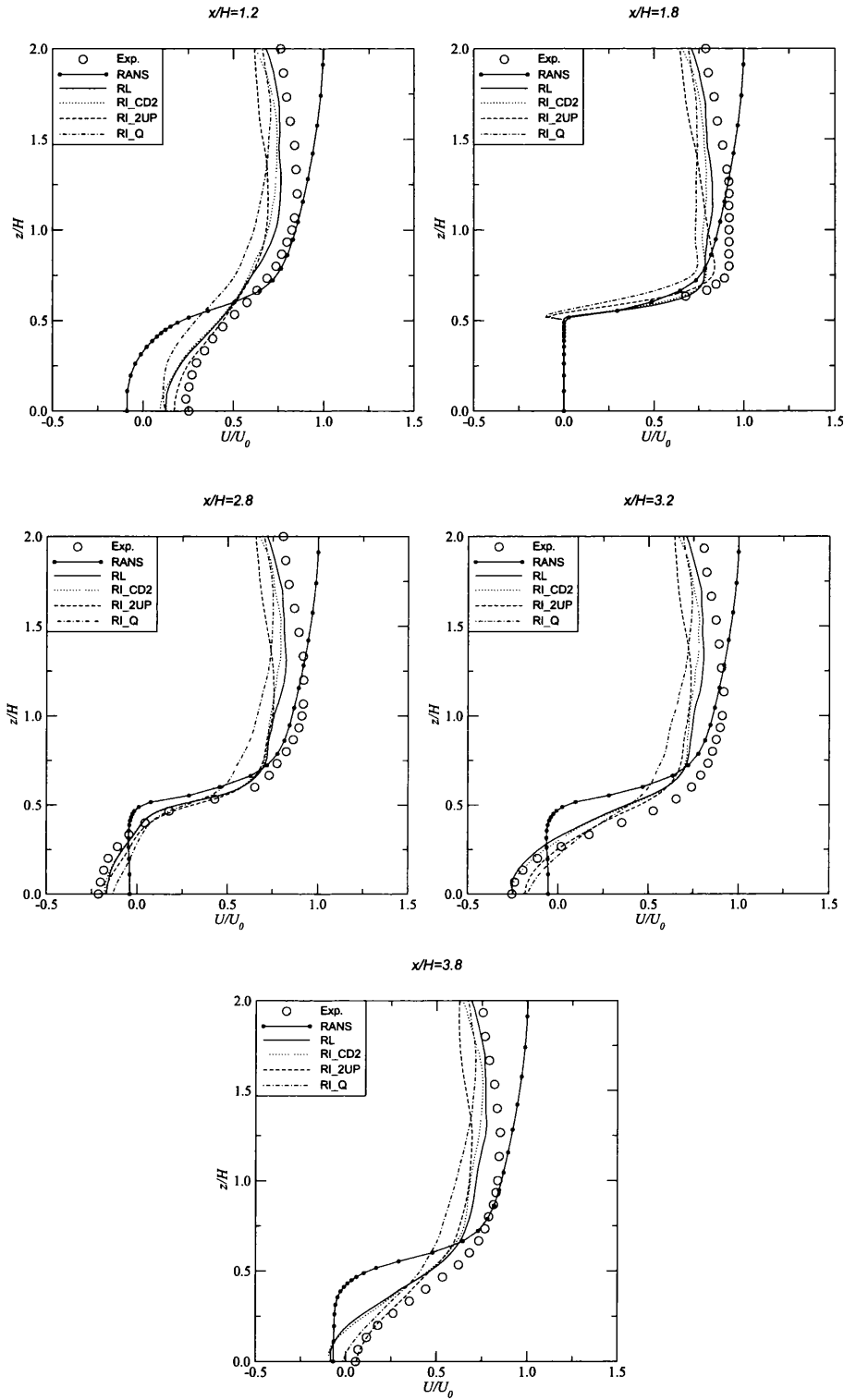


Figure A.38: Mean  $U$  velocity profiles at various  $x/h$ -locations ( $109 \times 109 \times 109$ ).



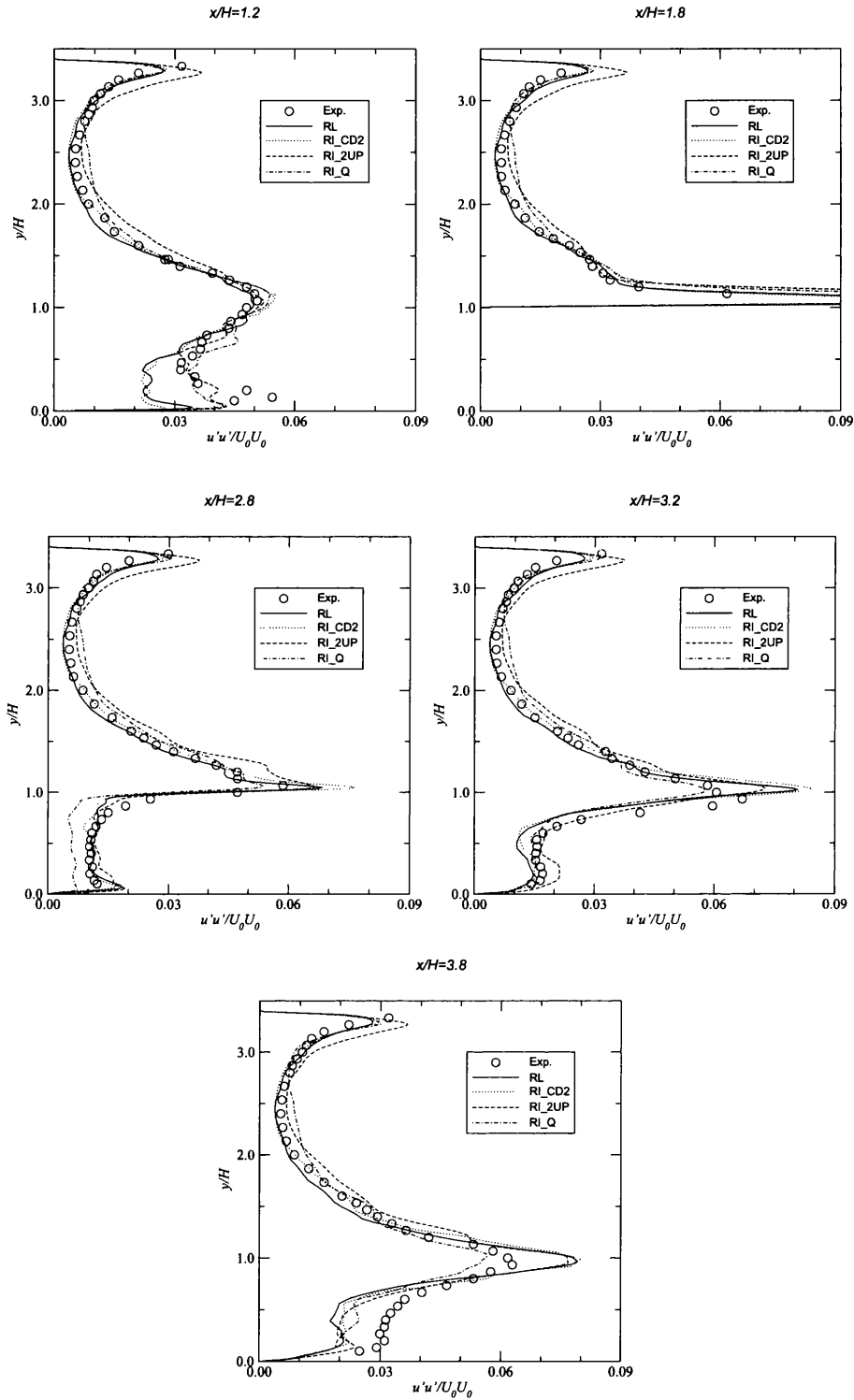
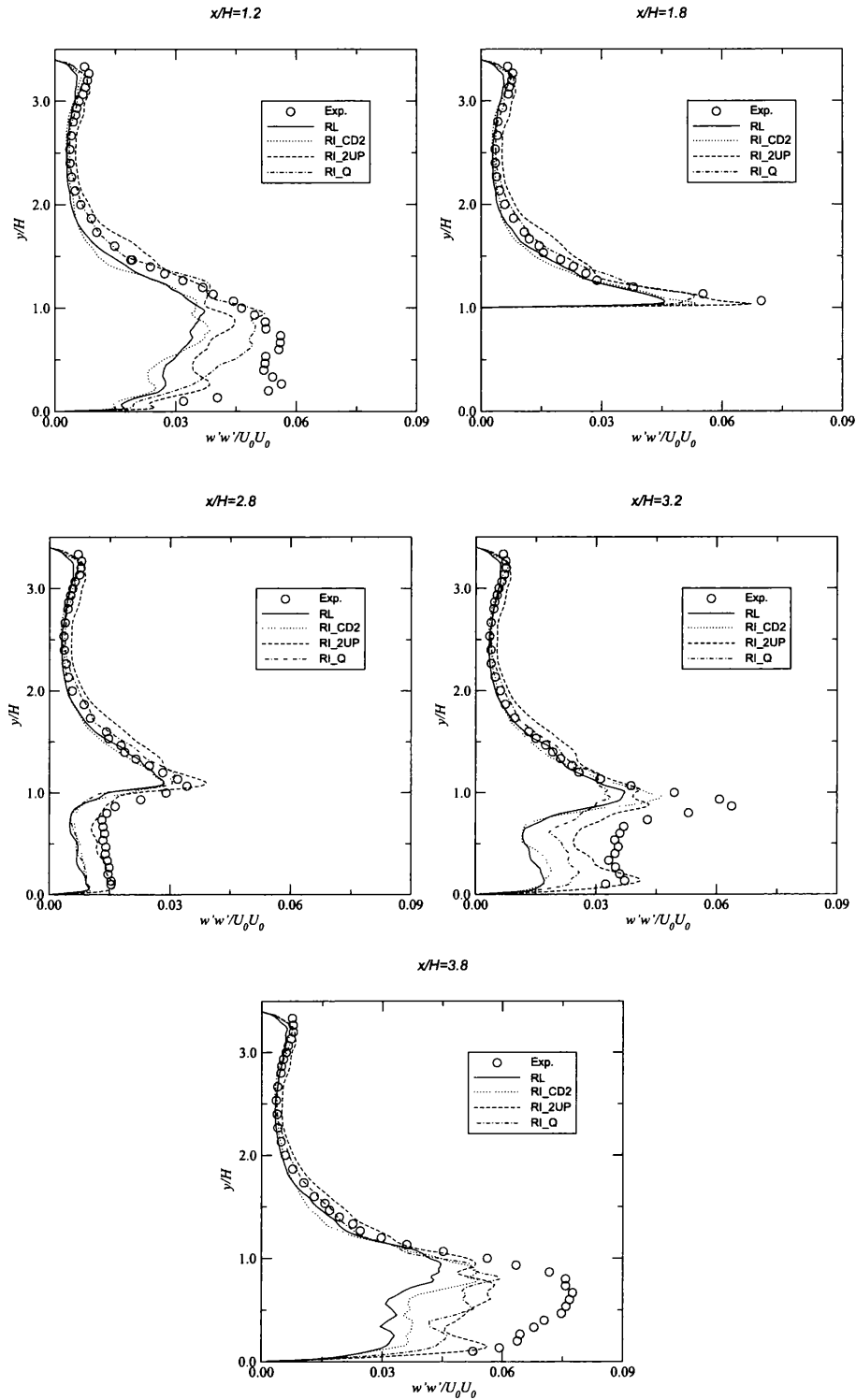
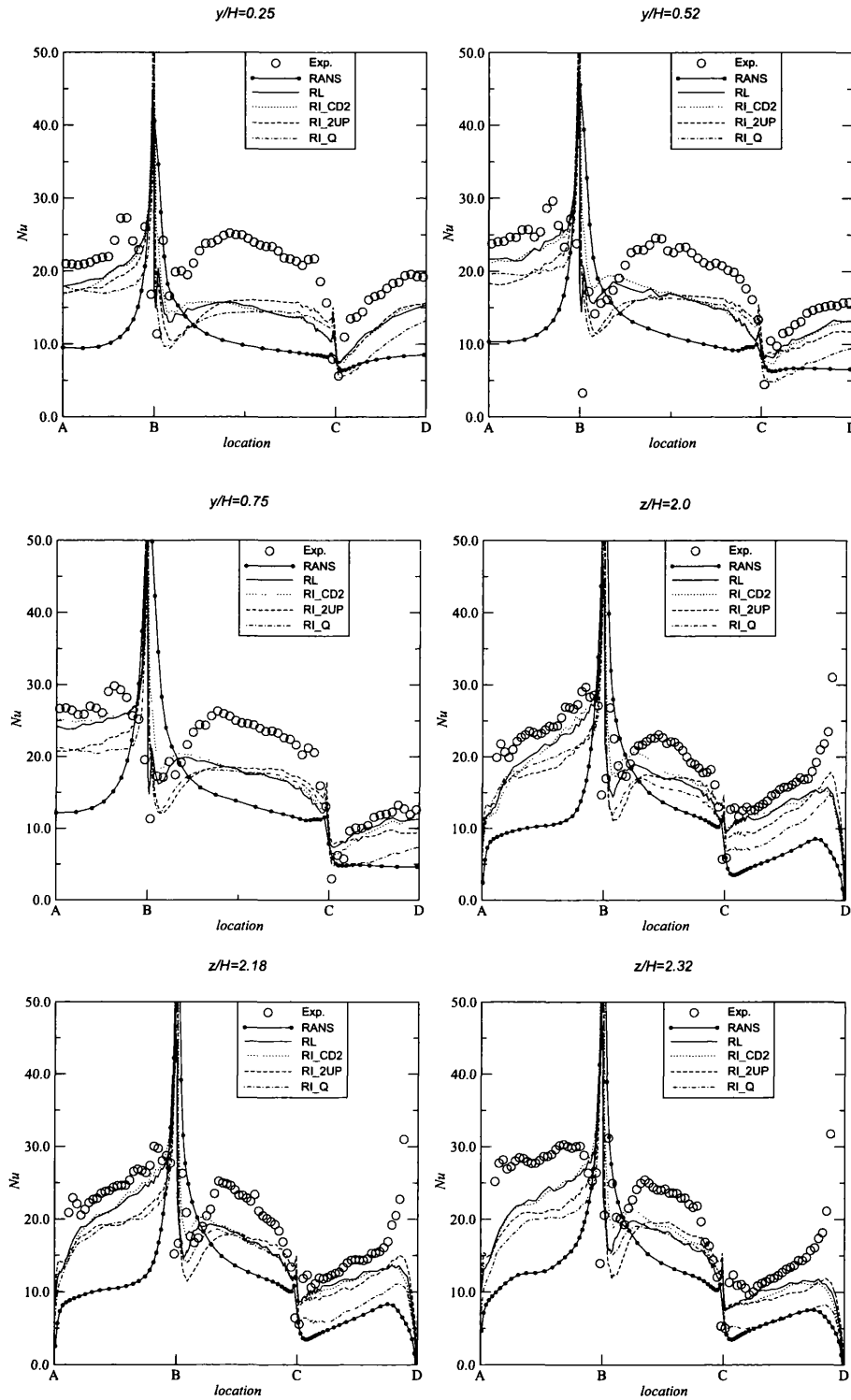


Figure A.39: Mean  $u'u'$  profiles at various  $x/h$ -locations ( $109 \times 109 \times 109$ ).

Figure A.40: Mean  $w'w'$  profiles at various  $x/h$ -locations ( $109 \times 109 \times 109$ ).

Figure A.41:  $Nu$  profiles around the heated cube ( $109 \times 109 \times 109$ ).

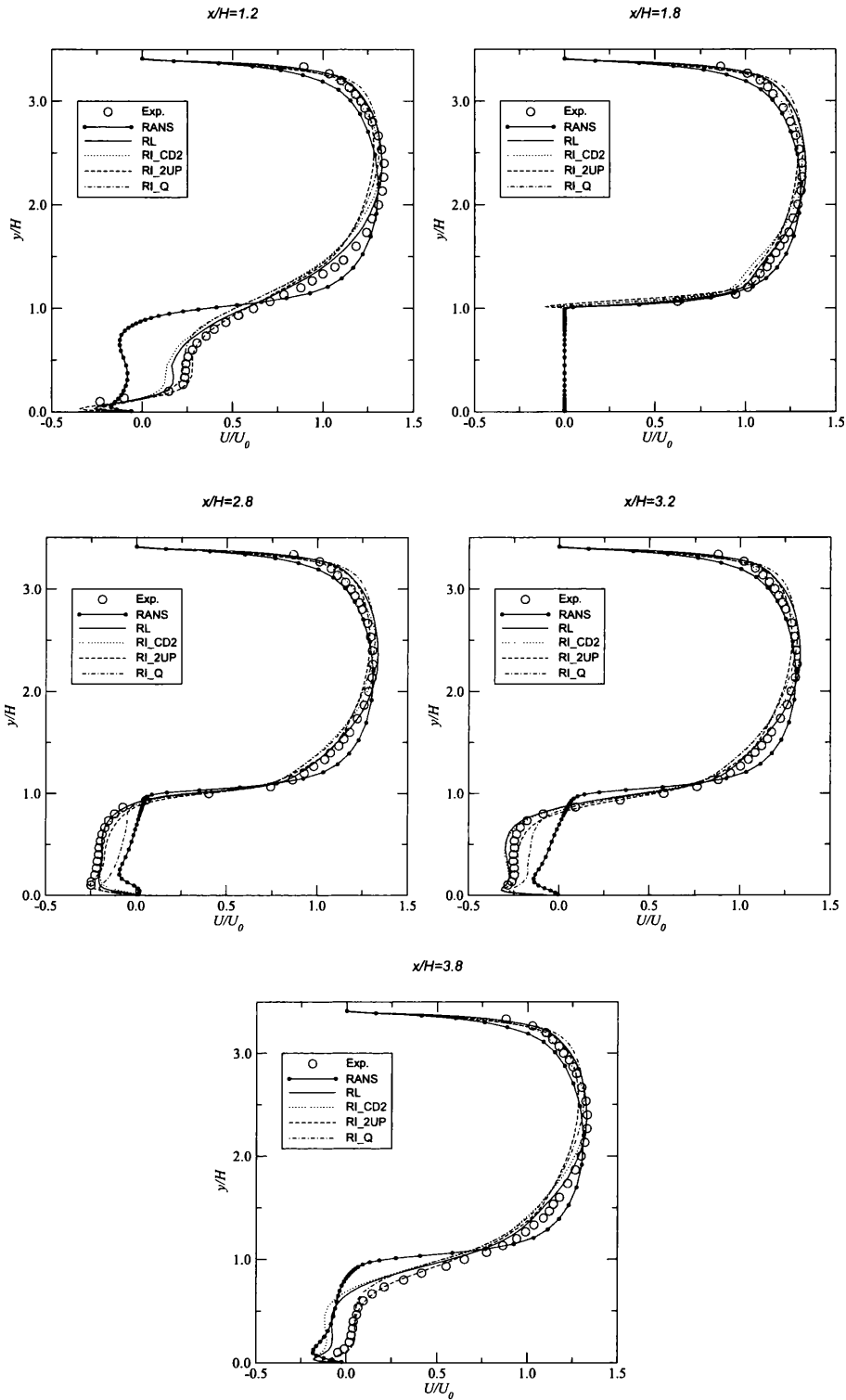


Figure A.42: Mean  $U$  velocity profiles at various  $x/h$ -locations ( $75 \times 75 \times 75$ ).

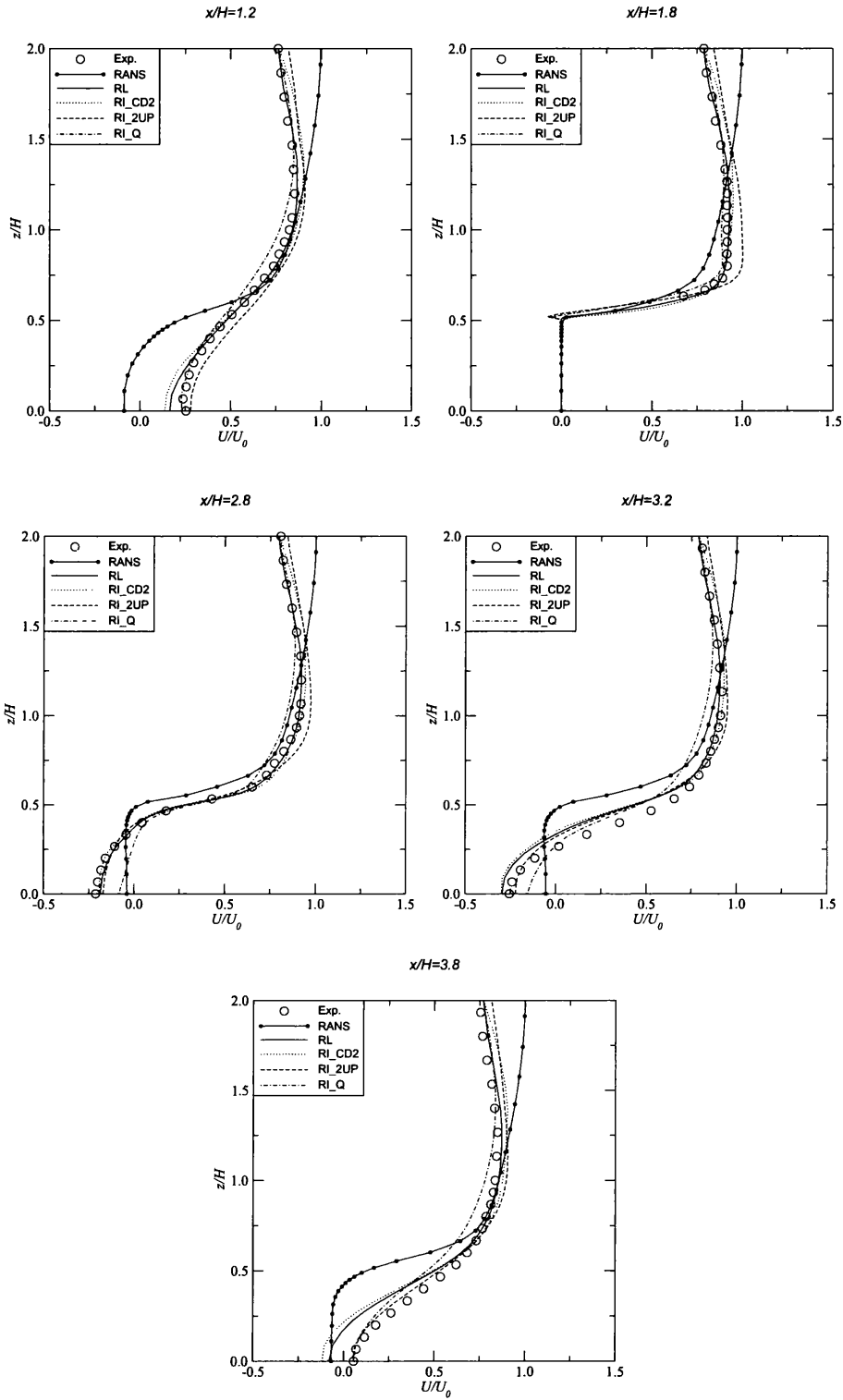


Figure A.43: Mean  $U$  velocity profiles at various  $x/h$ -locations ( $75 \times 75 \times 75$ ).

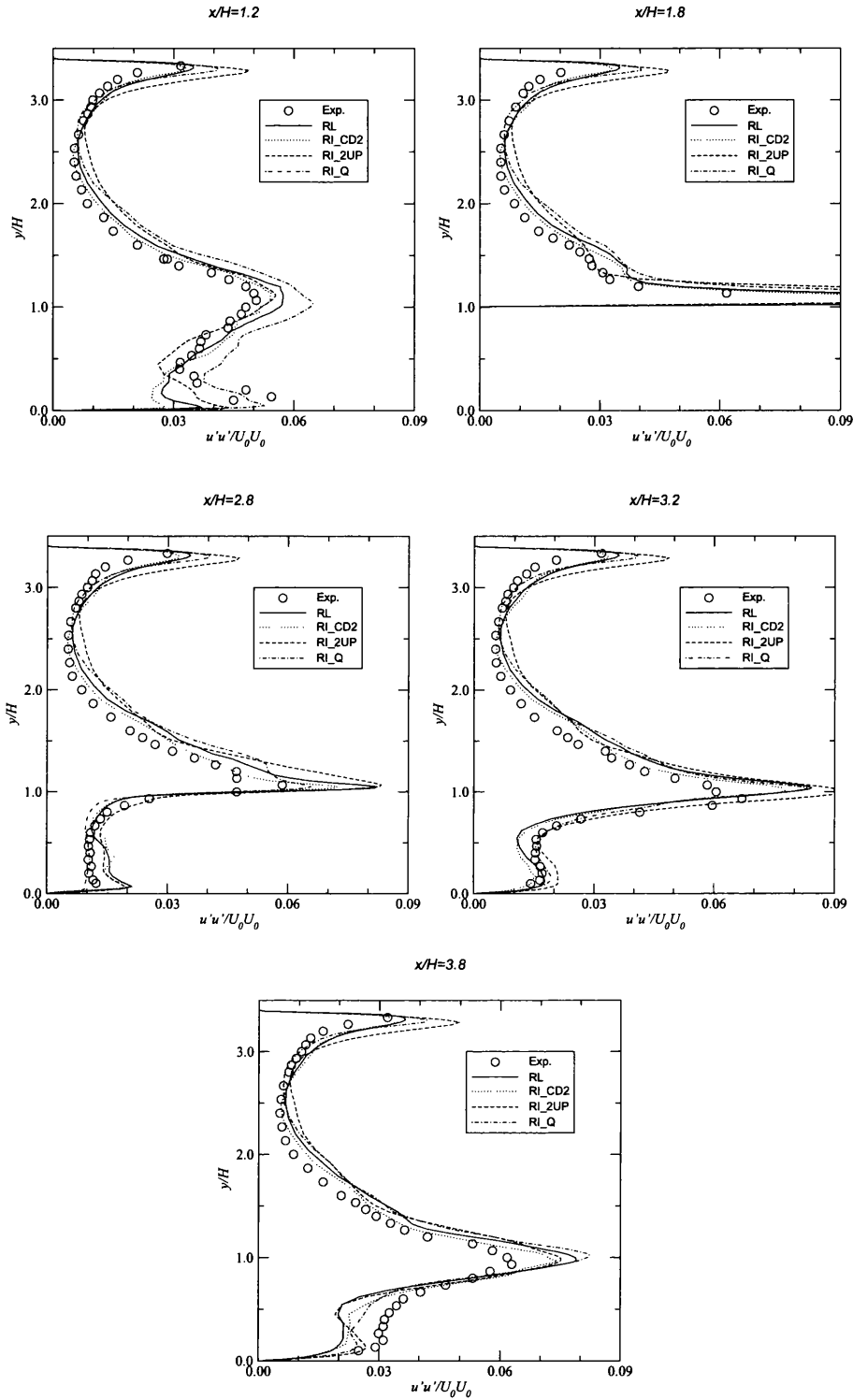


Figure A.44: Mean  $u'u'$  profiles at various  $x/h$ -locations ( $75 \times 75 \times 75$ ).

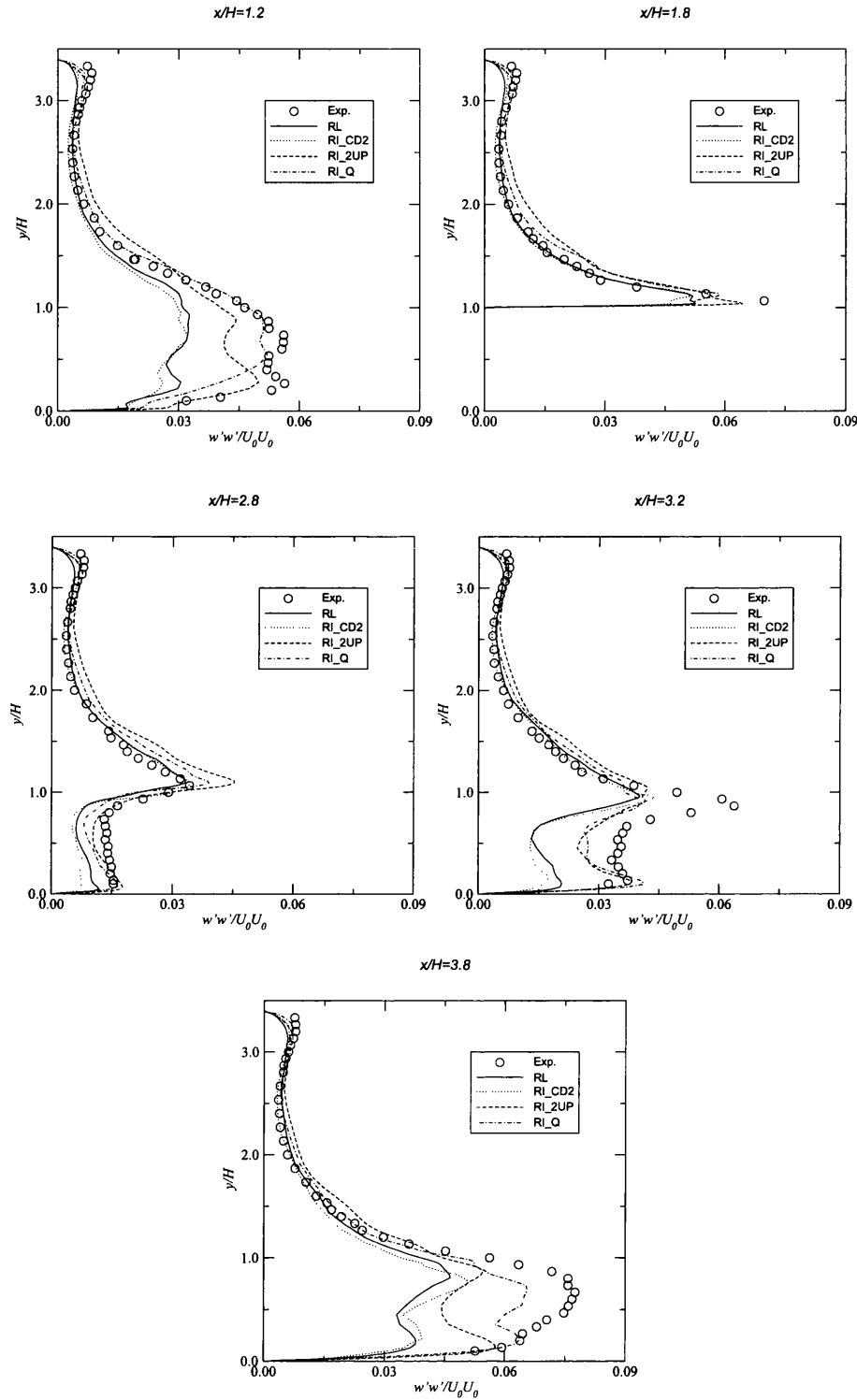
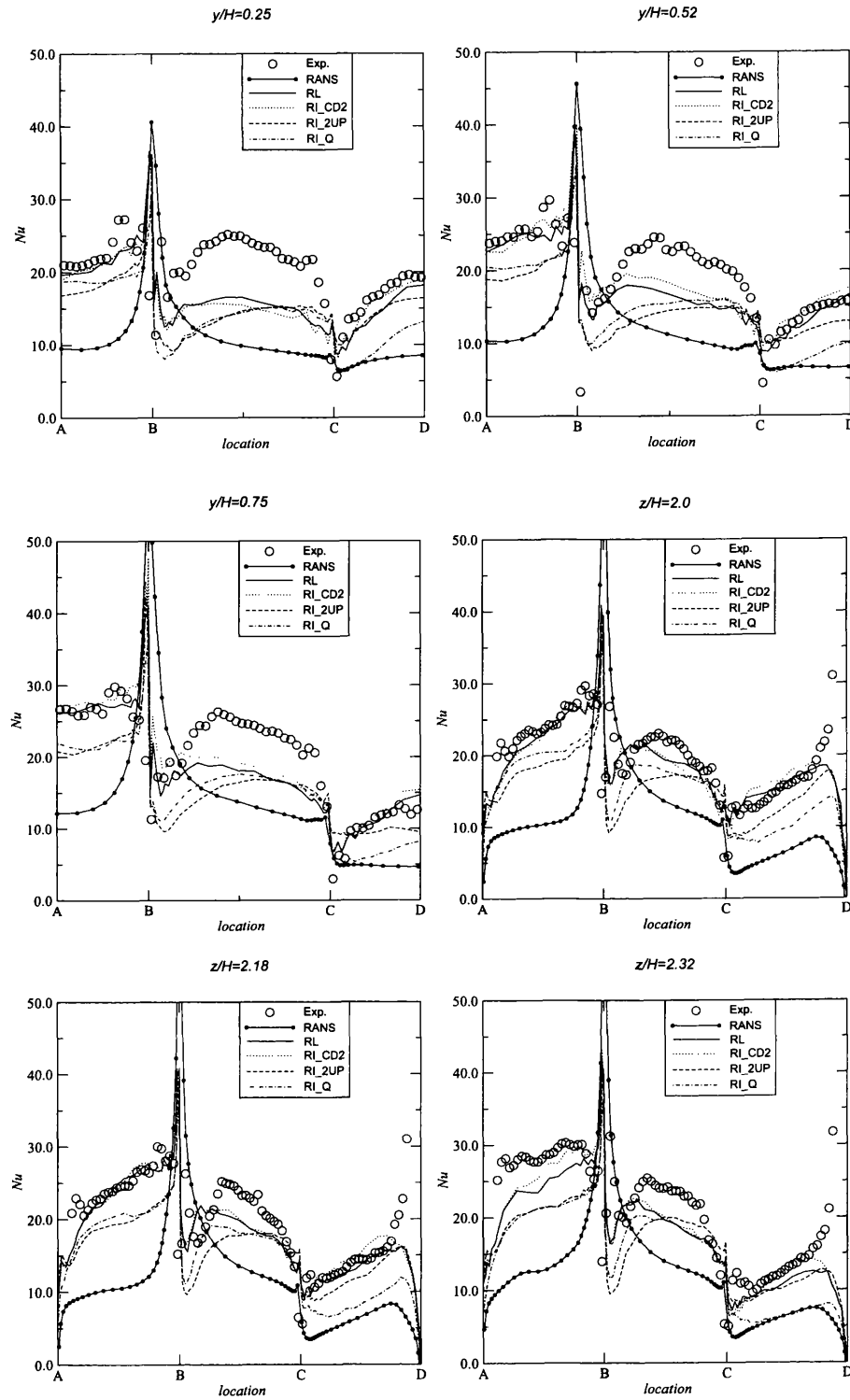
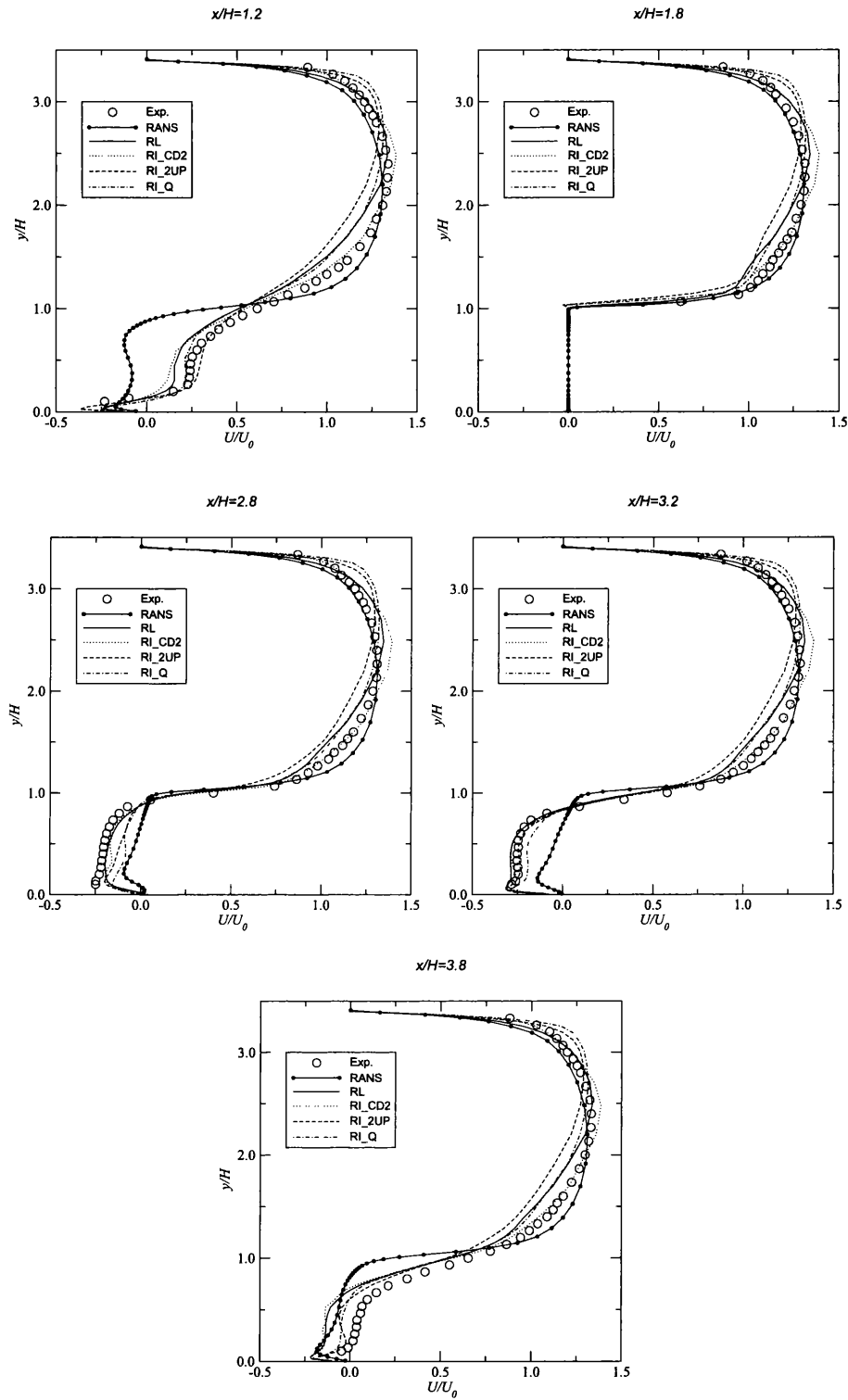


Figure A.45: Mean  $w'w'$  profiles at various  $x/h$ -locations ( $75 \times 75 \times 75$ ).

Figure A.46:  $Nu$  profiles around the heated cube ( $75 \times 75 \times 75$ ).



Figure A.47: Mean  $U$  velocity profiles at various  $x/h$ -locations ( $53 \times 51 \times 53$ ).

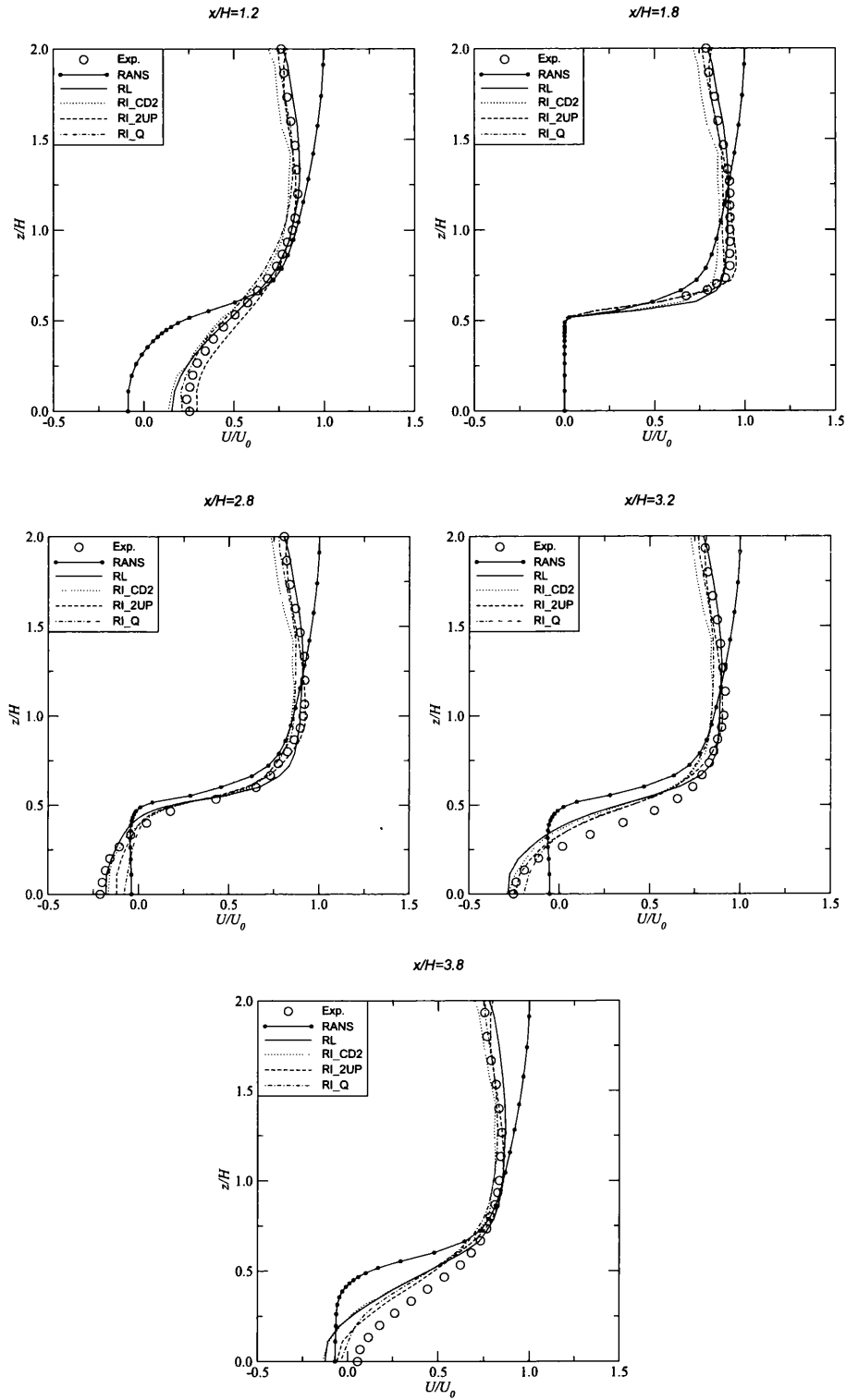


Figure A.48: Mean  $U$  velocity profiles at various  $x/h$ -locations ( $53 \times 51 \times 53$ ).

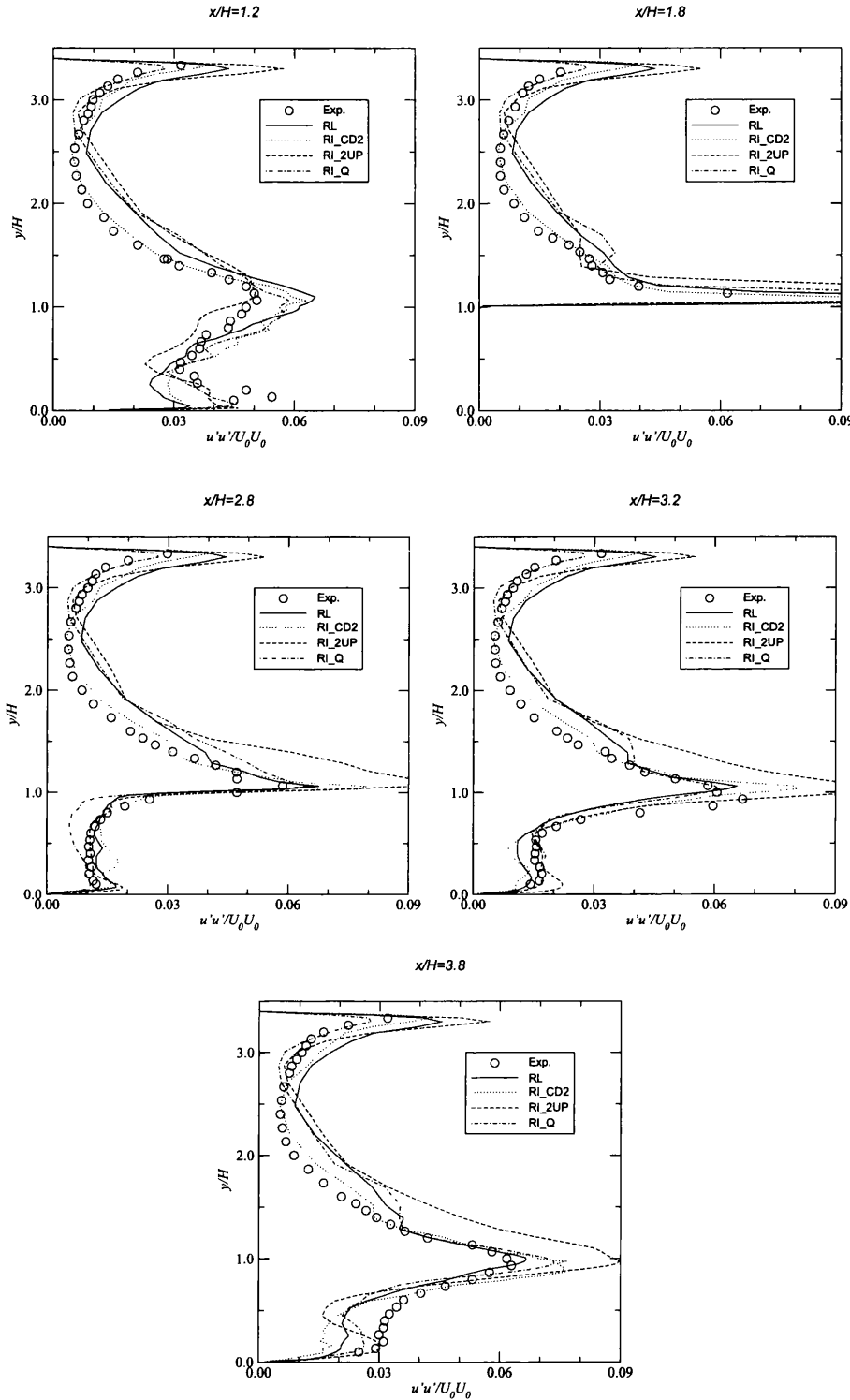


Figure A.49: Mean  $u'u'$  profiles at various  $x/h$ -locations ( $53 \times 51 \times 53$ ).

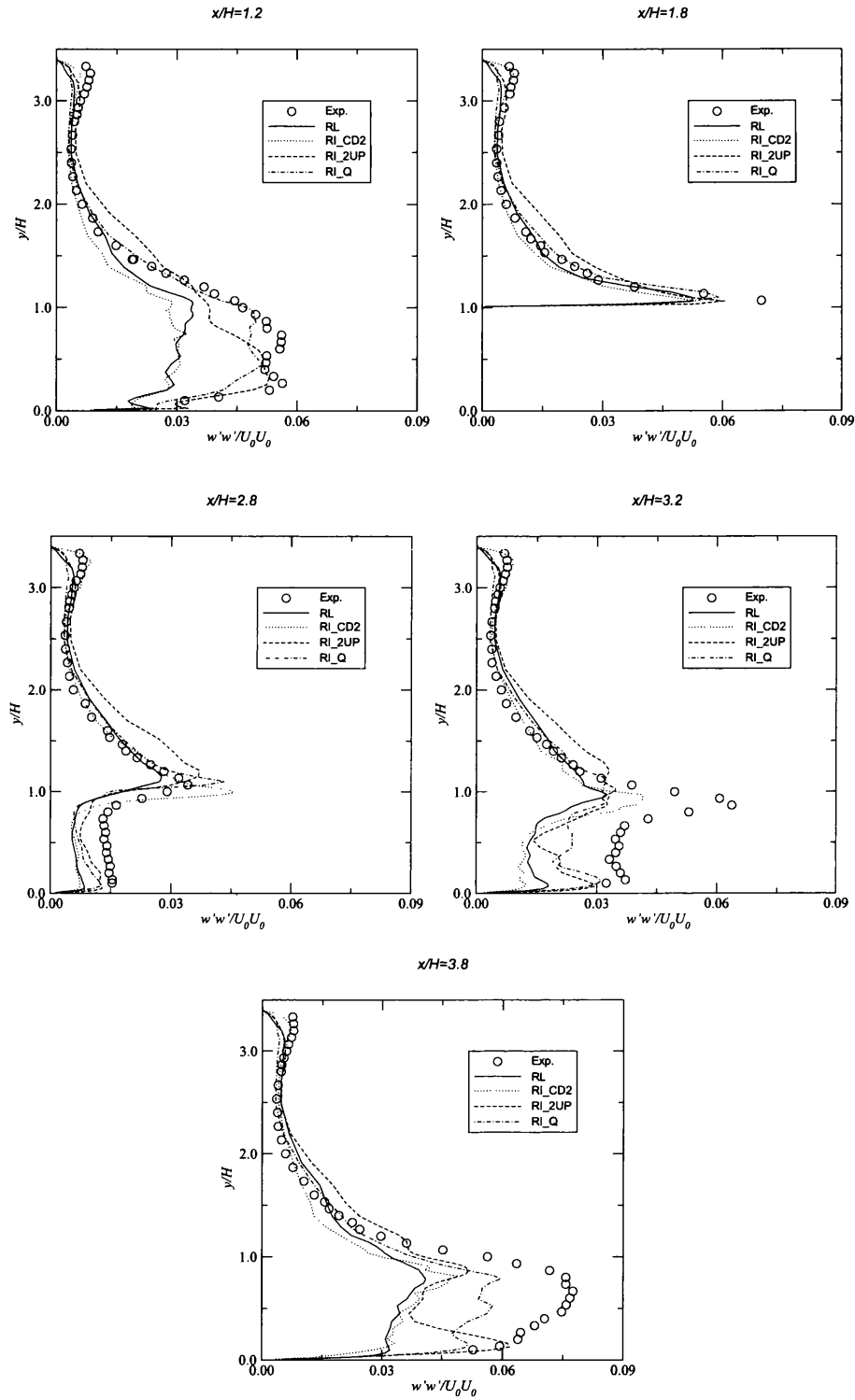
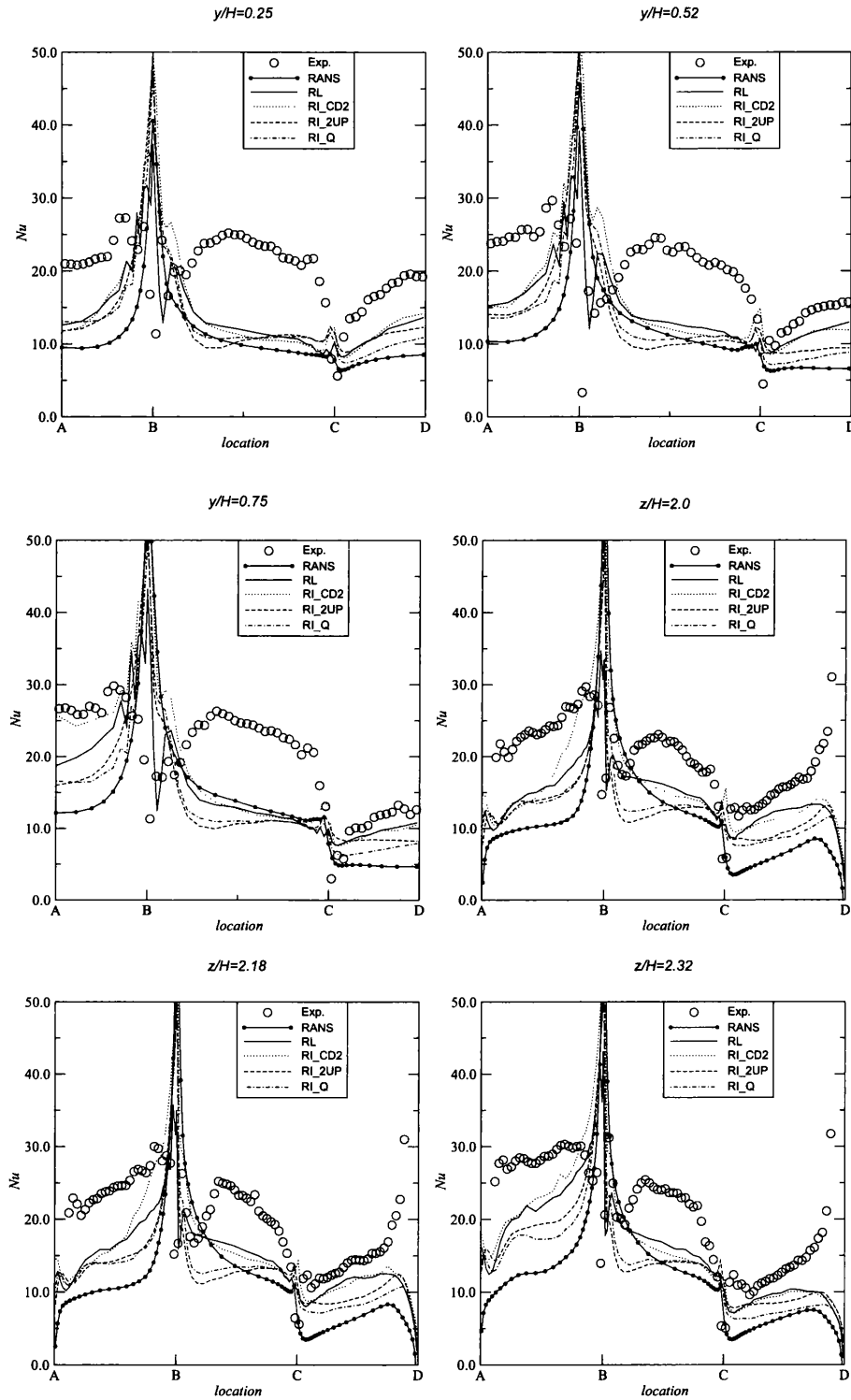
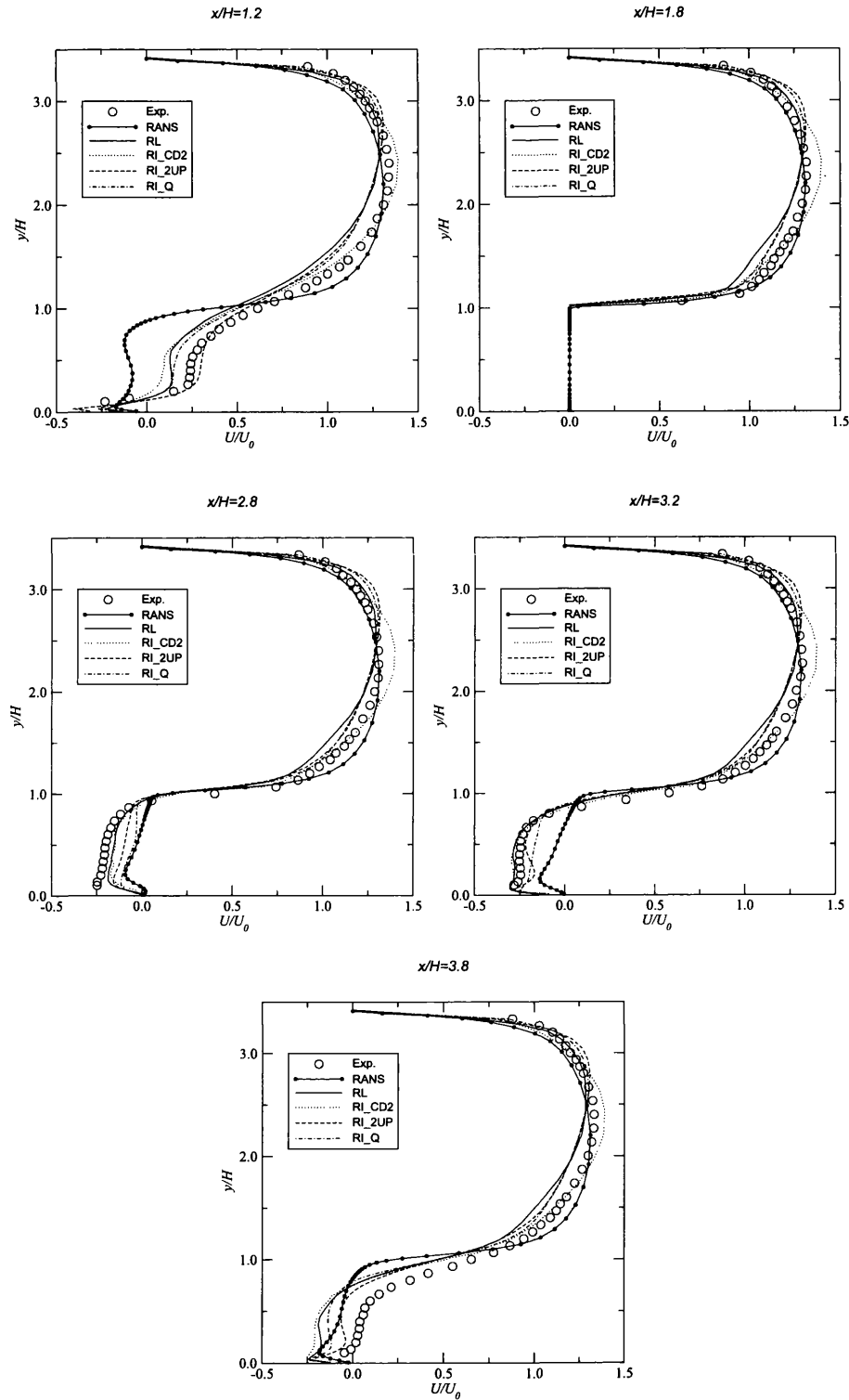
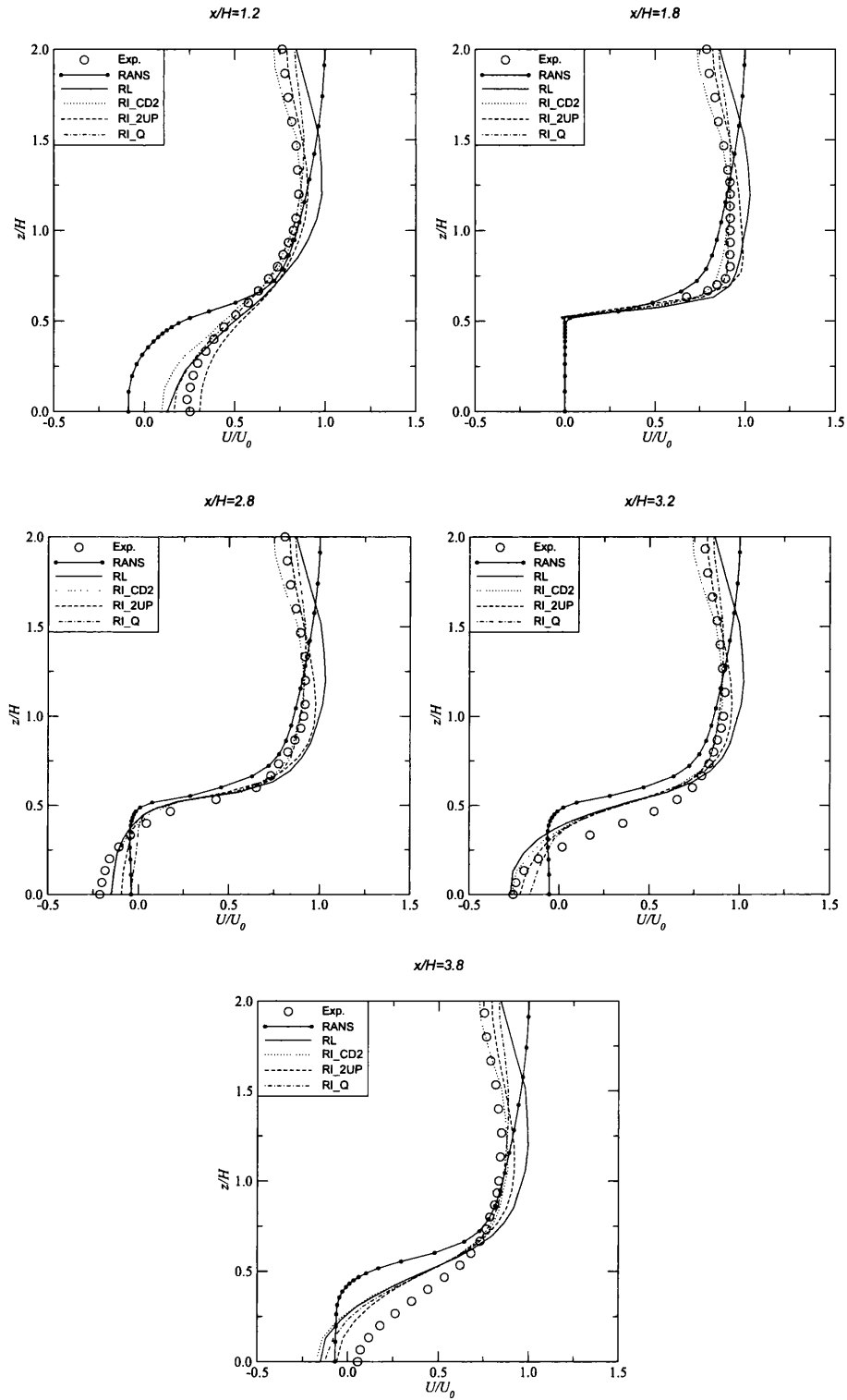
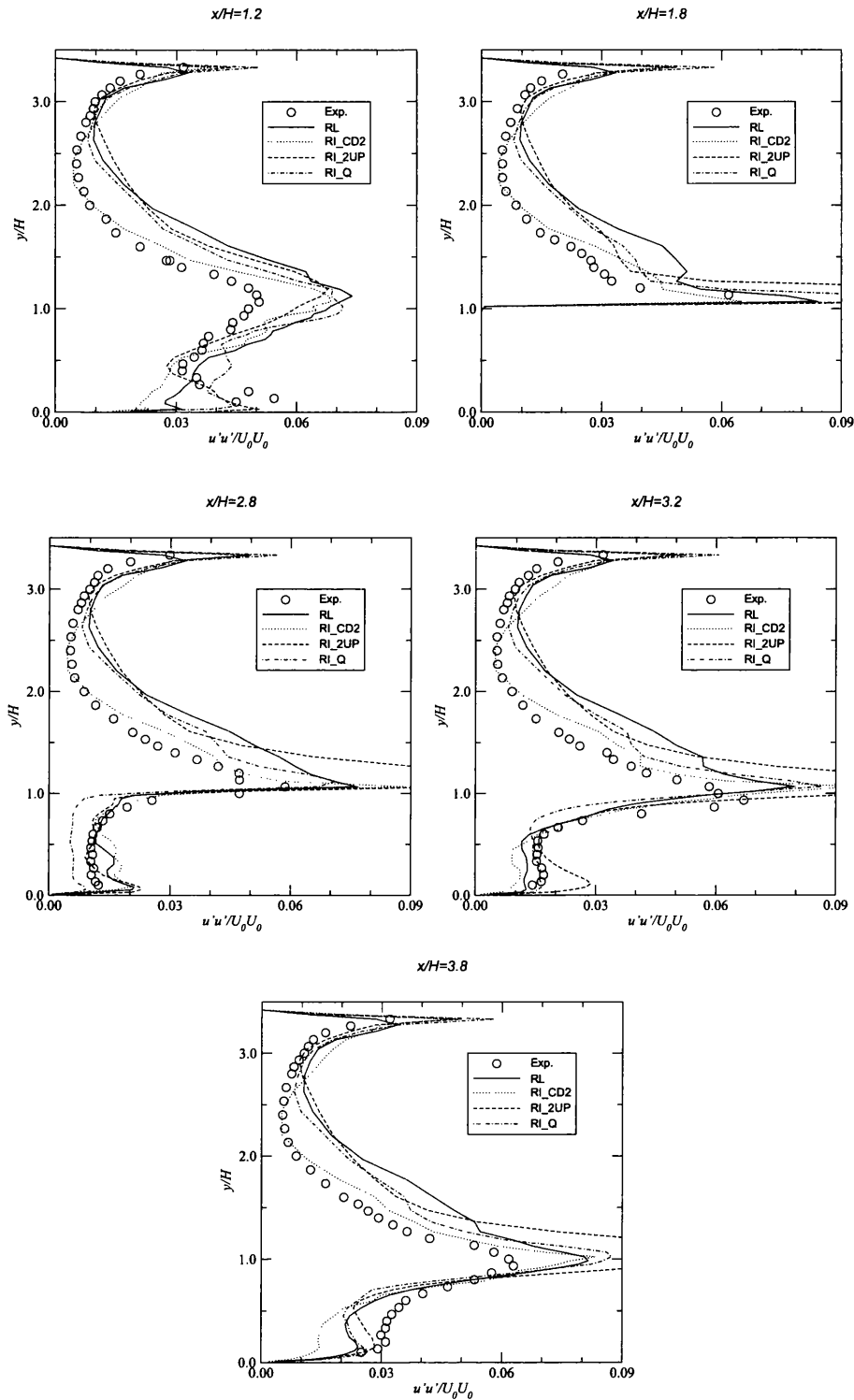


Figure A.50: Mean  $w'w'$  profiles at various  $x/h$ -locations ( $53 \times 51 \times 53$ ).

Figure A.51:  $Nu$  profiles around the heated cube ( $53 \times 51 \times 53$ ).

Figure A.52: Mean  $U$  velocity profiles at various  $x/h$ -locations ( $41 \times 45 \times 41$ ).

Figure A.53: Mean  $U$  velocity profiles at various  $x/h$ -locations ( $41 \times 45 \times 41$ ).

Figure A.54: Mean  $u'u'$  profiles at various  $x/h$ -locations ( $41 \times 45 \times 41$ ).



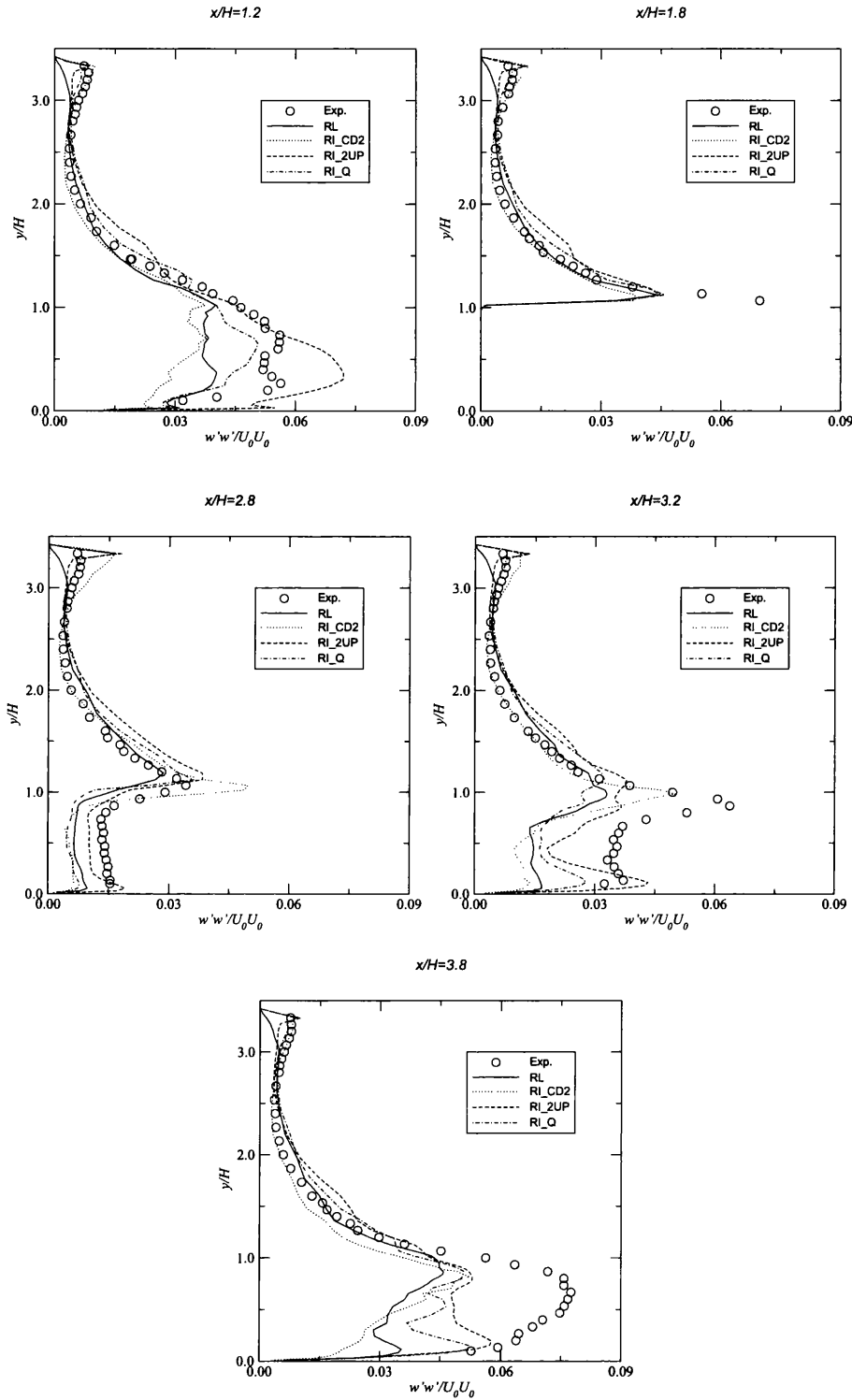


Figure A.55: Mean  $w'w'$  profiles at various  $x/h$ -locations ( $41 \times 45 \times 41$ ).

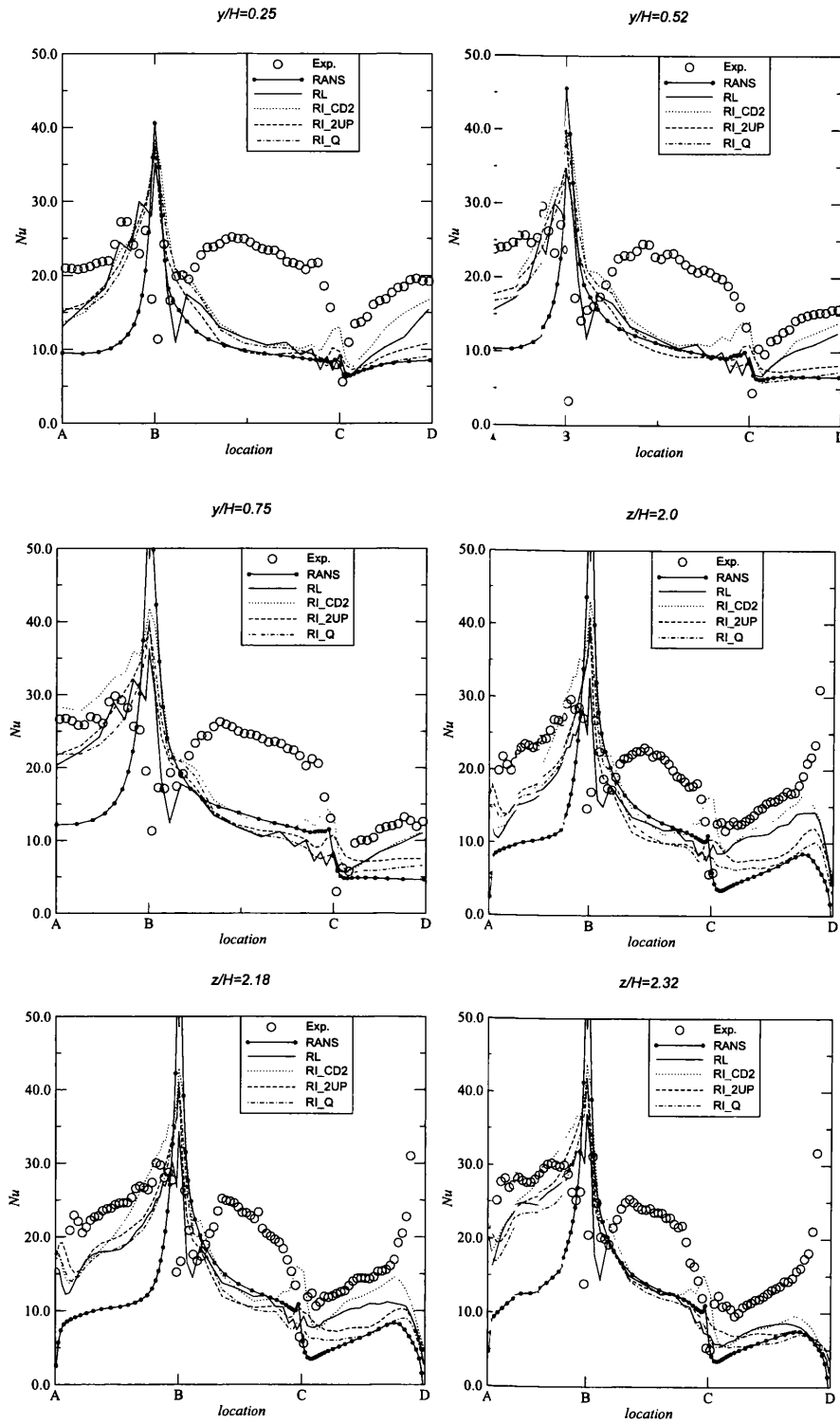
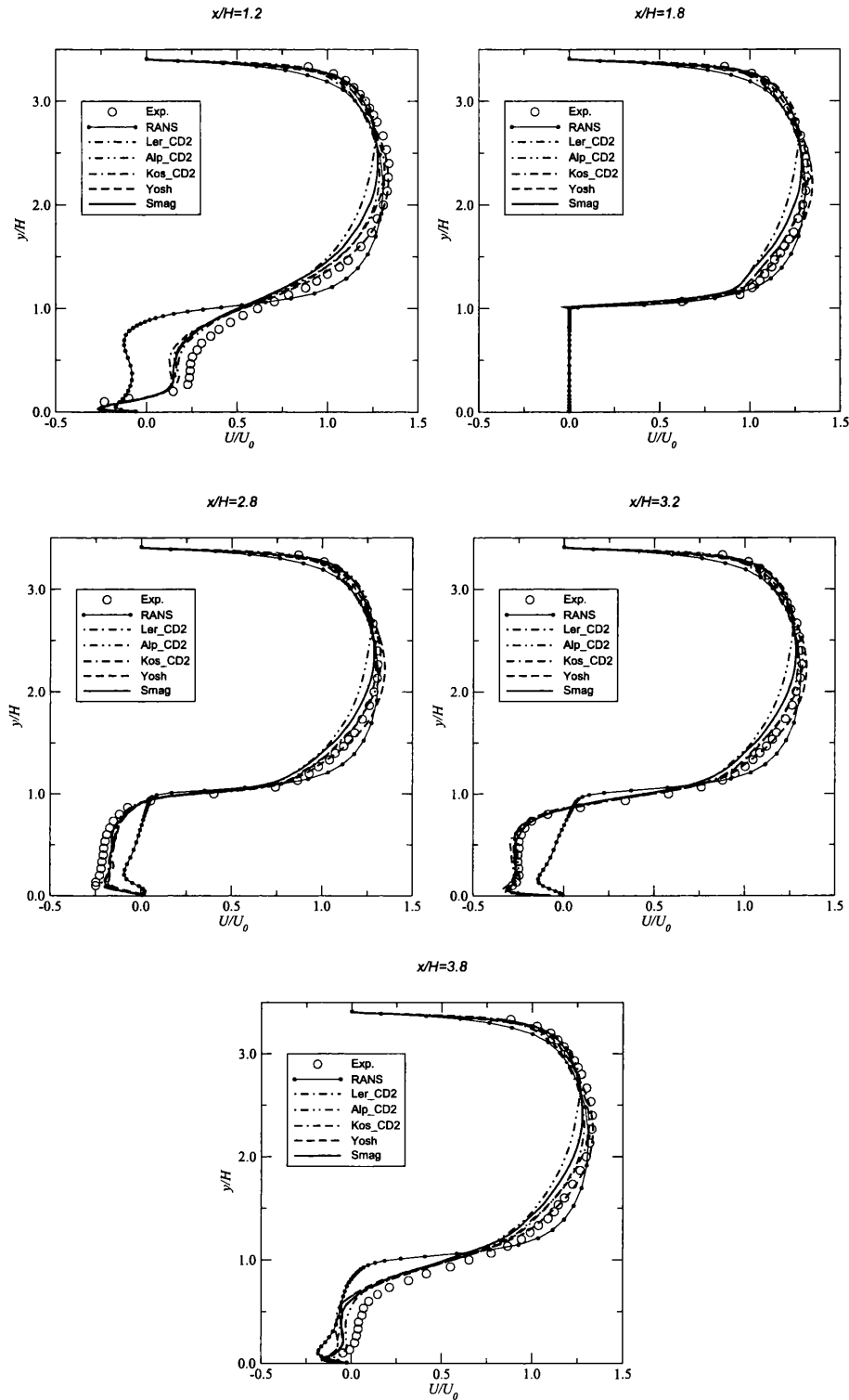


Figure A.56:  $Nu$  profiles around the hatd cube ( $41 \times 45 \times 41$ ).

Figure A.57: Mean  $U$  velocity profiles at various  $x/h$ -locations ( $109 \times 109 \times 109$ ).

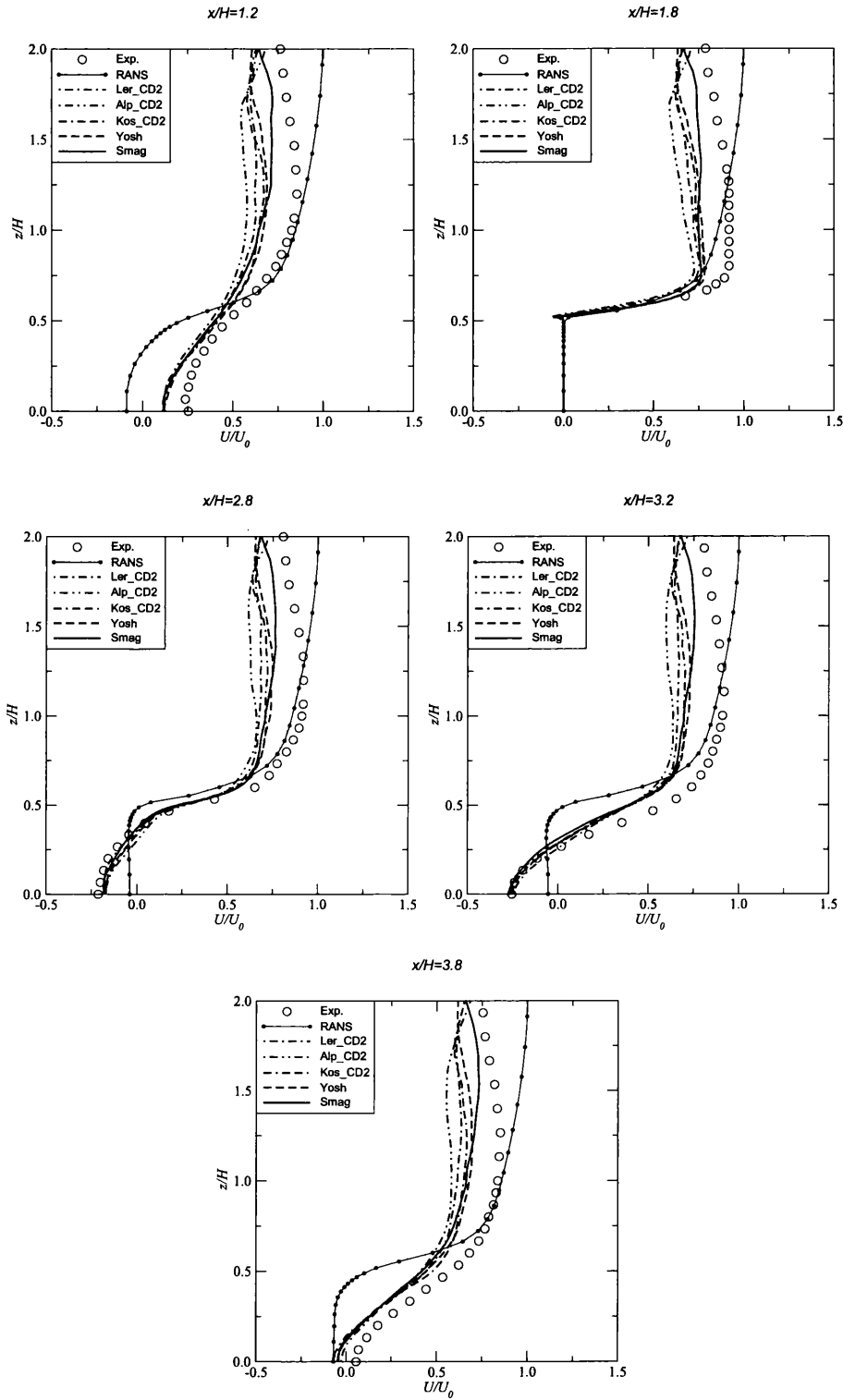
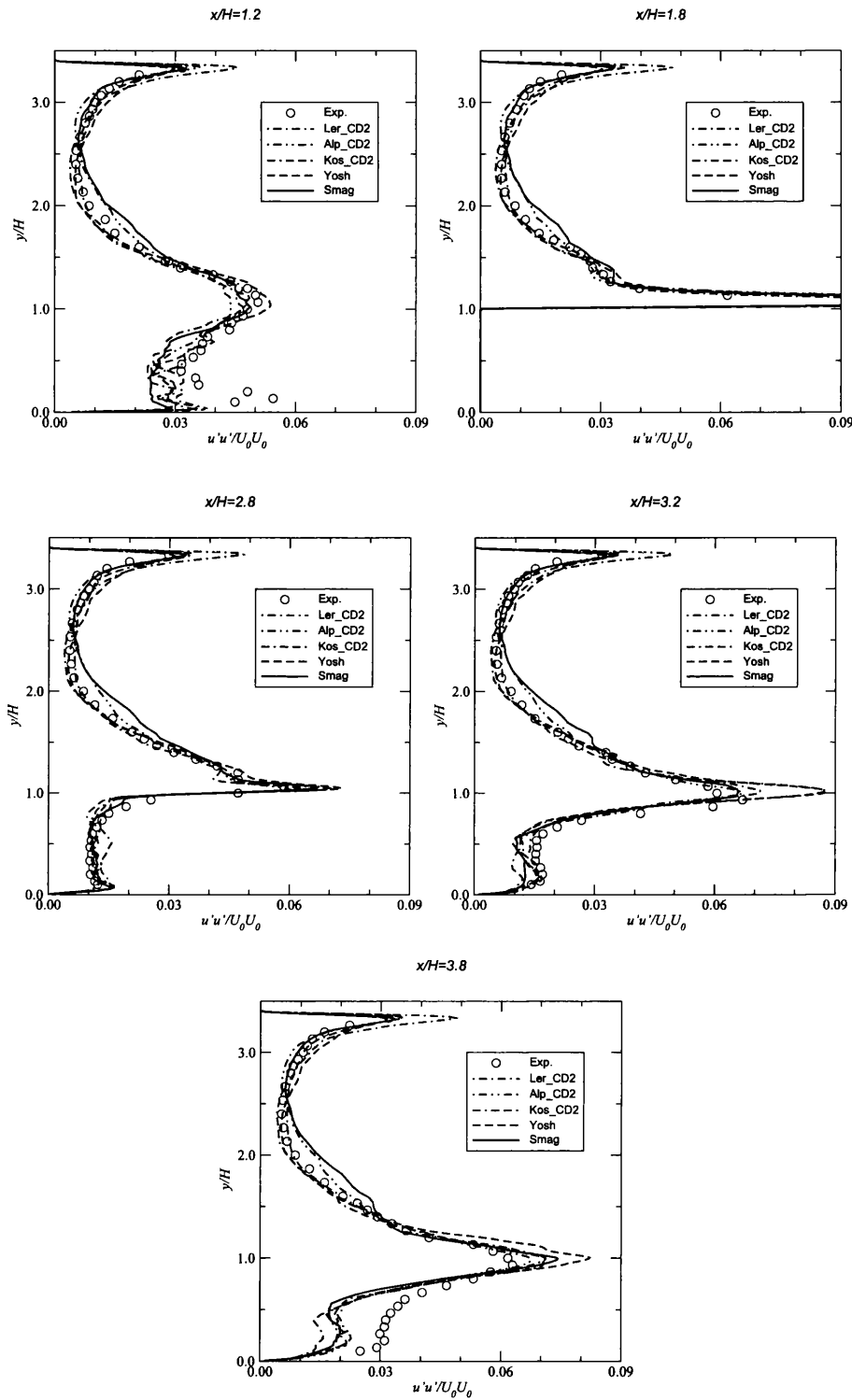


Figure A.58: Mean  $U$  velocity profiles at various  $x/h$ -locations ( $109 \times 109 \times 109$ ).

Figure A.59: Mean  $u'u'$  profiles at various  $x/h$ -locations ( $109 \times 109 \times 109$ ).

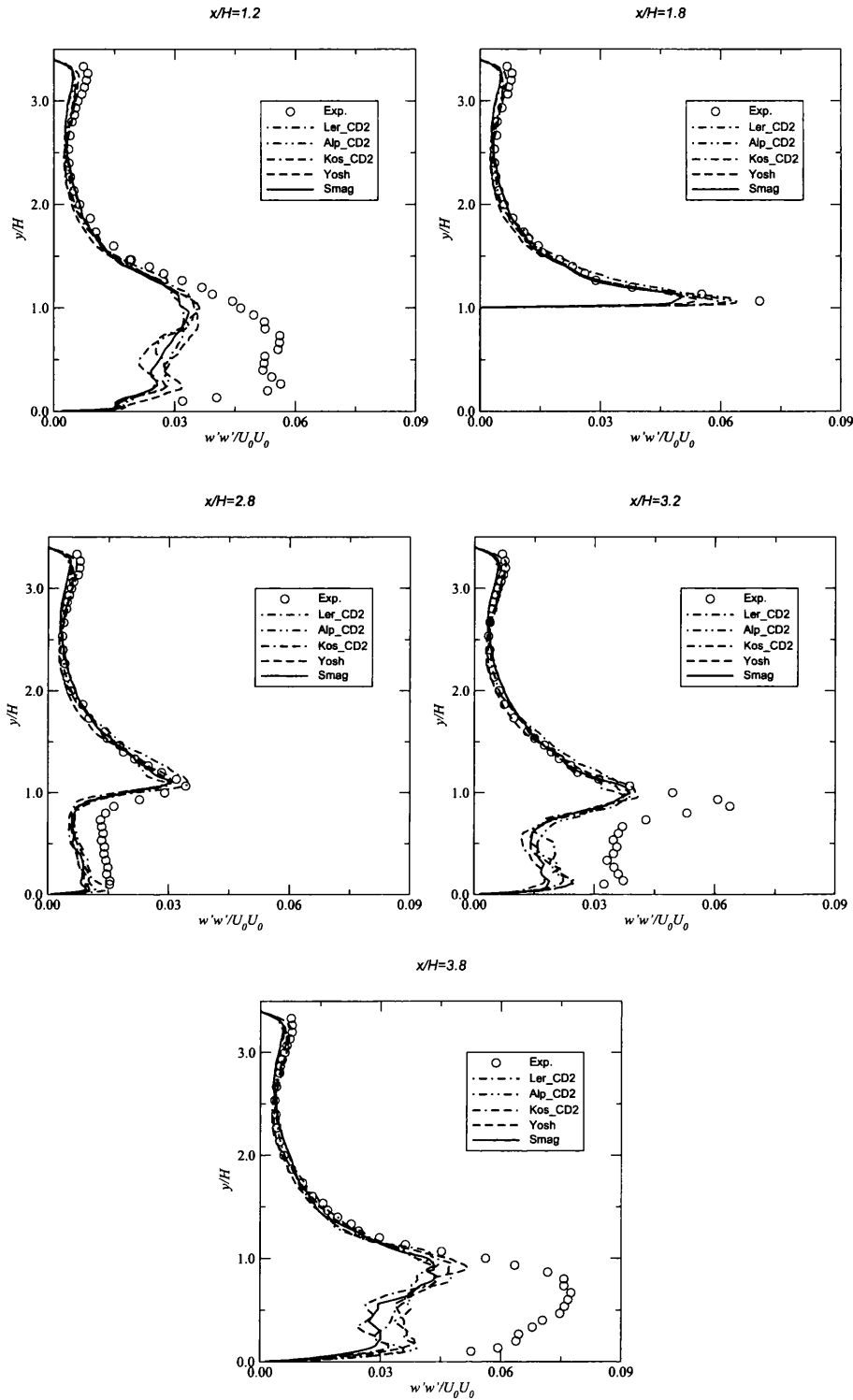
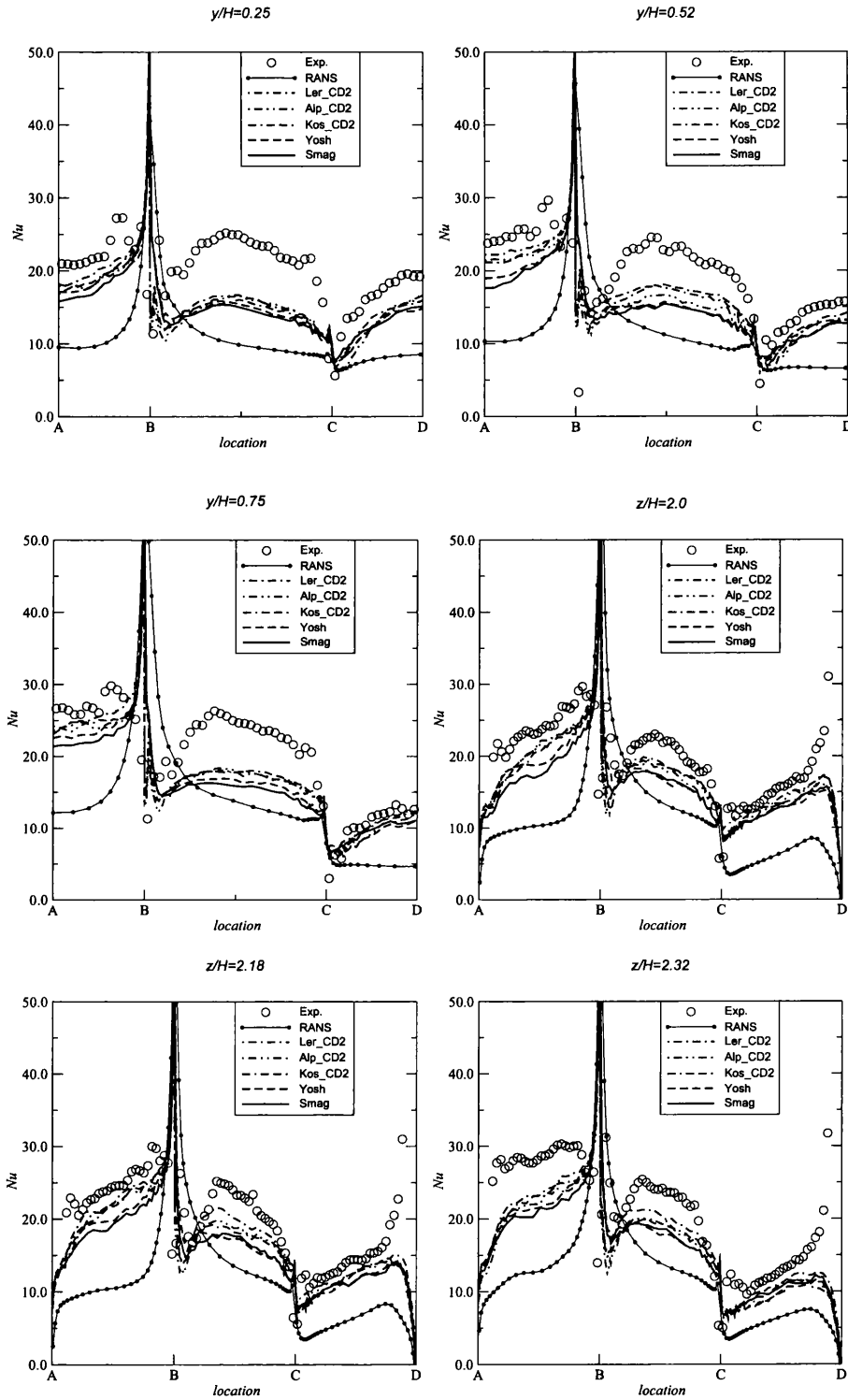


Figure A.60: Mean  $w'w'$  profiles at various  $x/h$ -locations ( $109 \times 109 \times 109$ ).

Figure A.61:  $Nu$  profiles around the heated cube ( $109 \times 109 \times 109$ ).

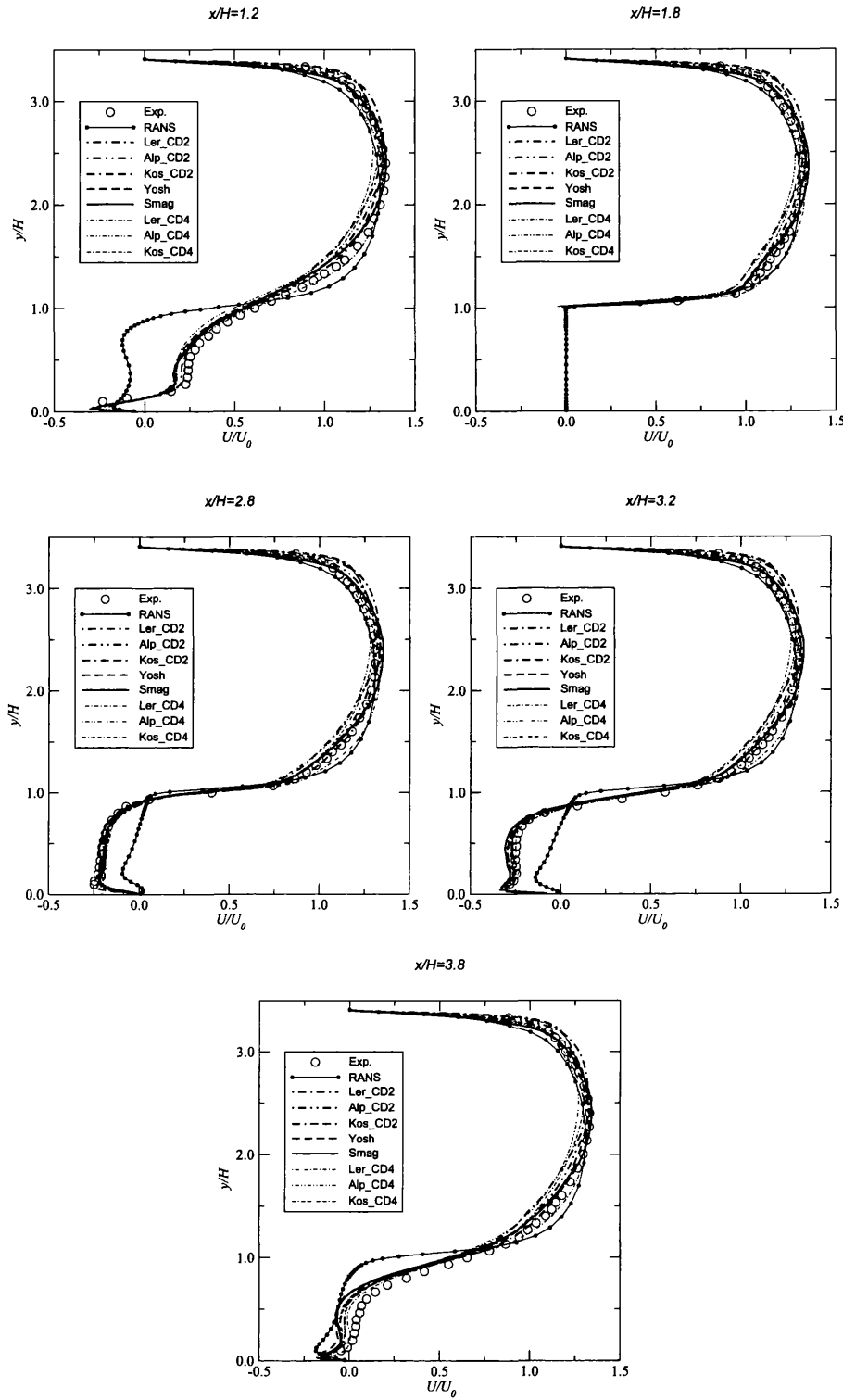


Figure A.62: Mean  $U$  velocity profiles at various  $x/h$ -locations ( $75 \times 75 \times 75$ ).



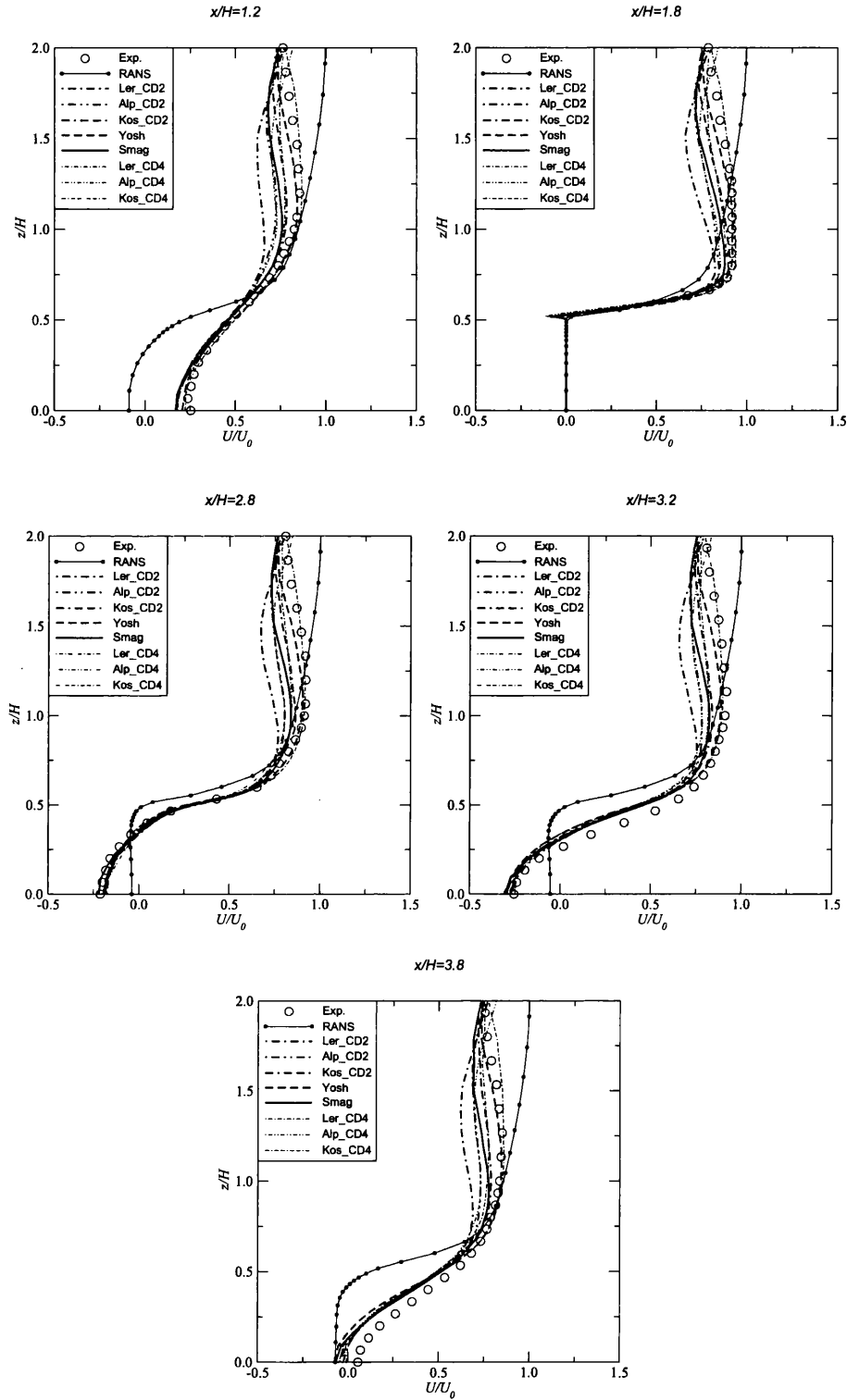


Figure A.63: Mean  $U$  velocity profiles at various  $x/h$ -locations ( $75 \times 75 \times 75$ ).

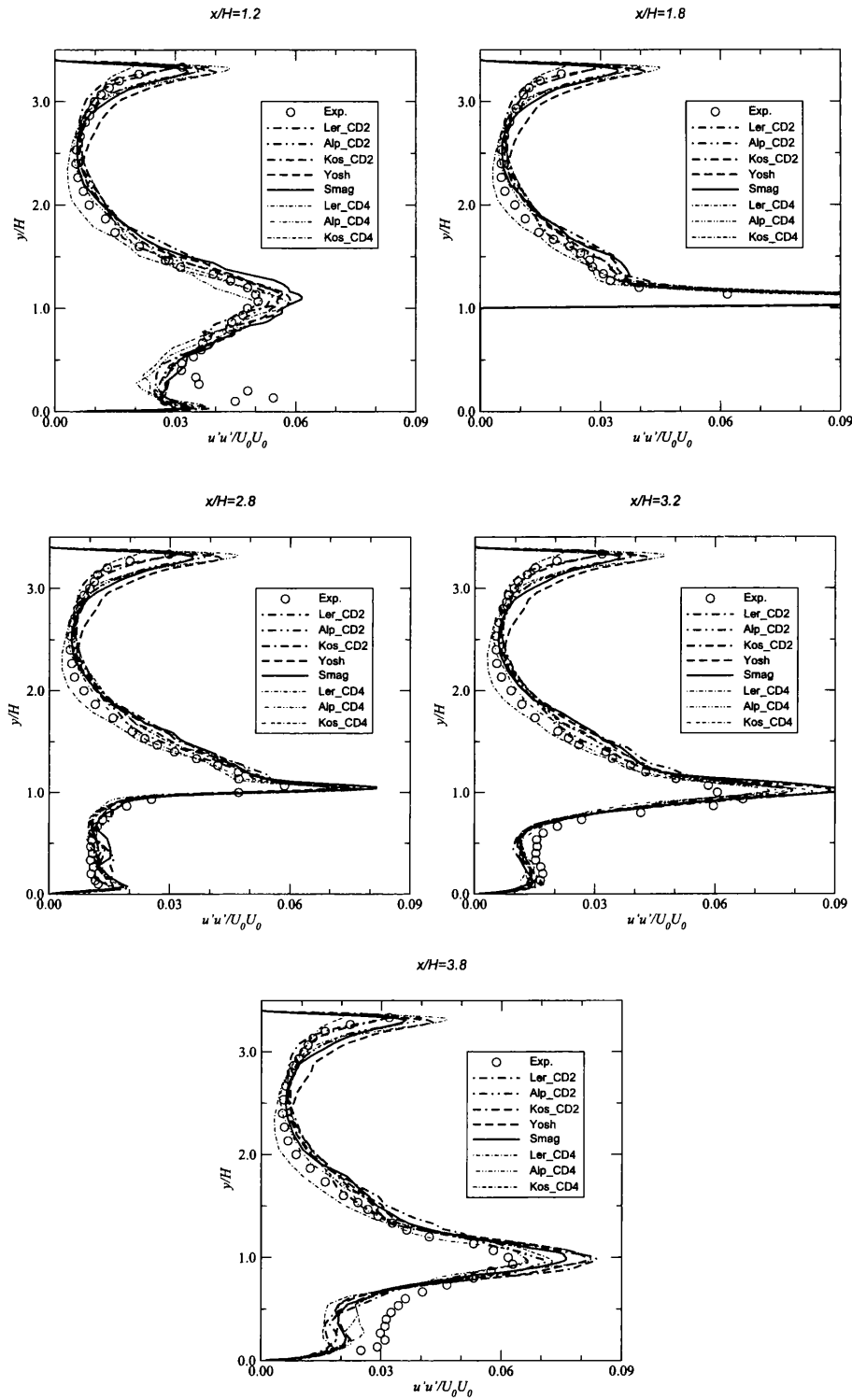


Figure A.64: Mean  $u'u'$  profiles at various  $x/h$ -locations ( $75 \times 75 \times 75$ ).

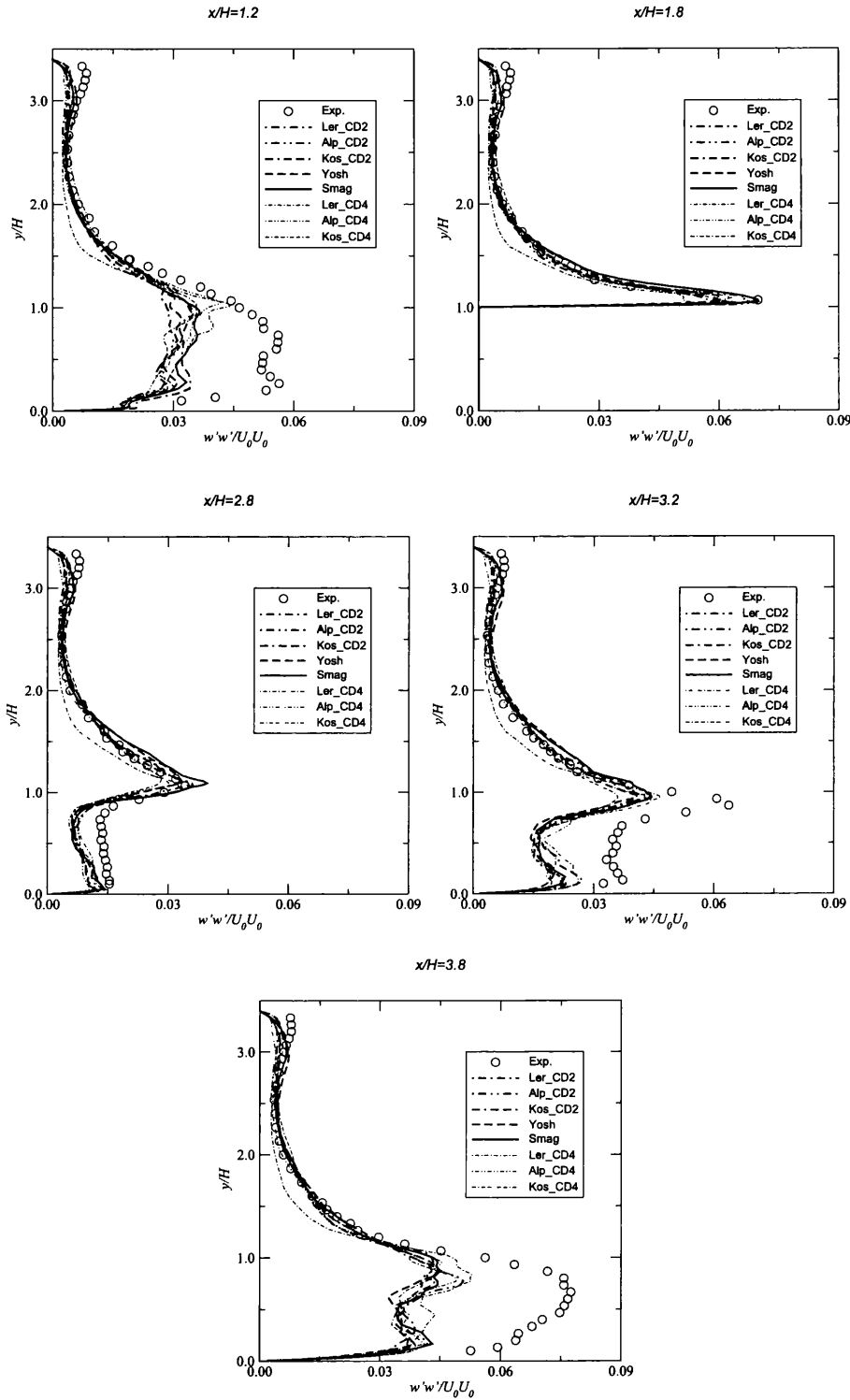


Figure A.65: Mean  $w'w'$  profiles at various  $x/h$ -locations ( $75 \times 75 \times 75$ ).

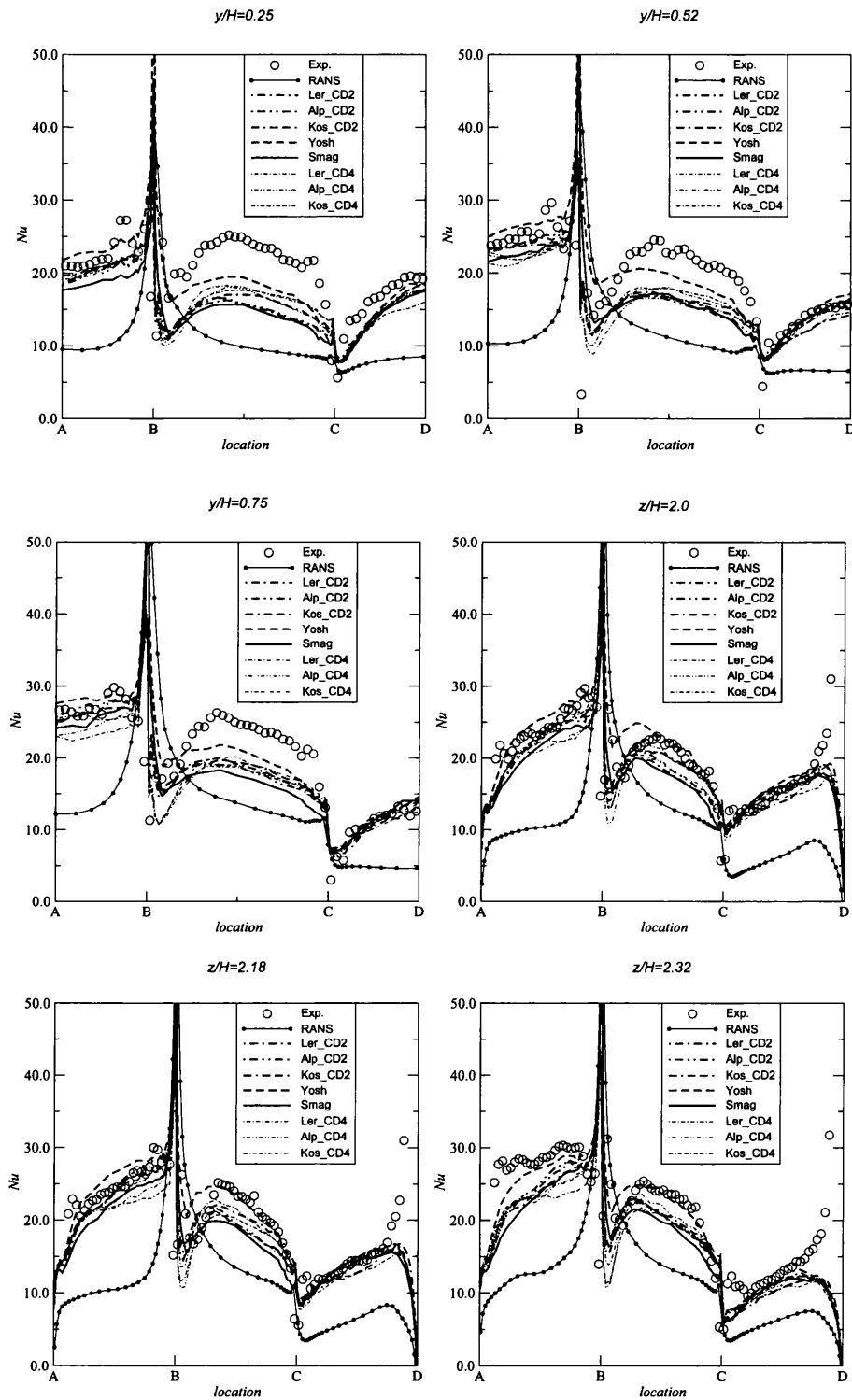
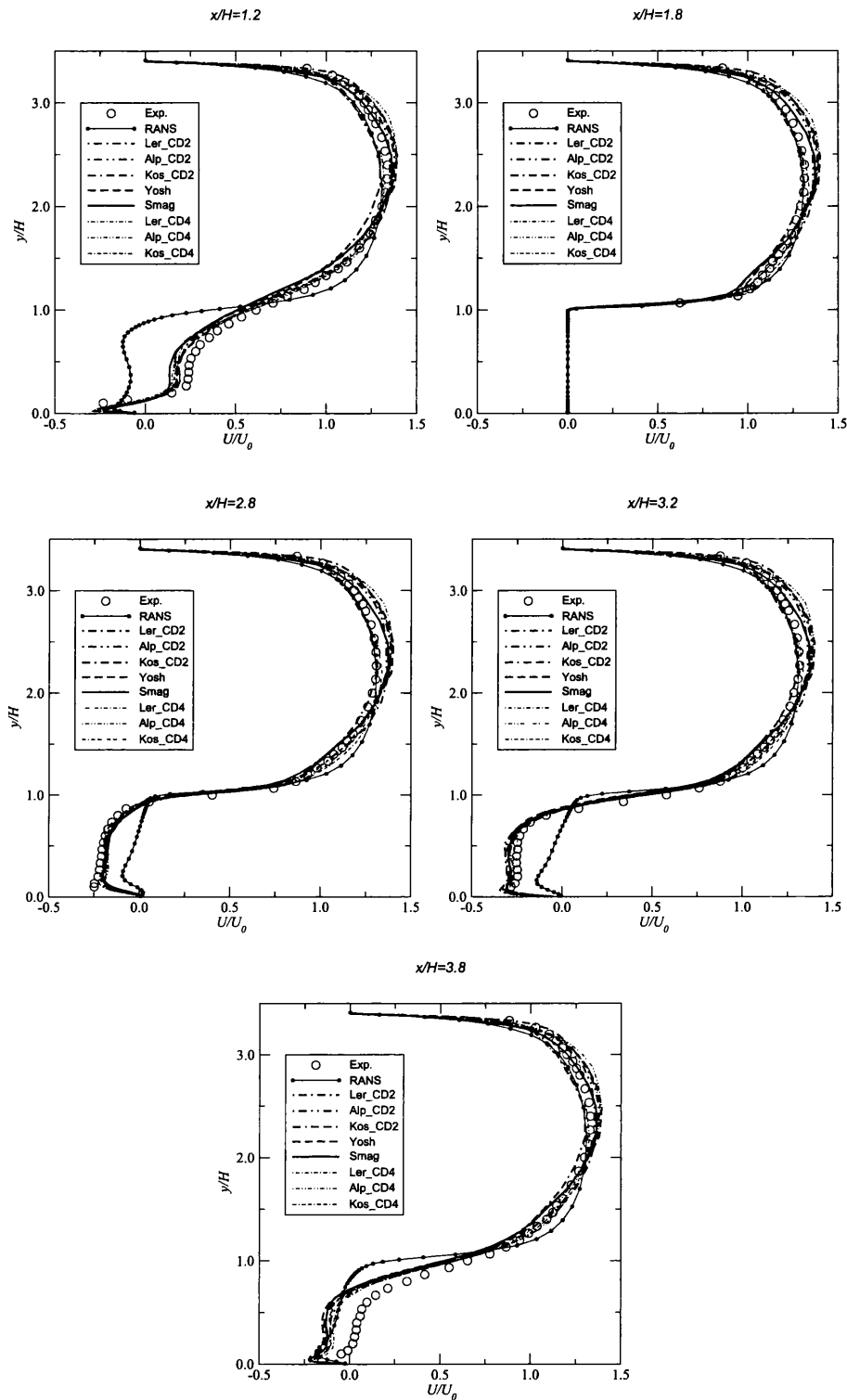


Figure A.66:  $Nu$  profiles around the heated cube ( $75 \times 75 \times 75$ ).

Figure A.67: Mean  $U$  velocity profiles at various  $x/h$ -locations ( $53 \times 51 \times 53$ ).

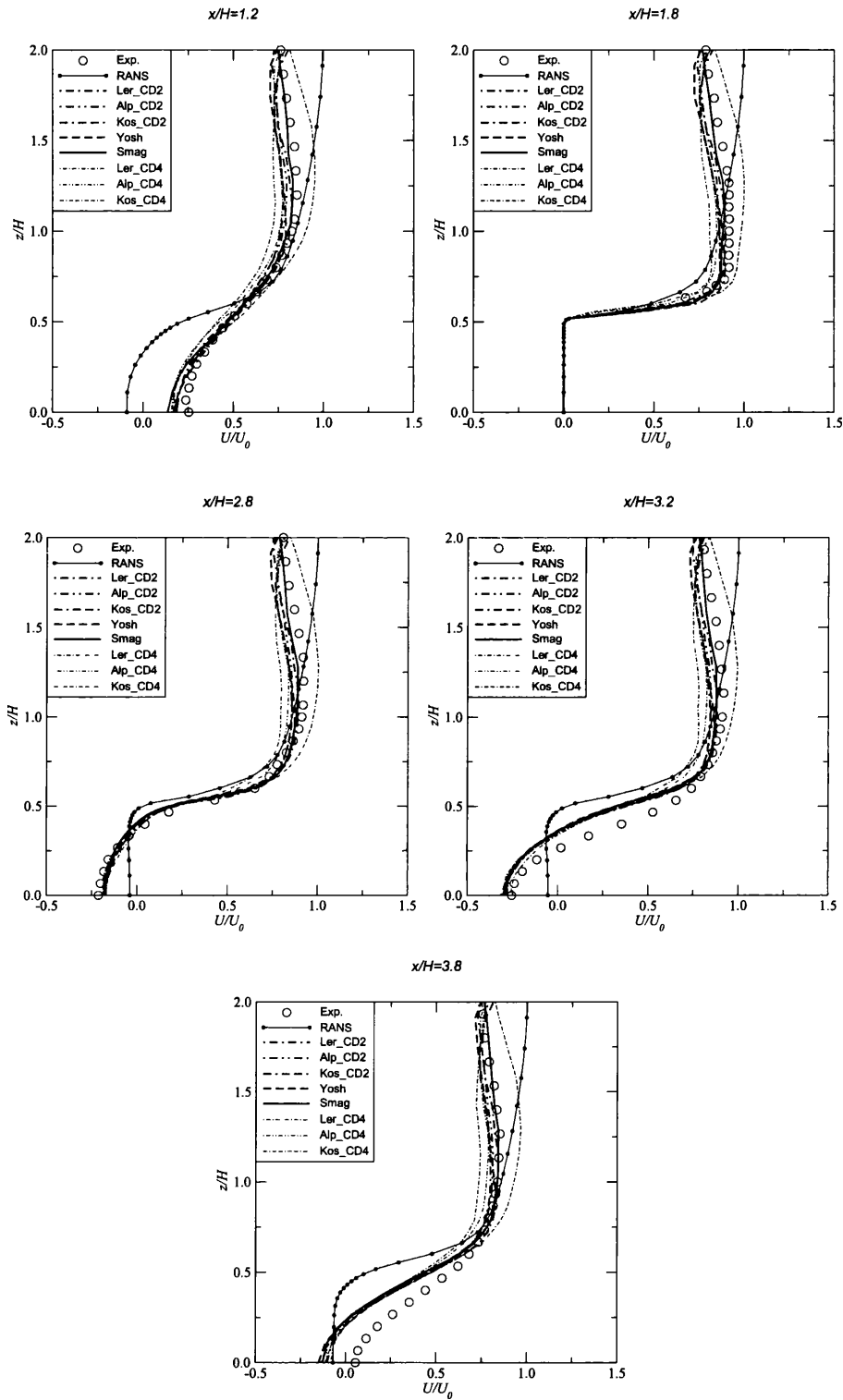


Figure A.68: Mean  $U$  velocity profiles at various  $x/h$ -locations ( $53 \times 51 \times 53$ ).

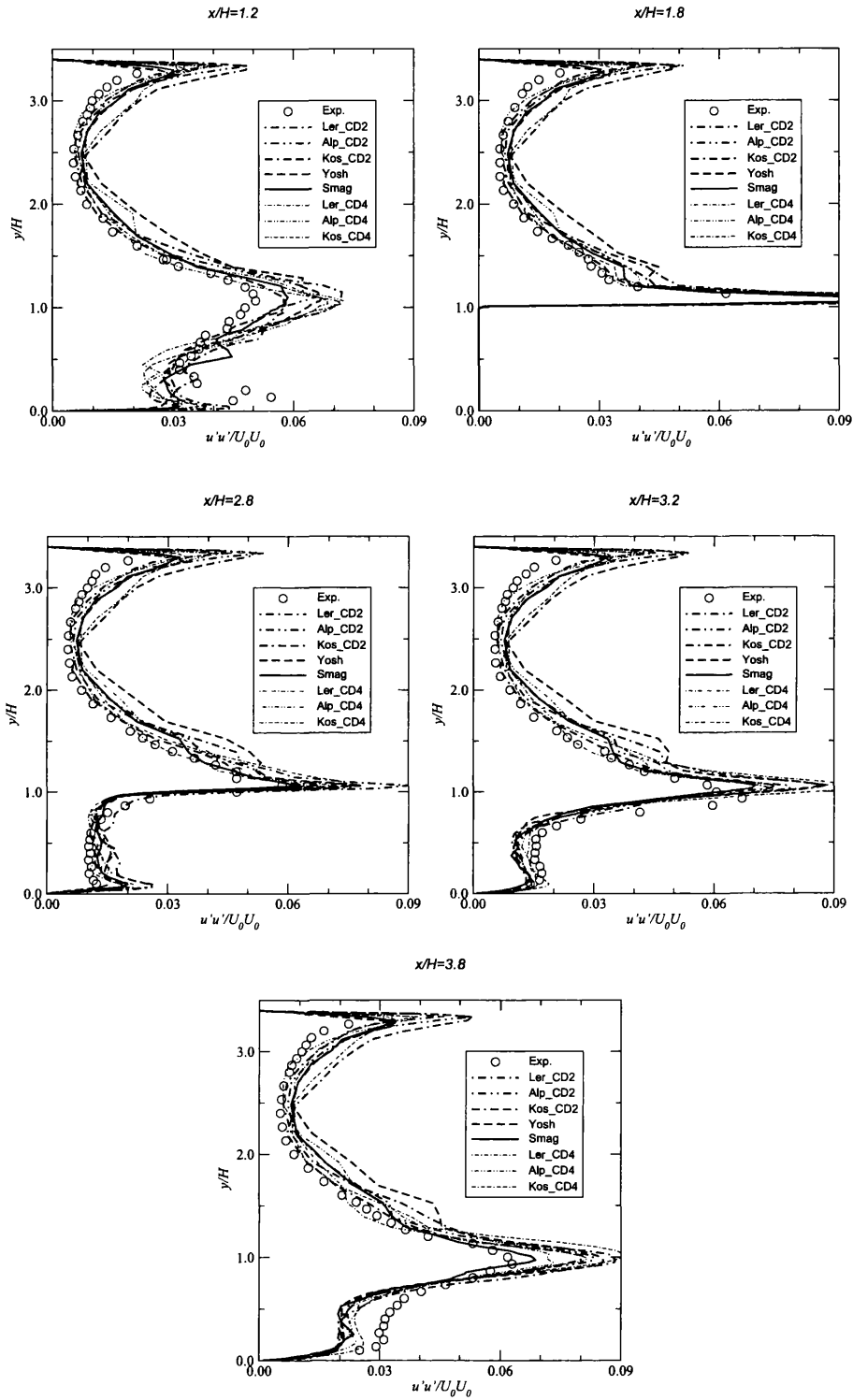


Figure A.69: Mean  $u'u'$  profiles at various  $x/h$ -locations ( $53 \times 51 \times 53$ ).

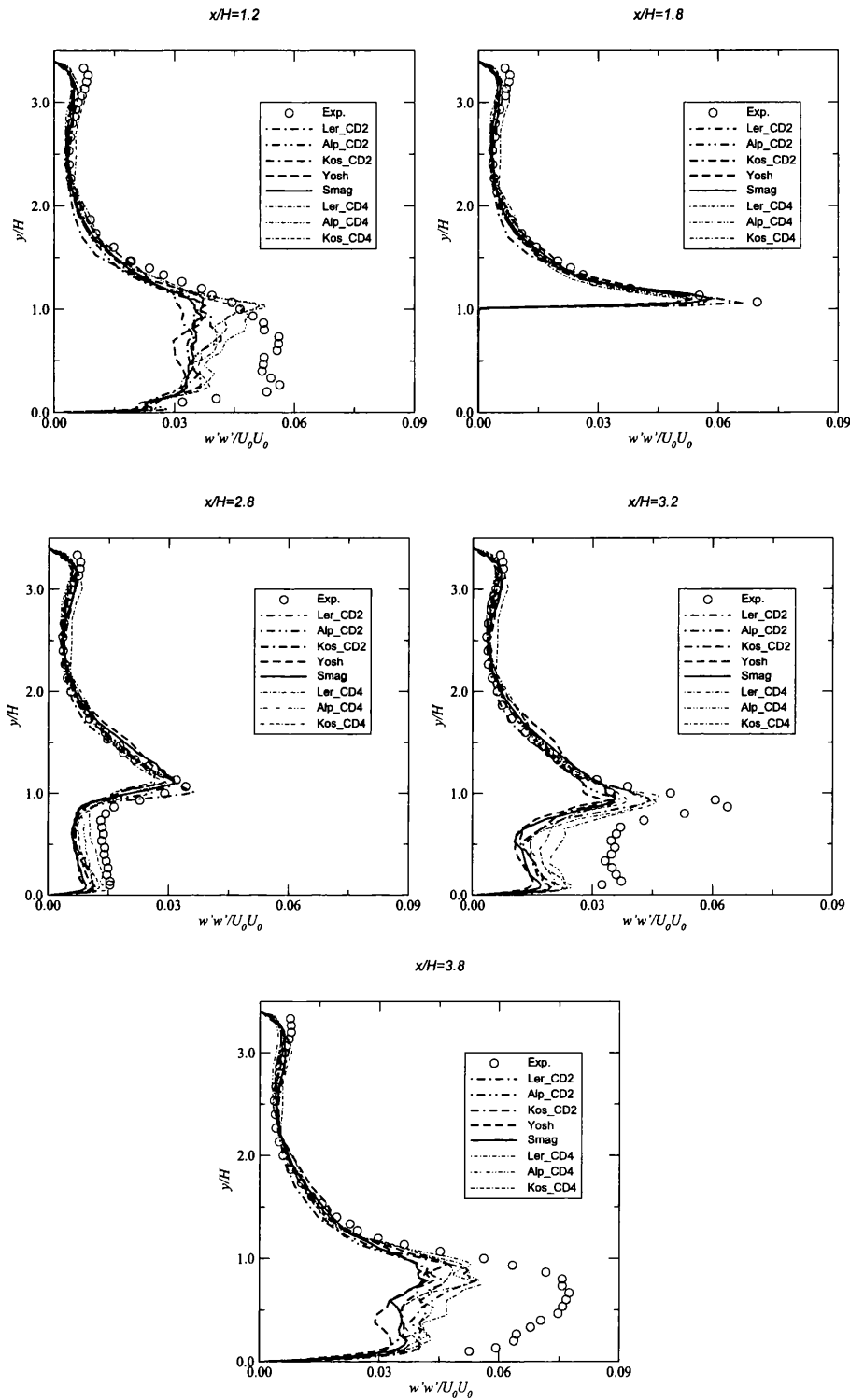


Figure A.70: Mean  $w'w'$  profiles at various  $x/h$ -locations ( $53 \times 51 \times 53$ ).



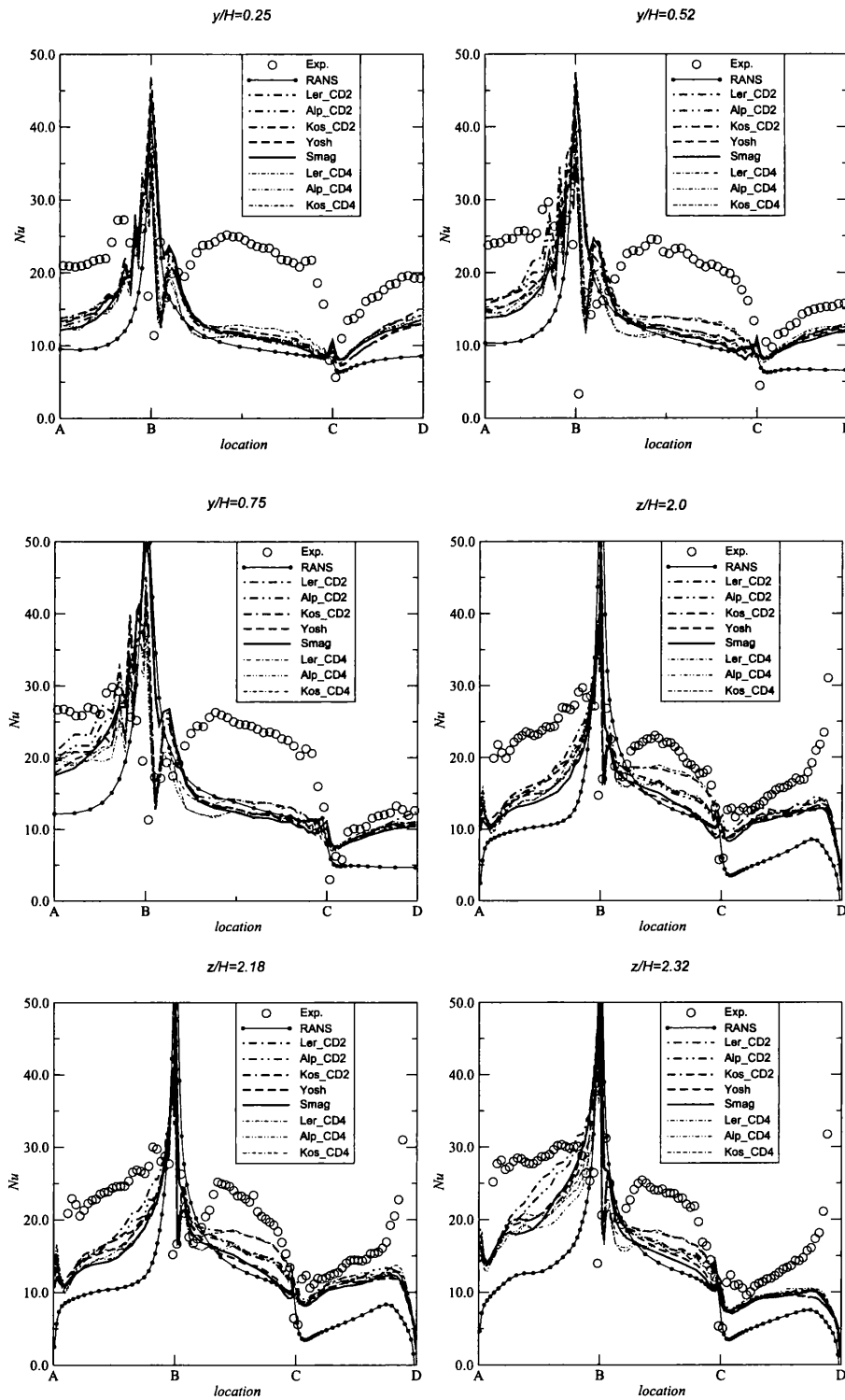
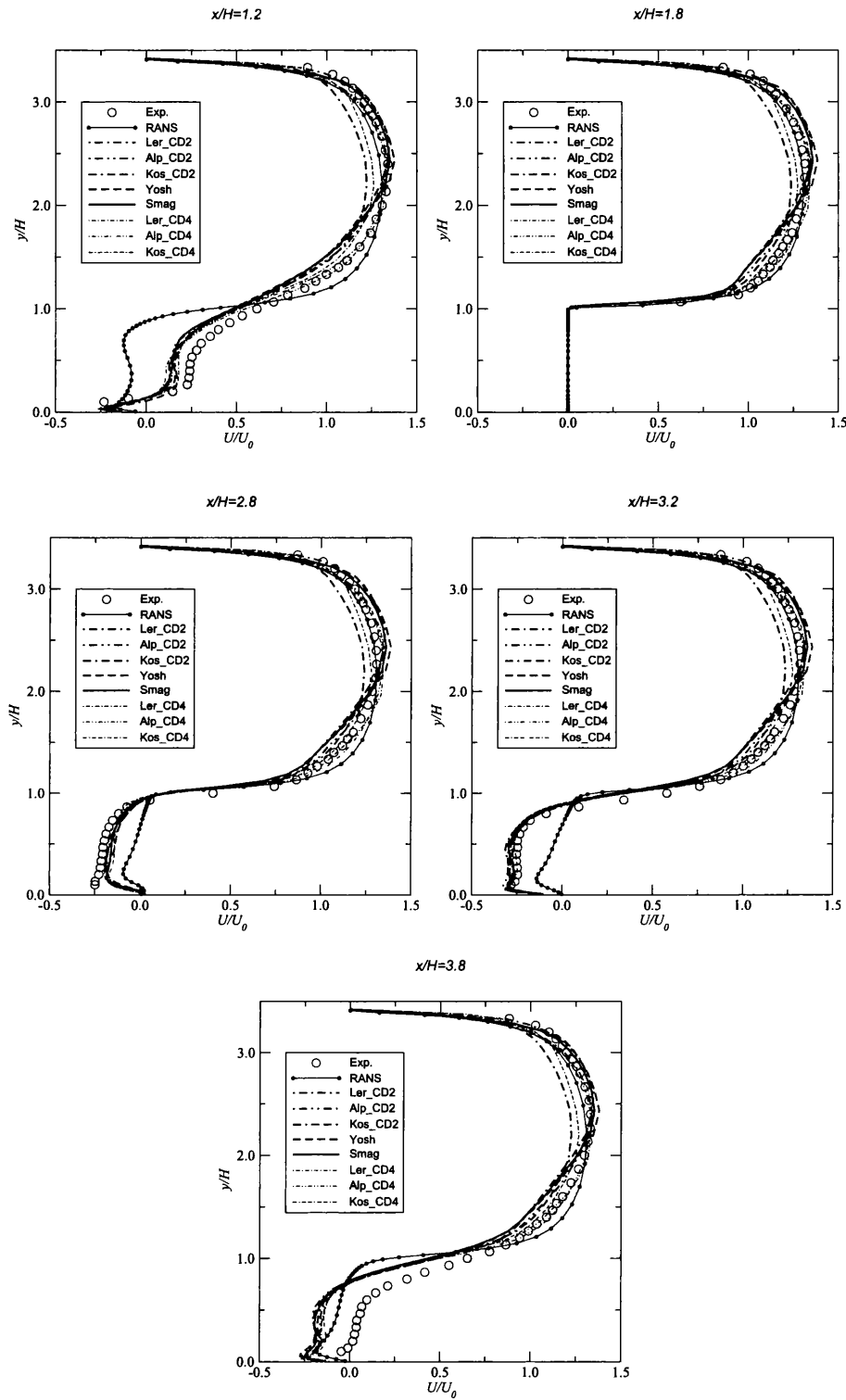


Figure A.71:  $Nu$  profiles around the heated cube ( $53 \times 51 \times 53$ ).

Figure A.72: Mean  $U$  velocity profiles at various  $x/h$ -locations ( $41 \times 45 \times 41$ ).

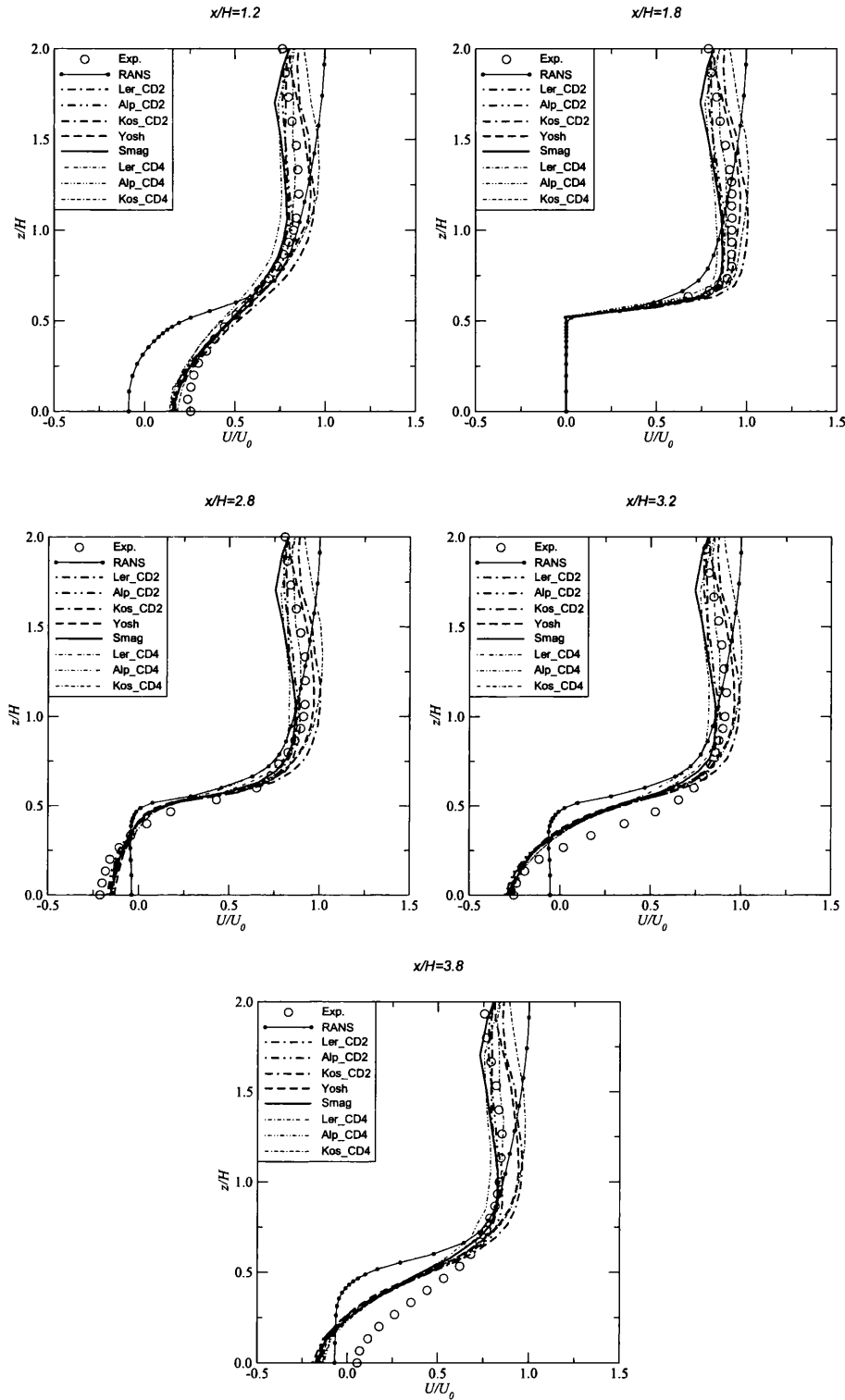


Figure A.73: Mean  $U$  velocity profiles at various  $x/h$ -locations ( $41 \times 45 \times 41$ ).

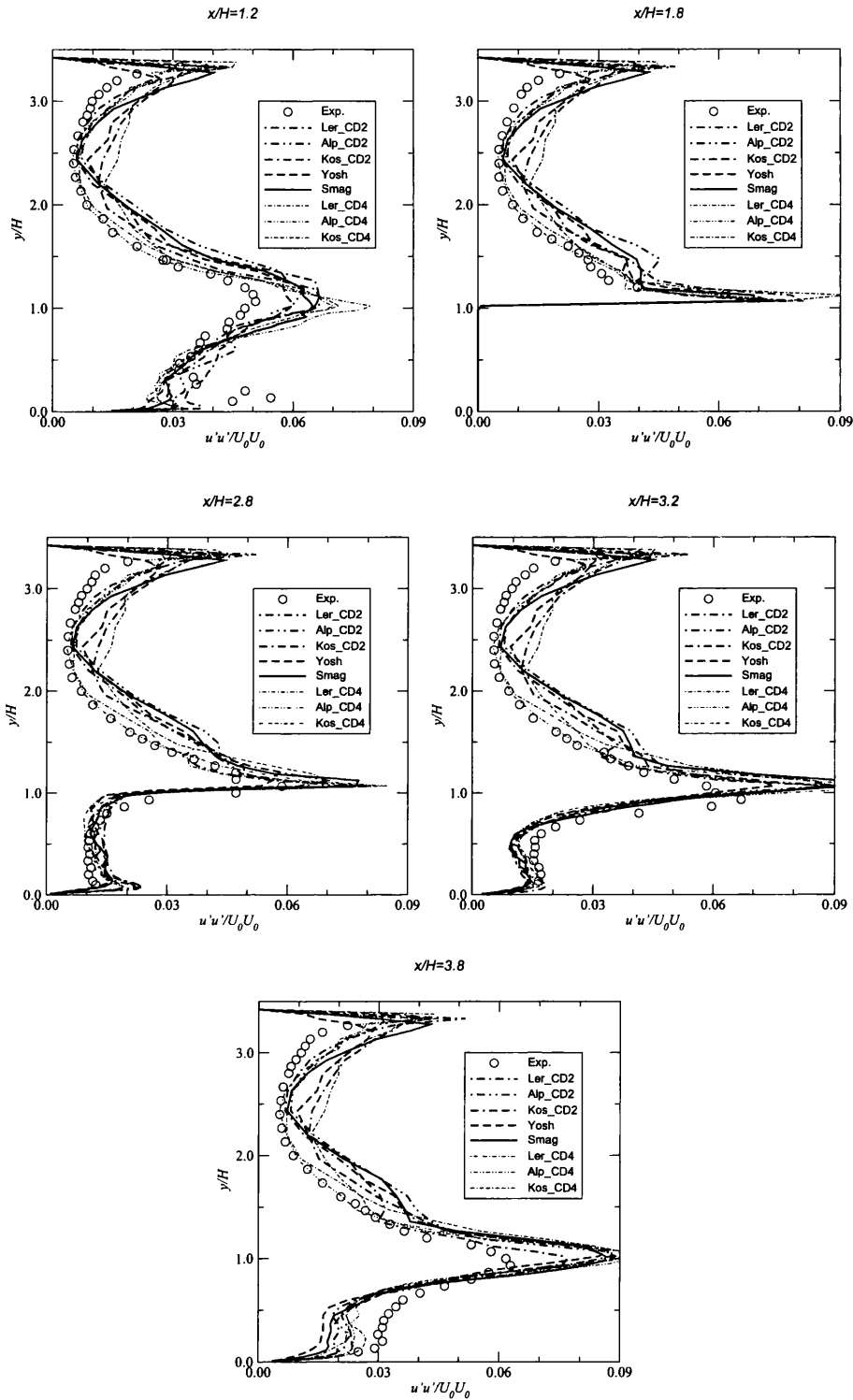


Figure A.74: Mean  $u'u'$  profiles at various  $x/h$ -locations ( $41 \times 45 \times 41$ ).

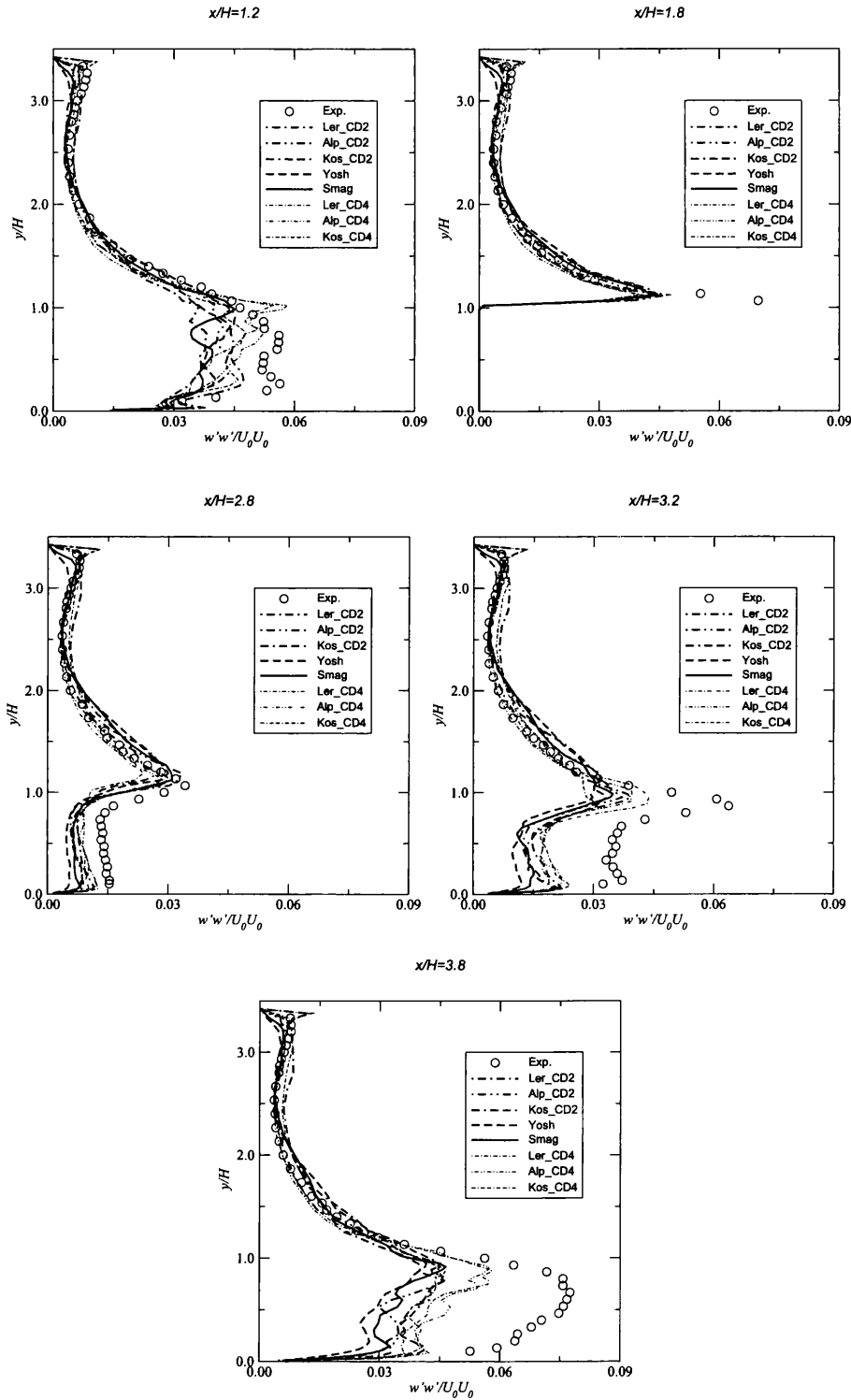
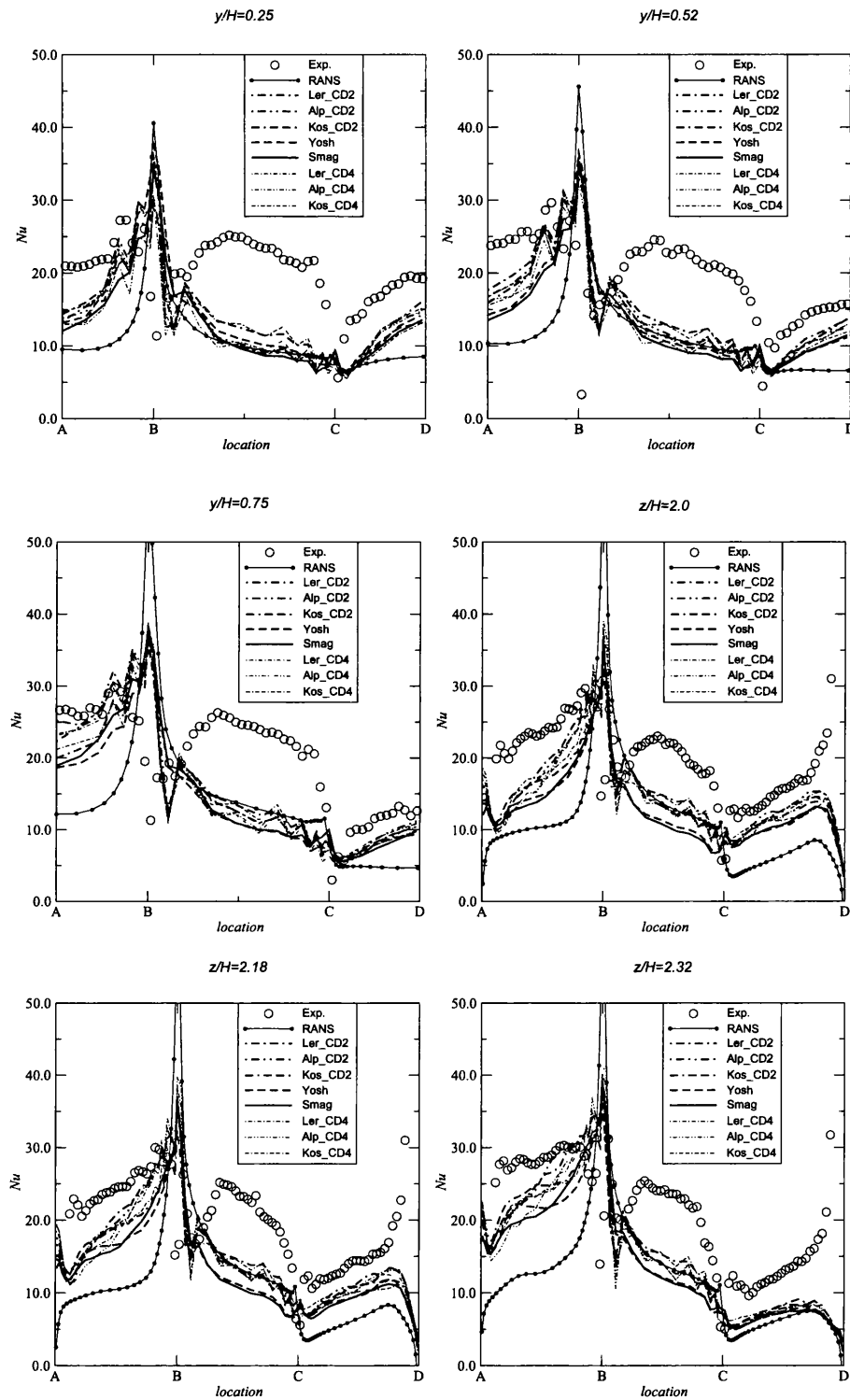


Figure A.75: Mean  $w'w'$  profiles at various  $x/h$ -locations ( $41 \times 45 \times 41$ ).

Figure A.76:  $Nu$  profiles around the heated cube ( $41 \times 45 \times 41$ ).

## A.3 CPU case plots

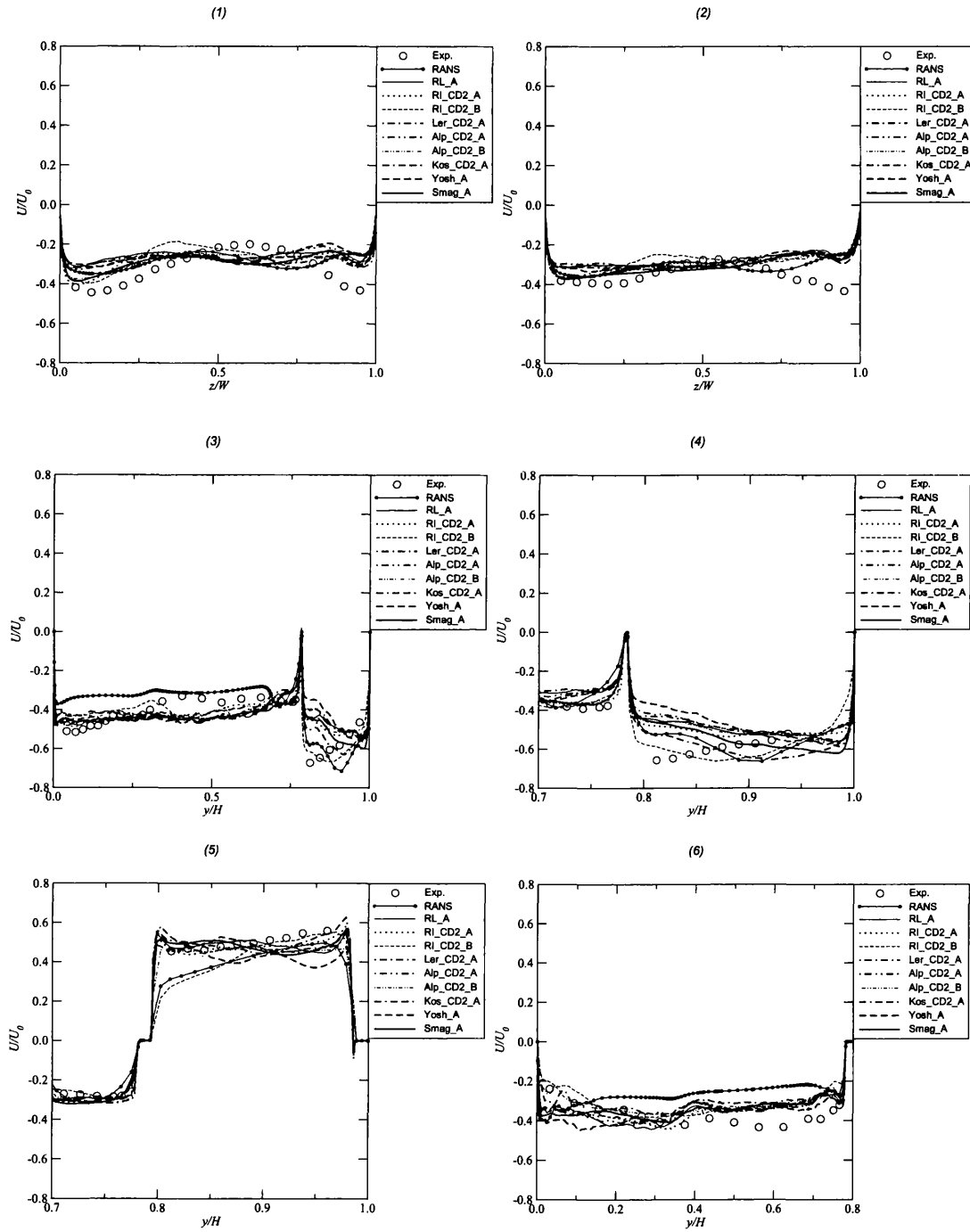


Figure A.77: Mean  $U$  velocity profiles (1-6).



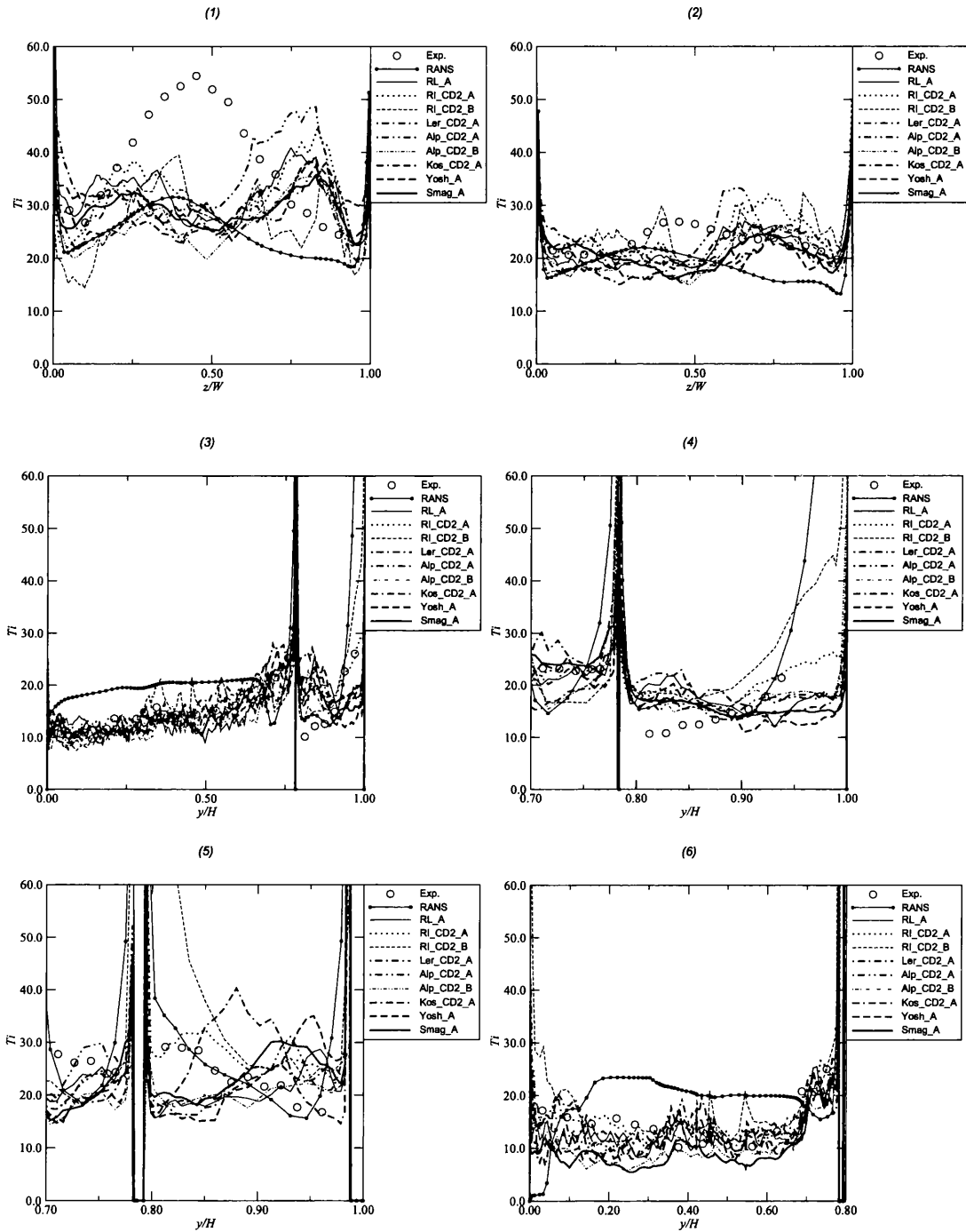


Figure A.78: Turbulence intensity (%) profiles (1-6).

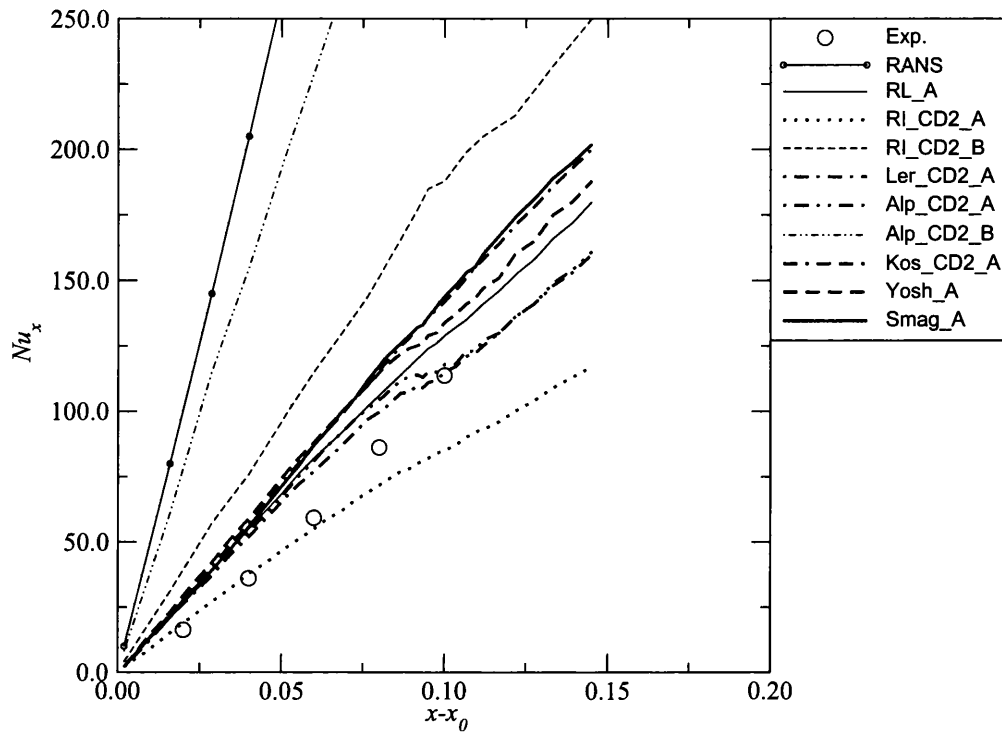


Figure A.79:  $Nu_x$  along the heater element.

# Appendix B

## Derivation and implementation of discretisation schemes

### B.1 Second order upwind scheme with positive coefficients

$$\int \frac{\partial}{\partial x} \rho u \phi + \int \frac{\partial}{\partial y} \rho v \phi - \int \mu \frac{\partial^2 \phi}{\partial x^2} - \int \mu \frac{\partial^2 \phi}{\partial y^2} = S \quad (\text{B.1})$$

This can be written as

$$\begin{aligned} c_e \phi_e - c_w \phi_w + d_w(\phi_P - \phi_W) - d_e(\phi_E - \phi_P) \\ + c_n \phi_n - c_s \phi_s + d_s(\phi_P - \phi_S) - d_n(\phi_N - \phi_P) = S \end{aligned} \quad (\text{B.2})$$

Where the line break separates the East-West (E-W) and North-South (N-S) terms respectively inline with the following one-dimensional treatment in each direction. For three dimensions we also include the Front-Back (F-B) terms. Here,  $c_e = (\rho u)_e \Delta y$ ,  $c_w = (\rho u)_w \Delta y$ ,  $d_e = (\mu \frac{\partial \phi}{\partial x})_e \Delta y$  and  $d_w = (\mu \frac{\partial \phi}{\partial x})_w \Delta y$ . Similar notation can be used for the N-S and F-B terms.

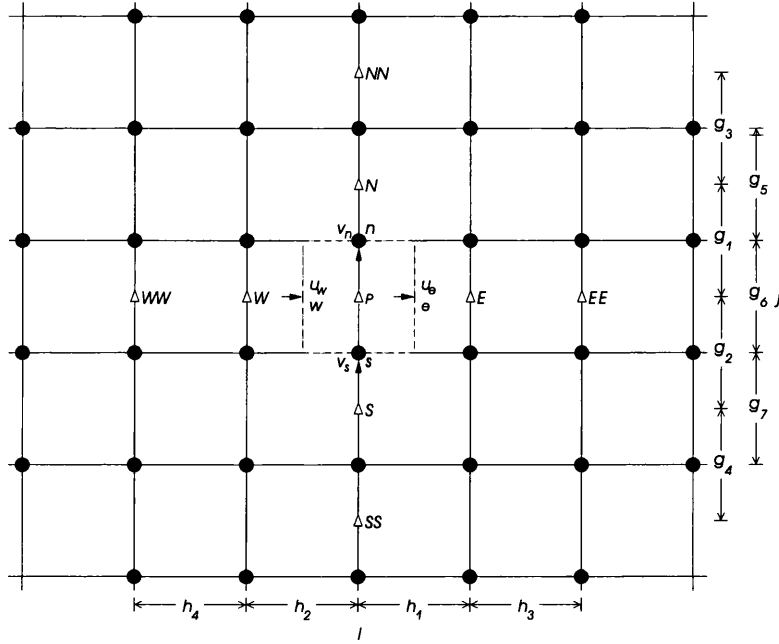


Figure B.1: Cell diagram for variable  $v$ , staggered in the  $j$ -direction.

Starting with the non-staggered variable  $u$  for the  $v$  momentum equation (E-W).

If  $u_w > 0$  then  $\phi_w$  is obtained from  $\phi_W$  and  $\phi_{WW}$ .

If  $u_w < 0$  then  $\phi_w$  is obtained from  $\phi_P$  and  $\phi_E$  (see Figure B.1).

Passing a straight line through the two relevant points with gradient  $m = \frac{\phi_W - \phi_{WW}}{h_4}$ , the velocity for the west cell face can then be written as:

$$\phi_w = \phi_W + \frac{1}{2} \frac{h_2}{h_4} (\phi_W - \phi_{WW}) \quad (\text{B.3})$$

Cell face values for different flow directions may be expressed as shown below by separating the nodal velocities.

$$\begin{aligned} u_w > 0 \quad \phi_w &= \left(1 + \frac{1}{2} \frac{h_2}{h_4}\right) \phi_W - \left(\frac{1}{2} \frac{h_2}{h_4}\right) \phi_{WW} \\ u_w < 0 \quad \phi_w &= \left(1 + \frac{1}{2} \frac{h_2}{h_1}\right) \phi_P - \left(\frac{1}{2} \frac{h_2}{h_1}\right) \phi_E \\ u_e > 0 \quad \phi_e &= \left(1 + \frac{1}{2} \frac{h_1}{h_2}\right) \phi_P - \left(\frac{1}{2} \frac{h_1}{h_2}\right) \phi_W \\ u_e < 0 \quad \phi_e &= \left(1 + \frac{1}{2} \frac{h_1}{h_3}\right) \phi_E - \left(\frac{1}{2} \frac{h_1}{h_3}\right) \phi_{EE} \end{aligned} \quad (\text{B.4})$$

Noting that  $|A, B|$  represents taking the maximum of  $A$  and  $B$ , substituting the expressions from B.4 into (B.2) and accounting for both flow directions:

$$\begin{aligned}
 & |c_e, 0| \left(1 + \frac{1}{2} \frac{h_1}{h_2}\right) \phi_P - |c_e, 0| \left(\frac{1}{2} \frac{h_1}{h_2}\right) \phi_W \\
 & \quad - |-c_e, 0| \left(1 + \frac{1}{2} \frac{h_1}{h_3}\right) \phi_E + |-c_e, 0| \left(\frac{1}{2} \frac{h_1}{h_3}\right) \phi_{EE} \\
 & \quad - |c_w, 0| \left(1 + \frac{1}{2} \frac{h_2}{h_4}\right) \phi_W + |c_w, 0| \left(\frac{1}{2} \frac{h_2}{h_4}\right) \phi_{WW} \\
 & \quad + |-c_w, 0| \left(1 + \frac{1}{2} \frac{h_2}{h_1}\right) \phi_P - |-c_w, 0| \left(\frac{1}{2} \frac{h_2}{h_1}\right) \phi_E \\
 & \hspace{15em} + Diff = 0 \quad (B.5)
 \end{aligned}$$

$$\begin{aligned}
 & |c_e, 0| \left(\frac{3}{2} + \frac{h_1 - h_2}{2h_2}\right) \phi_P - |c_e, 0| \left(\frac{1}{2} \frac{h_1}{h_2}\right) \phi_W \\
 & \quad - |-c_e, 0| \left(\frac{3}{2} + \frac{h_1 - h_3}{2h_3}\right) \phi_E + |-c_e, 0| \left(\frac{1}{2} \frac{h_1}{h_3}\right) \phi_{EE} \\
 & \quad - |c_w, 0| \left(\frac{3}{2} + \frac{h_2 - h_4}{2h_4}\right) \phi_W + |c_w, 0| \left(\frac{1}{2} \frac{h_2}{h_4}\right) \phi_{WW} \\
 & \quad + |-c_w, 0| \left(\frac{3}{2} + \frac{h_2 - h_1}{2h_1}\right) \phi_P - |-c_w, 0| \left(\frac{1}{2} \frac{h_2}{h_1}\right) \phi_E \\
 & \hspace{15em} + Diff = 0 \quad (B.6)
 \end{aligned}$$

$$\begin{aligned}
 \frac{3}{2} |c_e, 0| \phi_P + \frac{3}{2} |-c_w, 0| \phi_P &= \frac{3}{2} |-c_e, 0| \phi_E + \frac{3}{2} |c_w, 0| \phi_W \\
 & \quad + d_e \phi_E + d_w \phi_W - d_e \phi_P - d_w \phi_P + S \quad (B.7)
 \end{aligned}$$

Where,

$$\begin{aligned}
 S = & -|-c_e, 0| \frac{h_1}{2h_3} \phi_{EE} - |c_w, 0| \frac{h_2}{2h_4} \phi_{WW} \\
 & + |-c_w, 0| \frac{h_2}{2h_1} \phi_E + |c_e, 0| \frac{h_1}{2h_2} \phi_W \\
 & + |c_e, 0| \frac{h_2 - h_1}{2h_2} \phi_P + |-c_w, 0| \frac{h_1 - h_2}{2h_1} \phi_P \\
 & + |-c_e, 0| \frac{h_1 - h_3}{2h_3} \phi_E + |c_w, 0| \frac{h_2 - h_4}{2h_4} \phi_W \quad (\text{B.8})
 \end{aligned}$$

Subtracting  $\frac{3}{2}(c_e - c_w + c_n - c_s + c_f - c_b) = 0$  from the LHS of Equation B.7 ensures that  $a_p = \sum a_{nb}$  ( $nb$  refers to the neighbouring coefficients  $e, w, n, s, f, b$ ) regardless of flow direction. We have not treated the N-S and F-B directions yet, so we must not forget that we have subtracted these terms from  $a_p$  in these directions.

This leaves us with

$$\begin{aligned}
 & \left[ d_e + \frac{3}{2} |c_e, 0| - \frac{3}{2} c_e \right] \phi_P + \left[ d_w + \frac{3}{2} |-c_w, 0| + \frac{3}{2} c_w \right] \phi_P \\
 & = \left[ d_e + \frac{3}{2} |-c_e, 0| \right] \phi_E + \left[ d_w + \frac{3}{2} |c_w, 0| \right] \phi_W + S \quad (\text{B.9})
 \end{aligned}$$

Therefore  $a_e = d_e + \frac{3}{2} |-c_e, 0|$  and  $a_w = d_w + \frac{3}{2} |c_w, 0|$  which are always positive, increasing diagonal dominance of the coefficient matrix. Similar terms can be obtained for the N-S and F-B directions. The above would be the E-W treatment used for the  $v$  and  $w$  equations. Similarly the N-S treatment for the  $u$  equation can be obtained replacing  $e$  with  $n$  etc.

Considering the N-S direction for  $v$ :

If  $v_s > 0$  then  $\phi_s$  is obtained from  $\phi_S$  and  $\phi_{SS}$ .

If  $v_s < 0$  then  $\phi_s$  is obtained from  $\phi_P$  and  $\phi_N$ .

$$\begin{aligned}
 v_s > 0 \quad \phi_s &= \left(1 + \frac{1}{2} \frac{g_7}{g_4}\right) \phi_S - \left(\frac{1}{2} \frac{g_7}{g_4}\right) \phi_{SS} \\
 v_s < 0 \quad \phi_s &= \left(1 + \frac{1}{2} \frac{g_6}{g_1}\right) \phi_P - \left(\frac{1}{2} \frac{g_6}{g_1}\right) \phi_N \\
 v_n > 0 \quad \phi_n &= \left(1 + \frac{1}{2} \frac{g_6}{g_2}\right) \phi_P - \left(\frac{1}{2} \frac{g_6}{g_2}\right) \phi_S \\
 v_n < 0 \quad \phi_n &= \left(1 + \frac{1}{2} \frac{g_5}{g_3}\right) \phi_N - \left(\frac{1}{2} \frac{g_5}{g_3}\right) \phi_{NN}
 \end{aligned}$$

Taking the N-S terms from Equation B.2 and performing the same steps as before:

$$\begin{aligned}
 |c_n, 0| \left(1 + \frac{1}{2} \frac{g_6}{g_2}\right) \phi_P - |c_n, 0| \left(\frac{1}{2} \frac{g_6}{g_2}\right) \phi_S \\
 - |c_n, 0| \left(1 + \frac{1}{2} \frac{g_5}{g_3}\right) \phi_N + |c_n, 0| \left(\frac{1}{2} \frac{g_5}{g_3}\right) \phi_{NN} - \\
 |c_s, 0| \left(1 + \frac{1}{2} \frac{g_7}{g_4}\right) \phi_S + |c_s, 0| \left(\frac{1}{2} \frac{g_7}{g_4}\right) \phi_{SS} \\
 + |c_s, 0| \left(1 + \frac{1}{2} \frac{g_6}{g_1}\right) \phi_P - |c_s, 0| \left(\frac{1}{2} \frac{g_6}{g_1}\right) \phi_N \\
 + Diff = 0 \quad (\text{B.10})
 \end{aligned}$$

therefore

$$\begin{aligned}
 |c_n, 0| \left(\frac{3}{2} + \frac{g_6 - g_2}{2g_2}\right) \phi_P - |c_n, 0| \left(\frac{1}{2} \frac{g_6}{g_2}\right) \phi_S \\
 - |c_n, 0| \left(\frac{3}{2} + \frac{g_5 - g_3}{2g_3}\right) \phi_N + |c_n, 0| \left(\frac{1}{2} \frac{g_5}{g_3}\right) \phi_{NN} - \\
 |c_s, 0| \left(\frac{3}{2} + \frac{g_7 - g_4}{2g_4}\right) \phi_S + |c_s, 0| \left(\frac{1}{2} \frac{g_7}{g_4}\right) \phi_{SS} \\
 + |c_s, 0| \left(\frac{3}{2} + \frac{g_6 - g_1}{2g_1}\right) \phi_P - |c_s, 0| \left(\frac{1}{2} \frac{g_6}{g_1}\right) \phi_N \\
 + Diff = 0 \quad (\text{B.11})
 \end{aligned}$$

By inspection:

$$a_n = d_n + \frac{3}{2} |c_n, 0| \quad \text{and} \quad a_s = d_s + \frac{3}{2} |c_s, 0|$$

with source term

$$\begin{aligned}
 S = & -|c_n, 0| \frac{g_5}{2g_3} \phi_{NN} - |c_s, 0| \frac{g_7}{2g_4} \phi_{SS} \\
 & + |-c_s, 0| \frac{g_6}{2g_1} \phi_N + |c_n, 0| \frac{g_6}{2g_2} \phi_S \\
 & + |c_n, 0| \frac{g_2 - g_6}{2g_2} \phi_P + |-c_s, 0| \frac{g_1 - g_6}{2g_1} \phi_P \\
 & + |-c_n, 0| \frac{g_5 - g_3}{2g_3} \phi_N + |c_s, 0| \frac{g_7 - g_4}{2g_4} \phi_S \quad (\text{B.12})
 \end{aligned}$$

This represents the N-S treatment for the staggered variable  $v$  for the  $v$ -equation. Substitutions can be made for the E-W terms of the  $u$ -equation or the F-B terms of  $w$ -equation.

## B.2 QUICK scheme with positive coefficients

Starting with the E-W direction.

If  $u_w > 0$  : Fit a parabola through WW, W and P to find  $\phi_w$

If  $u_w < 0$  : Fit a parabola through E, P and W to find  $\phi_w$

For  $u_w > 0$

Take datum  $x = 0$  at W.

$$\phi - \phi_w = ax + bx^2 \quad (\text{B.13})$$

$$x = +h_2 : \phi_P - \phi_w = ah_2 + bh_2^2 \quad (\text{B.14})$$

$$x = -h_4 : \phi_{WW} - \phi_w = -ah_4 + bh_4^2 \quad (\text{B.15})$$



Multiplying by  $h_4^2$  and  $h_2^2$

$$h_4^2\phi_P - h_4^2\phi_W = ah_2h_4^2 + bh_2^2h_4^2 \quad (\text{B.16})$$

$$h_2^2\phi_{WW} - h_2^2\phi_W = -ah_4h_2^2 + bh_2^2h_4^2 \quad (\text{B.17})$$

Subtracting (B.17) from (B.16),

$$a = \frac{1}{h_2h_4(h_2 + h_4)} [h_4^2\phi_P - h_4^2\phi_W - h_2^2\phi_{WW} + h_2^2\phi_W] \quad (\text{B.18})$$

Dividing (B.16) by  $h_4$  and (B.17) by  $h_2$ ,

$$h_4\phi_P - h_4\phi_W = ah_2h_4 + bh_2^2h_4 \quad (\text{B.19})$$

$$h_2\phi_{WW} - h_2\phi_W = -ah_2h_4 + bh_4^2h_2 \quad (\text{B.20})$$

Adding (B.19) and (B.20),

$$b = \frac{1}{h_2h_4(h_2 + h_4)} [h_4\phi_P - h_4\phi_W + h_2\phi_{WW} - h_2\phi_W] \quad (\text{B.21})$$

At  $x = \frac{h_2}{2}$ ,

$$\begin{aligned} \phi_w - \phi_W = & \\ & \frac{\frac{h_2}{2} [h_4^2\phi_P - h_4^2\phi_W - h_2^2\phi_{WW} + h_2^2\phi_W] + \frac{h_2^2}{4} [h_4\phi_P - h_4\phi_W + h_2\phi_{WW} - h_2\phi_W]}{h_2h_4(h_2 + h_4)} \end{aligned} \quad (\text{B.22})$$

$$\begin{aligned}
 \phi_w &= (\phi_P \text{ terms :}) \\
 &\phi_P \frac{\left[ \frac{h_2 h_4^2}{2} + \frac{h_2^2 h_4}{4} \right]}{h_2 h_4 (h_2 + h_4)} \\
 &\equiv \phi_P \frac{\frac{1}{2} h_2 h_4 (h_4 + \frac{1}{2} h_2)}{h_2 h_4 (h_2 + h_4)} \\
 &\equiv \phi_P \frac{\frac{1}{2} (h_4 + \frac{1}{2} h_2)}{h_2 + h_4} \\
 &(+\phi_{WW} \text{ terms :}) \\
 &+ \phi_{WW} \frac{\left[ \frac{-h_2^3}{2} + \frac{h_2^2}{4} \right]}{h_2 h_4 (h_2 + h_4)} \\
 &\equiv -\phi_{WW} \frac{h_2^2}{4 h_4 (h_2 + h_4)} \\
 &\equiv -\phi_{WW} \frac{(\frac{1}{4} h_2^2)}{h_4 (h_2 + h_4)} \\
 &(+\phi_W \text{ terms :}) \\
 &+ \phi_W \frac{\left[ -\frac{h_2 h_4^2}{2} + \frac{h_2^3}{2} - \frac{h_2^2 h_4}{4} - \frac{h_2^3}{4} + h_2^2 h_4 + h_2 h_4^2 \right]}{h_2 h_4 (h_2 + h_4)} \\
 &\equiv +\phi_W \frac{\left[ \frac{h_2^3}{4} + \frac{3}{4} h_2^2 h_4 + \frac{1}{2} h_2 h_4^2 \right]}{h_2 h_4 (h_2 + h_4)} \\
 &\equiv \phi_W \frac{\left[ \frac{h_2^2}{4} (h_2 + h_4) + \frac{1}{2} h_2 h_4 (h_2 + h_4) \right]}{h_2 h_4 (h_2 + h_4)} \\
 &\equiv \phi_W \left[ \frac{1}{4} \frac{h_2}{h_4} + \frac{1}{2} \right]
 \end{aligned} \tag{B.23}$$

Therefore

$$\phi_w = \phi_P \frac{\left[ \frac{1}{2} (h_4 + \frac{1}{2} h_2) \right]}{h_2 + h_4} + \phi_W \left[ \frac{1}{4} \frac{h_2}{h_4} + \frac{1}{2} \right] - \phi_{WW} \frac{\left[ \frac{1}{4} h_2^2 \right]}{h_4 (h_2 + h_4)} \tag{B.24}$$

Hence by inspection:

$$\begin{aligned}
 u_w > 0 \quad \phi_w &= \frac{[\frac{1}{2}(h_4 + \frac{1}{2}h_2)]}{h_2 + h_4} \phi_P + \left[ \frac{1}{4} \frac{h_2}{h_4} + \frac{1}{2} \right] \phi_W - \frac{(\frac{1}{4}h_2^2)}{h_4(h_2 + h_4)} \phi_{WW} \\
 u_w < 0 \quad \phi_w &= \frac{[\frac{1}{2}(h_1 + \frac{1}{2}h_2)]}{h_1 + h_2} \phi_W + \left[ \frac{1}{4} \frac{h_2}{h_1} + \frac{1}{2} \right] \phi_P - \frac{(\frac{1}{4}h_2^2)}{h_1(h_1 + h_2)} \phi_E \\
 u_e > 0 \quad \phi_e &= \frac{[\frac{1}{2}(h_2 + \frac{1}{2}h_1)]}{h_1 + h_2} \phi_E + \left[ \frac{1}{4} \frac{h_1}{h_2} + \frac{1}{2} \right] \phi_P - \frac{(\frac{1}{4}h_1^2)}{h_2(h_1 + h_2)} \phi_W \\
 u_e < 0 \quad \phi_e &= \frac{[\frac{1}{2}(h_3 + \frac{1}{2}h_1)]}{h_1 + h_3} \phi_P + \left[ \frac{1}{4} \frac{h_1}{h_3} + \frac{1}{2} \right] \phi_E - \frac{(\frac{1}{4}h_1^2)}{h_3(h_1 + h_3)} \phi_{EE}
 \end{aligned} \tag{B.25}$$

$$c_e \phi_e - c_w \phi_w + Diff = 0 \tag{B.26}$$

$$\begin{aligned}
 & |c_e, 0| \frac{[\frac{1}{2}h_2 + \frac{1}{4}h_1]}{h_1 + h_2} \phi_E + |c_e, 0| \left[ \frac{1}{4} \frac{h_1}{h_2} + \frac{1}{2} \right] \phi_P - |c_e, 0| \frac{[\frac{1}{4}h_1^2]}{h_2(h_1 + h_2)} \phi_W \\
 & - |-c_e, 0| \frac{[\frac{1}{2}h_3 + \frac{1}{4}h_1]}{h_1 + h_3} \phi_P - |-c_e, 0| \left[ \frac{1}{4} \frac{h_1}{h_3} + \frac{1}{2} \right] \phi_E + |-c_e, 0| \frac{[\frac{1}{4}h_1^2]}{h_3(h_1 + h_3)} \phi_{EE} \\
 & - |c_w, 0| \frac{[\frac{1}{2}h_4 + \frac{1}{4}h_2]}{h_2 + h_4} \phi_P - |c_w, 0| \left[ \frac{1}{4} \frac{h_2}{h_4} + \frac{1}{2} \right] \phi_W + |c_w, 0| \frac{[\frac{1}{4}h_2^2]}{h_4(h_2 + h_4)} \phi_{WW} \\
 & + |-c_w, 0| \frac{[\frac{1}{2}h_1 + \frac{1}{4}h_2]}{h_1 + h_2} \phi_W + |-c_w, 0| \left[ \frac{1}{4} \frac{h_2}{h_1} + \frac{1}{2} \right] \phi_P - |-c_w, 0| \frac{[\frac{1}{4}h_2^2]}{h_1(h_1 + h_2)} \phi_E \\
 & + Diff = 0
 \end{aligned} \tag{B.27}$$

Putting  $\phi_{EE}$  and  $\phi_{WW}$  in the source term as they are outside the tri-diagonal method, the first batch of sources follows:

$$Su_1 = - |-c_e, 0| \frac{[\frac{1}{4}h_1^2]}{h_3(h_1 + h_3)} \phi_{EE} - |c_w, 0| \frac{[\frac{1}{4}h_2^2]}{h_4(h_2 + h_4)} \phi_{WW} \tag{B.28}$$

Considering the central column of terms in B.27

$$\begin{aligned}
 & |c_e, 0| \left[ \frac{3}{4} + \frac{1}{4} \left( \frac{h_1}{h_2} - 1 \right) \right] \phi_P + |-c_w, 0| \left[ \frac{3}{4} + \frac{1}{4} \left( \frac{h_2}{h_1} - 1 \right) \right] \phi_P \\
 & = |-c_e, 0| \left[ \frac{3}{4} + \frac{1}{4} \left( \frac{h_1}{h_3} - 1 \right) \right] \phi_E + |c_w, 0| \left[ \frac{3}{4} + \frac{1}{4} \left( \frac{h_2}{h_4} - 1 \right) \right] \phi_W \quad (\text{B.29})
 \end{aligned}$$

gives,

$$\frac{3}{4} |c_e, 0| \phi_P + \frac{3}{4} |-c_w, 0| \phi_P = \frac{3}{4} |-c_e, 0| \phi_E + \frac{3}{4} |c_w, 0| \phi_W \quad (\text{B.30})$$

and a second batch of sources

$$\begin{aligned}
 Su_2 = & |c_e, 0| \frac{1}{4} \left( 1 - \frac{h_1}{h_2} \right) \phi_P + |-c_w, 0| \frac{1}{4} \left( 1 - \frac{h_2}{h_1} \right) \phi_P \\
 & + |-c_e, 0| \frac{1}{4} \left( \frac{h_1}{h_3} - 1 \right) \phi_E + |c_w, 0| \frac{1}{4} \left( \frac{h_2}{h_4} - 1 \right) \phi_W \quad (\text{B.31})
 \end{aligned}$$

The third batch of sources comes from column 3 of B.27

$$Su_3 = |c_e, 0| \frac{\left[ \frac{1}{4} h_1^2 \right]}{h_2(h_1 + h_2)} \phi_W + |-c_w, 0| \frac{\left[ \frac{1}{4} h_2^2 \right]}{h_1(h_1 + h_2)} \phi_E \quad (\text{B.32})$$

The first column of B.27 gives the fourth source term

$$\begin{aligned}
 Su_4 = & |-c_e, 0| \frac{\left[ \frac{1}{2} h_3 + \frac{1}{4} h_1 \right]}{h_1 + h_3} \phi_P + |c_w, 0| \frac{\left[ \frac{1}{2} h_4 + \frac{1}{4} h_2 \right]}{h_2 + h_4} \phi_P \\
 & - |c_e, 0| \frac{\left[ \frac{1}{2} h_2 + \frac{1}{4} h_1 \right]}{h_1 + h_2} \phi_E - |-c_w, 0| \frac{\left[ \frac{1}{2} h_1 + \frac{1}{4} h_2 \right]}{h_1 + h_2} \phi_W \quad (\text{B.33})
 \end{aligned}$$

Reintroducing diffusion and subtracting  $\frac{3}{4}(c_e - c_w)$  from the LHS

$$\begin{aligned} \left[ d_e + \frac{3}{4} |c_e, 0| - \frac{3}{4} c_e \right] \phi_P + \left[ d_w + \frac{3}{4} |-c_w, 0| + \frac{3}{4} c_w \right] \phi_P \\ = \left[ d_e + \frac{3}{4} |-c_e, 0| \right] \phi_E + \left[ d_w + \frac{3}{4} |c_w, 0| \right] \phi_W \quad (\text{B.34}) \end{aligned}$$

Therefore  $a_e = d_e + \frac{3}{4} |-c_e, 0|$  and  $a_w = d_w + \frac{3}{4} |c_w, 0|$ , which are always positive, increasing diagonal dominance of the coefficient matrix. The final source term will become  $\sum_{n=1}^4 S u_n$ .

For the  $v$  equation in the  $y$ -direction:

For  $v_s > 0$ ,

$$\phi - \phi_S = ay + by^2$$

Taking the datum at  $S$ ,

$$y = +g_2 \rightarrow \phi_P - \phi_S = ag_2 + bg_2^2$$

$$y = -g_4 \rightarrow \phi_{SS} - \phi_S = -ag_4 + bg_4^2$$

$$a = \frac{1}{g_2 g_4 (g_2 + g_4)} [g_4^2 \phi_P - g_4^2 \phi_S - g_2^2 \phi_{SS} + g_2^2 \phi_S] \quad (\text{B.35})$$

$$b = \frac{1}{g_2 g_4 (g_2 + g_4)} [g_4 \phi_P - g_4 \phi_S + g_2 \phi_{SS} - g_2 \phi_S] \quad (\text{B.36})$$

at  $y = \frac{g_7}{2}$ ,

$$\begin{aligned} \phi_s - \phi_S = \frac{g_7}{2g_2 g_4 (g_2 + g_4)} [g_4^2 \phi_P - g_4^2 \phi_S - g_2^2 \phi_{SS} + g_2^2 \phi_S] \\ + \frac{g_7^2}{4g_2 g_4 (g_2 + g_4)} [g_4 \phi_P - g_4 \phi_S + g_2 \phi_{SS} - g_2 \phi_S] \quad (\text{B.37}) \end{aligned}$$

( $\phi_P$  terms:)

$$\frac{2g_7g_4^2 + g_7^2g_4}{4g_2g_4(g_2 + g_4)} \equiv \frac{\frac{1}{2}g_7\frac{g_4}{g_2} + \frac{1}{4}\frac{g_7^2}{g_2}}{g_2 + g_4} \equiv \frac{\frac{1}{2}\frac{g_7}{g_2}(g_4 + \frac{1}{2}g_7)}{g_2 + g_4} \quad (\text{B.38})$$

( $\phi_{SS}$  terms:)

$$\frac{-2g_7g_2^2 + g_7^2g_2}{4g_2g_4(g_2 + g_4)} \equiv \frac{-g_7(2g_2 - g_7)}{4g_4(g_2 + g_4)} \equiv \frac{-\frac{g_7}{g_4}(\frac{1}{2}g_2 - \frac{1}{4}g_7)}{(g_2 + g_4)} \quad (\text{B.39})$$

( $\phi_S$  terms:)

$$\begin{aligned} & 1 + \frac{-2g_4^2g_7 + 2g_7g_2^2 - g_7^2g_4 - g_7^2g_2}{4g_2g_4(g_2 + g_4)} \\ \equiv & \frac{4g_2^2g_4 + 4g_2g_4^2 - 2g_4^2g_7 + 2g_7g_2^2 - g_7^2g_4 - g_7^2g_2}{4g_2g_4(g_2 + g_4)} \\ \equiv & \frac{-g_7^2(g_2 + g_4) + 2g_7(g_2 - g_4)(g_2 + g_4) + 4g_2g_4(g_2 + g_4)}{4g_2g_4(g_2 + g_4)} \\ \equiv & \frac{2g_7(g_2 - g_4) + 4g_2g_4 - g_7^2}{4g_2g_4} \quad (\text{B.40}) \\ \equiv & \frac{g_7(2g_2 - g_7) + 2g_4(2g_2 - g_7)}{4g_2g_4} \\ \equiv & \frac{(2g_2 - g_7)(2g_4 + g_7)}{4g_2g_4} \\ \equiv & \frac{(g_2 - \frac{1}{2}g_7)(g_4 + \frac{1}{2}g_7)}{g_2g_4} \end{aligned}$$

This gives,

$$\begin{aligned}
 v_s > 0 : \phi_s &= \begin{bmatrix} \frac{\frac{1}{2}g_7(g_4 + \frac{1}{2}g_7)}{g_2 + g_4} \\ \frac{\frac{1}{2}g_6(g_1 + \frac{1}{2}g_6)}{g_1 + g_2} \\ \frac{\frac{1}{2}g_6(g_2 + \frac{1}{2}g_6)}{g_1 + g_2} \\ \frac{\frac{1}{2}g_5(g_3 + \frac{1}{2}g_5)}{g_3 + g_1} \end{bmatrix} \phi_P + \begin{bmatrix} \frac{(g_2 - \frac{1}{2}g_7)(g_4 + \frac{1}{2}g_7)}{g_2g_4} \\ \frac{(g_2 - \frac{1}{2}g_6)(g_1 + \frac{1}{2}g_6)}{g_1g_2} \\ \frac{(g_1 - \frac{1}{2}g_6)(g_2 + \frac{1}{2}g_6)}{g_1g_2} \\ \frac{(g_1 - \frac{1}{2}g_5)(g_3 + \frac{1}{2}g_5)}{g_3g_1} \end{bmatrix} \phi_S - \begin{bmatrix} \frac{\frac{g_7}{g_4}(\frac{1}{2}g_2 - \frac{1}{4}g_7)}{g_2 + g_4} \\ \frac{\frac{g_6}{g_1}(\frac{1}{2}g_2 - \frac{1}{4}g_6)}{g_1 + g_2} \\ \frac{\frac{g_6}{g_2}(\frac{1}{2}g_1 - \frac{1}{4}g_6)}{g_1 + g_2} \\ \frac{\frac{g_5}{g_3}(\frac{1}{2}g_1 - \frac{1}{4}g_5)}{g_3 + g_1} \end{bmatrix} \begin{matrix} \phi_{SS} \\ \phi_N \\ \phi_S \\ \phi_{NN} \end{matrix} \\
 v_s < 0 : \phi_s &= \begin{bmatrix} \frac{\frac{1}{2}g_6(g_1 + \frac{1}{2}g_6)}{g_1 + g_2} \\ \frac{\frac{1}{2}g_6(g_2 + \frac{1}{2}g_6)}{g_1 + g_2} \\ \frac{\frac{1}{2}g_5(g_3 + \frac{1}{2}g_5)}{g_3 + g_1} \end{bmatrix} \phi_S + \begin{bmatrix} \frac{(g_2 - \frac{1}{2}g_6)(g_1 + \frac{1}{2}g_6)}{g_1g_2} \\ \frac{(g_1 - \frac{1}{2}g_6)(g_2 + \frac{1}{2}g_6)}{g_1g_2} \\ \frac{(g_1 - \frac{1}{2}g_5)(g_3 + \frac{1}{2}g_5)}{g_3g_1} \end{bmatrix} \phi_P - \begin{bmatrix} \frac{\frac{g_6}{g_1}(\frac{1}{2}g_2 - \frac{1}{4}g_6)}{g_1 + g_2} \\ \frac{\frac{g_6}{g_2}(\frac{1}{2}g_1 - \frac{1}{4}g_6)}{g_1 + g_2} \\ \frac{\frac{g_5}{g_3}(\frac{1}{2}g_1 - \frac{1}{4}g_5)}{g_3 + g_1} \end{bmatrix} \begin{matrix} \phi_N \\ \phi_S \\ \phi_{NN} \end{matrix} \\
 v_n > 0 : \phi_n &= \begin{bmatrix} \frac{\frac{1}{2}g_6(g_1 + \frac{1}{2}g_6)}{g_1 + g_2} \\ \frac{\frac{1}{2}g_6(g_2 + \frac{1}{2}g_6)}{g_1 + g_2} \\ \frac{\frac{1}{2}g_5(g_3 + \frac{1}{2}g_5)}{g_3 + g_1} \end{bmatrix} \phi_N + \begin{bmatrix} \frac{(g_1 - \frac{1}{2}g_6)(g_2 + \frac{1}{2}g_6)}{g_1g_2} \\ \frac{(g_1 - \frac{1}{2}g_6)(g_2 + \frac{1}{2}g_6)}{g_1g_2} \\ \frac{(g_1 - \frac{1}{2}g_5)(g_3 + \frac{1}{2}g_5)}{g_3g_1} \end{bmatrix} \phi_P - \begin{bmatrix} \frac{\frac{g_6}{g_2}(\frac{1}{2}g_1 - \frac{1}{4}g_6)}{g_1 + g_2} \\ \frac{\frac{g_6}{g_2}(\frac{1}{2}g_1 - \frac{1}{4}g_6)}{g_1 + g_2} \\ \frac{\frac{g_5}{g_3}(\frac{1}{2}g_1 - \frac{1}{4}g_5)}{g_3 + g_1} \end{bmatrix} \begin{matrix} \phi_S \\ \phi_S \\ \phi_{NN} \end{matrix} \\
 v_n < 0 : \phi_n &= \begin{bmatrix} \frac{\frac{1}{2}g_5(g_3 + \frac{1}{2}g_5)}{g_3 + g_1} \\ \frac{\frac{1}{2}g_5(g_3 + \frac{1}{2}g_5)}{g_3 + g_1} \\ \frac{\frac{1}{2}g_5(g_3 + \frac{1}{2}g_5)}{g_3 + g_1} \end{bmatrix} \phi_P + \begin{bmatrix} \frac{(g_1 - \frac{1}{2}g_5)(g_3 + \frac{1}{2}g_5)}{g_3g_1} \\ \frac{(g_1 - \frac{1}{2}g_5)(g_3 + \frac{1}{2}g_5)}{g_3g_1} \\ \frac{(g_1 - \frac{1}{2}g_5)(g_3 + \frac{1}{2}g_5)}{g_3g_1} \end{bmatrix} \phi_N - \begin{bmatrix} \frac{\frac{g_5}{g_3}(\frac{1}{2}g_1 - \frac{1}{4}g_5)}{g_3 + g_1} \\ \frac{\frac{g_5}{g_3}(\frac{1}{2}g_1 - \frac{1}{4}g_5)}{g_3 + g_1} \\ \frac{\frac{g_5}{g_3}(\frac{1}{2}g_1 - \frac{1}{4}g_5)}{g_3 + g_1} \end{bmatrix} \begin{matrix} \phi_{NN} \\ \phi_{NN} \\ \phi_{NN} \end{matrix}
 \end{aligned} \tag{B.41}$$

Using  $c_n\phi_n - c_s\phi_s + Diff = 0$ ,

$$\begin{aligned}
 & |c_n, 0| \left[ \frac{\frac{1}{2}\frac{g_6}{g_1}(g_2 + \frac{1}{2}g_6)}{g_1 + g_2} \right] \phi_N + |c_n, 0| \left[ \frac{(g_1 - \frac{1}{2}g_6)(g_2 + \frac{1}{2}g_6)}{g_1g_2} \right] \phi_P - |c_n, 0| \left[ \frac{\frac{g_6}{g_2}(\frac{1}{2}g_1 - \frac{1}{4}g_6)}{g_1 + g_2} \right] \phi_S \\
 & - |-c_n, 0| \left[ \frac{\frac{1}{2}\frac{g_5}{g_1}(g_3 + \frac{1}{2}g_5)}{g_3 + g_1} \right] \phi_P - |-c_n, 0| \left[ \frac{(g_1 - \frac{1}{2}g_5)(g_3 + \frac{1}{2}g_5)}{g_3g_1} \right] \phi_N + |-c_n, 0| \left[ \frac{\frac{g_5}{g_3}(\frac{1}{2}g_1 - \frac{1}{4}g_5)}{g_3 + g_1} \right] \phi_{NN} \\
 & - |c_s, 0| \left[ \frac{\frac{1}{2}\frac{g_7}{g_2}(g_4 + \frac{1}{2}g_7)}{g_2 + g_4} \right] \phi_P - |c_s, 0| \left[ \frac{(g_2 - \frac{1}{2}g_7)(g_4 + \frac{1}{2}g_7)}{g_2g_4} \right] \phi_S + |c_s, 0| \left[ \frac{\frac{g_7}{g_4}(\frac{1}{2}g_2 - \frac{1}{4}g_7)}{g_2 + g_4} \right] \phi_{SS} \\
 & + |-c_s, 0| \left[ \frac{\frac{1}{2}\frac{g_6}{g_2}(g_1 + \frac{1}{2}g_6)}{g_1 + g_2} \right] \phi_S + |-c_s, 0| \left[ \frac{(g_2 - \frac{1}{2}g_6)(g_1 + \frac{1}{2}g_6)}{g_1g_2} \right] \phi_P - |-c_s, 0| \left[ \frac{\frac{g_6}{g_1}(\frac{1}{2}g_2 - \frac{1}{4}g_6)}{g_1 + g_2} \right] \phi_N \\
 & + Diff = 0
 \end{aligned} \tag{B.42}$$

Batch 1 sources:

$$Su_1 = -|-c_n, 0| \left[ \frac{\frac{g_5}{g_3}(\frac{1}{2}g_1 - \frac{1}{4}g_5)}{g_3 + g_1} \right] \phi_{NN} - |c_s, 0| \left[ \frac{\frac{g_7}{g_4}(\frac{1}{2}g_2 - \frac{1}{4}g_7)}{g_2 + g_4} \right] \phi_{SS} \tag{B.43}$$

Considering the central column of terms from B.42

$$\begin{aligned}
 & |c_n, 0| \left[ \frac{(g_1 - \frac{1}{2}g_6)(g_2 + \frac{1}{2}g_6)}{g_1g_2} \right] \phi_P + |-c_s, 0| \left[ \frac{(g_2 - \frac{1}{2}g_6)(g_1 + \frac{1}{2}g_6)}{g_1g_2} \right] \phi_P \\
 & = |-c_n, 0| \left[ \frac{(g_1 - \frac{1}{2}g_5)(g_3 + \frac{1}{2}g_5)}{g_3g_1} \right] \phi_N + |c_s, 0| \left[ \frac{(g_2 - \frac{1}{2}g_7)(g_4 + \frac{1}{2}g_7)}{g_2g_4} \right] \phi_S \quad (\text{B.44})
 \end{aligned}$$

Subtracting  $\frac{3}{4}(c_n - c_s)$  from the RHS gives.

$$\begin{aligned}
 & |c_n, 0| \frac{3}{4} \phi_P + |c_n, 0| \left[ \frac{(g_1 - \frac{1}{2}g_6)(g_2 + \frac{1}{2}g_6)}{g_1g_2} - \frac{3}{4} \right] \phi_P \\
 & \quad + |-c_s, 0| \frac{3}{4} \phi_P + |-c_s, 0| \left[ \frac{(g_2 - \frac{1}{2}g_6)(g_1 + \frac{1}{2}g_6)}{g_1g_2} - \frac{3}{4} \right] \phi_P \\
 & = |-c_n, 0| \frac{3}{4} \phi_N + |-c_n, 0| \left[ \frac{(g_1 - \frac{1}{2}g_5)(g_3 + \frac{1}{2}g_5)}{g_3g_1} - \frac{3}{4} \right] \phi_N \\
 & \quad + |c_s, 0| \frac{3}{4} \phi_S + |c_s, 0| \left[ \frac{(g_2 - \frac{1}{2}g_7)(g_4 + \frac{1}{2}g_7)}{g_2g_4} - \frac{3}{4} \right] \phi_S \quad (\text{B.45})
 \end{aligned}$$

Subtracting  $\frac{3}{4}(c_n - c_s)$  from the LHS ensures the terms for  $\phi_P$  are identical to those for  $\phi_N$  and  $\phi_S$ . Reintroducing diffusion gives

$$\begin{aligned}
 & \left[ d_n + \frac{3}{4} |c_n, 0| - \frac{3}{4} c_n \right] \phi_P + \left[ d_s + \frac{3}{4} |-c_s, 0| + \frac{3}{4} c_s \right] \phi_P \\
 & = \left[ d_n + \frac{3}{4} |-c_n, 0| \right] \phi_N + \left[ d_s + \frac{3}{4} |c_s, 0| \right] \phi_S \quad (\text{B.46})
 \end{aligned}$$

Giving the standard form of the coefficients  $a_n = d_n + \frac{3}{4} |-c_n, 0|$  and  $a_s = d_s + \frac{3}{4} |c_s, 0|$  and a source term:



$$\begin{aligned}
 Su_2 = & |c_n, 0| \left[ \frac{3}{4} - \frac{(g_1 - \frac{1}{2}g_6)(g_2 + \frac{1}{2}g_6)}{g_1g_2} \right] \phi_P + |-c_s, 0| \left[ \frac{3}{4} - \frac{(g_2 - \frac{1}{2}g_6)(g_1 + \frac{1}{2}g_6)}{g_1g_2} \right] \phi_P \\
 & + |-c_n, 0| \left[ \frac{(g_1 - \frac{1}{2}g_5)(g_3 + \frac{1}{2}g_5)}{g_3g_1} - \frac{3}{4} \right] \phi_N + |c_s, 0| \left[ \frac{(g_2 - \frac{1}{2}g_7)(g_4 + \frac{1}{2}g_7)}{g_2g_4} - \frac{3}{4} \right] \phi_S
 \end{aligned} \tag{B.47}$$

The third source can be shown to be

$$Su_3 = |c_n, 0| \left[ \frac{g_6}{g_2} \frac{(\frac{1}{2}g_1 - \frac{1}{4}g_6)}{g_1 + g_2} \right] \phi_S + |-c_s, 0| \left[ \frac{g_6}{g_1} \frac{(\frac{1}{2}g_2 - \frac{1}{4}g_6)}{g_1 + g_2} \right] \phi_N \tag{B.48}$$

and the fourth source:

$$\begin{aligned}
 Su_4 = & -|c_n, 0| \left[ \frac{\frac{1}{2}g_6}{g_1} \frac{(g_2 + \frac{1}{2}g_6)}{(g_1 + g_2)} \right] \phi_N + |-c_n, 0| \left[ \frac{\frac{1}{2}g_5}{g_1} \frac{(g_3 + \frac{1}{2}g_5)}{(g_1 + g_3)} \right] \phi_P \\
 & + |c_s, 0| \left[ \frac{\frac{1}{2}g_7}{g_2} \frac{(g_4 + \frac{1}{2}g_7)}{(g_2 + g_4)} \right] \phi_P - |-c_s, 0| \left[ \frac{\frac{1}{2}g_5}{g_2} \frac{(g_1 + \frac{1}{2}g_6)}{(g_1 + g_2)} \right] \phi_S
 \end{aligned} \tag{B.49}$$

Similarly terms for the other directions and equations can be obtained.

### B.3 Implementation of generalised cell face approximations

Using the standard first order upwind scheme to define the neighbour coefficients  $a_p, a_e, a_w$ , extra source terms are required to create a higher order scheme.

For the CD4 scheme, we start by using

$$c_e\phi_e - c_w\phi_w = 0 \quad (\text{B.50})$$

where

$$\phi_e = \alpha_1\phi_W + \alpha_2\phi_P + \alpha_3\phi_E + \alpha_4\phi_{EE} \quad (\text{B.51})$$

$$\phi_w = \alpha_1\phi_{WW} + \alpha_2\phi_W + \alpha_3\phi_P + \alpha_4\phi_E \quad (\text{B.52})$$

with the  $\alpha$  terms representing the coefficients of the polynomial representation in Equation 4.7.

Taking all terms to the RHS,

$$\begin{aligned} 0 = & -c_e\alpha_1\phi_W - c_e\alpha_2\phi_P - c_e\alpha_3\phi_E - c_e\alpha_4\phi_{EE} \\ & + c_w\alpha_1\phi_{WW} + c_w\alpha_2\phi_W + c_w\alpha_3\phi_P + c_w\alpha_4\phi_E \end{aligned} \quad (\text{B.53})$$

Terms of (B.53) are added as a source term, however this alone does not conform to the general form of  $a_p = \sum a_{nb}$ .

If we take the terms for each  $\phi$  term we can write

$$a_e = (c_w\alpha_4 - c_e\alpha_3) \quad a_w = (c_w\alpha_2 - c_e\alpha_1) \quad (\text{B.54})$$

$$a_{ee} = -c_e\alpha_4 \quad a_{ww} = c_w\alpha_1 \quad (\text{B.55})$$

$$a_p = a_e + a_w + a_{ee} + a_{ww} \quad (\text{B.56})$$

$a_p\phi_P = \sum a_{nb}\phi_{NB}$  can be rearranged as

$$\begin{aligned}
 0 = & c_w \alpha_4 \phi_E - c_w \alpha_3 \phi_E + c_w \alpha_2 \phi_W - c_e \alpha_1 \phi_W \\
 & - c_e \alpha_4 \phi_{EE} + c_w \alpha_1 \phi_{WW} \\
 & - c_w \alpha_4 \phi_P + c_e \alpha_3 \phi_P - c_w \alpha_2 \phi_P \\
 & + c_e \alpha_1 \phi_P + c_e \alpha_4 \phi_P - c_w \alpha_1 \phi_P \quad (\text{B.57})
 \end{aligned}$$

This is the source term required and is obtained by adding  $(c_e - c_w)\phi_P$  to the RHS of (B.53). Adding this extra term to (B.53) is more convenient as the cell face velocities,  $u_e$  and  $u_w$ , are used in the  $c_e$  and  $c_w$  terms and also used in the extra source term. The extra source term can then be written as

$$S_{CD4} = (c_w \phi_w) - (c_e \phi_e) + (c_e - c_w) \phi_P \quad (\text{B.58})$$

To leave only the higher order discretisation, the initial first order convective terms must be cancelled via another source,  $S_{1UP}$ , which is easily computed when the neighbour coefficients are generated and is given by (B.59).

$$S_{1UP} = C_e^{1UP}(\phi_P - \phi_E) + C_w^{1UP}(\phi_P - \phi_W) \quad (\text{B.59})$$

Here,  $C_e^{1UP}$  and  $C_w^{1UP}$  are the convective part of the standard first order upwind neighbour coefficients ( $|-c_e, 0|$  and  $|c_w, 0|$ ) respectively). Terms for the N-S and F-B directions can be added by inspection. Time dependence can also be added by taking into account older time levels in the discretised equations.